Mission Requirements Analysis and Level 2 Error Characterization for CarbonSat Nadir Observations over Land

WP 1100, 2000 & 4100 Report

ESA Study
CarbonSat Earth Explorer 8 Candidate Mission
“Level-1 Level-2 (L1L2) Performance Assessment Study“
ESA Contract N^{o} 4000109814/13/NL/FF/lf

Lead author:
Michael.Buchwitz@iup.physik.uni-bremen.de,
Institute of Environmental Physics (IUP) / Institute of Remote Sensing (IFE),
University of Bremen (UB), Bremen, Germany

Co-authors:
H. Bovensmann, T. Krings, M. Reuter, V. V. Rozanov, P. Liebing, IUP-UB, Germany
J. Landgraf, F. Alkemade, SRON, Utrecht, The Netherlands

Change log

Version	Date	Status	Reason for change
Draft 0.1	31 July 2014	Made available for study team members for initial inputs	New document
Draft 1	19 Aug 2014	As submitted	Additional content added (polarization, non-linearity, etc.)
Draft 2	26 Sept 2014	As submitted	SRON inputs added (spatial co-registration, polarization); (primarily) text changes related to “degree of polarization” (Sections 8.2 and 9.4); minor editorial improvements at various places
Draft 3	13 Jan 2015	As submitted	ESA comments on Draft 2 considered; some figures added; several improvements related to “post-MTR” assessments (e.g., revised sections on polarization incl. max. DOP and related L2 errors, Integrated Energy (IE) and related aspects, new assessment related to inhomogeneous scenes, etc.); description of new gain matrix files; remaining SRON inputs added; several minor editorial improvements at various places
Draft 4	17 Mar 2015	Made available for project internal use.	Update error budget; improved sections on Integrated Energy (IE) and heterogeneous scenes / Pseudo Noise (PN); new sub-sections added (reference spectra for out-of-band straylight assessments, angle of polarization (AOP), SWIR-2 fitwindow studies); several minor editorial improvements at various places
Draft 5	2 June 2015	Made available for project internal use.	Error budget section improved (e.g., typo in error budget corrected, split of ESRA uncertainties into components). New polarization histogram figure from SRON included. Several minor editorial improvements at various places.
Version 1	25 June 2015	As submitted	HSS section added. Several minor editorial improvements at various places.
Version 1.1	2 Dec 2015	As submitted	Comments from ESA (YM) considered
Version 1.2	3 Dec 2015	As submitted	Comment from ESA (YM) considered

Table of Contents

1. Executive Summary

This document describes CarbonSat mission requirements analysis and Level 2 error characterization approaches and results as obtained within the ESA Study "CarbonSat Earth Explorer 8 Candidate Mission - Level-1 Level-2 (L1L2) Performance Assessment Study".

This study ("CSL1L2-II study") is a follow-on study of a predecessor study ("CSL1L2-I study") whose results are reported in the final report of that study **/CS L1L2-I-Study FR/**.

In this CSL1L2-II study primarily those aspects are covered which have not or not been fully been covered via the predecessor study. The predecessor study led to improved mission requirements and within this follow-on study requirements have been further consolidated. This is also true for aspects related to Level 2 error characterization, an aspect closely related to instrument requirements.

CarbonSat's main observation mode is the "nadir mode". In the context of CarbonSat and this document this essentially means "all CarbonSat observations except those acquired under sun-glint (or glitter) conditions over water". CarbonSat will also perform observations in "sun-glint mode", especially to improve the quality of the CO_2 and CH_4 data products over oceans. A final decision about the observation strategy has not yet been made. Therefore it is not yet exactly known what fraction of the observations will be made under sun-glint conditions. However, sun-glint conditions will very likely only be encountered for a relatively small fraction of the total number of observations. Most of the observations will be made in nadir mode, i.e., outside of sun-glint conditions. This document ("nadir TN") focuses on nadir mode observations over land. Ocean sun-glint related aspects are reported in a separate document ("glint TN").

Aspects covered in this document are: Update of Level 2 error budget, a description of the simulation framework used for error analysis, update of Level 2 error analysis due to clouds and aerosols, reference spectra ("gain matrix" files, polarized radiance spectra, etc.), radiometric, spectral and spatial co-registration related requirements, for example. The main findings related to the aspects covered in this document are summarized in Section 4 ("Error budget").

In summary, various assessments have been carried out related to CarbonSat Level 1 requirement and Level 2 error characterization and an improved Level 2 error budget has been established (see Sect. 4). Requirements as given in the Missions Requirements Document (MRD, version 1.2) have either been confirmed or recommendations for modifications have been given, which typically resulted in somewhat relaxed requirements.

2. Purpose of Document

A focus of this study is on further consolidating the CarbonSat mission requirements.

In this document CarbonSat mission requirements analysis results are reported. It is described which requirements have been addressed, why they have been addressed, which analysis methods have been used and what the results are.

This activity is a continuation of the activities which had been performed in a precursor study **/CS L1L2-I-Study FR/**.

This document focusses on CarbonSat nadir mode observations over land. Ocean sun-glint related aspects are covered in a separate document.

Another focus is the Level 2 error characterization for the nadir mode observations over land. Aspects covered are bias correction methods, stricter quality filtering, etc., with the goal to reduce systematic biases as much as possible.

3. Introduction

This document describes the Work Package (WP) 1100, 2000 and 4100 results of the ESA study “CarbonSat Earth Explorer 8 Candidate Mission - Level-1 Level-2 (L1L2) Performance Assessment Study”.

.

WP 1100 summarizes the results generated in the other nadir mode related WPs (2000 and 4100) and compiles an error budget for the Level 2 errors. This error budget related activity is described in a separate section (the following one) in this document referring to the results generated in the other WPs, which are reported in other sections of this document.

WP 2000 focusses on “Mission Requirements Analysis” focussing on Level 1 data and is linking L1 requirements with L2 expected performance.
WP 2000 consists of the following sub-WPs:

- **WP 2100**: “Co-registration”
- **WP 2200**: “Analysis impact of dynamic range requirement over land”
- **WP 2300**: “Signal-to-Noise Ratio (SNR) requirements for High Spatial Sampling (HSS) channels”
- **WP 2400**: “Integrated energy and spatial under-/oversampling: Impact on point source emission estimates”
- **WP 2500**: “Retrieval simulations for dedicated Level-1 requirements – Nadir Land”.

WP 4100 focusses on Level 2 error characterization for the nadir mode observations over land. Aspects covered are bias correction methods, stricter quality filtering and other aspects which contribute to the goal to reduce systematic biases as much as possible.

Starting point for the activities described in this document was the latest version of the CarbonSat Mission Requirements Document (MRD), which was available at the beginning of this study. This document is MRDv1.2 **/CS MRD v1.2, 2013/**.

Furthermore, the analysis continued from the XCO_2 and XCH_4, i.e., Level 2 (L2), error budget (EB), version 1 (v1), which had been established in the precursor study **/CS L1L2-I-Study FR/**.

Within this document it is reported to what extent certain Level 1 (L1) requirements can/need to be optimized taking into account the L2 error budget. However, the L2 error budget has some flexibility, i.e., there is some freedom on how to split the required maximum permitted total L2 error into its various components. This is done using an iterative approach by investigating how to optimally split the total error into its components. For example, if one or several requirements need to be relaxed it needs to be identified which other requirements need to be tightened such that the

overall L2 error meets the user requirement. The EB is presented in the following section and its content is referred to in later sections of this document where it is reported how the estimated performance of CarbonSat is related to the required performance as listed in the L2 EB. On the other hand, the EB section also contains a high-level summary reporting how the L2 error budget components are related to the individual mission requirements addressed in this document.

4. Updated Level 2 error budget for nadir observations over land

In this section an updated error budget (EB) for the CarbonSat nadir observations over land is presented and described (Work Package WP 1100).

The final EB version 5 (EBv5) originates from the initial error budget (EBv1), which had been established in the predecessor study **/CS L1L2-I-Study FR/ /Buchwitz et al., 2013c/**. Within the framework of this project, EBv1 has been updated to consider the detailed results presented later in this document. The updated EBv5 is shown in **Table 1**.

Table 1 lists overall uncertainties for random and systematic errors of all identified error sources. Overall uncertainty has been computed via root-sum-square (RSS) from the random and systematic components.

The individual errors have been added to obtain total errors (see bottom right “Total (root-sum-square (RSS))”, which are compared with the required performance as listed in the cells directly below. The listed values of the required threshold performance are from the CarbonSat Mission Requirements Documents (MRD) v1.2 **/CS MRD v1.2, 2013/**.

As shown in this document, for most of the values listed in **Table 1**,a large number of simulated retrievals have been performed to establish the errors (for example for errors related to clouds and aerosols and instrument related errors). For some other parameters, however, the values have to be interpreted as a requirement (e.g., for spectroscopy).

In particular for the various instrument related requirements it has been investigated within this study to what extent the mission requirements given in MRDv1.2 **/CS MRD v1.2, 2013/** can be relaxed or need to be strengthened. The main purpose of this document is to present the analysis which have been carried out to address this and related aspects. Therefore, the numbers listed in **Table 1** are referred to at several places in this document.

Note that especially the instrument related error sources listed in **Table 1** may consist of several components as explained in more detail later in this document.

CarbonSat XCO_2 and XCH_4 Error Budget Nadir/Land (v5)						
Error source	**Overall uncertainty**		**Required maximum error**			
			Random error per sounding "Precision"		**Systematic error** (monthly regional-scale, non-constant part only) "Relative accuracy"	
Algorithm	**XCO_2 [ppm]**	**XCH_4 [ppb]**	**XCO_2 [ppm]**	**XCH_4 [ppb]**	**XCO_2 [ppm]**	**XCH_4 [ppb]**
Clouds & aerosols	0.50	4.24	0.40	3.00	0.30	3.00
Meteorology (p_o, T, H_2O)	0.14	1.13	0.10	0.80	0.10	0.80
Spectroscopy	0.14	1.13	0.10	0.80	0.10	0.80
Other	0.14	1.13	0.10	0.80	0.10	0.80
Instrument (Threshold)						
Signal-to-Noise Ratio (SNR)	1.20	9.00	1.20	9.00	0.00	0.00
Radiometric: Multiplicative / absolute Multiplicative / relative Additive (zero level offset)	 0.20 0.45 0.20	 1.97 4.47 1.97	 0.17 0.40 0.17	 1.80 4.00 1.80	 0.10 0.20 0.10	 0.80 2.00 0.80
Instrument Spectral Response Function (ISRF)	0.20	1.97	0.17	1.80	0.10	0.80
Spectral calibration	0.20	1.97	0.17	1.80	0.10	0.80
Spatio-temporal co-registration	0.48	3.00	0.48	3.00	0.00	0.00
Heteogeneous scenes / Pseudo Noise (PN)	0.32	2.62	0.30	2.50	0.10	0.80
Other	0.14	1.13	0.10	0.80	0.10	0.80
Total (root-sum-square (RSS)):			**1.50**	**11.69**	**0.47**	**4.33**
Required (MRDv1.2, threshold (T)):			**3.00**	**12.00**	**0.50**	**5.00**
All values 1-sigma						

Table 1: CarbonSat error budget for the XCO_2 and XCH_4 data products over land version 5 (EBv5). EBv5 is an update of EBv1 presented in **/Buchwitz et al., 2013c/**.

For example error source "Radiometric Multiplicative / relative" consist of three major components:

- Effective Spectral Radiometric Accuracy (ESRA),
- Relative Spectral Radiometric Accuracy (RSRA) and
- Relative Spatial Radiometric Accuracy (RxRA), as explained in **Sect. 9.3**),

whereas error source "Radiometric Multiplicative / absolute" is primarily related to the Absolute Radiometric Accuracy (ARA) requirement (see **Sect. 9.7**).

ESRA covers the following four components and the allocated overall uncertainties for XCO_2 / XCH_4 are:

- Polarization: 0.1 ppm / 1 ppb
- Non-linearity: 0.3 ppm / 3 ppb
- Straylight: 0.16 ppm / 2 ppb
- Diffuser specles: 0.16 ppm / 2 ppb

Total RSS: 0.39 ppm / 4.3 ppb

In the following it is described for each error source how the corresponding values listed in **Table 1** have been derived and/or how they have to be interpreted:

Algorithm: Clouds & aerosols:

Clouds and aerosols are known to be a major error source for satellite XCO_2 and XCH_4 retrievals (see, e.g., **/Buchwitz et al., 2013a/** and references given therein) as – via scattering - they influence the light path in the atmosphere. Scattering effects are, in principle, considered using "Full Physics" (FP) retrieval algorithms such as BESD/C (see **/Bovensmann et al., 2010/** and **/Buchwitz et al., 2013a/**), which has been used within this study for CarbonSat nadir observations over land. However, some error typically remains.

This error has systematic but also random components. The size of these components depends on the spatio-temporal averaging interval but also on the time and location of the observations. They depend on how much aerosol and cloud parameters vary within a given spatio-temporal averaging interval and to what extent these variations can be considered by the retrieval algorithm. How large these errors are not only depends on the instrument. The more information on aerosols and clouds the instrument observations provide, and the better the retrieval algorithm can extract and use this information, the smaller the cloud and aerosol related XCO_2 and XCH_4 errors will be.

Error due to clouds and aerosols for CarbonSat observations over land and ocean have been addressed in quite some detail already in the predecessor study **/CS L1L2-I-Study FR/**. Error due to clouds and aerosols have also been assessed in the framework of the ESA LOGOFLUX study **/Chimot et al., 2014/** and key results have been published in the peer-reviewed literature /**Buchwitz et al., 2013a/**.

Within this study additional assessments are presented using the latest version of the BESD/C retrieval algorithm (see **Sect. 6**).

The various analysis carried out for CarbonSat indicate that the cloud and aerosol related errors listed in **Table 1** are realistic, as shown in, for example, **Sect. 6**, and in **/Buchwitz et al., 2013a/**.

In **/Buchwitz et al., 2013a/** it is shown that, for example for Europe, 97.7% of the quality filtered XCO_2 observations have biases below 0.5 ppm and 66.7% are below 0.3 ppm, and similar results have also been obtained for other regions such as the USA, China and Amazonia. For XCH_4 it has been shown that for Europe 81.1% of the observations have biases less than 2 ppb and 99.7% have biases less than 4 ppb and similar results have also been obtained for other regions. For monthly averages at 5^ox5^o spatial resolution the residual XCO_2 biases are mostly in the +/-0.4 ppm range for XCO_2 and mostly in the +/-3 ppb range for XCH_4. However, these estimates are derived using somewhat simplified assumptions as, for example, aerosol type related errors have not been considered in **/Buchwitz et al., 2013a/**. Therefore, within this study and within the parallel LOGOFLUX-II study, a focus was on also considering aerosol type related errors (and partially also aerosol profile related errors). Adding additional error sources increases the error. Therefore, a bias correction scheme has been developed to reduce systematic errors. Furthermore, the retrieval algorithm has also been improved focussing on reducing aerosol and cirrus related errors. As shown in this document (especially in **Sect. 6** and **Sect. 7.2**) and in **/Buchwitz et al., 2014/** these improvements result in overall errors which are even somewhat smaller than the errors shown in **/Buchwitz et al., 2013a/** even if aerosol type related errors are included.

Overall it is therefore concluded that the errors for clouds and aerosols as listed in **Table 1** are realistic and may even have some margin.

Algorithm: Meteorology:

The CarbonSat spectra contain information on atmospheric temperature, surface pressure and on the water vapour vertical column. Information on these parameters is retrieved via BESD/C in addition to XCO_2 and XCH_4. For temperature a temperature profile shift is retrieved, for the pressure profile a profile scaling factor is retrieved and the water vapour vertical column is also retrieved. However, surface pressure is tightly constrained in the latest version of the BESD/C retrieval algorithm in order to be able to better retrieve scattering related cloud and aerosol parameters. It can be assumed that high quality information on surface pressure (or even pressure profiles) will be available from meteorological centres such as ECMWF. The same is true for other meteorological parameters such as temperature and humidity profiles.

The availability of reliable a priori information together with the high information content of the CarbonSat spectra w.r.t. these parameters will ensure that XCO_2 and XCH_4 errors due meteorological parameters will be quite small, i.e., close to or possibly even less than the errors listed in **Table 1**.

Algorithm: Spectroscopy:

Spectroscopic data are input data for the retrieval algorithm and errors in the spectroscopic data will result in errors of the retrieved XCO_2 and XCH_4 data products. Improving spectroscopic input data is an area where significant progress has been made during recent years (e.g., in support of NASA's OCO-2 mission) and significant further improvements can be expected for the coming years. In order to quantify the impact of spectroscopic errors one needs reliable spectroscopic error estimates at least for all major lines and all potentially critical parameters of these lines. Within this study no detailed simulations have been carried out (this would have required to assume certain errors). The values listed in **Table 1** are therefore only rough estimates. They have to be interpreted as a requirement.

Algorithm: Other:

Placeholder for potentially missing algorithm related aspects and/or additional margin.

Instrument: Signal-to-Noise Ratio (SNR):

Signal-to-Noise Ratios (SNRs) for CarbonSat radiance spectra have been computed using a CarbonSat instrument model **/Bovensmann et al., 2010/** and using the required SNR (threshold) performance as specified in MRD v1.2 **/CS MRD v1.2, 2013/**. The BESD/C retrieval algorithm has been used to compute how noise on the radiance maps onto XCO_2 and XCH_4 random errors ("theoretical retrieval precision").

The values listed in **Table 1** are consistent with the many results related to this aspect which have been obtained in related ESA studies **/CS L1L2-I-Study FR/ /Chimot et al., 2014/,** in peer-reviewed publications **/Bovensmann et al., 2010/ /Buchwitz et al., 2013a/** and via the latest simulations reported in this document.

Instrument: Radiometric: Multiplicative: absolute and relative:

Several requirements are listed in the MRD v1.2 **/CS MRD v1.2, 2013/** related to multiplicative radiometric errors.

Errors which have spectral features, which may correlate with the spectral features of interest, i.e., most notably with the absorption features of CO_2 and CH_4, are the most relevant.

However, quantifying the resulting XCO_2 and XCH_4 errors requires realistic estimates of the expected erroneous spectral instrument features (or residual calibration errors). This information is currently not available.

Erroneous spectral features may be due to residual errors related to polarization, straylight or other aspects. To deal with this, so called Gain Matrices (GMs) have been generated and delivered to ESA (e.g., **Sect. 8.1**). The GMs can be used in combination with the expected spectral radiance error to compute the resulting XCO_2 and XCH_4 errors. The delivered GMs have been / are used during instrument design and optimization in order to make sure that the requirements on the XCO_2 and XCH_4 errors are not exceeded. Some aspects related to this are discussed in the document such as errors related to non-linearity (see **Sect. 13**) and polarization (see **Sect. 17**).

To deal with spectral features a dedicated requirement has been formulated in the MRD v1.2 **/CS MRD v1.2, 2013/**, the "Effective Spectral Radiometric Accuracy (ESRA)" requirement and the delivered GMs are a key component of this requirement.

Despite the GM approach, some radiometric errors which result in spectral features have been investigated in detail, e.g., polarization related errors. XCO_2 and XCH_4 biases resulting from polarization related radiance errors have been assessed using simulated CarbonSat nadir mode retrievals. It has been found that the biases can be very large if no correction is applied and a fully polarization sensitive instrument is used (this was not a surprise but expected). In this case the biases can be as large as several ppm for XCO_2 and several 10 ppb for XCH_4. For example, the XCO_2 bias is approx. 2.5 ppm for SZA 50^o. In this case the degree of polarization (DOP) is 0.6 (60%) in the NIR band. Note that DOP corresponds to the Polarization Sensitivity (PS) as used in MR-OBS-280 of **/CS MRD v1.2, 2013/**, where it is required that PS is less than 2% (T). If the PS is reduced from 60% to 2% (as required) and assuming that linear error analysis is valid, this would correspond to a XCO_2 bias of 0.083 ppm (= 2.5 / 30), which would be in line with the polarization related error as listed above (< 0.1 ppm (T)). For XCH_4 the bias can be as large as 25 ppb without correction. In this case DOP is 90% in the NIR band. If the PS reduced from 90% to 2% and assuming that linear error analysis is valid, this would correspond to a XCH_4 bias of ~0.6 ppb (= 25 / 45), which would be in line with the polarization related error as listed above (< 1 ppb). Polarization related radiance errors have also been computed using several instrument Mueller Matrices as provided by industry. If the radiance errors are computed using these instrument Mueller Matrices, the biases are reduced to below 0.02 ppm for XCO_2 and below 0.15 ppb for XCH_4. Assuming that the instrument performance as modelled using the provided Mueller Matrices is realistic, it is concluded that polarization related XCO_2 and XCH_4 biases will be very small. Based on the required / estimated polarization sensitivity and the analysis performed it is concluded that the errors listed above are realistic.

Requirements for multiplicative radiometric errors which do not have spectral features are formulated via a number of other requirements, most notably the "Relative Spectral Radiometric Accuracy" (RSRA) and the "Relative Spatial Radiometric Accuracy" (RxRA) requirements as formulated in MRD v1.2 **/CS MRD v1.2, 2013/**. Within this study detailed simulations have been carried out to quantify XCO_2 and

XCH_4 errors resulting from RSRA and RxRA related errors (see **Sect. 9.3**). It has been found that the values as listed in **/CS MRD v1.2, 2013/** can be somewhat relaxed, should this be necessary.

Absolute Radiometric Accuracy (ARA) is needed, for example, to retrieve accurate surface albedos (as done via a BESD/C pre-processing algorithm). This aspect is discussed in **Sect. 9.7** and the values listed in **Table 1** are consistent with this analysis. Note that certain aspects related to ARA are also covered by the zero level offset (ZLO), RSRA, RxRA and other requirements, as these requirements (also) constrain the possible deviations of the measured radiance from the true radiance.

Instrument: Radiometric: Additive (zero level offset):

This aspect has been investigated in detail in this study (**Sect. 9.2**). It has been shown that the errors as listed in **Table 1** are likely not exceeded, even if the ZLO requirement as given in MRD v1.2 **/CS MRD v1.2, 2013/** would be somewhat relaxed. This however requires some assumptions with respect to the wavelength dependence of the ZLO and also requires a correction procedure during Level1-2 processing.

Instrument: Instrument Spectral Response Function (ISRF) / Homogeneous scenes:

An initial assessment of XCO_2 and XCH_4 errors due to errors of the Instrument Spectral Response Function (ISRF) for homogeneous scenes has been carried out in the framework of the predecessor study **/CS L1L2-I-Study FR/**. It has been shown using worst case assumptions that errors can be as large as about ~1 ppm for XCO_2 and ~5-10 ppb for XCH_4. It is however not clear how likely the worst case assumptions are and what the characteristics of the resulting XCO_2 and XCH_4 errors are. If the ISRF error would be constant, than it likely will be relatively easy to correct for this error to a significant extent. But even if the errors listed above are not constant and if they are a realistic estimate for peak-to-peak errors, this would mean that a 1-sigma error would very likely be 4 or more times smaller (assuming peak-to-peak corresponds to 4-sigma), i.e., ~0.2 ppm for XCO_2 and ~1-2 ppb for XCH_4, which is close to the errors listed **Table 1** for this error source. It is therefore concluded that the values listed in **Table 1** for this error source are reasonable to good estimates. Note that errors due to inhomogeneous scenes causing “Pseudo Noise” (PN) have been excluded here as this aspect is covered separately (see **Sect. 9.6**).

Instrument: Spectral calibration:

The impact of spectral calibration errors on the quality of the retrieved XCO_2 and XCH_4 is mitigated using “shift and squeeze/stretch” parameters which are part of the retrieval algorithm BESD/C. Critical are only wavelength calibration errors which cannot be modelled using shift and squeeze/stretch. To what extent these errors exist is currently unknown. The values listed in **Table 1** are therefore not based on assuming how a residual error may look like but have to be interpreted as a requirement rather than an established fact.

Instrument: Spatio-temporal co-registration:

It has been estimated that mis-registration error on CarbonSat CO_2 and CH_4 column retrieval due to differences in surface elevation for single-band co-registration errors between 5-20% of the instrument footprint, or 100-400 m, respectively. Pixel elevation has been estimated from the SRTM3 data set. CH_4 and CO_2 retrievals are performed using the RemoTeC model for simulated CarbonSat measurements. Based on two model atmospheres with a boundary layer aerosol and an elevated scattering layer, the mean retrieval error on the retrieved CH_4 and CO_2 total column is estimated over China.

For CO_2, the mean co-registration errors are somewhat higher but do not exceed 0.2 ppm/0.05% (goal) and 0.3 ppm/0.07% (threshold). To assess this error contribution, we have to consider also co-registration errors due to the spatially heterogeneity of optically thin cirrus clouds in the observed scene. In the previous study, this was estimated to be ≤ 0.4 ppm for the required instrument performance. Keeping in mind that the total CO_2 temporal-spatial co-registration error must be less than 0.5 ppm, we conclude that the estimated performance is within the error budget but leaves no room for relaxation.

On smaller spatial scales, retrieval errors can exceed these values. However, we have shown that the pixel internal elevation variability can be used as an effective data filter to reject most critical scenes. Errors due to spatial mis-registration of bands can be interpreted as a pseudo-noise contribution and so the assigned total co-registration error of about 0.1% of the CarbonSat error budget can be distributed between the two relevant error sources, i.e. spatial variability of cirrus and surface elevation, in a statistical manner. This yields a maximum of 0.07% for the maximum co-registration errors due to surface elevation differences between different bands.

Thus, it is concluded that the CarbonSat inter-band co-registration requirements is supported by the error analysis of this study but no room is left for a relaxation of this requirement.

Instrument: Heterogeneous scenes / Pseudo Noise (PN):

Assessments have been carried out in the framework of the predecessor study to quantify the so-called “Pseudo Noise” arising from inhomogeneous spectrometer entrance slit illumination in case of inhomogeneous scenes ***/CS L1L2-I-Study FR/***. If uncorrected at instrument level inhomogeneous slit illumination will result in fluctuations of the ISRF, i.e., will result in ISRF changes which vary from ground pixel to ground pixel. If not considered or not fully considered in the retrieval this will primarily result in enhanced noise (random error) of the retrieved XCO_2 and XCH_4 and, depending on scene, also one some residual bias when computing spatio-temporal averages.

Simulated retrievals have been carried out in the predecessor study ***/CS L1L2-I-Study FR/*** and it has been found that for worst case situations (using a limited number of cases) the precision degradation can be 60% for XCO_2 (e.g., 1.6 ppm instead of 1 ppm) and 35% for XCH_4 (e.g., 13.5 ppb instead of 10 ppb). Typical errors are expected to be much smaller but it had been highlighted that this needs to be confirmed by analysing more scenes and by also using more realistic ISRF perturbations than was possible for the predecessor study.

To address this, additional simulations have been carried out in this study based on (extreme) artificial scenes and realistic inhomogeneous scenes using high spatial resolution Airborne Visible / Infrared Imaging Spectrometer (AVIRIS) radiances. The results indicate that the performance as listed in the error budget (**Table 1**) for error source “Heterogeneous scenes / Pseudo Noise (PN)“ can be achieved if the additional ISRF error due to inhomogeneous scenes is less than about 2% of the maximum value of the unperturbed ISRF.

Instrument: Other:

Place holder for not yet considered instrument related aspects and/or additional margin.

5. CarbonSat simulation framework

5.1. Overview

A simulation framework has been developed in order to generate – for pre-selected scenarios (e.g., atmospheric composition and surface properties) – simulated CarbonSat spectra and to perform corresponding XCO_2 and XCH_4 retrievals in order to obtain XCO_2 and XCH_4 random and systematic errors and averaging kernels.

The simulation framework used for this study is essentially identical to the framework used in the predecessor study.

Figure 1 presents an overview of the simulation framework for CarbonSat's nadir mode observations over land. A similar framework has also been generated for CarbonSat's glint mode observations over ocean (described separately in the technical note on glint-mode observation related aspects).

The framework consists of a data base with atmospheric and surface information, a Radiative Transfer Model (RTM), a CarbonSat instrument simulator and a L1-to-L2 (L1-2) retrieval program.

The XCO_2 and XCH_4 random errors are available via the standard output of the (Optimal Estimation based) retrieval program. They are primarily determined by the instrument noise (but to some extent they also depend on the definition of the state vector as used for the retrieval program). The retrieval program essentially maps the spectral errors onto the random error of the retrieved parameters. The retrieval program also generates the averaging kernels as standard output.

Systematic errors are computed via "retrieved – true", where the true values for XCO_2 and XCH_4 have been obtained from the known model atmosphere used to generate the modelled CarbonSat spectrum.

The individual components of the simulation framework are shortly described in the following sub-sections.

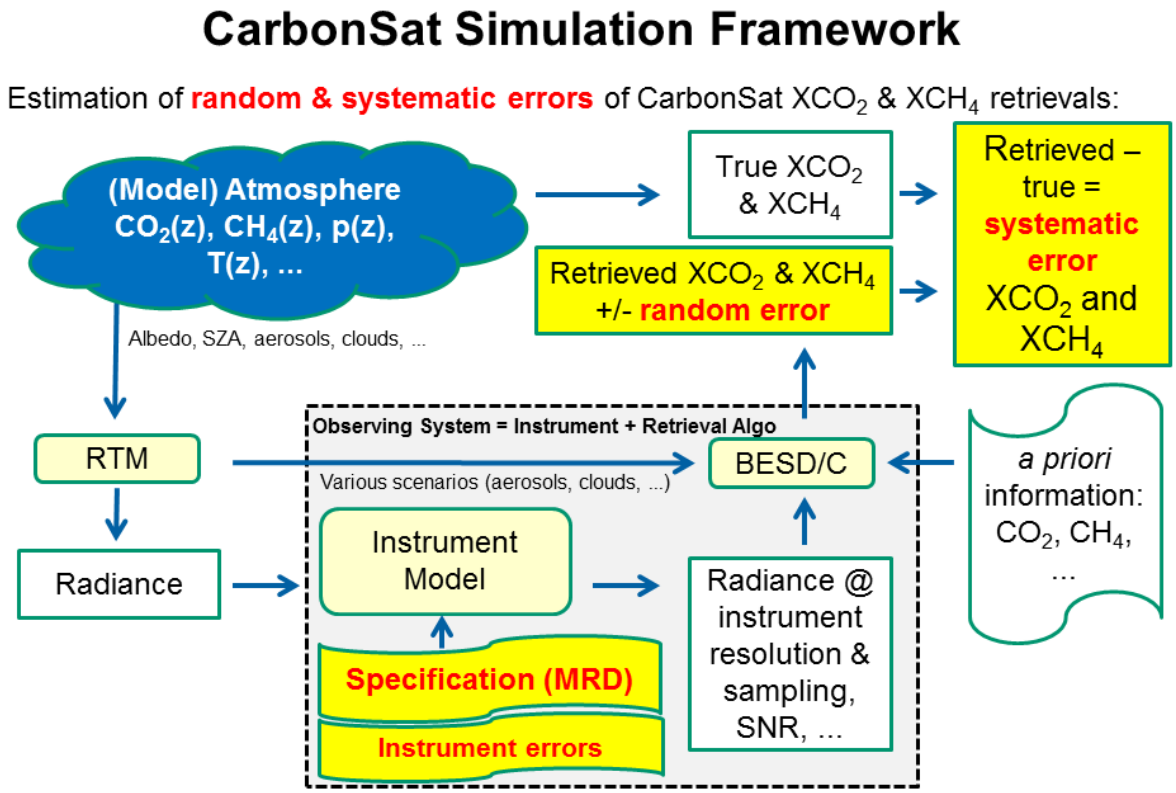

Figure 1: CarbonSat simulation framework.

5.2. Radiative transfer model

The Radiative Transfer Model (RTM) used by IUP-UB is SCIATRAN **/Rozanov et al., 2005, 2006, 2014/**. In the context of this study SCIATRAN has been used to compute monochromatic radiance spectra for the CarbonSat spectral bands for various scenarios defined by, e.g., solar zenith angle, surface reflectivity, atmospheric composition, etc. The same version of SCIATRAN had also been used in the predecessor study **/CS L1L2-I-Study FR/**.

5.3. CarbonSat instrument simulator

The CarbonSat instrument simulator at University of Bremen has the same functionality as the instrument simulator used by University of Leicester for the CarbonSat ocean sun-glint observations.

Monochromatic spectra are convolved with the CarbonSat Instrument Line Shape (ILS) function (a Gaussian ILS is assumed in this document if not stated otherwise) and mapped onto the spectral grid of CarbonSat according to spectral sampling and band pass. Noise is calculated for each spectral element according to the Signal-to-Noise Ratio (SNR) specification.

The IUP-UB CarbonSat instrument simulator is described in **/Buchwitz et al., 2013a/** and **/Bovensmann et al., 2010/**. It had also been used in the predecessor study **/CS L1L2-I-Study FR/**.

The most relevant CarbonSat instrument parameters are listed in **Table 2**. Simulated CarbonSat spectra are shown in **Figure 2** and **Figure 3**.

Figure 2 is based on using the previous SNR model **/Buchwitz et al., 2013a/** and **Figure 3** is based on using the latest SNR model **/CS MRD v1.2, 2013/** with parameters corresponding to the threshold performance.

Both SNR models have been used for the results shown in this document. The latest SNR model gives higher SNR values in the continuum, as can be seen by comparing **Figure 3** with **Figure 2**, but lower SNR values in the line centers. As also shown in this document, both SNR models give nearly identical performance in terms of XCO_2 and XCH_4 precision and accuracy.

Parameter	Spectral band			Comment
	NIR	SWIR-1	SWIR-2	
Spectral range [nm]	747 - 773	1590 - 1675	1925 - 2095	-
Spectral resolution FWHM [nm]	0.1	0.3	0.55	FWHM is the "Full Width at Half Maximum" of the Instrument Spectral Response Function (ISRF)
Spectral Sampling Ratio (SSR) [1/FWHM]	3	3	3	SSR is the number of spectral elements (detector pixel) per spectral resolution FWHM.
Signal-to-Noise Ratio (SNR) [-] (threshold performance)	386 / 473 @ 2.0×10^{13}	prev. / latest 323 / 347 @ 4.1×10^{12}	236 / 274 @ 9.9×10^{11}	Single observation Signal-to-Noise Ratio (SNR) @ given radiance in photons/s/nm/cm^2/sr using two SNR models, the previous model (**/Buchwitz et al., 2013a/**) and the latest model (**/CS MRD v1.2, 2013/**)

Table 2: Instrument parameters for the CarbonSat simulations.

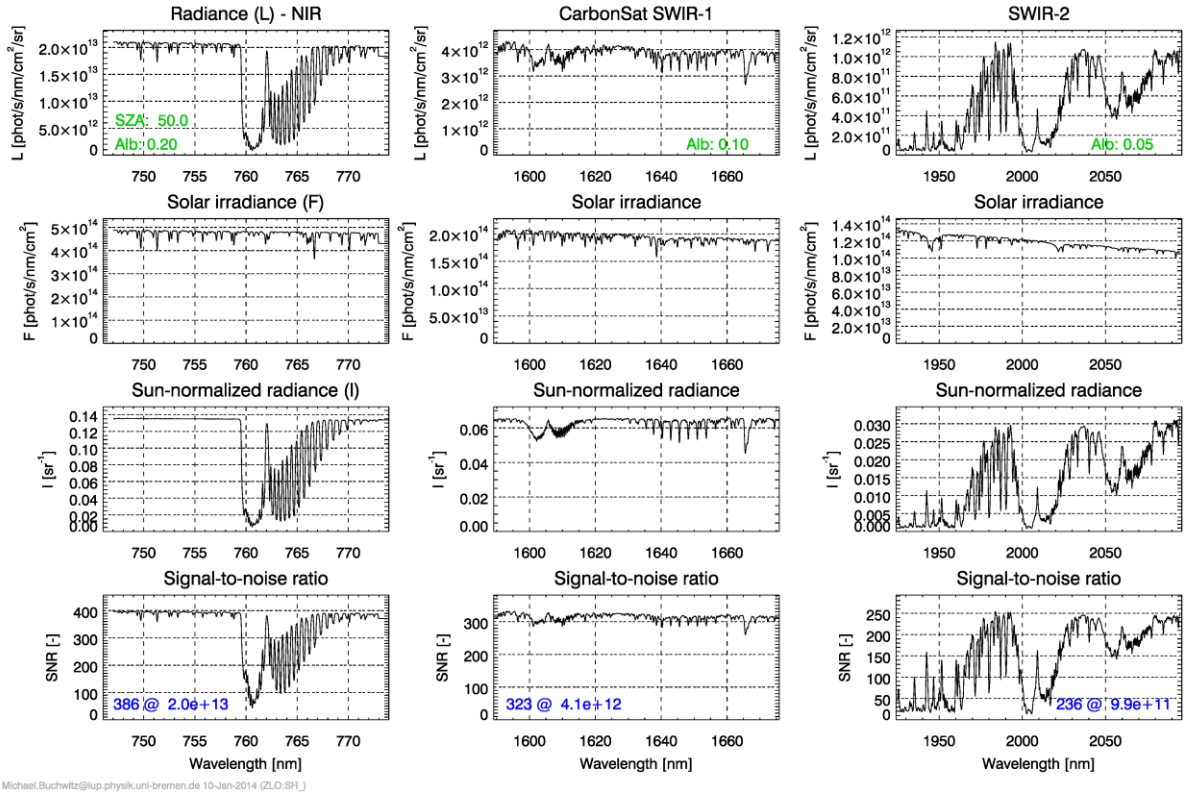

Figure 2: Simulated CarbonSat spectra for a scenario with vegetation surface albedo and SZA = 50^o ("VEG50"). Here the "previous SNR model" **/Buchwitz et al., 2013a/** has been used. This model has been used for some of the results shown in this document. It has lower SNR in the continuum but higher SNR in the absorption lines compared to the latest version of the SNR model shown in **Figure 3**. Overall, it is essentially equivalent for XCO_2 and XCH_4 retrieval in terms of precision and accuracy as shown in this document.

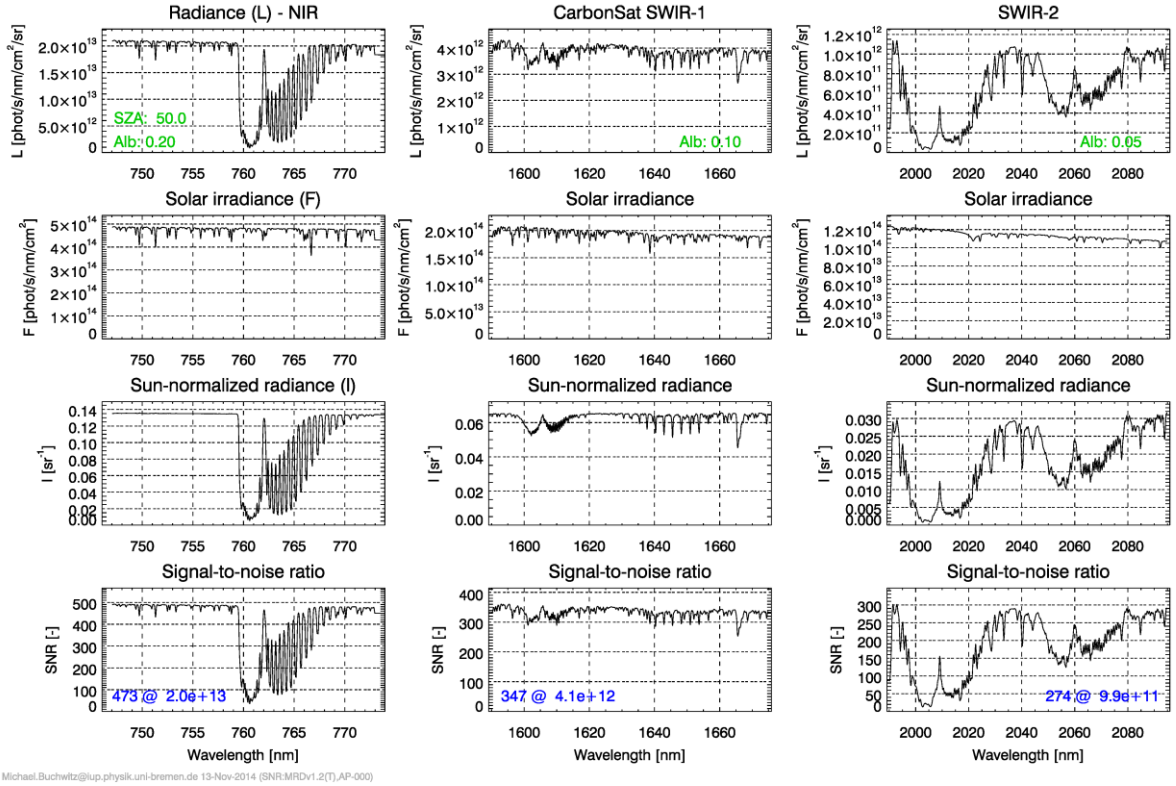

Figure 3: As **Figure 2** but for the latest SNR model **/CS MRD v1.2, 2013/**. Note that here only the "red" (long wavelength) part of band SWIR-2 is shown (SWIR-2B and SWIR-2C) as used for BESD/C optimal estimation 3-band retrieval. The "blue" part (SWIR-2A) is used for pre-processing and not shown here.

5.4. Retrieval method BESD/C

The BESD/C retrieval algorithm is described in detail in **/Bovensmann et al., 2010/** and **/Buchwitz et al., 2013a/**. BESD/C had also been used in the predecessor study **/CS L1L2-I-Study FR/**.

In short, BESD/C is a "Full Physics" (FP) retrieval algorithm based on Optimal Estimation (OE) **/Rodgers, 2000/** applied to all three CarbonSat spectral bands simultaneously ("3-band approach"). **Figure 4** presents an overview about the OE mathematical formulas, which are explained in detail elsewhere (e.g., **/Rodgers, 2000/**, **/Bovensmann et al., 2010/**). BESD/C uses the RTM SCIATRAN as forward model **/Rozanov et al., 2005, 2006, 2014/**.

Matrix K, shown in **Figure 4**, is the BESD/C Jacobian matrix and **Figure 5** shows a typical example (x-y zoom are shown in **Figure 6** and **Figure 7**).

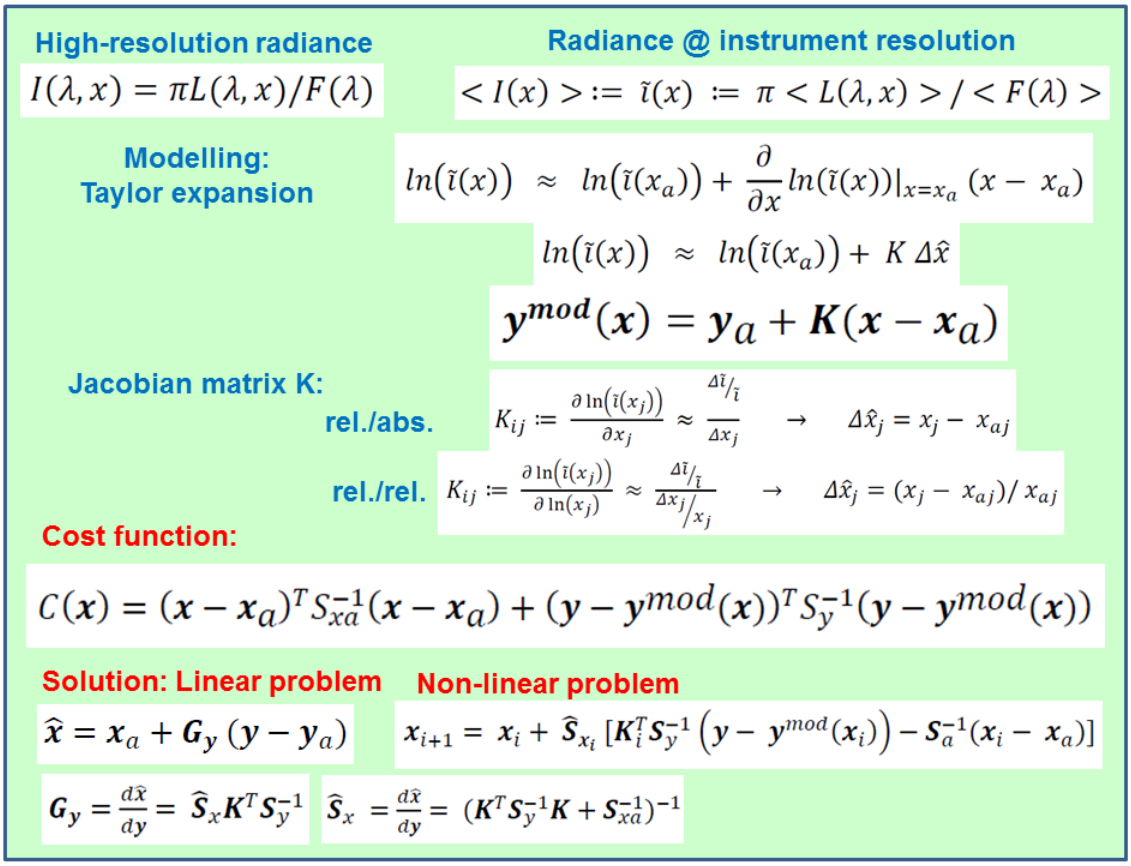

Figure 4: Overview Optimal Estimation (OE) formulas as used by BESD/C. For OE in general please see **/Rodgers, 2000/** and for the CarbonSat retrieval applications see **/Bovensmann et al., 2010/**. Matrix K is the BESD/C Jacobian matrix.

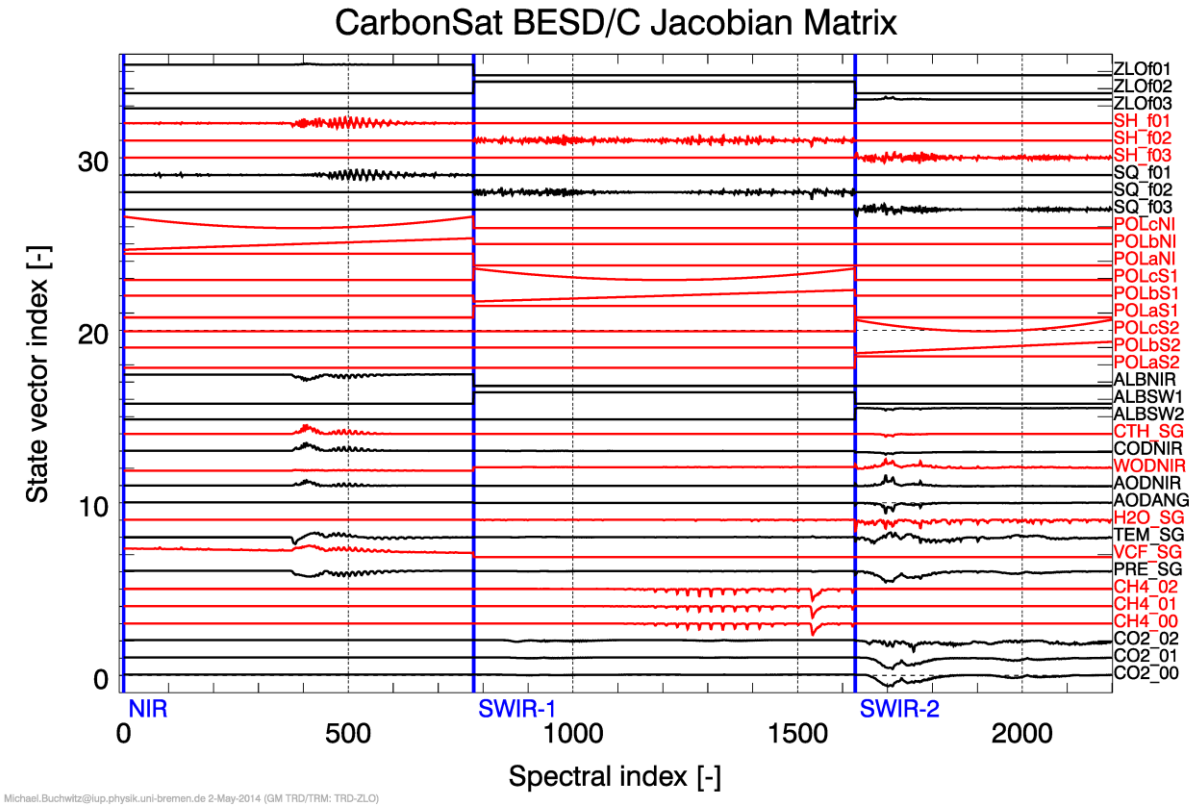

Figure 5: Example for a typical CarbonSat BESD/C Jacobian matrix. See **/Buchwitz et al., 2013a/** and **/Bovensmann et al., 2010/** for details. x-y-zooms are shown in **Figure 6** and **Figure 7**.

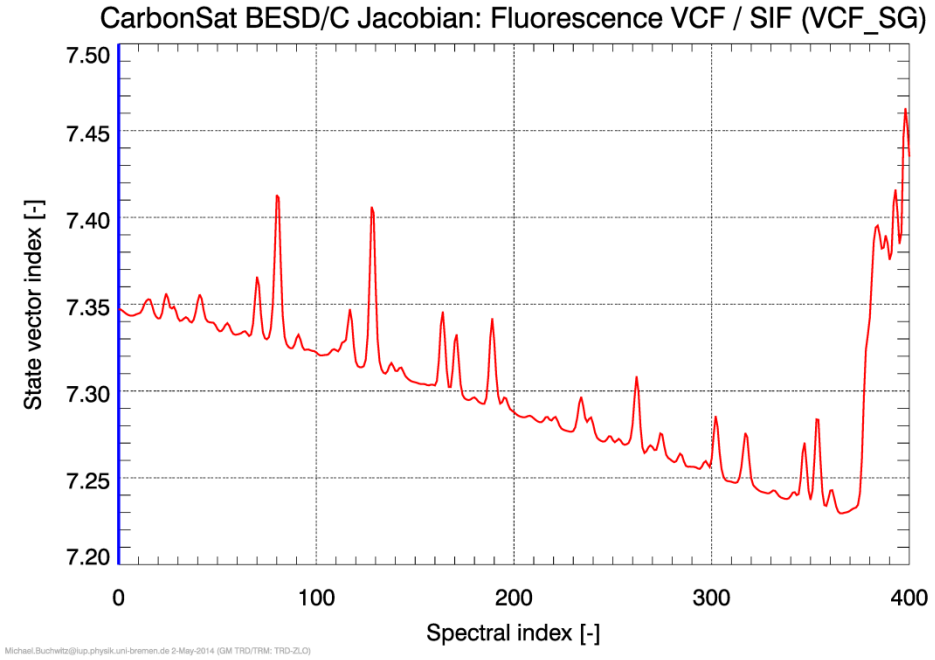

Figure 6: Zoom into previous figure to show details of the Vegetation Fluorescence / Solar Induced Fluorescence (VCF/SIF) Jacobian located in the blue end (shortest wavelengths around 755 nm) of CarbonSats NIR band. The spectral features are correlated with clear solar Fraunhofer lines whose relative depths depends on VCF/SIF emission and this region will be used to retrieve VCF/SIF at 755 nm from CarbonSat **/Buchwitz et al., 2013a/** and is used within this study to obtain a priori and first guess VCF/SIR information for the full 3-band BESD/C Optimal Estimation (OE) retrieval.

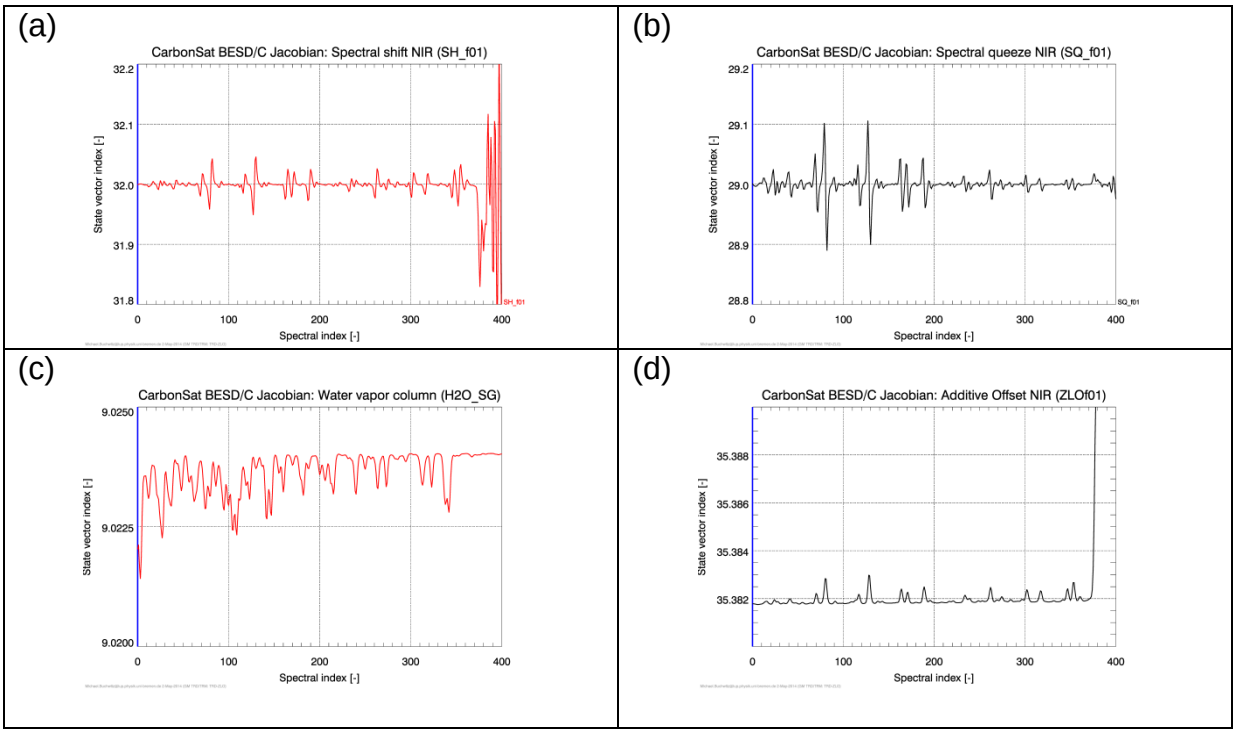

Figure 7: As **Figure 6** but for (a) spectral shift, (b) spectral squeeze, (c) water vapour column and (d) additive radiance offset (or zero-level-offset (ZLO)).

Figure 8 shows an overview about BESD/C. Five quantities are retrieved via pre-processing steps to obtain first guess and *a priori* values for five state vector elements used as input for the OE 3-band retrieval: (i) Surface albedo in each band (3 values obtained from the continuum radiance in each of the 3 bands), (ii) Vegetation Chlorophyll or Solar Induced Fluorescence (VCF/SIF) (obtained from clear solar Fraunhofer lines located around 755 nm, see **/Buchwitz et al., 2013a/**) and (iii) Cirrus Optical Depth (COD) retrieved from the saturated water vapour band located in the 1939 nm spectral region.

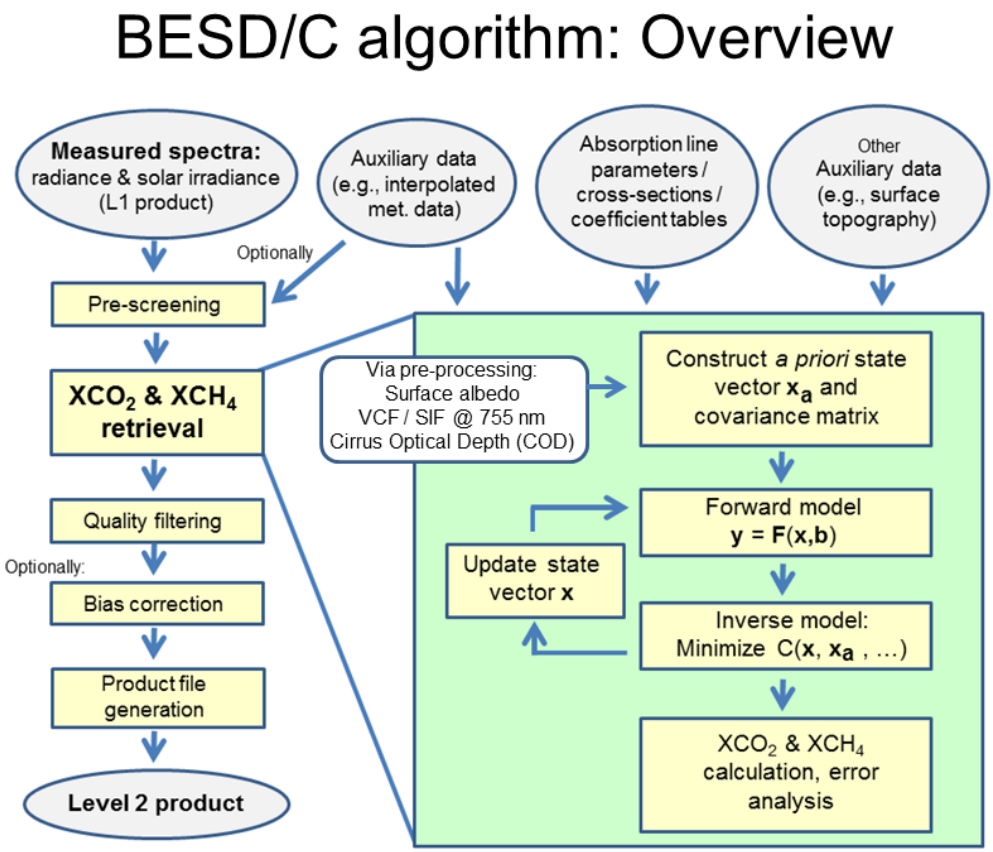

Figure 8: Overview BESD/C retrieval algorithm used for simulated CarbonSat retrievals for nadir mode observations over land.

6. Errors due to clouds and aerosols

6.1. Overview and results from previous investigations

XCO_2 and XCH_4 retrieval errors due to clouds and aerosols have already been assessed in detail within the predecessor study **/CS L1L2-I-Study FR/** and in the ESA LOGOFLUX study **Chimot et al., 2014/**and key results have also been published in the peer-reviewed literature /**Buchwitz et al., 2013a/**. Therefore we here give only a short update to present some new (improved) results obtained with the latest version of BESD/C.

Before this some radiance spectra are shown for illustration. **Figure 9** - **Figure 11** show radiance spectra at CarbonSat resolution and radiance ratios for a CO_2 perturbation by +4 ppm (i.e., by adding an altitude independent offset to the entire profile) (**Figure 9**), by doubling the Cirrus Optical Depth (COD, **Figure 10**) and by doubling the amount of aerosols (**Figure 11**).

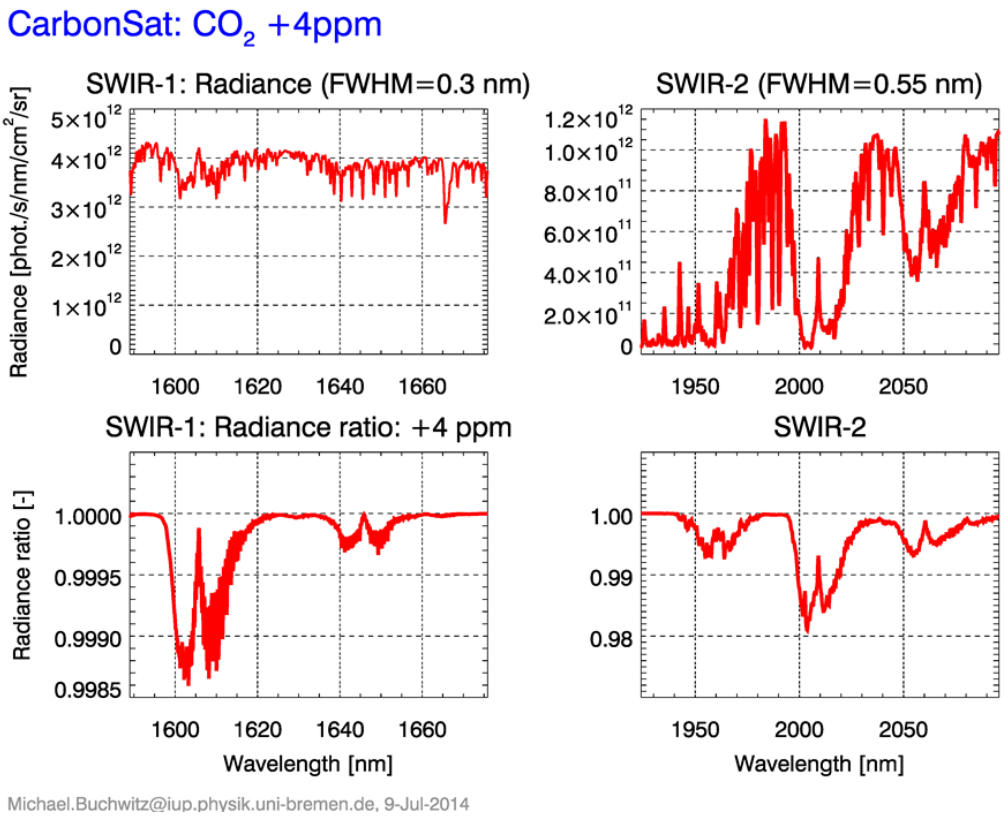

Figure 9: Radiance (top) and radiance ratio (bottom). The radiance ratio is the ratio of the radiance for an enhanced CO_2 profile (by adding +4 ppm to the unperturbed profile) and the radiance for the unperturbed CO_2 profile. For these simulations a Solar Zenith Angle (SZA) of 50^o has been used, vegetation albedo (NIR: 0.2, SWIR-2: 0.1, SWIR-2: 0.05) and the US Standard Atmosphere (but using a CO_2 vertical profile scaled to 390 ppm).

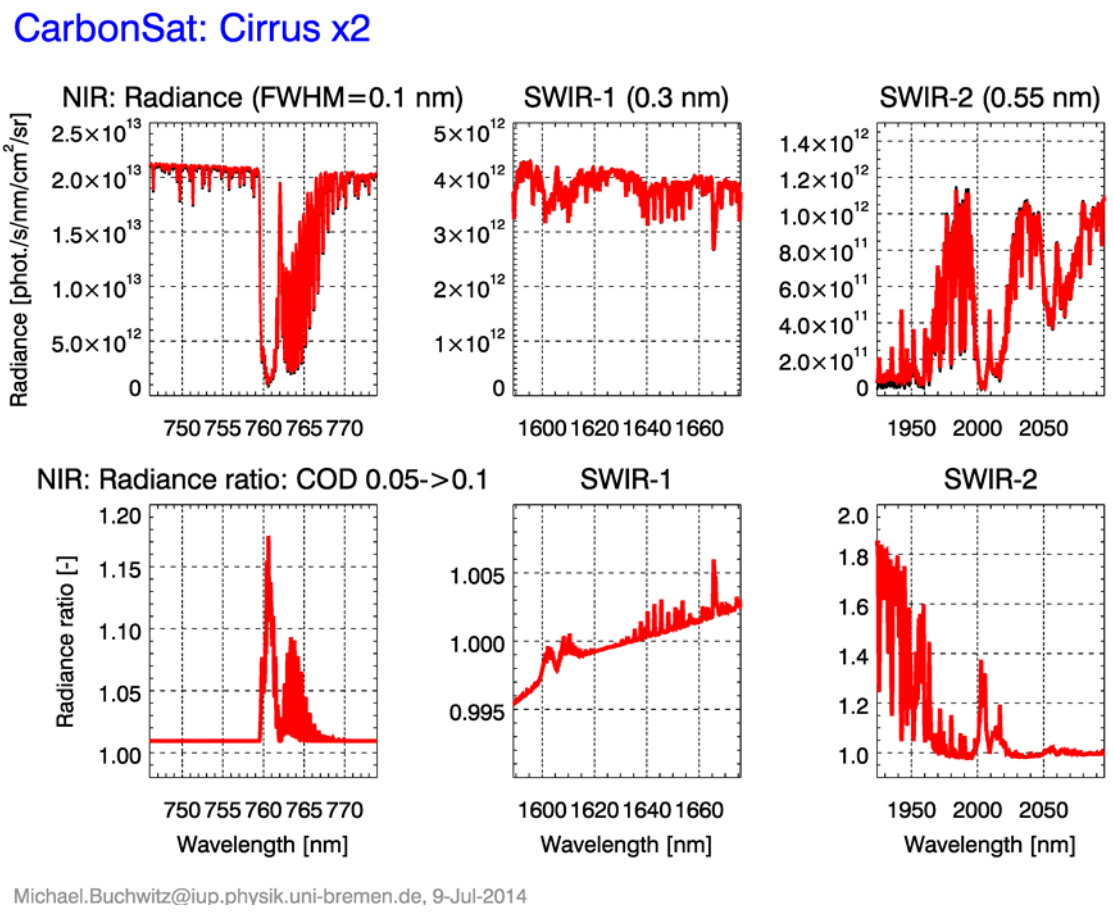

Figure 10: As **Figure 9** but for a perturbation of the cirrus scenario by increasing the Cirrus Optical Depth (COD) from 0.05 to 0.1. The cirrus is located at 10 km altitude.

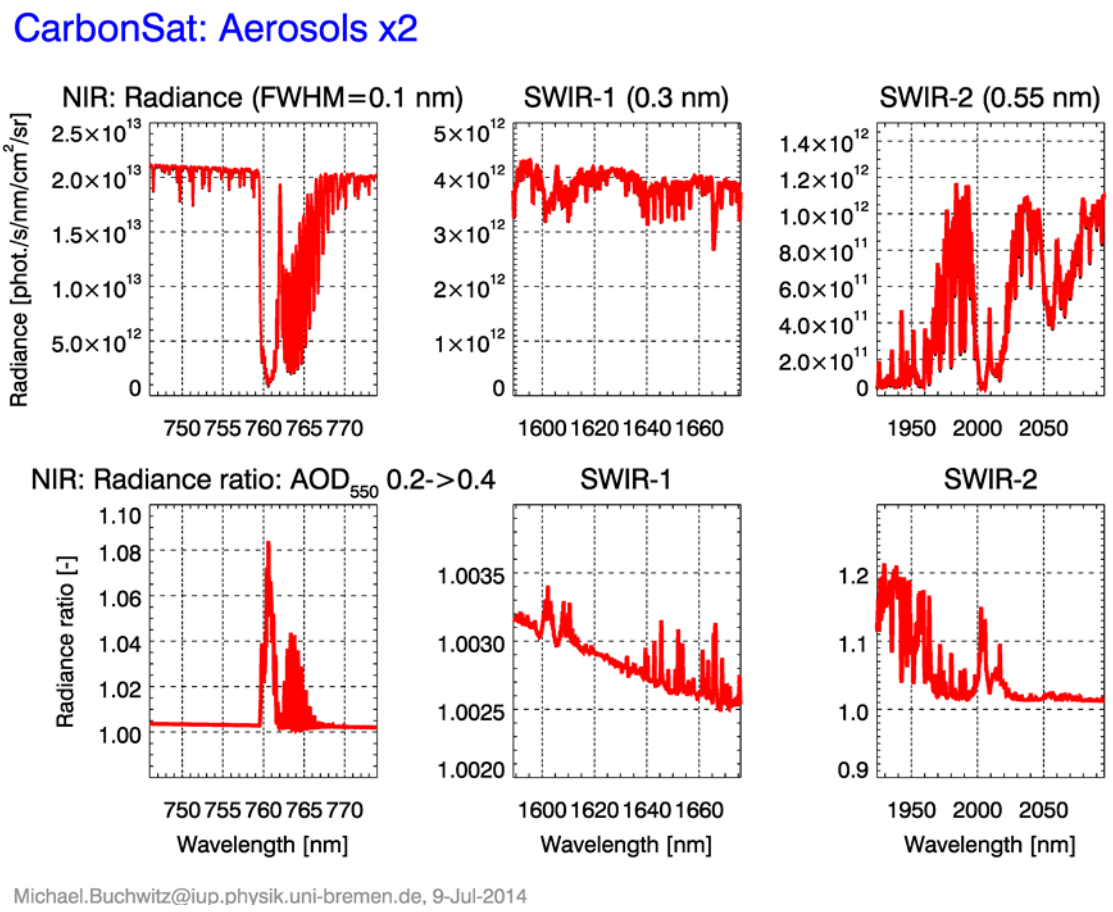

Figure 11: As **Figure 9** but for a perturbation of the aerosol scenario by increasing the Aerosol Optical Depth (AOD, at 550 nm) from 0.2 to 0.4. The aerosol type is “Continental Average” (CA) and the aerosol profile peaks in the boundary layer (0-2 km).

6.2. Cirrus Optical Depth retrieval via Pre-Processing (PP)

A major improvement was the use of the saturated water vapour band located in CarbonSat's SWIR-2 band around 1939 nm. A simple pre-processing algorithm has been developed and implemented to retrieve Cirrus Optical Depth (COD) using the radiance at 1939 nm to be used as *a priori* and first guess for the full BESD/C 3-band OE retrieval method.

Using simulations it has been found that to a very good approximation the radiance around the 1939 nm spectral region – a region with very strong water vapour absorption – depends linearly on COD: The radiance is essentially zero if no cirrus clouds are present and the radiance is approximately 1.85×10^{11} photons/s/nm/cm^2/sr for COD = 0.2.

Based on these findings a Pre-Processing (PP) algorithm has been implemented in BESD/C to obtain *a priori* and first guess values for state vector element COD using this formula:

$$\text{COD a priori} = 0.2 \times \text{RAD} / (1.85 \times 10^{11})$$

where RAD is the measured radiance (in photons/s/nm/cm^2/sr) at 1939 nm (more precisely: RAD is computed as the average radiance in the 1938 – 1940 nm spectral region).

How well this algorithm works is illustrated in the following:

Figure 12 shows XCO_2 and XCH_4 retrieval results for the "previous" **/Buchwitz et al., 2013a/** BESD/C algorithm version, where the *a priori* value for COD was a constant pre-defined value (= 0.05).

Figure 13 and **Figure 14** show that using the "new" retrieval scheme with *a priori* COD retrieved in a pre-processing step from the 1939 nm spectral region the biases are much reduced such that essentially all scenarios are "good" and strict quality filtering for too high clouds and aerosols optical depth (i.e., requiring that retrieved COD+AOD+WOD < 0.3) is not needed any more. This is also confirmed for other aerosol types (see **Figure 15** - **Figure 20**).

This shows that BESD/C has been significantly improved with respect to systematic errors caused by cirrus clouds and aerosols due to the availability of better information on cirrus clouds, which can be obtained via a relatively simple pre-processing step.

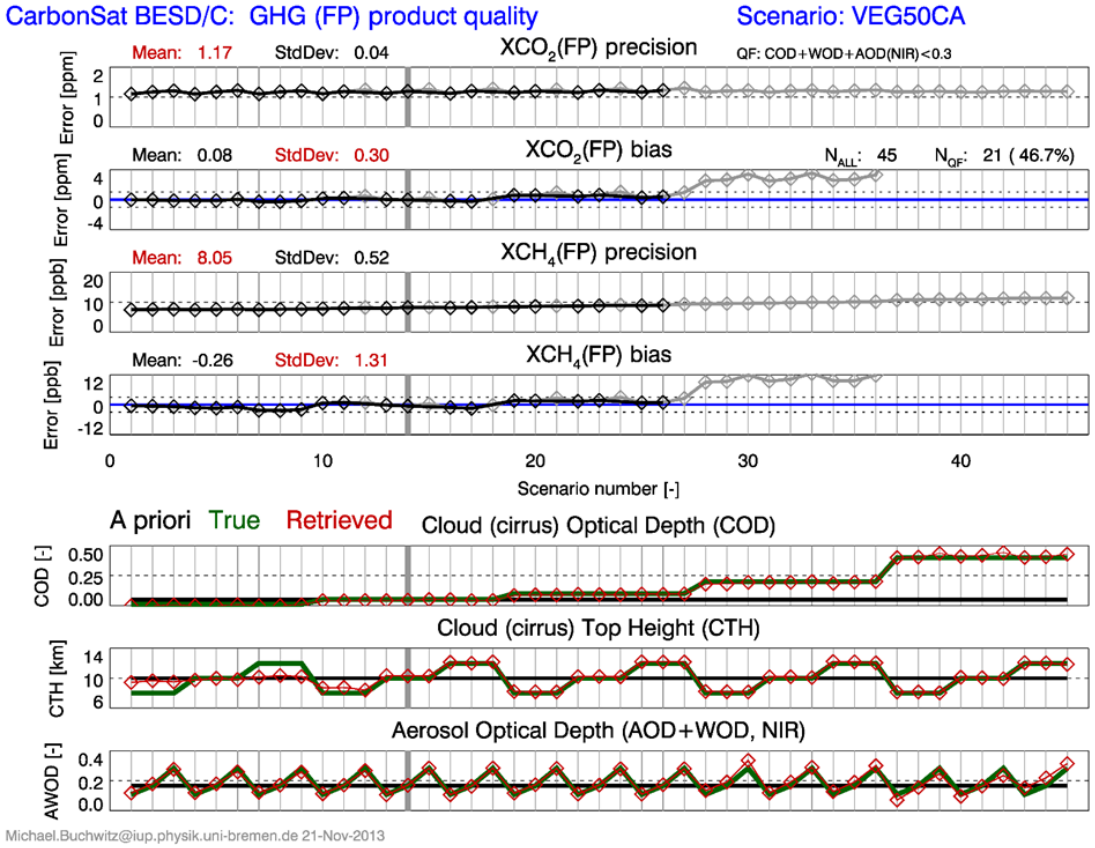

Figure 12: "Previous" BESD/C retrieval results obtained when not using COD retrieved from the 1939 nm spectral region via pre-processing. Shown are XCO_2 and XCH_4 errors (top 4 panels) for 45 different combinations of COD, CTH and AOD (bottom 3 panels). Top 4 panels: All retrieval results are shown in grey and the "good retrievals" as identified via the quality filtering scheme (see /**Buchwitz et al., 2013a/**), are shown in black. Here the criterium for a "good observation" is that the sum of the retrieved COD+AOD+WOD is less than 0.3 (WOD is the optical thickness of a low lying water cloud, which is one of the BESD/C state vector elements). As can be seen, the COD *a priori* value is 0.05 for all 45 scenarios (see black line in COD panel). As can also be seen, COD can be well retrieved (compare the green line (= true COD) with the red symbols (= retrieved COD)) and also AOD+WOD can be well retrieved. As can also be seen, the XCO_2 and XCH_4 biases are increasing when the conditions of the true (= observed) atmosphere deviate from the retrieval assumptions (see grey vertical bar indicating a scenario with: COD = 0.05, CTH = 10 km, AOD+WOD = approx. 0.18). However, these "difficult scenarios" are mostly identified and "flagged bad" by the quality filtering scheme. In this case (vegetation albedo, SZA 50^o and continental average (CA) aerosol **/Hess et al., 1998/**) 21 of the 45 scenarios are flagged "good", i.e., 46.7%.

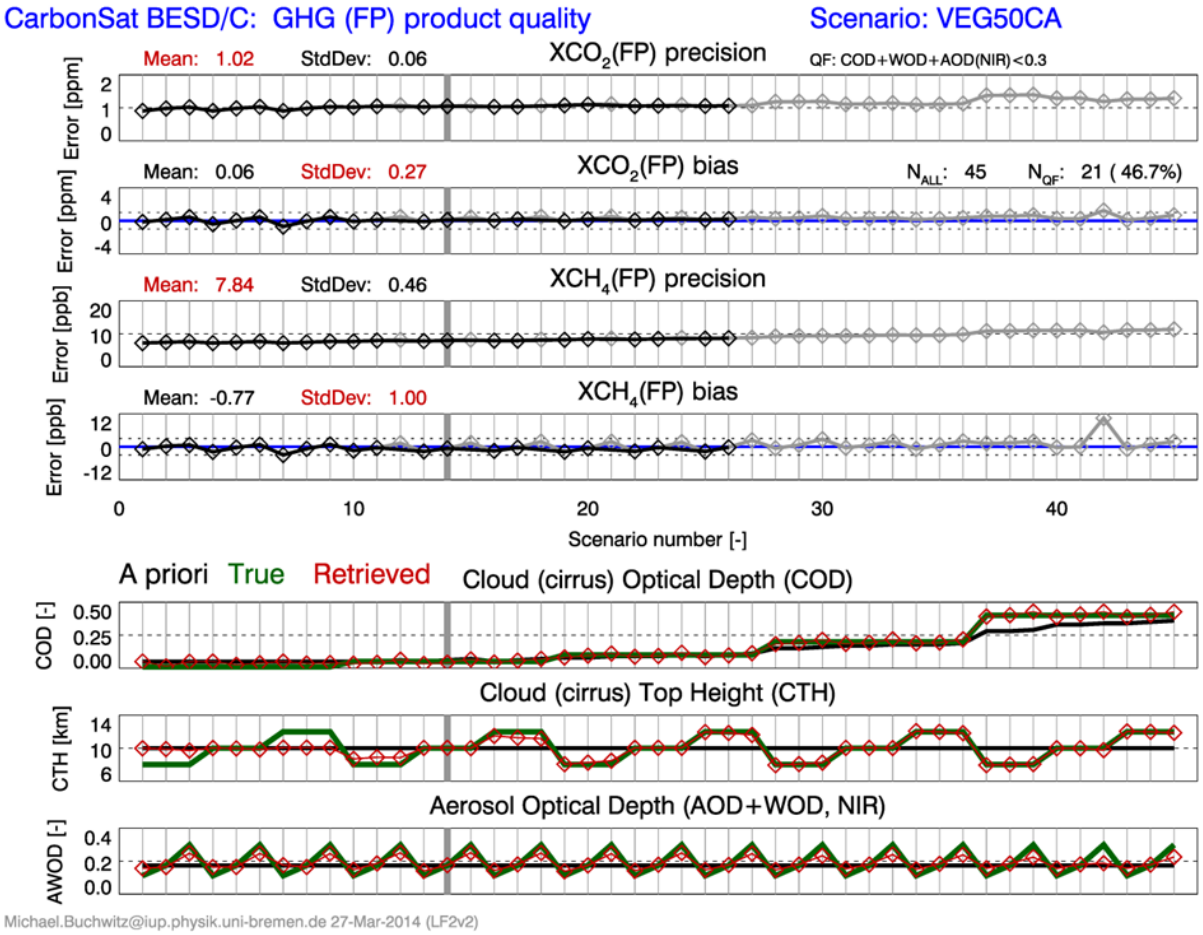

Figure 13: "New" BESD/C results: As **Figure 12** but using the new COD pre-processing scheme using the radiance at and around the 1939 nm spectral region. As can be seen, reasonable to good COD *a priori* values can be obtained using this method (see COD panel: compare the black line (retrieved) with the green line (true COD)). As a consequence, the XCO_2 and XCH_4 biases are much reduced (compare with **Figure 12**).

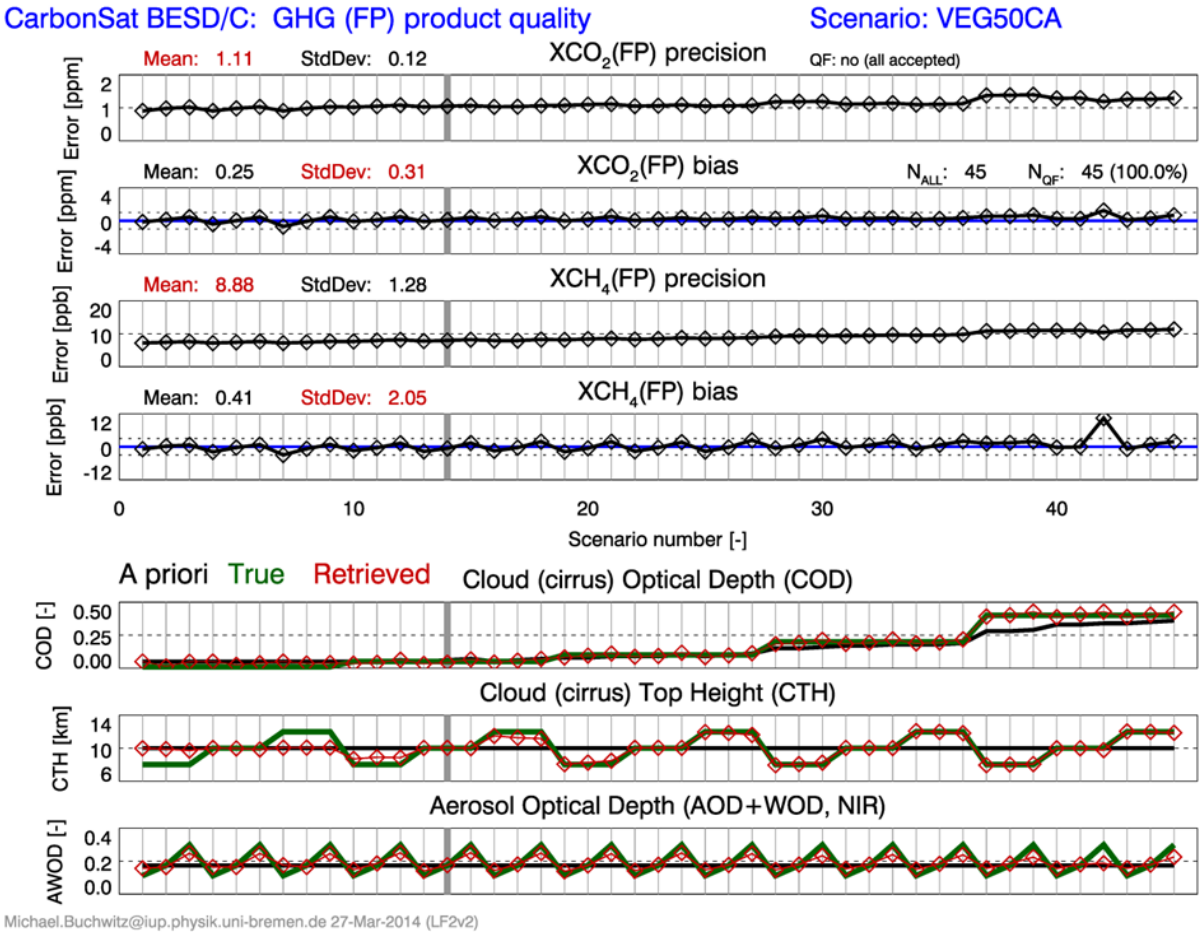

Figure 14: As **Figure 13** but flagging all observations as “good” because the COD+AOD+WOD < 0.3 quality filter (see **Figure 12**) is not needed any more.

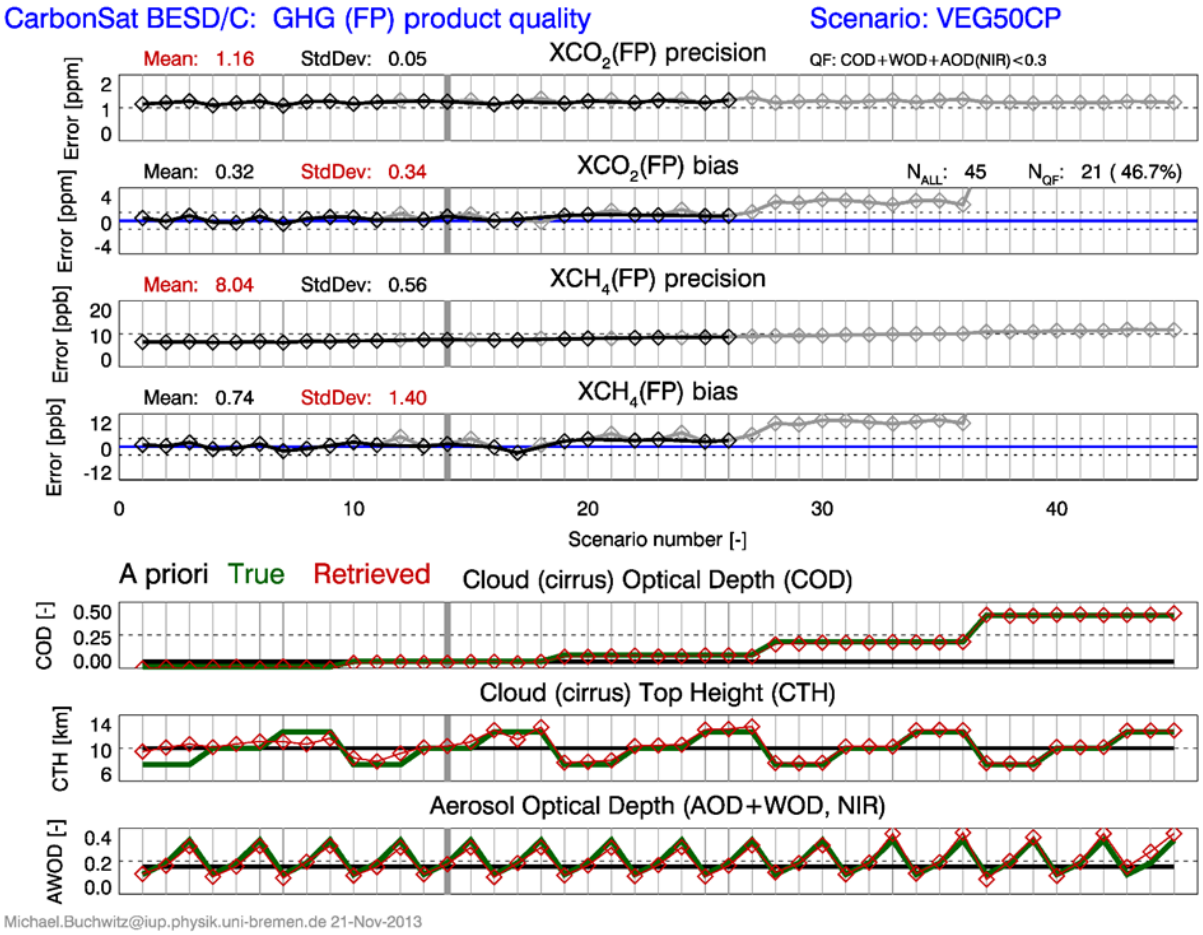

Figure 15: As **Figure 12** , i.e., “previous BESD/C”, but for scenarios with Continental Polluted (CP) aerosols **/Hess et al., 1998/** (note: BESD/C still assumes Continental Average (CA) aerosols **/Hess et al., 1998/** for the retrieval).

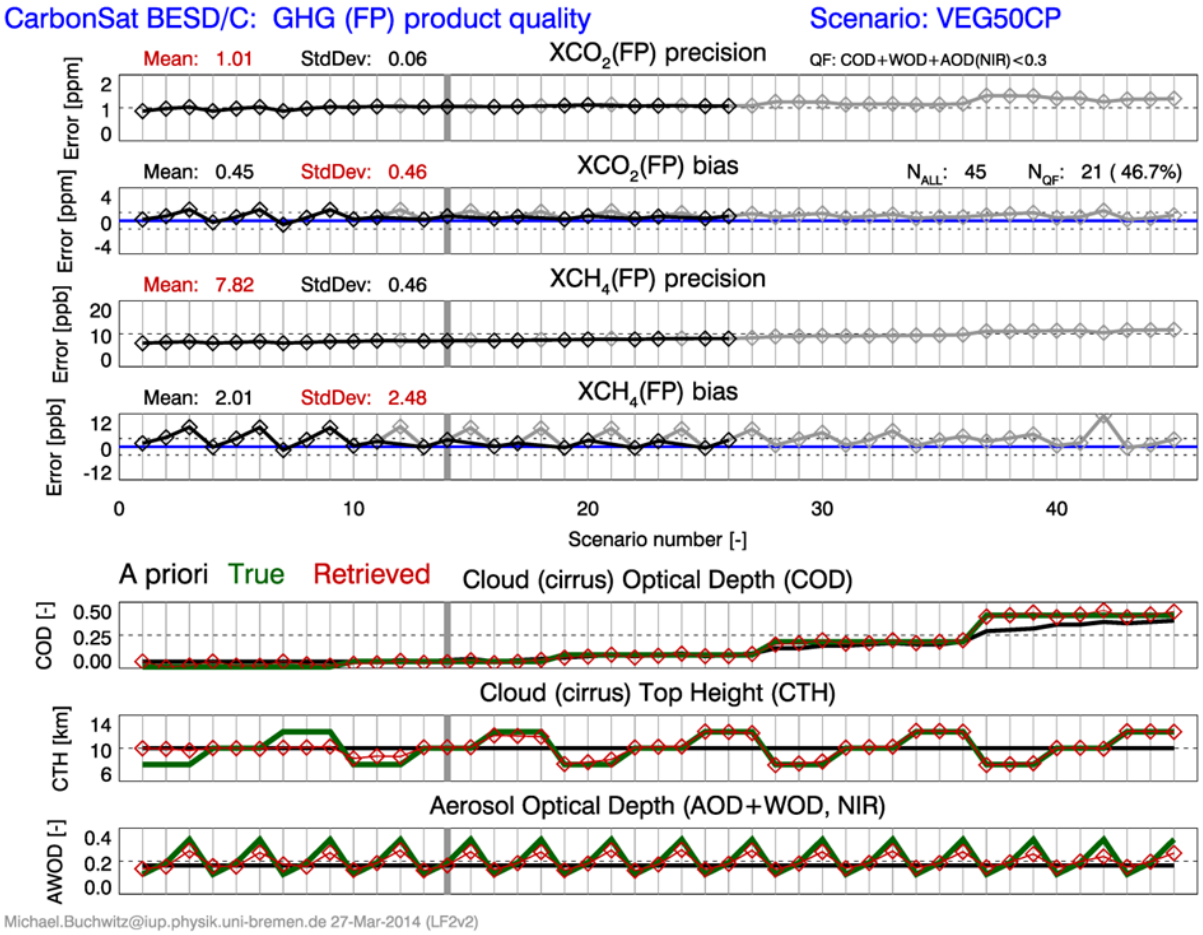

Figure 16: "New" BESD/C results: As **Figure 15** but using the new COD pre-processing scheme using the radiance at and around the 1939 nm spectral region.

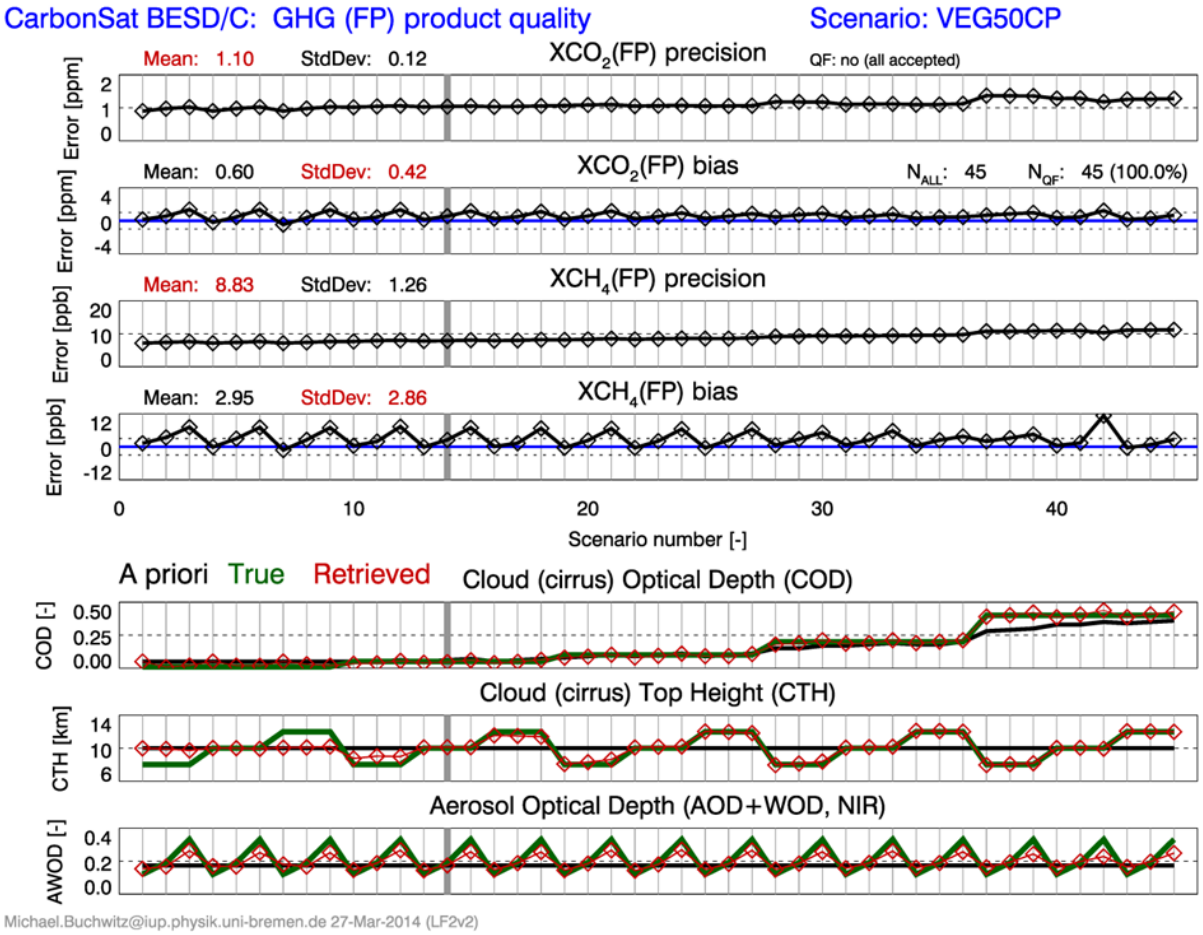

Figure 17: As **Figure 16** but flagging all observations as “good” because the COD+AOD+WOD < 0.3 quality filter (see **Figure 12**) is not needed any more.

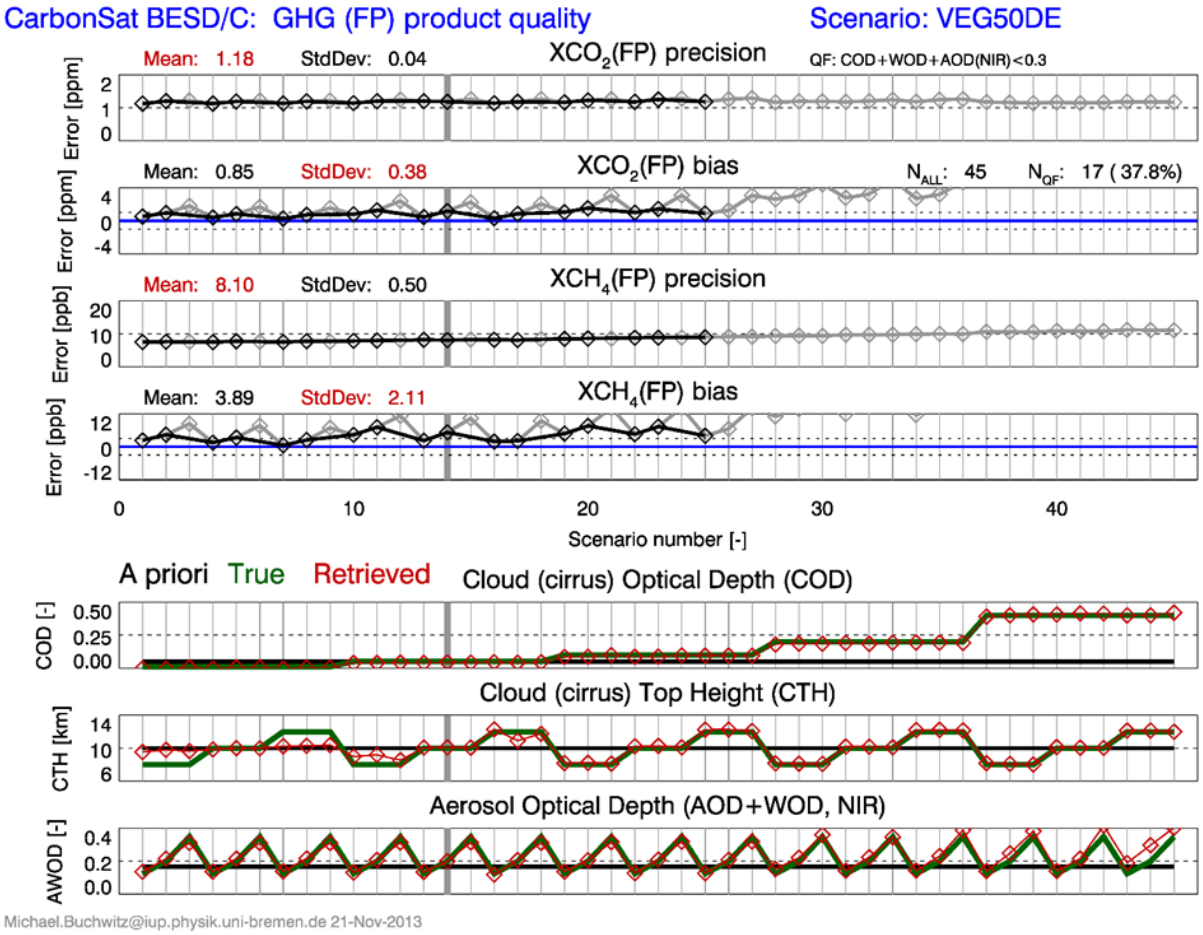

Figure 18: As **Figure 12** , i.e., “previous BESD/C”, but for scenarios with Desert (DE) aerosols **/Hess et al., 1998/** (note: BESD/C still assumes Continental Average (CA) aerosols **/Hess et al., 1998/**).

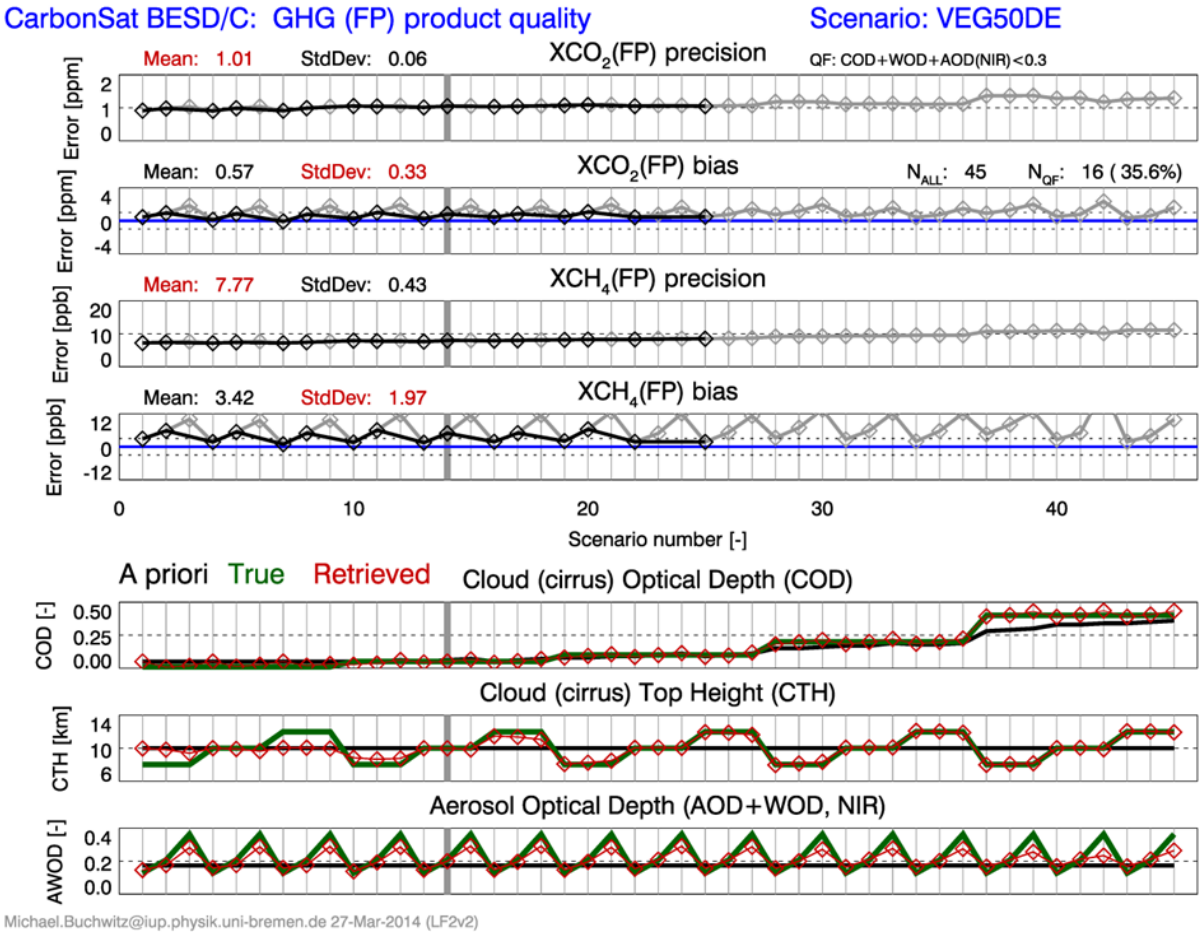

Figure 19: "New" BESD/C results: As **Figure 18** but using the new COD pre-processing scheme using the radiance at and around the 1939 nm spectral region.

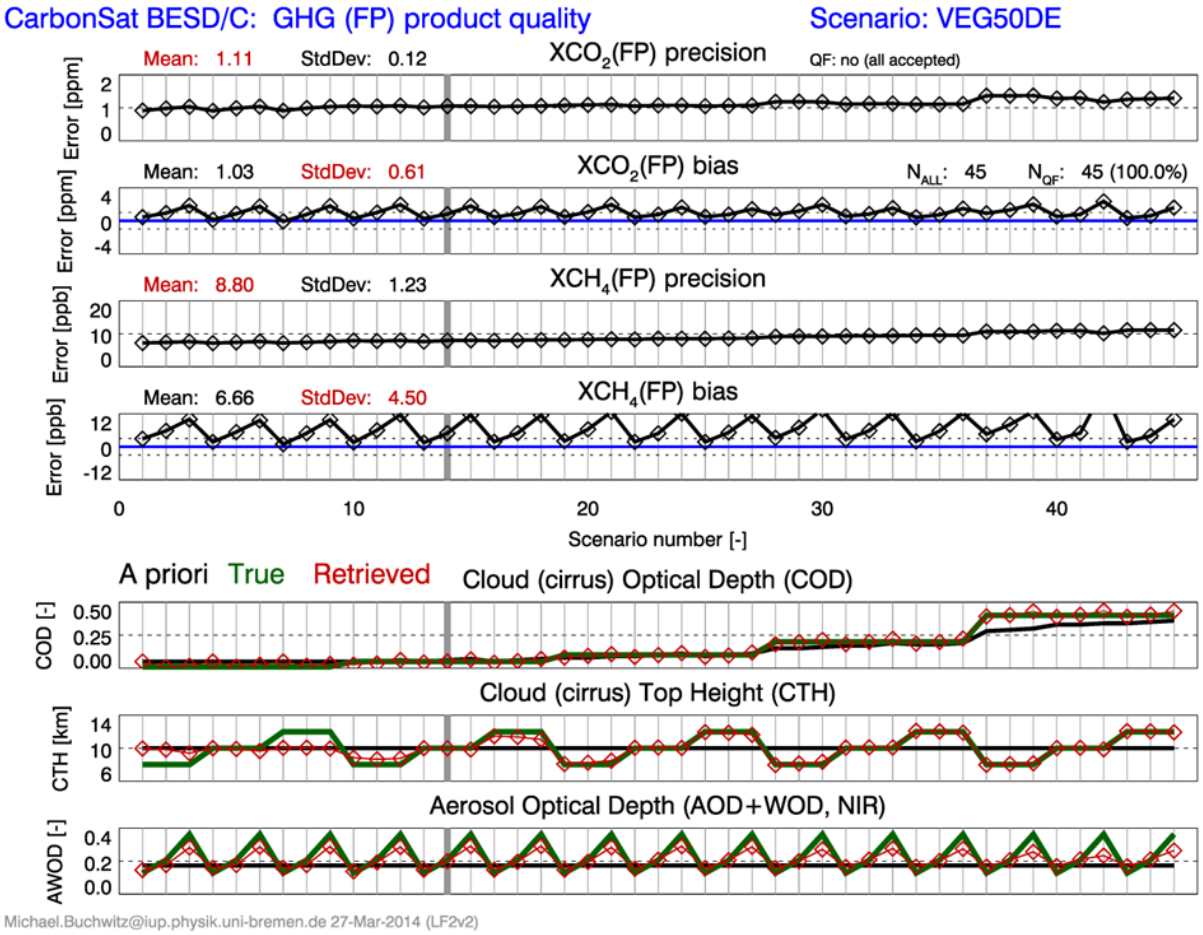

Figure 20: As **Figure 18** but flagging all observations as “good”.

7. Strategies for bias reduction for nadir observations over land

In this section strategies to further improve the expected quality of the CarbonSat XCO_2 and XCH_4 retrievals are discussed focussing on XCO_2 systematic errors (reduction of biases). This includes a literature review but also latest results from the improved BESD/C retrieval algorithm and attempts for *a posteriori* bias correction.

7.1. Strategies for XCH_4 and XCO_2 bias corrections (SRON)

This section summarizes bias corrections for XCO_2 and XCH_4 retrievals over land from nadir viewing satellite observations of SCIAMACHY on ENVISAT and TANSO-FTS onboard GOSAT.

In recent times, several algorithms have been developed to infer atmospheric column information on CH_4 and CO_2 from satellite shortwave infrared measurements. Most of the algorithms apply a pre-processing screening, which aims to filter out corrupted Level 1 spectra and exposures where thick clouds are within the instrument FOV. Moreover after Level-1 to Level-2 processing, an additional data filtering is applied based on Level-2 data quality flags. The post-screened data product can be improved further using empirical bias corrections due to instrument malfunction and retrieval algorithm artifacts. These corrections are derived from comparisons of the satellite product with collocated on-ground TCCON measurements. In this review, we consider the baseline algorithms employed to process the GHG-CCI project of ESA's Climate Change Initiative (CCI), which are listed **Table 3**.

Product	Instrument	Algorithm	Reference
XCO_2	SCIAMACHY	BESD	Reuter et al., 2011
XCO_2	TANSO	OCFP	Cogan et al., 2012
XCO_2	TANSO	RemoTeC	Butz et al., 2011
XCH_4	SCIAMACHY	IMAP	Frankenberg et al., 2011
XCH_4	SCIAMACHY	WDMD	Schneising et al., 2011
XCH_4	TANSO	OCPR	Parker et al., 2011
XCH_4	TANSO	RemoTeC	Butz et al., 2011

Table 3: XCO_2 and XCH_4 baseline algorithms selected within ESA's Climate Change Initiative (CCI).

Corresponding Product User Guides (PUG) and Algorithm Theoretical Basis Documents (ATBD), available at http://www.esa-ghg-cci.org/, describe the algorithms in detail. In the following, we summarize current bias mitigation approaches as part of a data post processing for each algorithm.

7.1.1. BESD algorithm for XCO_2 retrieval

The Bremen Optimal Estimation DOAS (BESD) algorithm **/Reuter et al., 2011, 2014/** is designed to analyze SCIAMACHY sun normalized radiance measurements to retrieve XCO_2. BESD is a full physics algorithm, which uses measurements in the O_2-A absorption band to retrieve scattering information of clouds and aerosols. This information is transferred to the CO_2 absorption band at 1580 nm by simultaneously fitting the spectra measured in both spectral regions. The algorithm (v02.00.08) includes post-processing data filters to reject potentially corrupted results. The filter is based on acceptance ranges of a set retrieval parameters. A list of all of post-processing quality filters are given by **/Reuter et al., 2014/**. To mitigate remaining biases on the SCIAMACHY CO_2 product with respect to TCCON ground-based measurements, **/Reuter et al., 2014/** employ a neural network with multilayer perceptron architecture to describe the systematics in the differences between the BESD XCO_2 fields and collocated TCCON ground-based measurements. The network employs 15 retrieval and instrument parameters as its input:

- Zero order polynomial coefficient of the spectral surface albedo in the O_2 A band
- FWHM of the ISRF in the O_2 A band
- Three polynomial coefficient of the spectral surface albedo in the 1.6 µm CO_2 band
- FWHM of the ISRF in the 1.6 µm CO_2 band
- Cloud water/ice path
- Aerosol profile scaling factor
- Surface pressure
- Surface height
- Solar zenith angle
- Line of sight angle
- Detector temperature of channel 4
- Throughput channel 6 (ASM mirror, ESM diffusor)
- Throughput channel 6 (ESM mirror, pointing))

The network is trained using differences between the BESD XCO_2 product and collocated TCCON observations.

7.1.2. OCFP algorithm for XCO_2 retrieval

The OCFP algorithm is the University of Leicester full physics retrieval algorithm, which is a modification of the original Orbiting Carbon Observatory (OCO) full physics retrieval algorithm but modified for the use on GOSAT spectra. For its XCO_2 data product, a bias correction is applied after post-processing quality flag filtering. The post filtering is similar to the BESD approach with quality flags defined by **/Parker et al., 2014/**. A bias correction on the retrieved XCO_2 is calculated via a regression

analysis of the difference between the GOSAT XCO_2 and TCCON XCO_2, similar to the approach of **/Wunch et al., 2011/**. This analysis determined that there was a strong correlation between the difference to the TCCON data to the ratio between the band 1 and band 2 albedo values A_1 and A_2.
The bias correction applied to the data is

$$\mathrm{XCO}_2^{corr} = \mathrm{XCO}_2 - (b_0 + b_1 \frac{A_1}{A_2})$$

with coefficients

$b_0 = -1.8104455$

$b_1 = 2.3757403$

7.1.3. RemoTeC algorithm for XCO_2 retrieval

The RemoTeC CO_2 and CH_4 full-physics products are retrieved from GOSAT TANSO-FTS NIR and SWIR spectra using the RemoTeC algorithm that is being jointly developed at SRON Netherlands Institute for Space Research and the Karlsruhe Institute for Technology (KIT). The algorithm retrieves simultaneously CH_4 and CO_2, as well as three aerosol parameters representing their amount, height distribution and size distribution. Also the RemoTeC algorithm applies a post-filtering, based on data quality flags defined in **/Detmers et al, 2014/**. Subsequently, the Level-2 product is bias-corrected utilizing correlations of the difference between the RemoTeC XCO_2 product and collocated TCCON measurements with retrieval parameters. It was found that the error in XCO_2 correlates with the aerosol filter

$$j = t_{SWIR}^{aer} \frac{h}{a}$$

where t_{SWIR}^{aer} is the aerosol optical depth in the SWIR , h is the height of the retrieved aerosol layer and α represents the reciprocal of the aerosol size parameter. The aerosol filter has large values for scenes with high AOT, large particles, high in the atmosphere, which are the most difficult cases in terms of light path adjustment. Based on this correlation, the following bias correction has been developed for XCO_2:

$$\mathrm{XCO}_2^{corr} = \mathrm{XCO}_2 (a + bj)$$

with

a = 1.0041, b = 2.22E-5 for H-gain data

and

a= 1.0032, b = 8.08e-6 for M-gain data.

The bias correction parameters are obtained from fits to the GOSAT-TCCON differences.

7.1.4. IMAP algorithm for XCH_4 retrieval

The IMAP-DOAS XCH_4 products are retrieved from SCIAMACHY SWIR spectra (channel 6) using the IMAP-DOAS algorithm that has been developed at University of Heidelberg and SRON **/Frankenberg et al., 2014/**. The algorithm independently retrieves vertical column densities of both CH_4 and CO_2 under the assumption of a non-scattering atmosphere. The concurrently retrieved CO_2 column as well as model assumptions of XCO_2 are then used to derive XCH_4 from the retrieved vertical columns. This approach is also known as methane proxy retrieval. A tentative bias correction was introduced to correct for a residual water vapor interference, which cannot be excluded given the low spectral resolution and small amount of pixels used in the SCIAMACHY CH_4 retrieval.

The current version implements the following correction:

$$XCH_4^{corr} = XCH_4 - a\log_{10}(C_{H2O}) + b$$

with a=37.67 and b=845. Here, C_{H2O} is the ECMWF water vapour column in molec./cm^2 and XCH_4 is given in ppb.

7.1.5. WFM-DOAS algorithm for XCH_4 retrieval

WFM-DOAS algorithm is designed to retrieve XCO_2 and XCH_4, from NIR and SWIR nadir spectra recorded by the SCIAMACHY instrument onboard ENVISAT. **/Schneising et al., 2014a/** and references therein).

After post-processing quality filtering, a post-processing correction is applied to minimize residual systematic retrieval biases. For the most recent version (v3.6 upward) a linear regression correction similar to **/Wunch et al., 2011/** is applied,

$$XCO_2^{corr} = 0.9\ XCO_2 - 36\ \tfrac{ppm}{\%}\ O_2^{err} - 4\ ppm\ I +$$
$$1\ \tfrac{ppm}{\%} CO_2^{err} - 1.8\ ppm\ H_2O^{para} - 27\ ppm * O_2^{para} -$$
$$18.5\ ppm\ n^{sol} - 135\ ppm\ t + 0.17\ ppm\ \tfrac{cm2}{g}\ H_2O + 237\ ppm$$

Thereby, O_2^{err} and CO_2^{err} are the column errors in % estimated from fit quality and the diagonal elements of the covariance matrix, I is the sun-normalized radiance at 1560 nm, and t is the SCIAMACHY nadir throughput at 750 nm derived by solar measurements. H_2O^{para} is the ratio of the radiance at 1.4 µm to the clear-sky radiance minus 1, O_2^{para} is the ratio of the retrieved O_2 column to the a-priori column determined by surface elevation, and n^{sol} is the geometric intra-annual solar variability factor accounting for the variable distance of the Earth to the Sun.

Moreover, H_2O is the simultaneously retrieved water vapour vertical column amount in g cm^{-2}. An additional term (0.5 ppm pm^{-1} - f_a) accounts for a small drift of the

instrument slit function before 2004, identified using retrieved slit functions of the Bremen Optimal Estimation DOAS (BESD) XCO_2 algorithm **/Reuter et al., 2011/**, where f_a is the corresponding slit function anomaly in pm.

7.1.6. RemoTeC algorithm for XCH_4 retrieval

The full-physics RemoTeC algorithm retrieved simultaneously CO_2 and CH_4 abundances from GOSAT NIR and SWIR measurements and relies on the same post-processing data quality filter. However, the bias correction differs for both products. For methane, Level-2 data are corrected by

$$\mathrm{XCH}_4^{corr} = \mathrm{XCH}_4(a + b\alpha)$$

where α is the reciprocal of the aerosol size parameter,

a = 0.98712 b = 0.019585 for H-gain data

and

a= 0.99628, b = -0.00419 for M -gain data.

The bias correction parameters are obtained from fits to the GOSAT-TCCON differences.

Overall, the empirical bias correction approaches discussed in this section rely on a post-processing correction of corresponding Level-2 products using differences between the retrieval results and collocated ground-based measurements to mitigate instrument malfunction and retrieval artifacts.

The main drawback of this approach is that it aggravates an independent validation of the corrected Level-2 data product, because the correction approach and the validation mostly rely on the same dataset.

Furthermore, the spatiotemporal density of validation measurements in combination with stringent collocation requirements with satellite observations commonly limits the generalization ability of the dataset and just as well of the bias-correction.

Keeping this in mind, the stringent CarbonSat Level-1 requirement are indispensably linked with this mission. However considering the tight CarbonSat requirements on XCO_2 and XCH_4, a bias correction should be also considered as an optional part of the Level-1 to Level-2 data processing. Here, the high spatial sampling of the CarbonSat mission will be an asset to develop a reliable CarbonSat XCH_4 and XCO_2 correction method.

In particular, a specific observation mode for calibration purposes (like the OCO target mode where a selected ground target is observed for the entire length of a ground pass) is not required for this mission.

7.2. Assessment of bias correction using TCCON

This aspect has also been addressed in the parallel LOGOFLUX-II (LF-II) study, which is a follow-on study of the LOGOFLUX-I (LF-I) study **/Chimot et al., 2014/**.

A major activity of the LF-II study was to generate one year of simulated CarbonSat Level 2 data in the form of “Level 2 error” (L2e) files. Specifically the task was to improve the LF-I L2e file data set, which is described in **/Buchwitz et al., 2013a/** and **/Chimot et al., 2014/**, with respect to the following aspects:

- (i) improve the parameterization of the XCO_2 and XCH_4 systematic errors by also considering aerosol type related errors
- (ii) reduce the XCO_2 and XCH_4 systematic errors by using TCCON data for a posteriori bias correction

As shown in **/Buchwitz et al., 2014/** this has been achieved by

- (i) adding a parameterization for aerosol type (and partially also profile) related errors using the aerosol Angstrom exponent as a proxy for aerosol type
- (ii) using the CarbonSat overpasses over the TCCON site Lamont, Oklahoma, USA, to obtain regression coefficients for a bias correction using three parameters which are either well known (SZA) or can be well retrieved (surface albedo in the NIR and SWIR-1 band); the obtained regression coefficients (4 values for XCO_2 and 4 values for XCH_4, where the forth value is for a constant term, i.e., the overall bias) are then applied to the global data for bias correction

Figure 21 illustrates the impact of the bias correction for XCO_2 at Lamont. As expected, the mean bias is very small (0.03 ppm) and the standard deviation of the bias is significantly reduced if the bias correction is applied. Similar improvements have been obtained for XCH_4 and also at other sites, i.e., other locations than Lamont (see **/Buchwitz et al., 2014/**). This indicates that using one TCCON site only helps to significantly reduce the biases, at least for simulations. For real data very likely several TCCON sites need to be used but this needs to be confirmed using real CarbonSat data.

A comparison of systematic and random XCO_2 and XCH_4 error statistics for four regions is shown in **Figure 22** (with bias correction) and **Figure 23** (without bias correction). As can be seen, the biases are typically significantly reduced when the bias correction has been applied although here also error type related errors are considered. For example, systematic errors over the USA were less than 0. 3 ppm for 69.8 % of all XCO_2 observations when no bias correction is applied (**Figure 23**) and this fraction increases to 99.2% with bias correction (**Figure 22**). For Europe the fraction improves from to 66.7% to 96.3%.

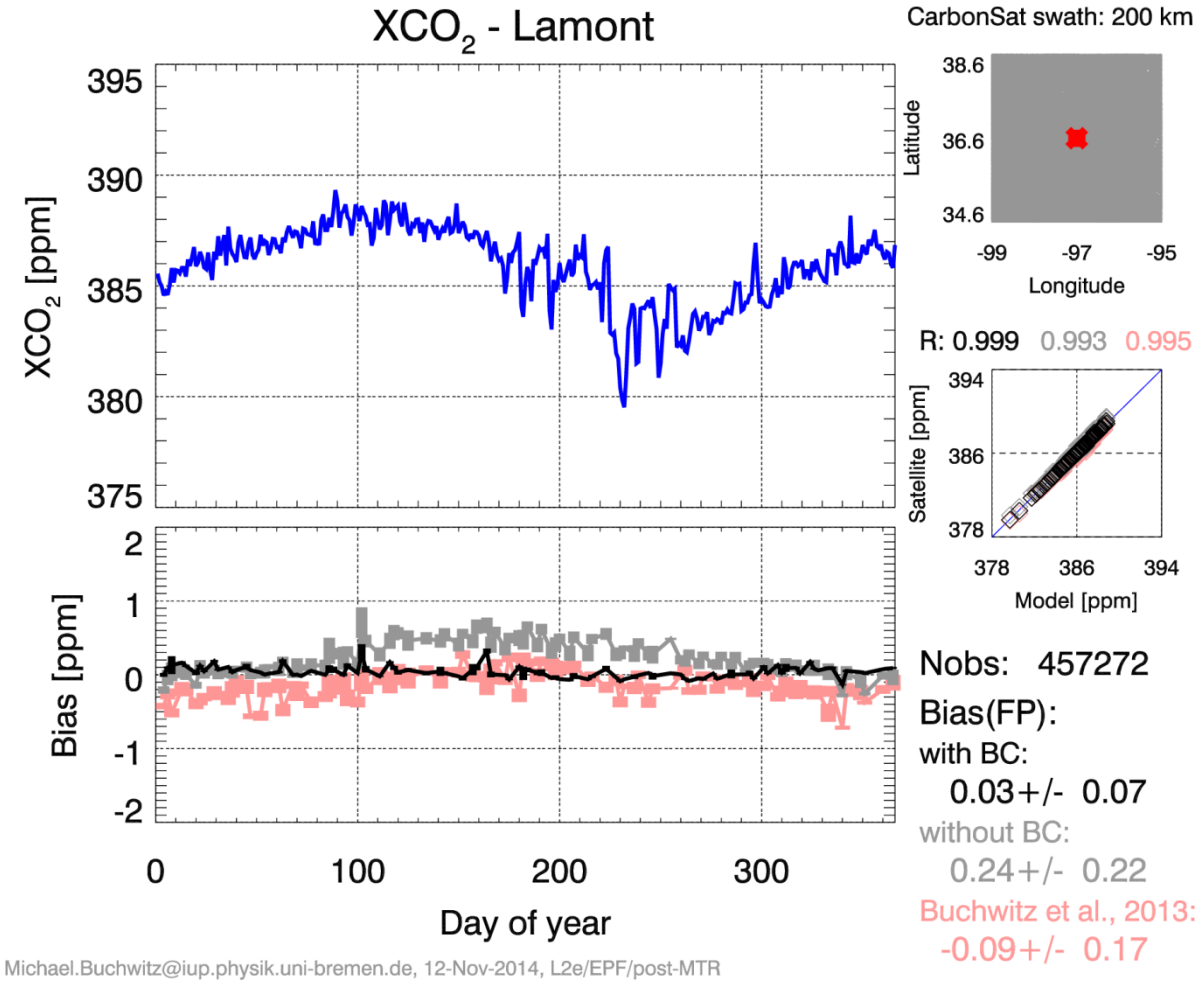

Figure 21: Illustration of the result of the bias correction (BC) for XCO_2 at Lamont: XCO_2 (top left: modelled XCO_2 using NOAA's CarbonTracker **/Peters et al., 2007/**) and XCO_2 bias (bottom left) at Lamont (location see top right panel: red cross: Lamont, area: Lamont +/- 2o, grey area: CarbonSat observations, white area: none as all locations in the surrounding of Lamont are covered using a one year data set of cloud free CarbonSat observations). Top left: The grey curve shows the daily biases computed with the new error parameterization method as explained in detail in **/Buchwitz et al., 2014/**. The black curve shows the same biases but after bias correction (BC). The light red curve shows the biases computed as described in **/Buchwitz et al., 2013a/** which neglects aerosol type related errors. In total Nobs=457272 (quality filtered) CarbonSat observations have been used here. The mean bias after BC is 0.03 ppm (bottom right) and its standard deviation is 0.07 ppm (1-sigma). Without BC the bias is 0.24+/-0.22 and -0.09+/-0.17 when aerosol type related errors are neglected.

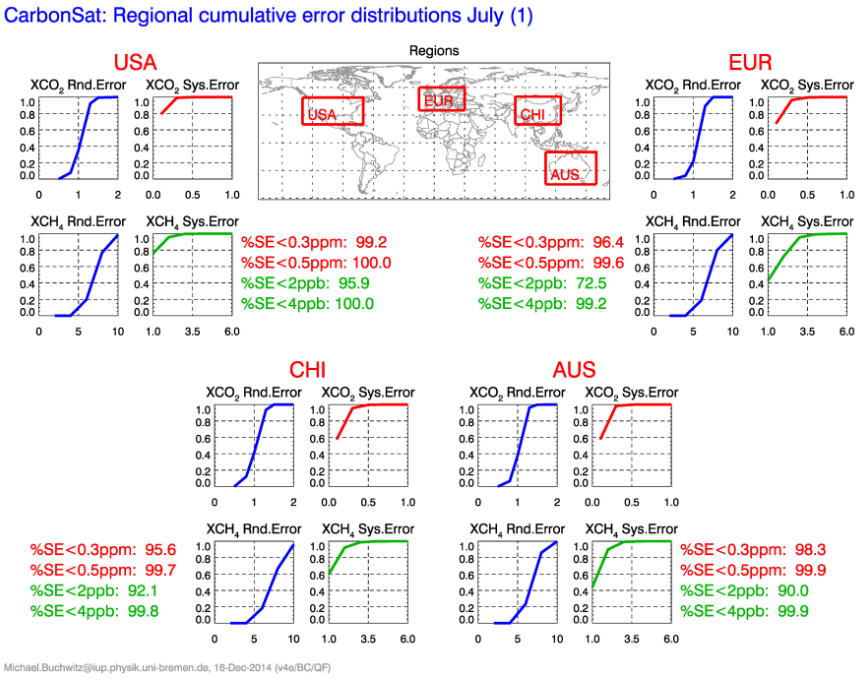

Figure 22: Regional error statistics for four regions during July for the new CarbonSat data set with bias correction applied. SE = systematic error, RE = random error.

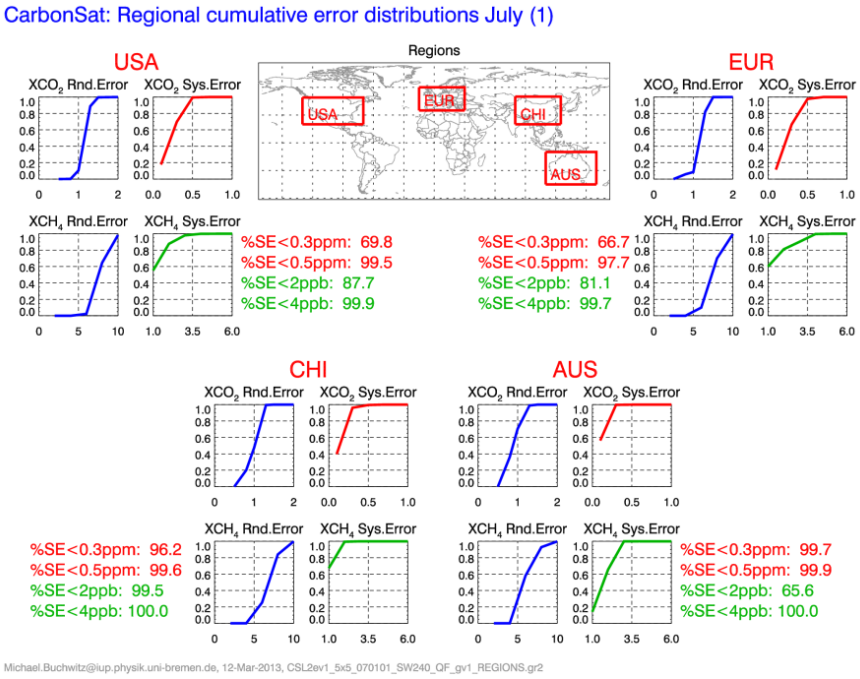

Figure 23: As **Figure 22** but for the previous version of the simulated CarbonSat data, i.e., without bias correction (from: **/Buchwitz et al., 2013a/**).

7.3. Optimization of quality filtering

It has already been shown in **Sect 6**., that thanks to the new pre-processing scheme based on the 1939 nm spectral region to obtain *a priori* and first guess information on cirrus clouds (COD) the previously used quality filtering scheme (e.g., ***/Buchwitz et al., 2013a/***) can be significantly relaxed without degrading the quality of the XCO_2 and XCH_4 retrievals.

With the new scheme essentially no *a priori* knowledge on COD is needed any more as this can be well retrieved from the CarbonSat data and this dramatically improved the quality of the results.

7.4. Specific calibration requirements for bias reduction and/or better characterization

So far no specific calibration requirements for bias reduction and/or better characterization of biases have been identified.

8. Reference Spectra

The term “Reference Spectra” as used here refers to reference data (mostly spectra) generated based on requirements defined by ESA. They are used in the context of mission requirements formulation (e.g., **/CS MRD v1.2, 2013/**) and/or performance assessments as carried out by ESA, industry and/or the project partners of this study.

A comprehensive set of reference data have been generated and delivered to ESA within the framework of the “CSL1L2-I” precursor study **/CS L1L2-I-Study FR/** and are documented in a technical report **/CS RefSpec v5, 2013/**.

In the framework of this study additional reference data have been generated as described in the following sub-sections.

8.1. Gain Matrices (GMs)

During the CSL1L2-I precursor study it has been identified (see **/CS L1L2-I-Study FR/**) that requirements related to spectral features, in particular requirements related to relative spectral radiometric accuracy, would highly benefit using a formulation based on Level 2 performance needs rather than defining directly requirements on the quality of the spectra, i.e., on the Level 1 performance.

The link from Level 1 to Level 2 is provided via a L1-to-L2 retrieval algorithm (e.g., BESD/C). In the context of linear error analysis L1 errors can be mapped onto L2 errors using matrix multiplication.

A Gain Matrix (GM) as used in the context of this study is a matrix which consists of 3 columns, i.e., is defined by 3 vectors. How these GMs are defined and used is explained in the following sub-section followed by a description of updated GMs, which have been generated in the framework of this study and delivered to ESA.

8.1.1. Gain Matrix Method

In this section the Gain Matrix Method (GMM) is described (see also ***/CS L1L2-I-Study FR/***).

Using a Gain Matrix (GM), G, the relative error of the reflectance spectrum, Δy (a vector), can be mapped onto the error of a geophysical parameter of interest, Δx:

$$\Delta x = G\,\Delta y$$

Here, Δy (which is dimensionless) is the multiplicative reflectance relative error spectrum (i.e., a value of 0.01 corresponds to a +1% error) or the ratio of a spectrum with error divided by the error-free spectrum (in this case a +1% error corresponds to 1.01).

To illustrate how Δy is defined, here some examples, using reflectance ratios:

- If Δy = 1.0 (for certain wavelengths), the reflectance has no (systematic) error (at these wavelength).
- If Δy = +1.001 (for certain wavelengths), the reflectance has a (systematic) error of +0.1% (at these wavelengths).
- If Δy = +0.999 (for certain wavelengths), the reflectance has a (systematic) error of -0.1% (at these wavelengths).

Equation Δx = G Δy needs to be applied to three G's (three 1-dimensional vectors (per scenario)):

- G0 is the "Normalized $_{CO2}$ vertical column" "G"; G0 is a (1-dimensional) vector with number of elements = number of spectral samples of all three CarbonSat bands (concatenated).
- G1: same as G0 but for methane (CH_4).
- G2: same as G0 but for Surface Pressure (PRE) or, equivalent, the normalized air (AIR) column.

Recipe how to use the three G vectors

For each of the three G vectors (i.e., Go, G1, G2), compute the following three numbers (scalars) by computing the scalar product (<|>) of each G vector with reflectance error spectrum (vector) Δy as follows (the sum extends over all elements of vectors G = number of elements of vector Δy):

- $\Delta x0 = \langle Go \mid \Delta y \rangle := \Sigma_i\, Go_i \times \Delta y_i$
- $\Delta x1 = \langle G1 \mid \Delta y \rangle := \Sigma_i\, G1_i \times \Delta y_i$
- $\Delta x2 = \langle G2 \mid \Delta y \rangle := \Sigma_i\, G2_i \times \Delta y_i$

To compute these numbers, it is required to interpolate the reflectance error spectrum onto the wavelength grid of the G vectors in order to obtain a Δy_i value for each wavelength (λ_i) as given in the GM file(s). These three numbers can be interpreted as:

- $\Delta x0$ is the relative error of the CO_2 vertical column (i.e., if $\Delta x0 = +0.01$, the retrieved CO_2 column would have a systematic error of +1%)
- $\Delta x1$: as $\Delta x0$ but for methane
- $\Delta x2$: as $\Delta x0$ but for the surface pressure / air column (e.g., if $\Delta x2 = -0.01$ the retrieved surface pressure / air column would have a systematic error of -1%)

Compute the XCO_2 and XCH_4 biases:

- B^{XCO2} := XCO_2 bias in ppm = $((1+\Delta x0)/(1+\Delta x2) -1) * 100 * C^{CO2} * m$
- B^{XCH4} := XCH_4 bias in ppb = $((1+\Delta x1)/(1+\Delta x2) -1) * 100 * C^{CH4} * m$

with

- C^{CO2} = CO_2 conversion factor (ppm per percent) = 4.0
- C^{CH4} = CH_4 conversion factor (ppb per percent) = 18.0
- m = GM approach margin factor needed to account for the fact that the GM approach is uncertain due to the dependence of the GM on (highly variable) geophysical parameters and because a “Worst Case (WC) GM” cannot be defined (as the WC GM also depends on Δy).

Application: Relative Spectral Radiometric Accuracy (RSRA) requirement: The GM part of the RSRA requirement is met if (note: abs() denotes taking the absolute value):

- $abs(B^{XCO2}) < B^{XCO2}$(required) AND
- $abs(B^{XCH4}) < B^{XCH4}$(required)

where

- B^{XCO2}(required) = 0.2 ppm (see above)
- B^{XCH4}(required) = 2.0 ppb (see above)

The GMM has been used in **/CS MRD v1.2, 2013/**.

The GMM is summarized in **Figure 24**. More details are given in the following sub-sections.

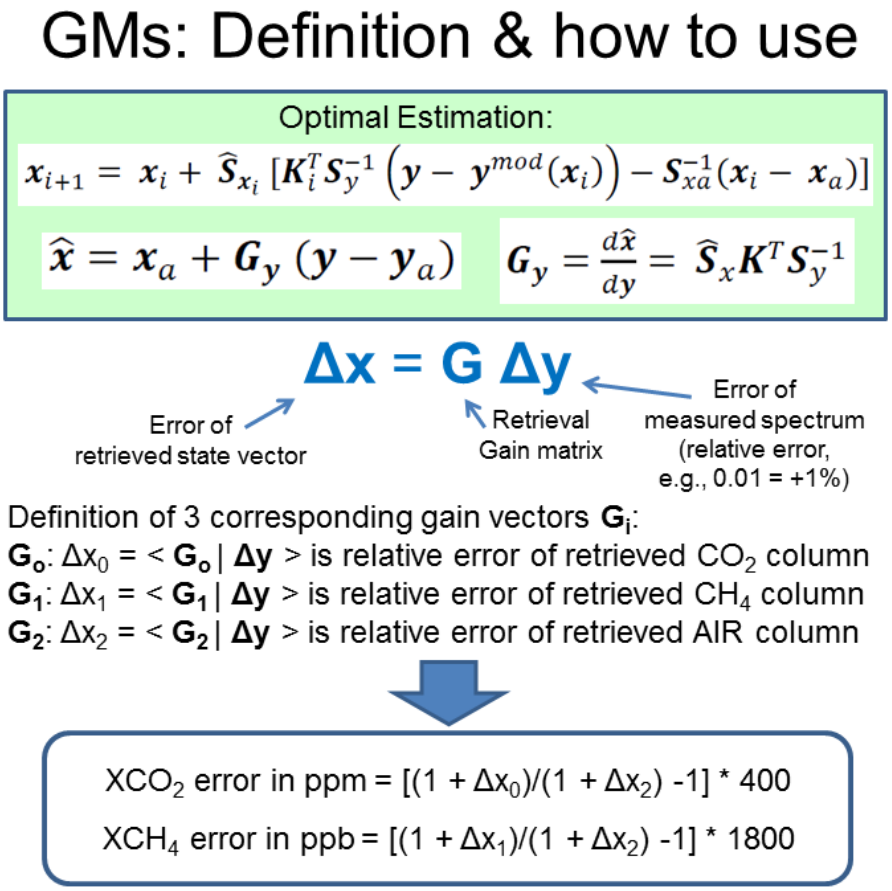

Figure 24: Gain Matrices (GMs): Definition and how to use.

8.1.2. GM scenarios TRD and TRM

Gain matrices (GMs) for two main scenarios have been generated and delivered to ESA (GMs for other scenarios are described later in this document).

The definition of these two scenarios is shown in **Table 4**.

Scenario	ID	SZA	Surface albedo		
			NIR	SWIR-1	SWIR-2
Tropical Dark	**TRD**	0^o	0.1	0.05	0.05
Tropical Dynamic Range Maximum	**TRM**	0^o	0.5	0.4	0.4

Table 4: Definition of scenarios TRD and TRM.

8.1.3. GMs for scenarios TRD and TRM (v3)

The version 3 TRD and TRM GMs are an update of the version 2 GMs (**Sect. 8.1.4**).

The (only) difference between the v3 and v2 GMs is that for v3 three additional state vector elements (one per CarbonSat spectral band) have been added to the BESD/C state vector, namely the so-called “zero-level offset” (ZLO) state vector elements.

Each of them corresponds to one additional column of the BESD/C Jacobian matrix containing the radiance response (change) related to an additive radiance offset in the corresponding band (note that these ZLO Jacobians are not constant although the radiance offset is constant, because BESD/C is based on using the logarithm of the sun-normalized radiance).

As will be shown later in this document, adding these three ZLO state vector elements make the retrieval less sensitive to additive radiometric errors.

The version 3 (v3) GM for scenario TRD is shown in **Figure 25** and the one for scenario TRM in **Figure 26**.

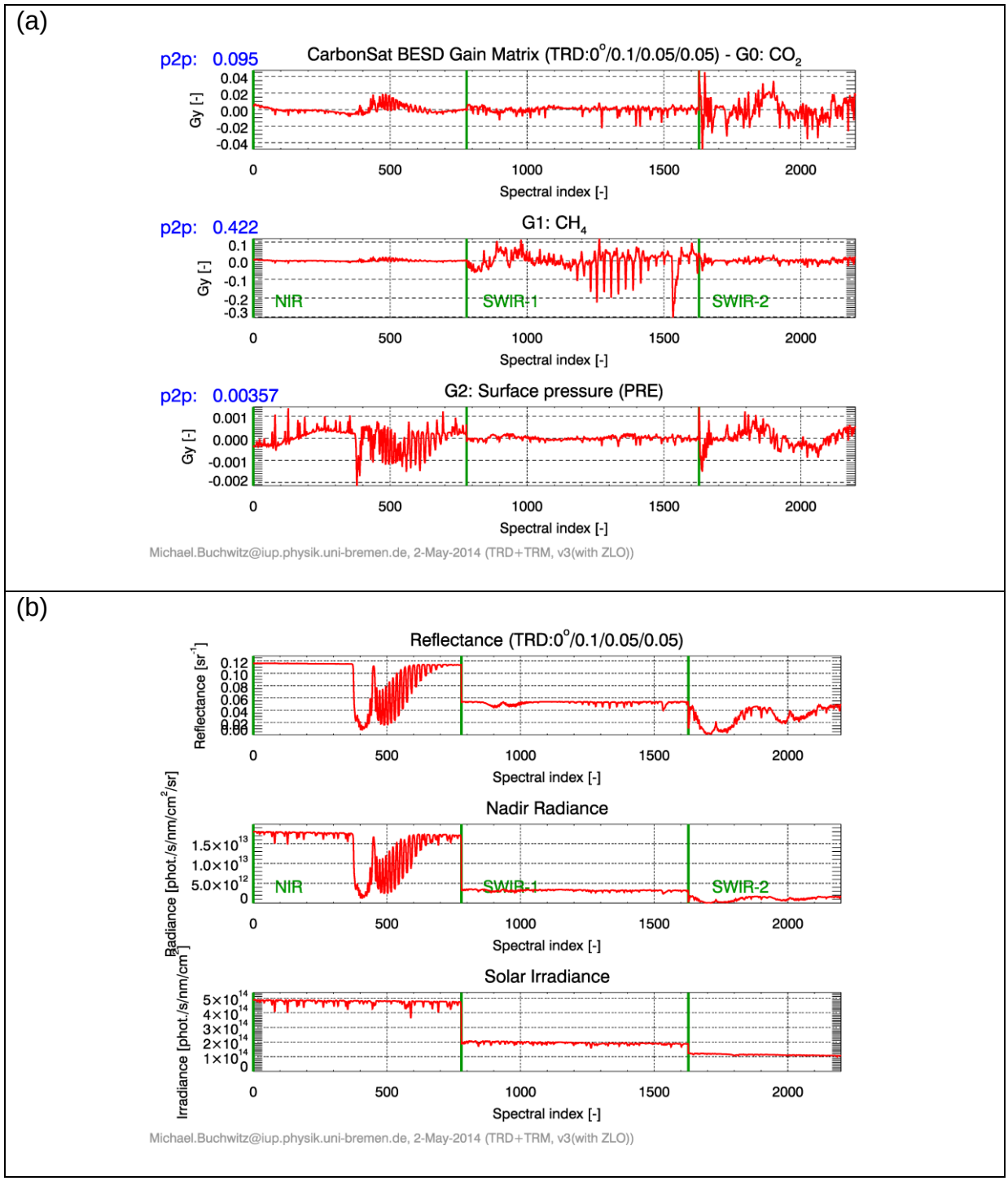

Figure 25: Gain matrix (GM) version 3 (v3) for scenario TRD. **(a)** The three columns of the GM: G0 (top), G1 (middle) and G2 (bottom). **(b)**: Corresponding reflectance, nadir radiance and solar irradiance spectra.

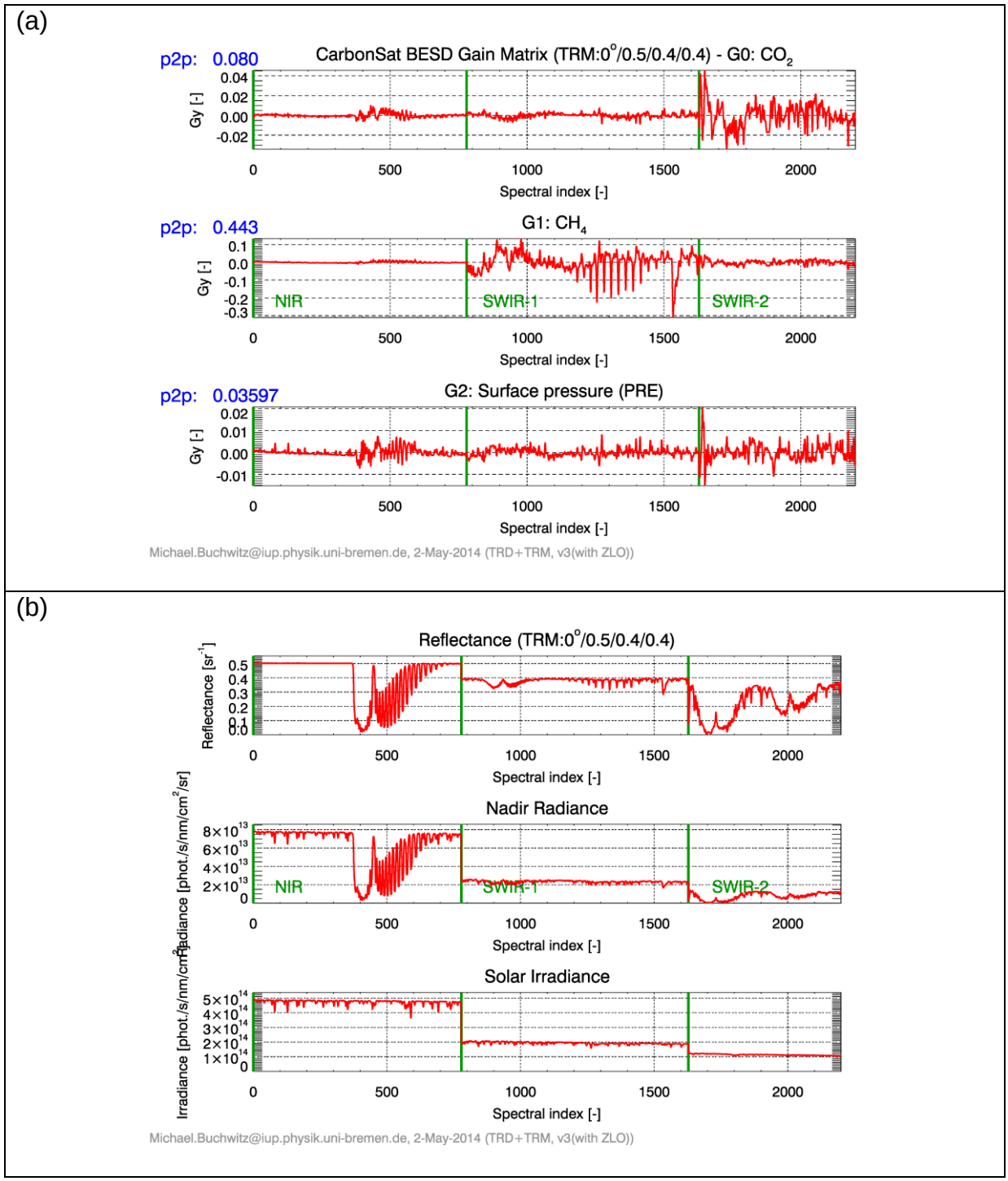

Figure 26: As **Figure 25** but for scenario TRM (v3).

8.1.4. GMs for scenarios TRD and TRM (v2)

Initially, version 2 (v2) GMs for scenarios TRD and TRM have been generated and delivered to ESA. The only difference compared to the v3 GMs described in the previous section are: state vector elements “ZLO” have not been used for BESD/C. **Figure 27** shows the GM for scenario TRD and **Figure 28** for TRM.

(a)

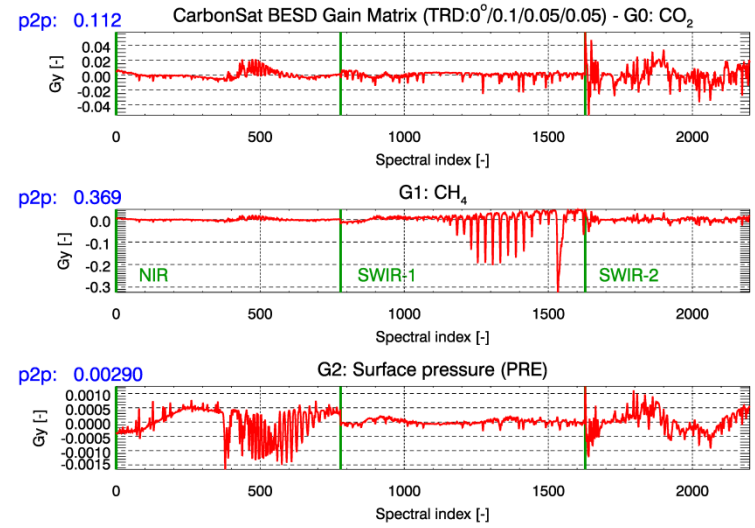

(b)

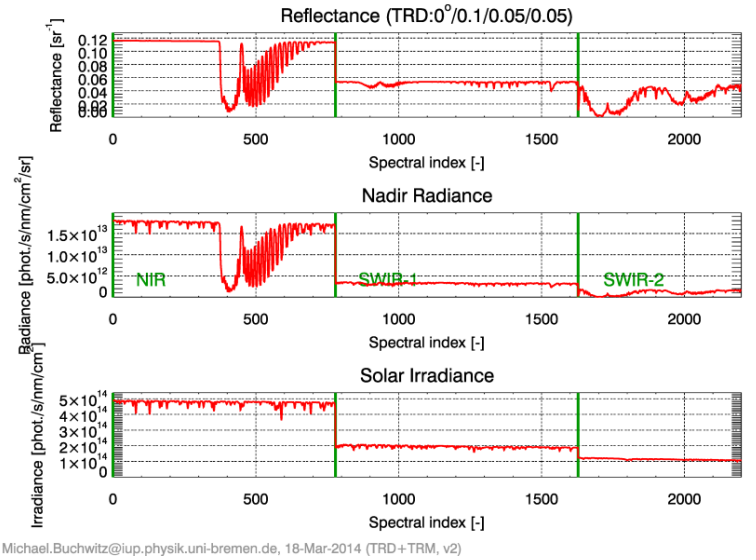

Figure 27: As **Figure 25** but for TRD GM v2.

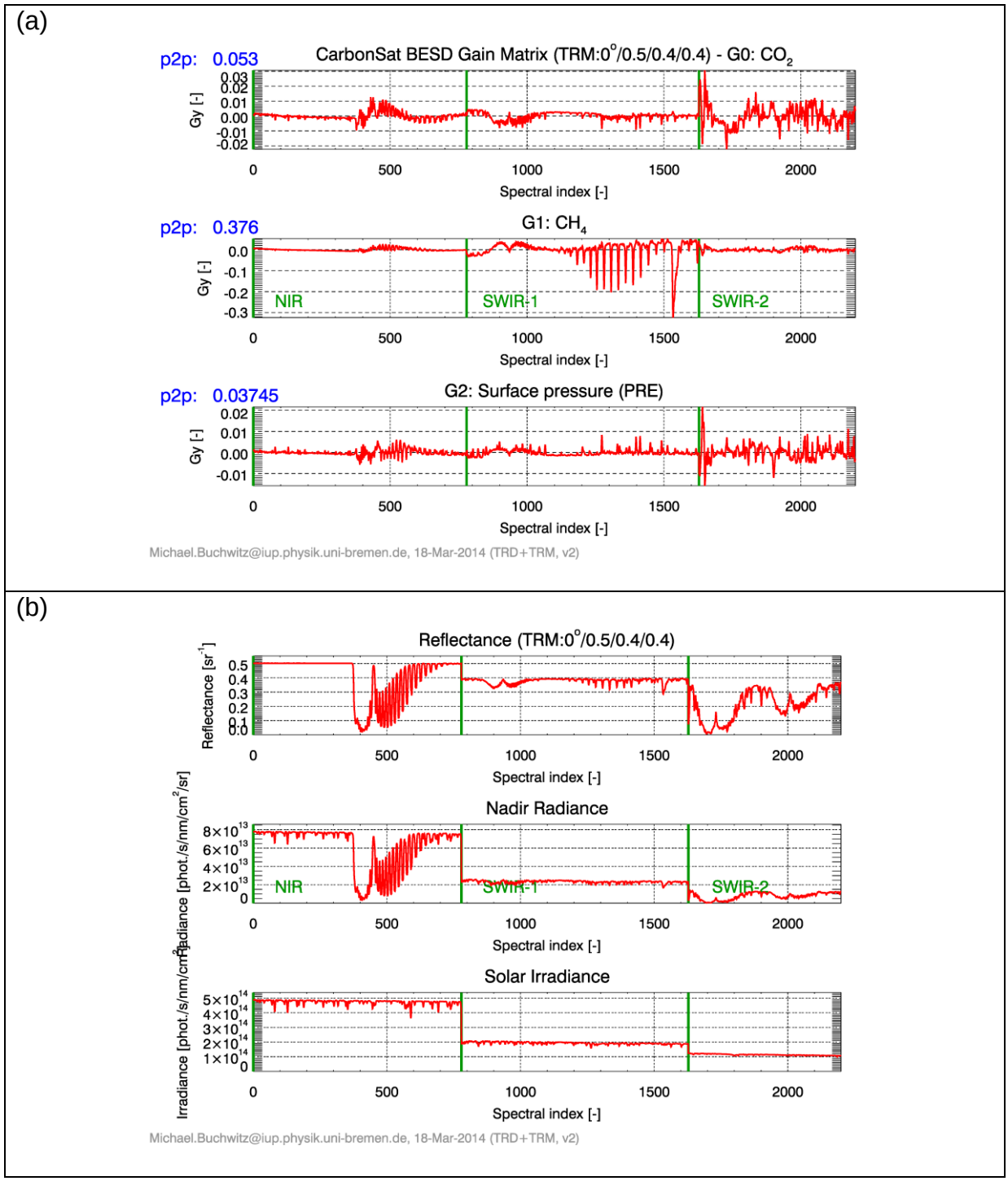

Figure 28: As **Figure 26** but for TRM GM v2.

8.1.5. GMs and reference spectra for VEG and TBW scenarios

Here gains and reference spectra for five other scenarios are described. The settings to compute them are identical to the ones as used for the TRD and TRM scenario gain files (see **Sect. 8.1.2**).

The definition of these scenarios is given in **Table 5**.

Scenario	ID	SZA	Surface albedo		
			NIR	SWIR-1	SWIR-2
Tropical Bright with Water cloud	**TBW**	0^o	0.7	0.2	0.2
Mid latitude vegetation	**VEG50**	50^o	0.2	0.1	0.05
High latitude vegetation	**VEG70**	70^o	0.2	0.1	0.05
Mid latitude vegetation bright 1 (x2x2x2)	**VEG22250**	50^o	0.4	0.2	0.1
Mid latitude vegetation bright 2 (x2x2x4)	**VEG22450**	50^o	0.4	0.2	0.2

Table 5: Definition of scenarios for additional gain matrices and reference spectra.

The corresponding gain matrix files and underlying high-resolution solar irradiance and radiance spectra (sampling 0.002 nm in all bands) have been delivered to ESA on 9-Jan-2015.

The corresponding figures are shown in **Figure 29** to **Figure 33**.

(a)

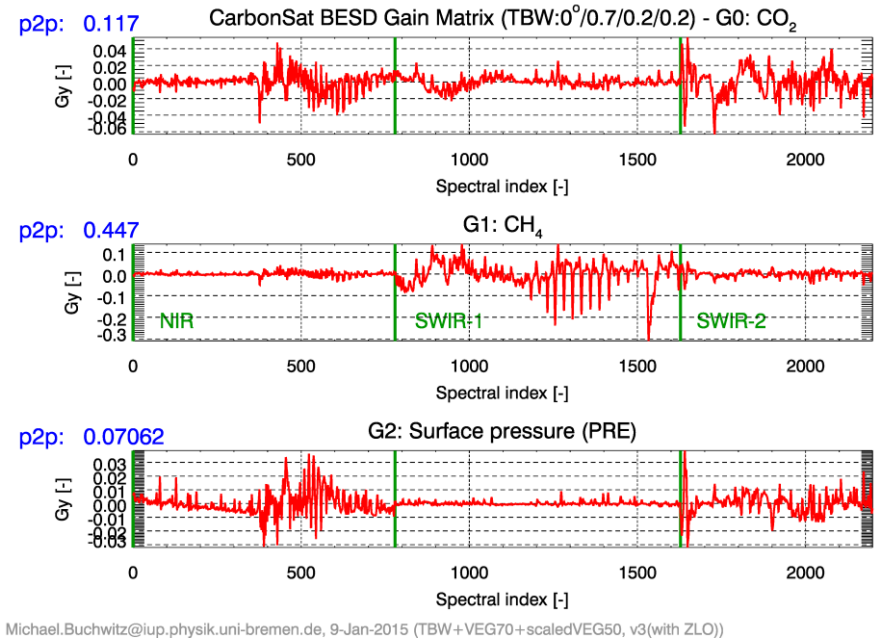

(b)

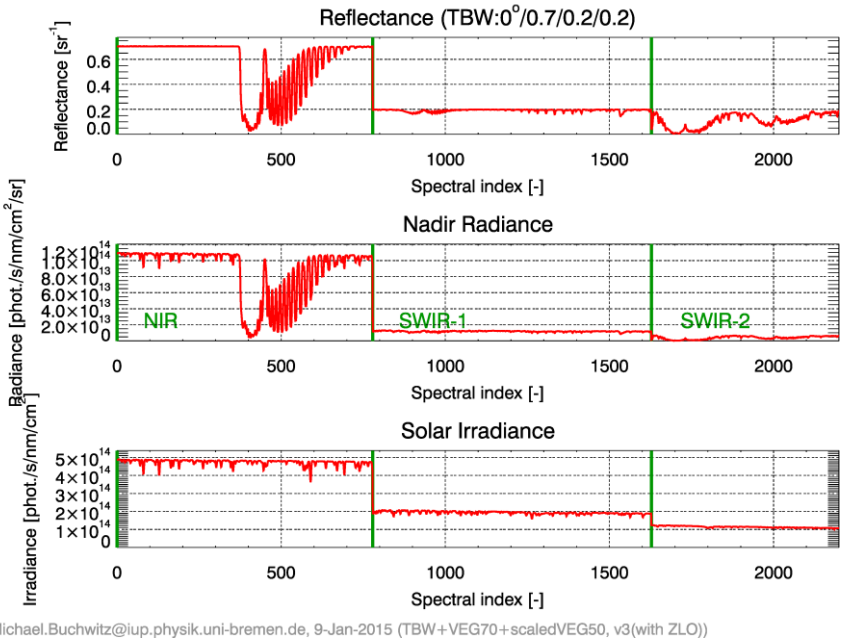

Figure 29: As **Figure 25** but for scenario TBW.

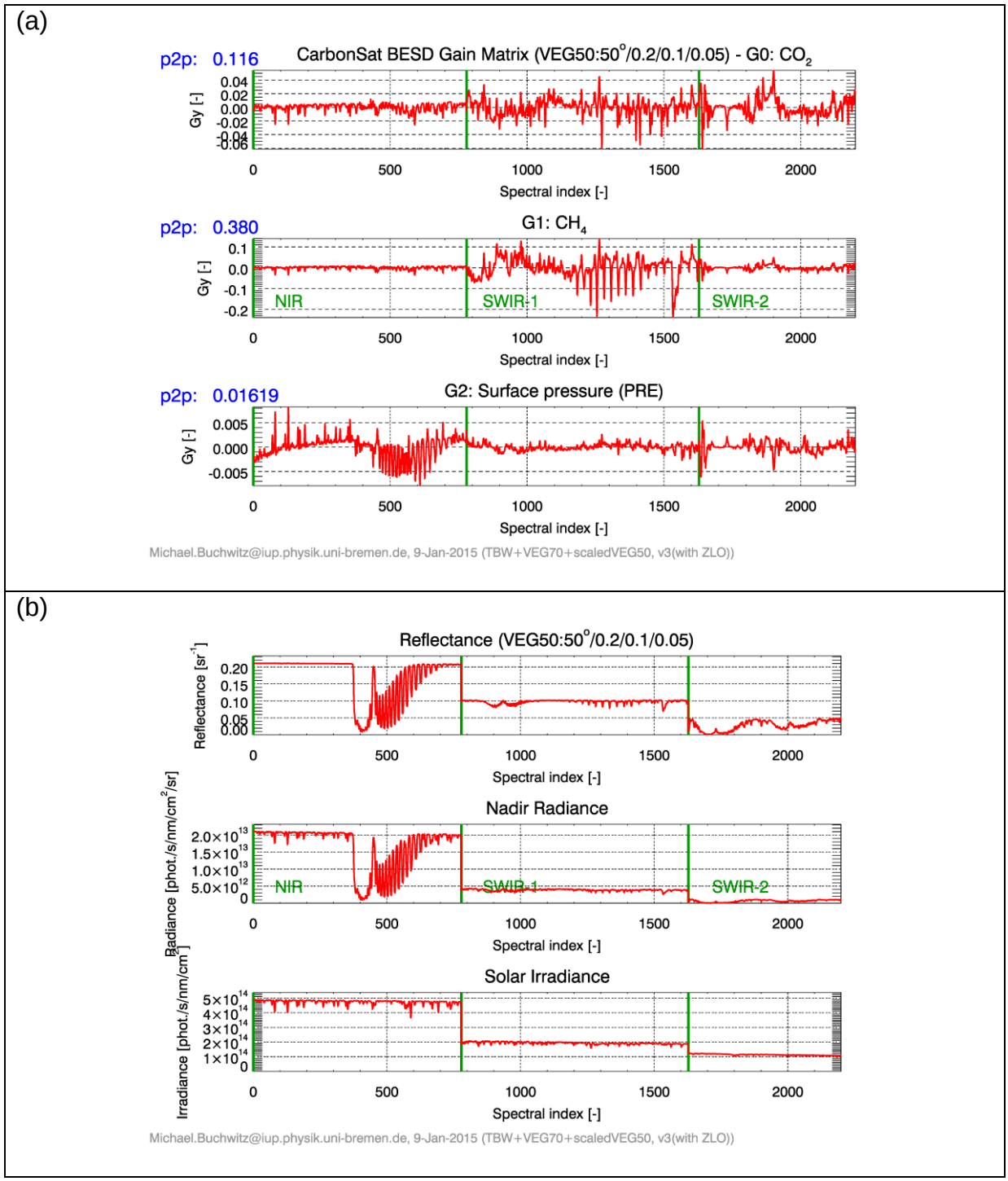

Figure 30: As **Figure 25** but for scenario VEG50.

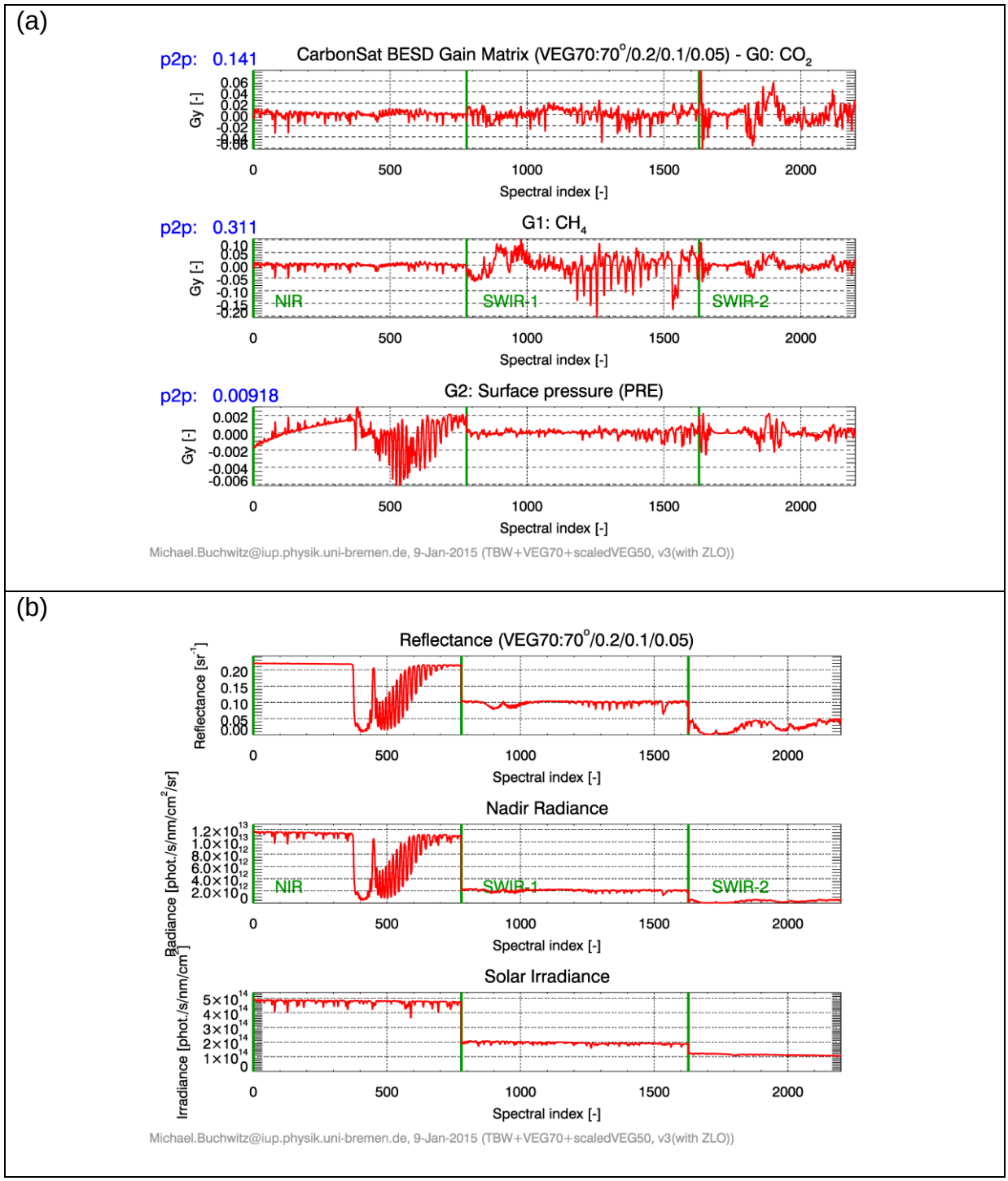

Figure 31: As **Figure 25** but for scenario VEG70.

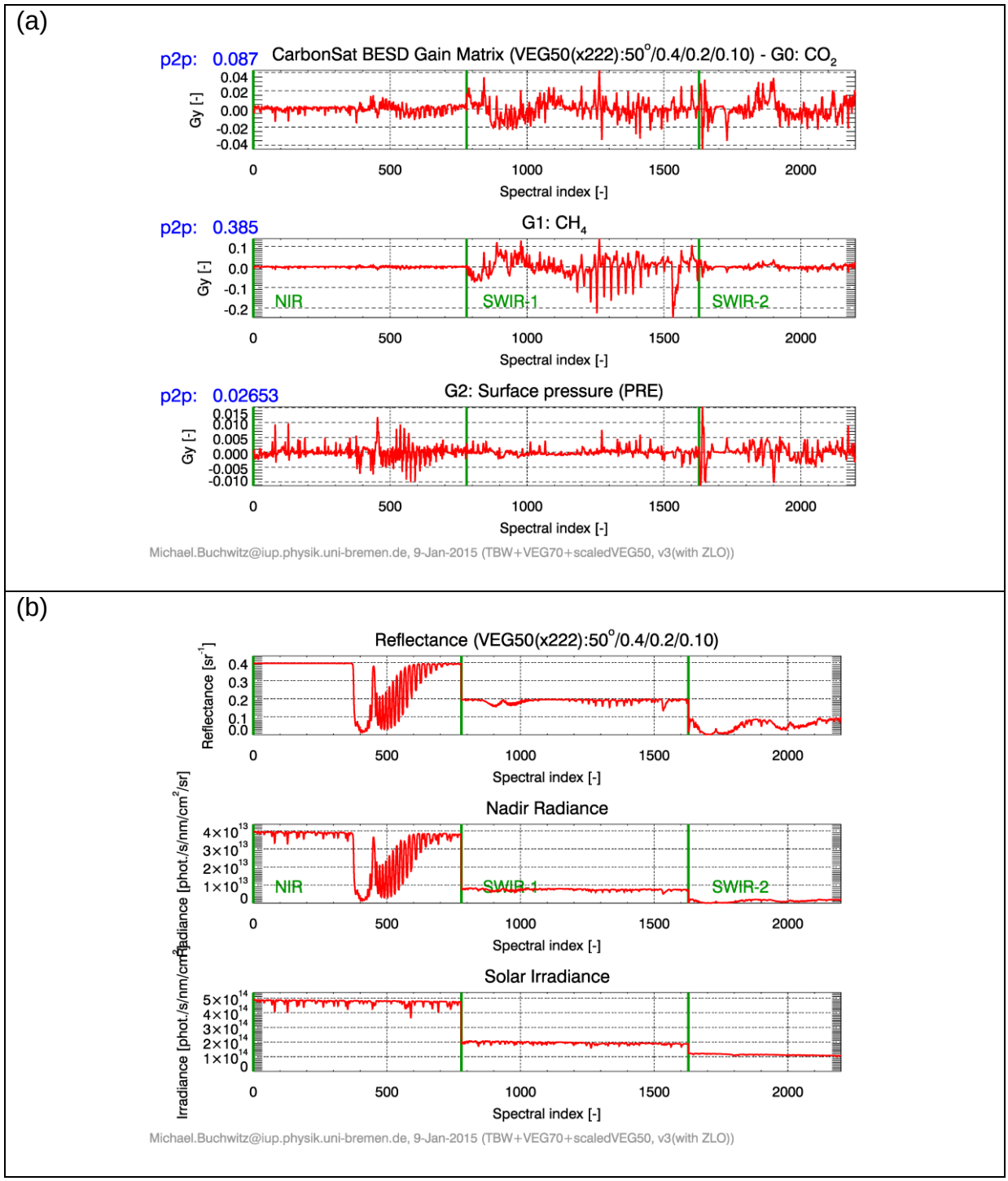

Figure 32: As **Figure 25** but for scenario VEG22250.

(a)

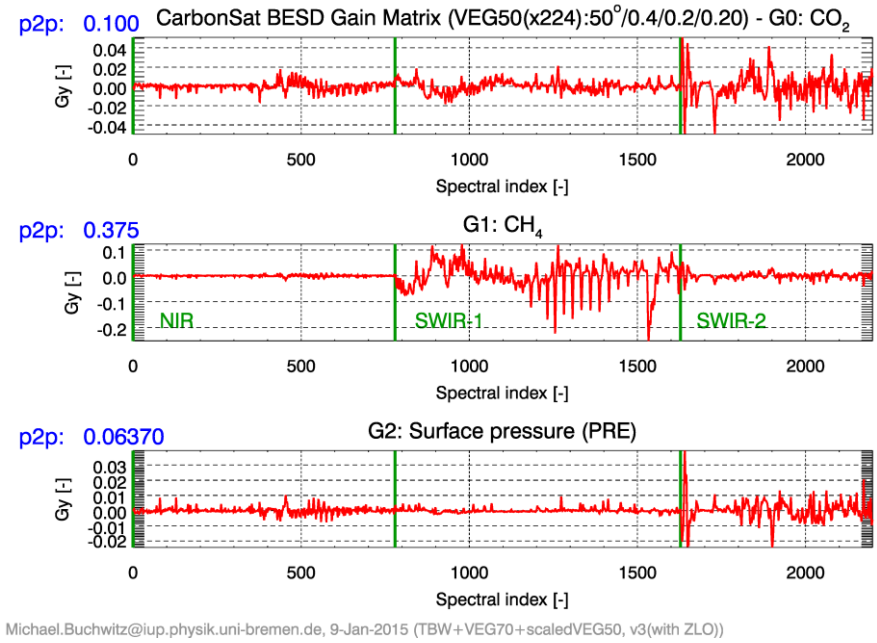

(b)

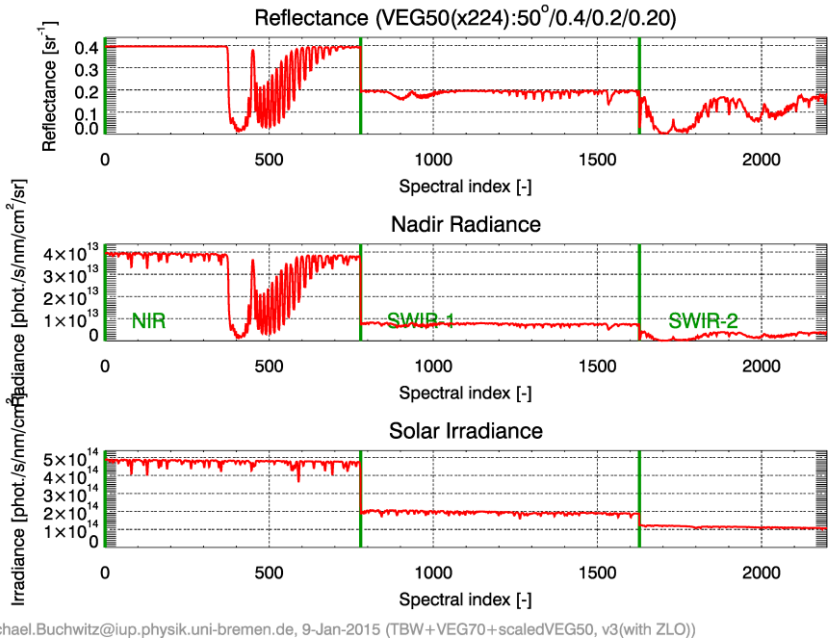

Figure 33: As **Figure 25** but for scenario VEG22450.

8.2. Reference spectra with polarization

Radiance spectra with polarization have been computed with the latest version of the RTM SCIATRAN (v3.4). These spectra have been generated using the latest specification of the CarbonSat spectral bands (**Table 2**).

8.2.1. Verification of SCIATRAN spectra

Before the SCIATRAN reference spectra are described and presented we first show some results from comparisons with independent RTM simulations performed at SRON (provided by J. Landgraf, SRON).

The radiance spectra correspond to clear sky scenes with a Lambertian surface. For these conditions very good agreement can be expected. Differences are however not expected to be zero due to, e.g., different modelling of Rayleigh scattering and due to the use of different solar irradiance spectra (no attempts have been made to fully harmonize the radiative transfer simulations with respect to these aspects).

As can be seen from the results shown below, the IUP / SCIATRAN and the SRON spectra agree well.

Comparison scenario No. 1:

- Lambertian surface with albedo 0.0.
- SZA: 60^o
- VZA 0^o (AZI: undefined)
- Clear sky (no aerosols or clouds)

Note that results for this scenario are also shown in **/Stam et al., 1999/**:

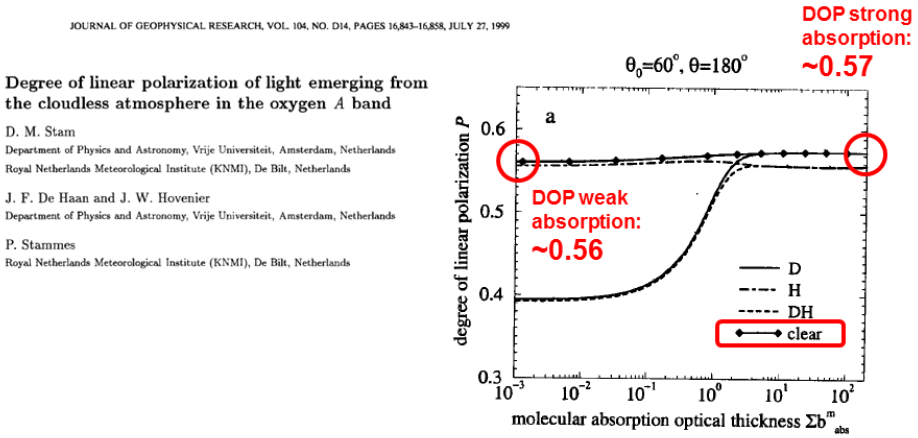

Figure 34: Results for comparison scenario No. 1 as shown in **/Stam et al., 1999/**. As can be seen, DOP in the O_2 A band varies between 0.56 (optically thin continuum) and 0.57 (center of strong absorption lines).

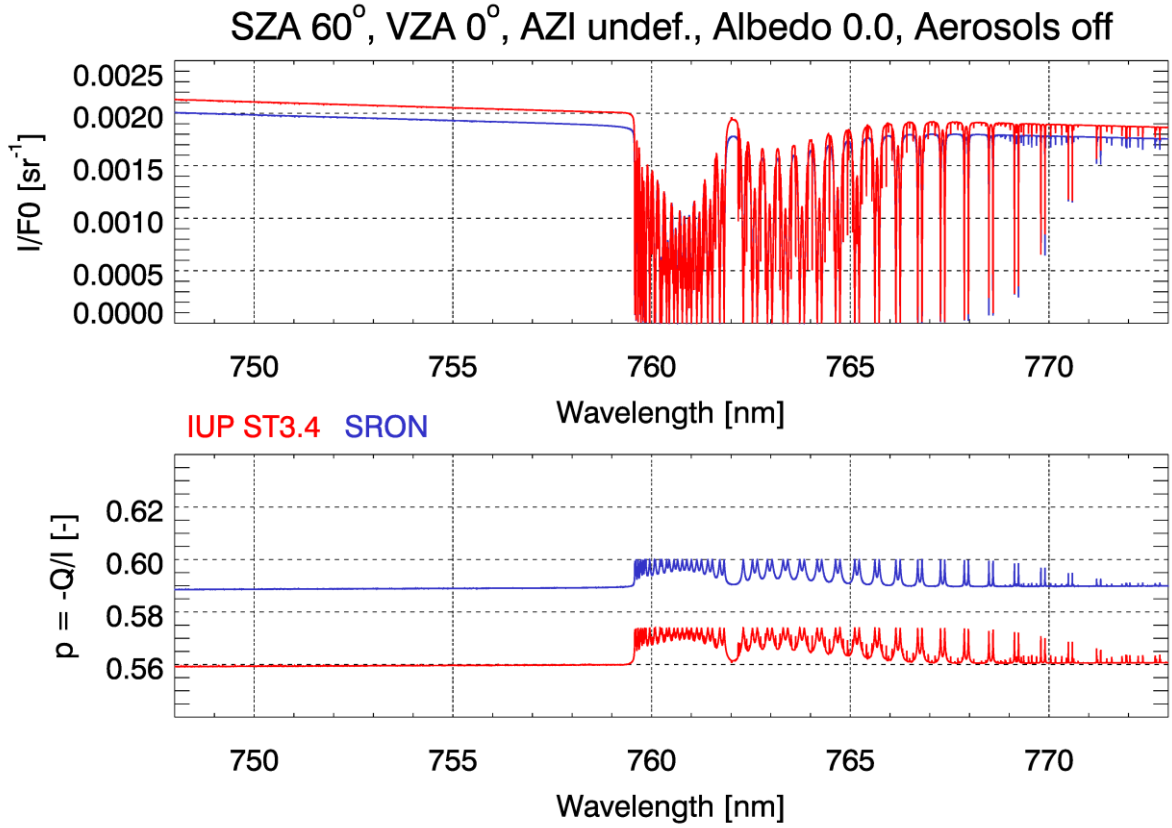

Figure 35: Comparison results for comparison scenario No. 1. As can be seen, there is good agreement between the spectra of IUP's SCIATRAN and SRON's RTM. For SCIATRAN DOP varies in the range 0.56 (weak absorption) to 0.57 (strong absorption) in perfect agreement with **/Stam et al., 1999/** (see **Figure 34**).

Comparison scenario No. 2:

- Lambertian surface with albedo 0.1.
- SZA: 70°
- VZA 15° (AZI: looking towards sun, i.e., AZI = 0° for SCIATRAN)
- Clear sky (no aerosols or clouds)

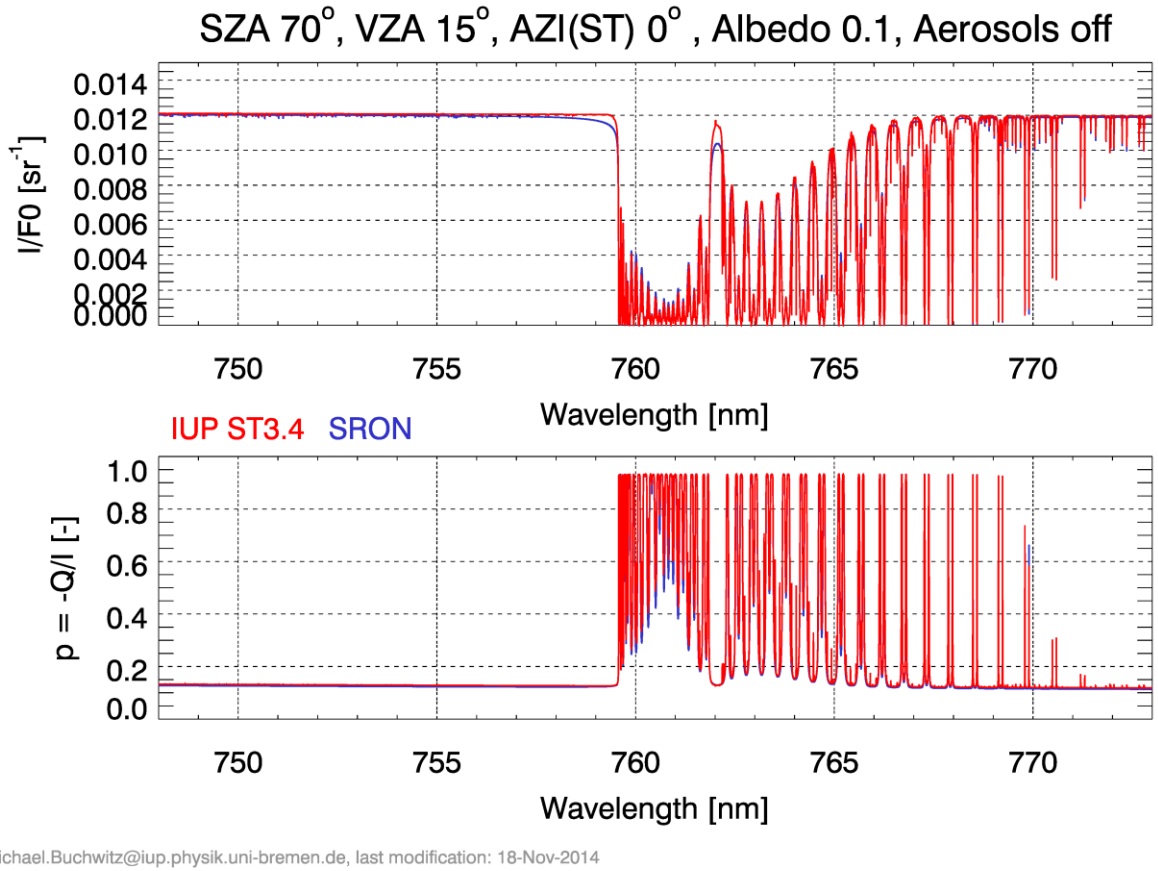

Figure 36: Comparison between the IUP SCIATRAN v3.4 and SRON RTM simulations for comparison scenario No.2. As can be seen, there is reasonable to good agreement between the spectra of the two RTMs. A zoom into this figures is shown in **Figure 37**.

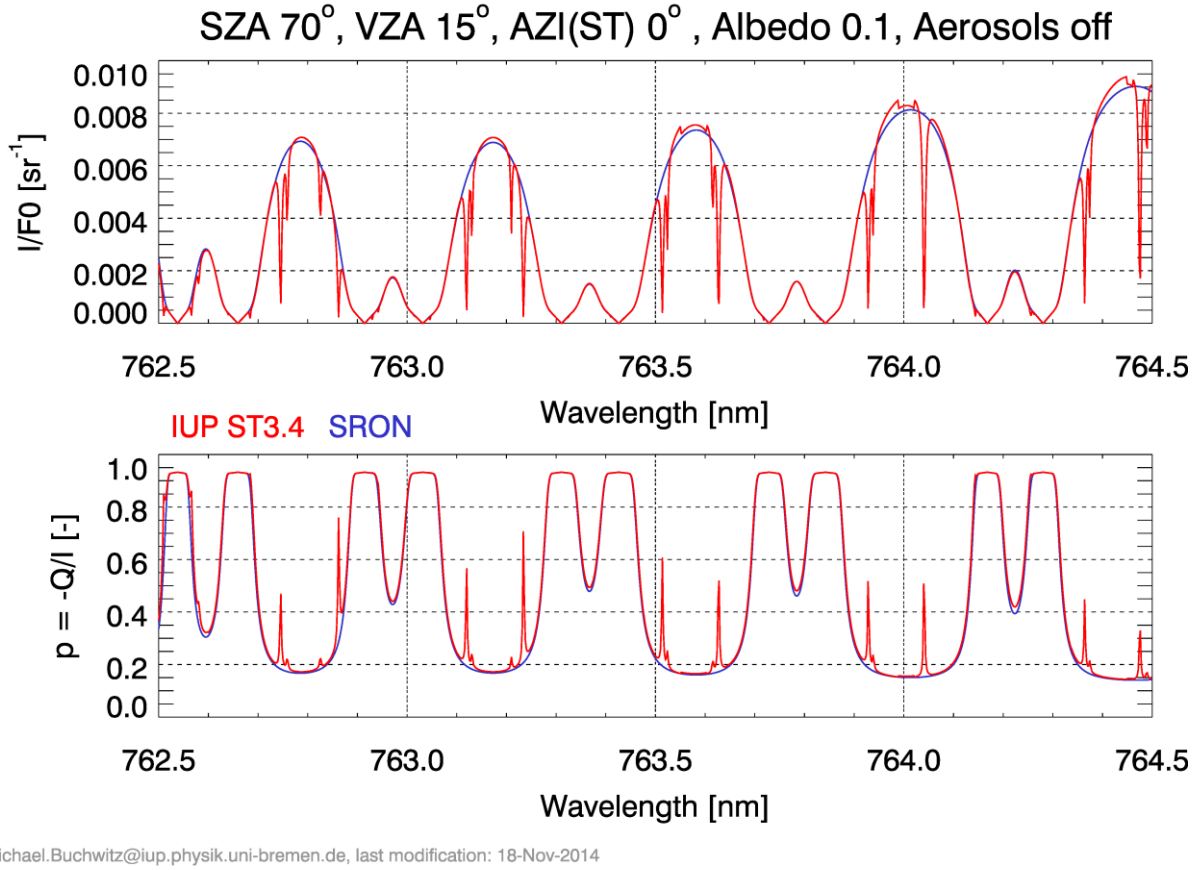

Figure 37: Zoom into **Figure 36**. As can be seen, there is reasonable to good agreement between the two spectra. There is nearly perfect agreement for the “overall shape” but differences in the detailed structures. These differences are due to the use of different solar irradiance input spectra (the spectrum used by IUP is at higher spectral resolution and has therefore “deeper lines”, as shown in the following two figures **Figure 38** (IUP spectra) and **Figure 39** (SRON spectra)).

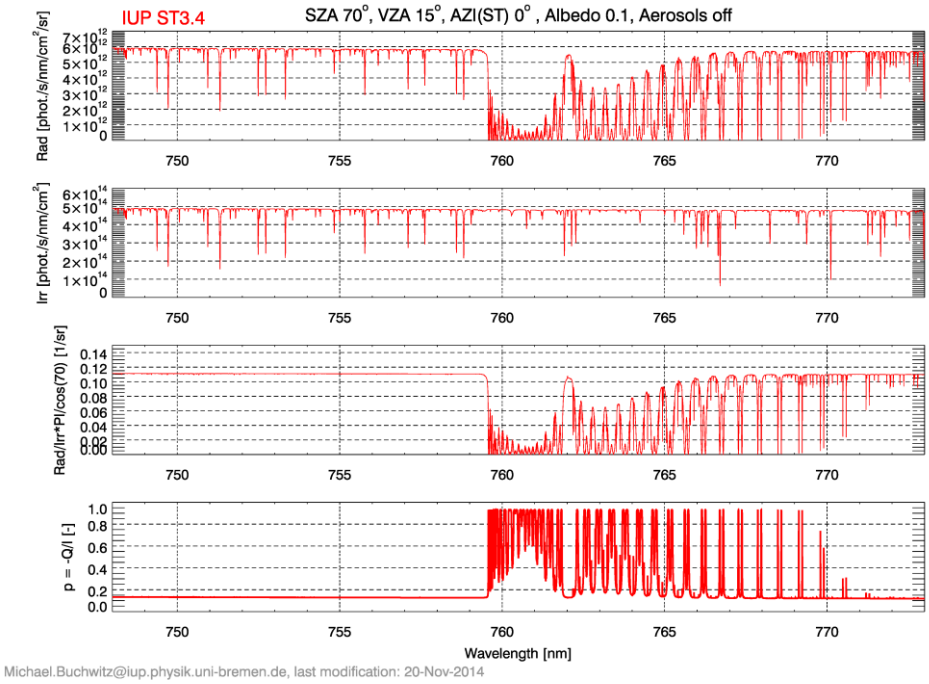

Figure 38: SCIATRAN spectra for comparison scenario No. 2 (the corresponding SRON spectra are shown in **Figure 39**).

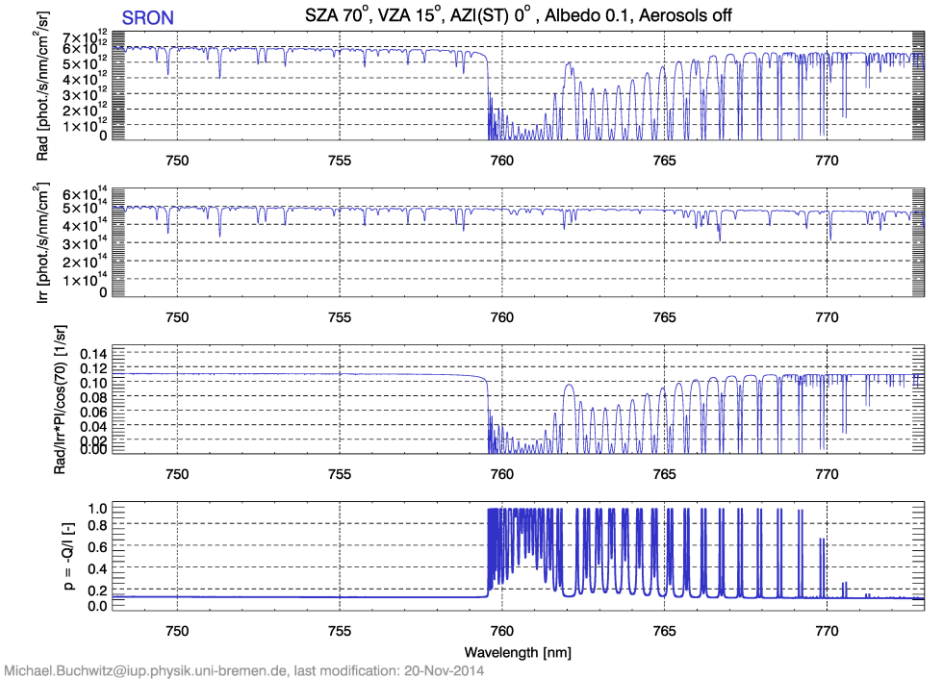

Figure 39: SRON spectra for comparison scenario No. 2 (the corresponding IUP SCIATRAN spectra are shown in **Figure 38**).

8.2.2. Polarized reference spectra for Lambertian surface

Figure 40 shows radiance spectra with polarization and the degree of linear polarization for the CarbonSat NIR band as computed with the RTM SCIATRAN v3.4.

Scenario:

- SZA 70^o,
- relative azimuth angle (AZI) 0^o (note that for SCIATRAN 0^o means looking to the sun whereas 180^o means looking away from the sun),
- Viewing Zenith Angle (VZA) 15^o (e.g., edge of swath and/or assuming a certain pitch angle) and
- vegetation albedo (here: NIR: 0.1, SWIR-1 and SWIR-2: 0.05).

The light red lines correspond to high-resolution monochromatic radiances (computed using a spectral sampling of 0.002 nm) and the blue lines are the spectra at CarbonSat spectral resolution (here: 0.1 nm FWHM for the NIR band).

Also shown is the degree of linear polarization (DOP). The DOP has been computed as follows (see bottom panel; note: Stokes components U and V are zero, e.g., U is zero because AZI=0^o and V is negligible for atmospheric observations):

- The light red curve corresponds to the monochromatic (or "line-by-line" (LBL)) DOP: $p_{LBL} := |Q_{LBL}|/I_{LBL} = |Q|/I = \sqrt{(Q^2)}/I$ (all equivalent).
- The blue curve shows the convolved LBL DOP: $\langle p_{LBL} \rangle := \langle |Q|/I \rangle$.
- The green curve shows the DOP if computed using convolved Q and I spectra $\langle Q \rangle$ and $\langle I \rangle$, i.e., $p_c := \sqrt{(\langle Q \rangle^2)}/\langle I \rangle$.

Note that for CarbonSat the relevant DOP spectra are those denoted p_c (= green curve). These DOP spectra are computed via the ratio of two "observed" radiance spectra ($\langle |Q| \rangle$ and $\langle I \rangle$), i.e., spectra measured at CarbonSat resolution (they can be measured for example on-ground and used to compute the DOP).

As can be seen, the maximum DOP (see p_c , green curve) in the centre of the O_2-A band (~761 nm) is ~0.8.

Figure 41 and
Figure 42 show the corresponding SCIATRAN spectra for the SWIR-1 (FWHM 0.3 nm; sampling 0.008 nm) and SWIR-2 bands (FWHM 0.55 nm; sampling 0.02 nm), respectively.

For SWIR-1 the maximum DOP value (see p_c) is 0.015 (**Figure 29**).

For SWIR-2 DOP can reach its maximum value of 1.0 (
Figure 42). More specifically, the maximum value of the degree of linear polarization is:

- SWIR-2A (1925 – 1990 nm): 1.0 for p_c
- SWIR-2B (1990 – 2043 nm): ~0.5 for p_c
- SWIR-2C (2043 – 2095 nm): ~0.02 for p_c

The (monochromatic) Stokes vector spectra have been made available for ESA for CarbonSat related purposes.

They are stored on the IUP CSL1L2 ftp server:

Main directory for all reference spectra described in this section:

- RefSpec/Radiances_polarization/ RefSpec_Polarization_2Dec2014/

Sub-directory for this scenario:

- SZA70_VZA150_AZI000_ ALB010005005_clear /

For each band (NIR, SWIR-1, SWIR-2) a high-resolution (monochromatic) nadir radiance spectrum is provided:

- rad_pol_sza70_lam_nir.dat
- rad_pol_sza70_lam_sw1.dat
- rad_pol_sza70_lam_sw2.dat

In addition a solar irradiance spectrum is provided for each band:

- irrad_nir.dat
- irrad_sw1.dat
- irrad_sw2.dat

They are stored in sub-directory:

- SolarIrradiance/

The files are ASCII files with a header followed by a table of data with 5 columns: wavelength [nm] and the Stokes radiance components I, Q, U, V in [photons/s/nm/cm^2/sr].

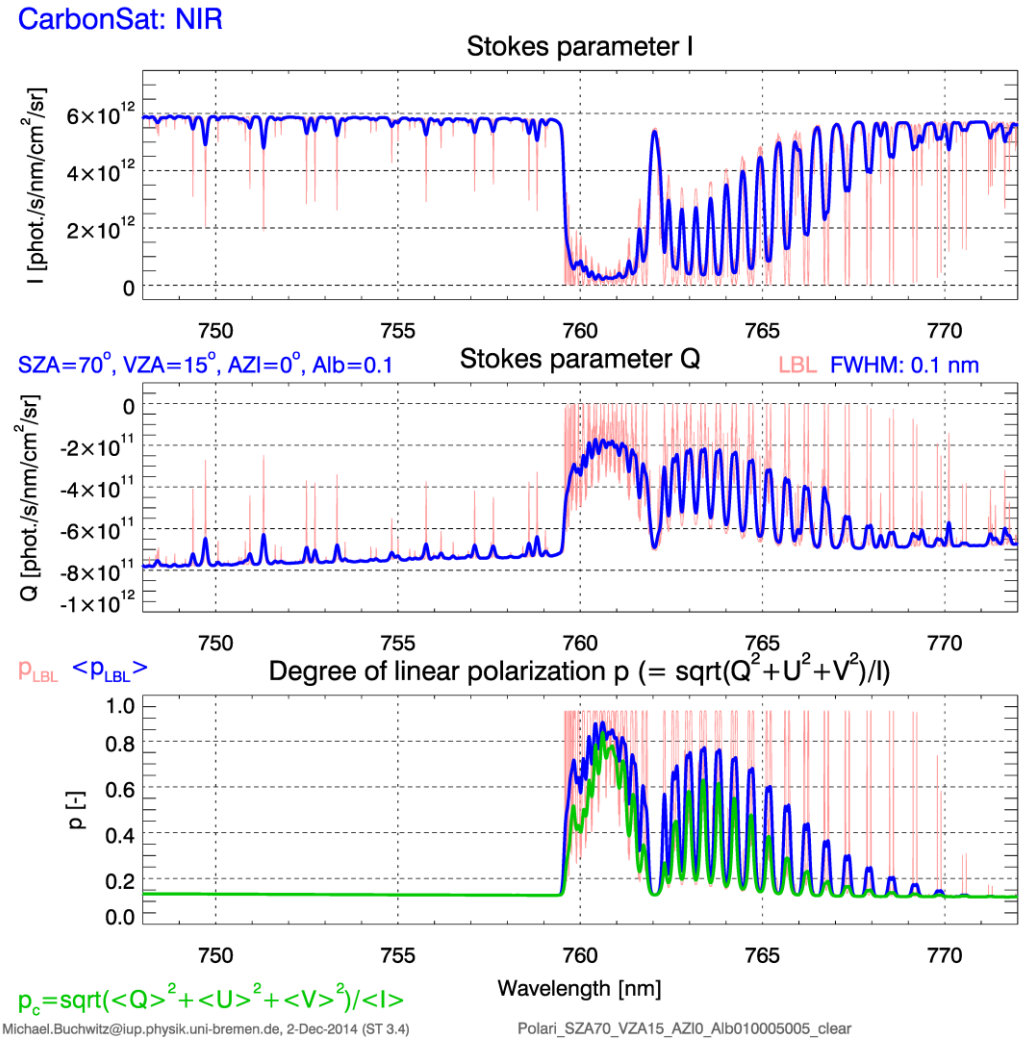

Figure 40: CarbonSat radiance spectra and degree of linear polarization (DOP): Top: Stokes parameter *I* (= total radiance), middle: Stokes parameter *Q* (= linear polarized radiance), and bottom: corresponding degree of linear polarization *p* computed via $p = |Q|/I$ (note that $U = V = 0$). Scenario: SZA 70°, relative azimuth angle (AZI) 0° (= looking to the sun), Viewing Zenith Angle (VZA) 15° and vegetation albedo (here: NIR: 0.1, SWIR-1 and SWIR-2: 0.05). The light red lines correspond to high-resolution monochromatic radiances (computed using a spectral sampling of 0.002 nm) and the blue lines (and the green line for DOP) are the spectra at CarbonSat spectral resolution (here: 0.1 nm FWHM). As can be seen, the relevant degree of linear polarization (pc = green curve) is approximately 0.8.

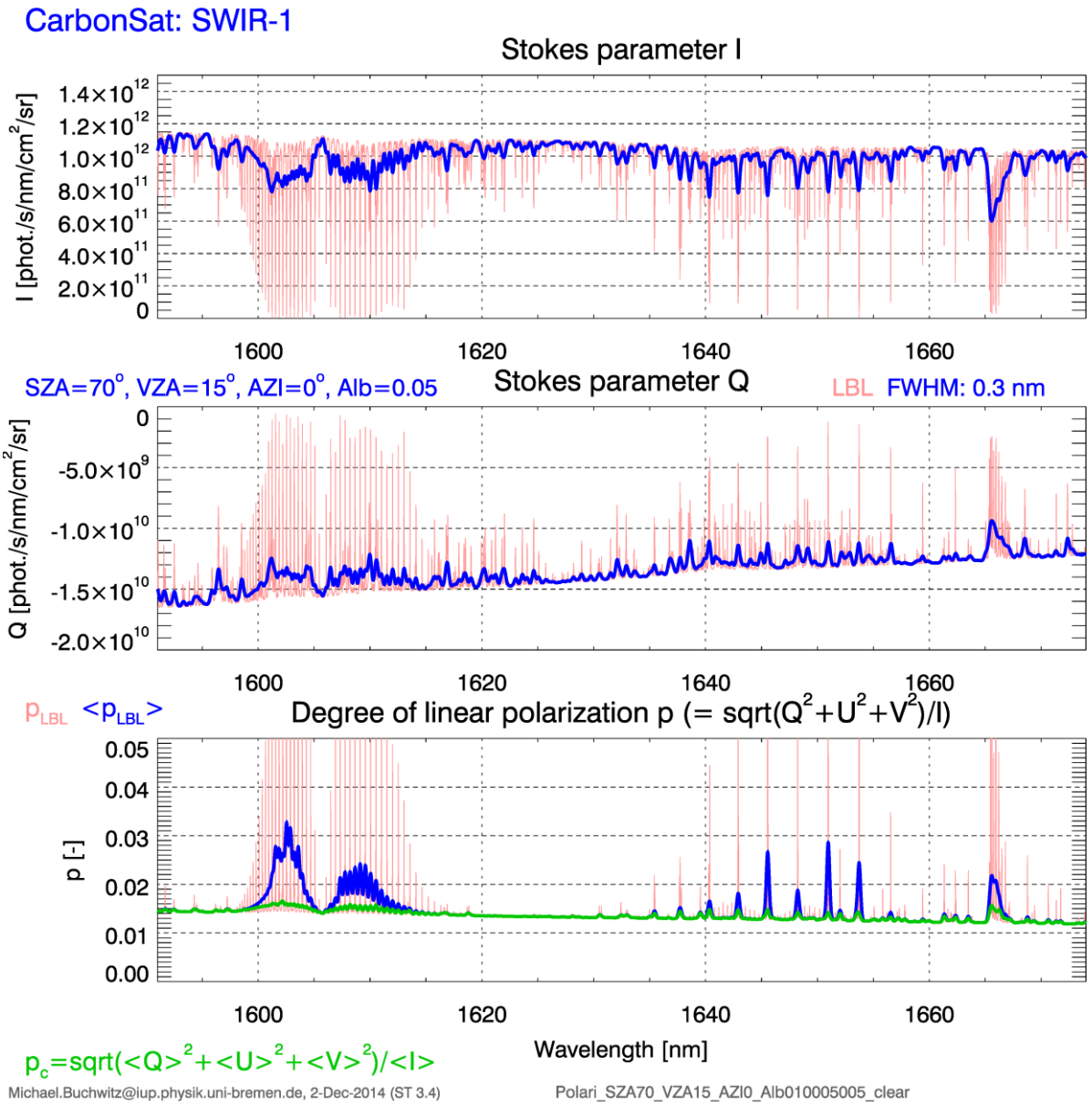

Figure 41: As **Figure 40** but for the CarbonSat SWIR-1 band. Spectral sampling 0.008 nm.

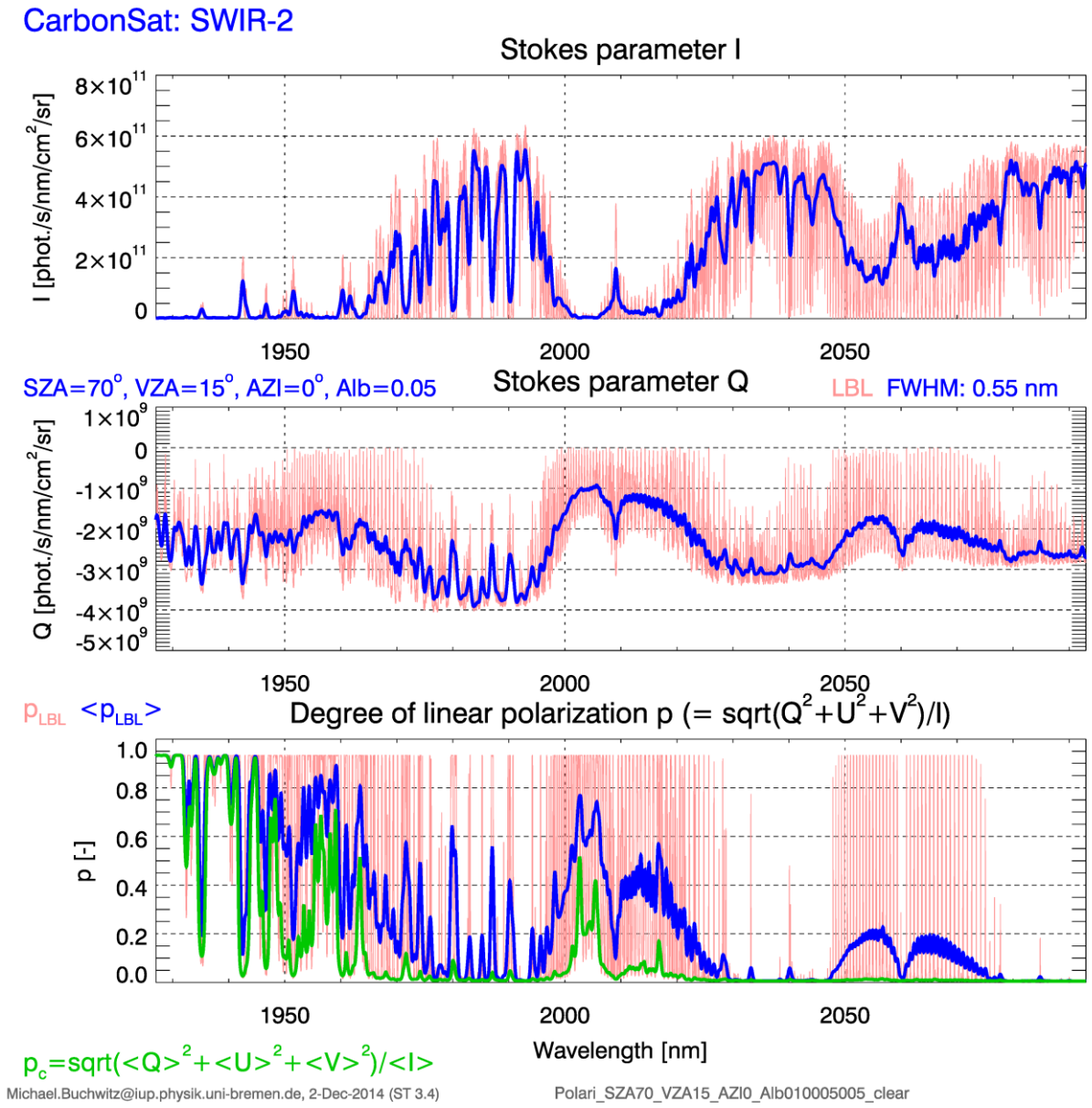

Figure 42: As **Figure 40** but for the CarbonSat SWIR-2 band. Spectral sampling 0.02 nm.

Figure 43 -
Figure 45 show the corresponding spectra for SZA = 50°. They are stored in sub-directory for this scenario:

- SZA50_VZA150_AZI000_ ALB010005005_clear /

For each band (NIR, SWIR-1, SWIR-2) a high-resolution (monochromatic) nadir radiance spectrum is provided:

- rad_pol_sza50_lam_nir.dat
- rad_pol_sza50_lam_sw1.dat
- rad_pol_sza50_lam_sw2.dat

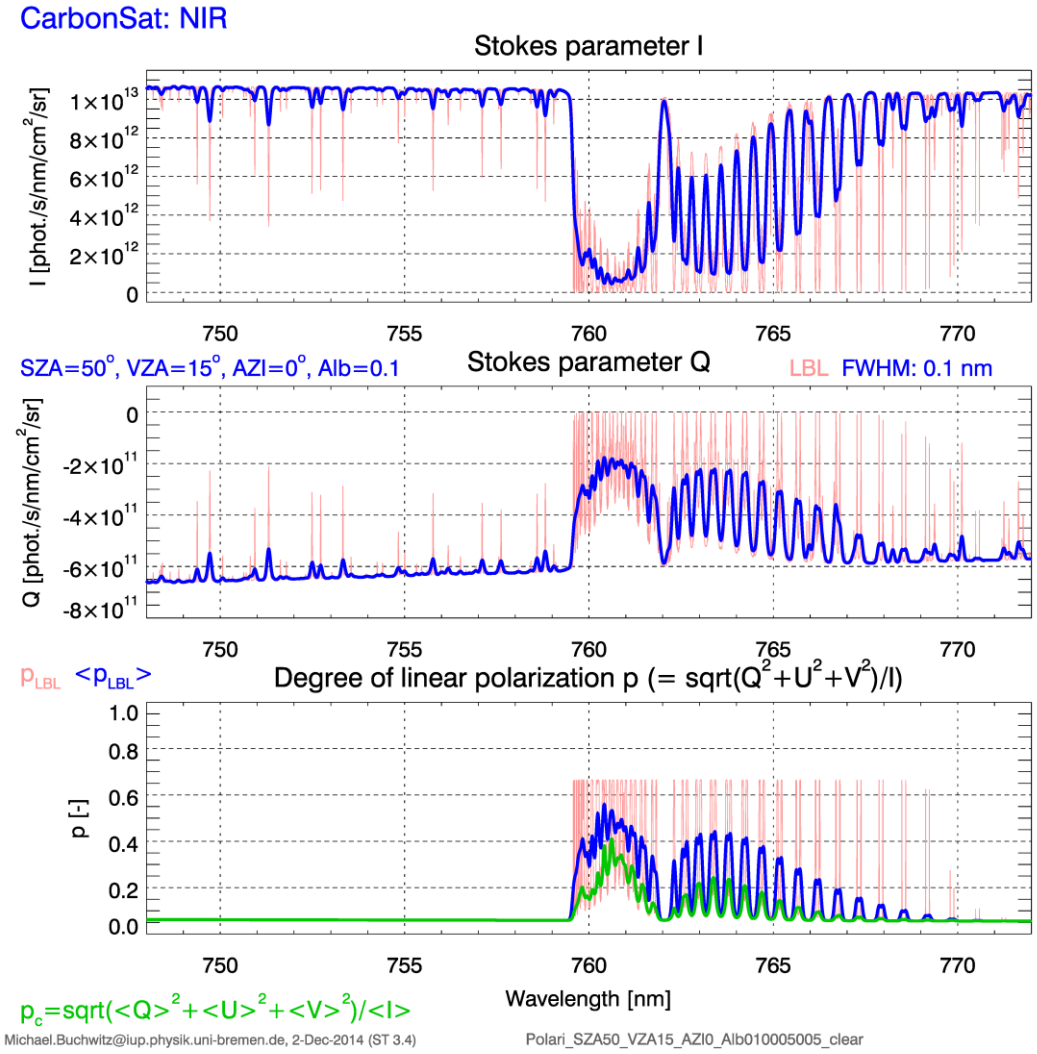

Figure 43: As **Figure 40** but for SZA 50°.

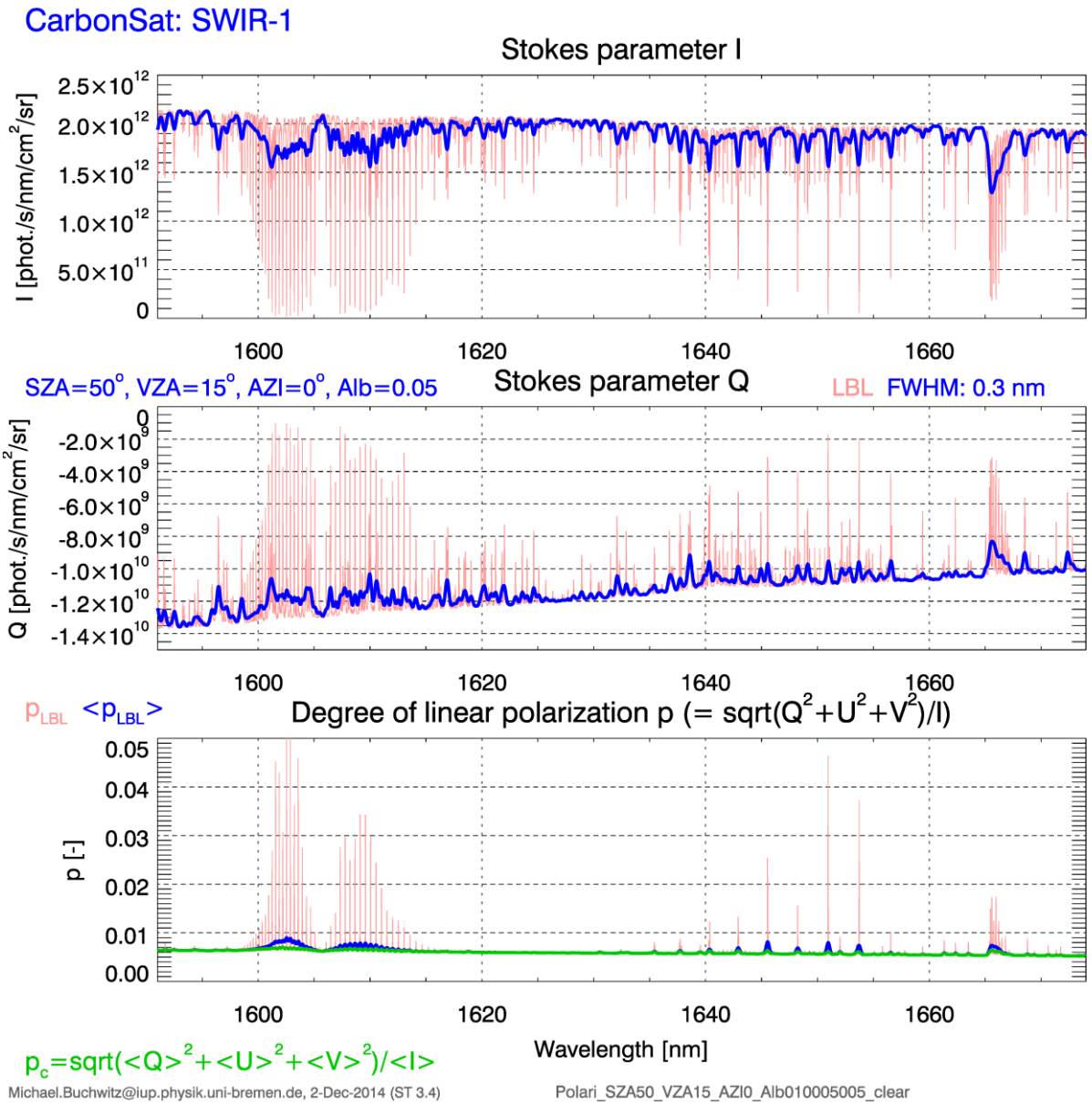

Figure 44: As **Figure 43** but for the CarbonSat SWIR-1 band.

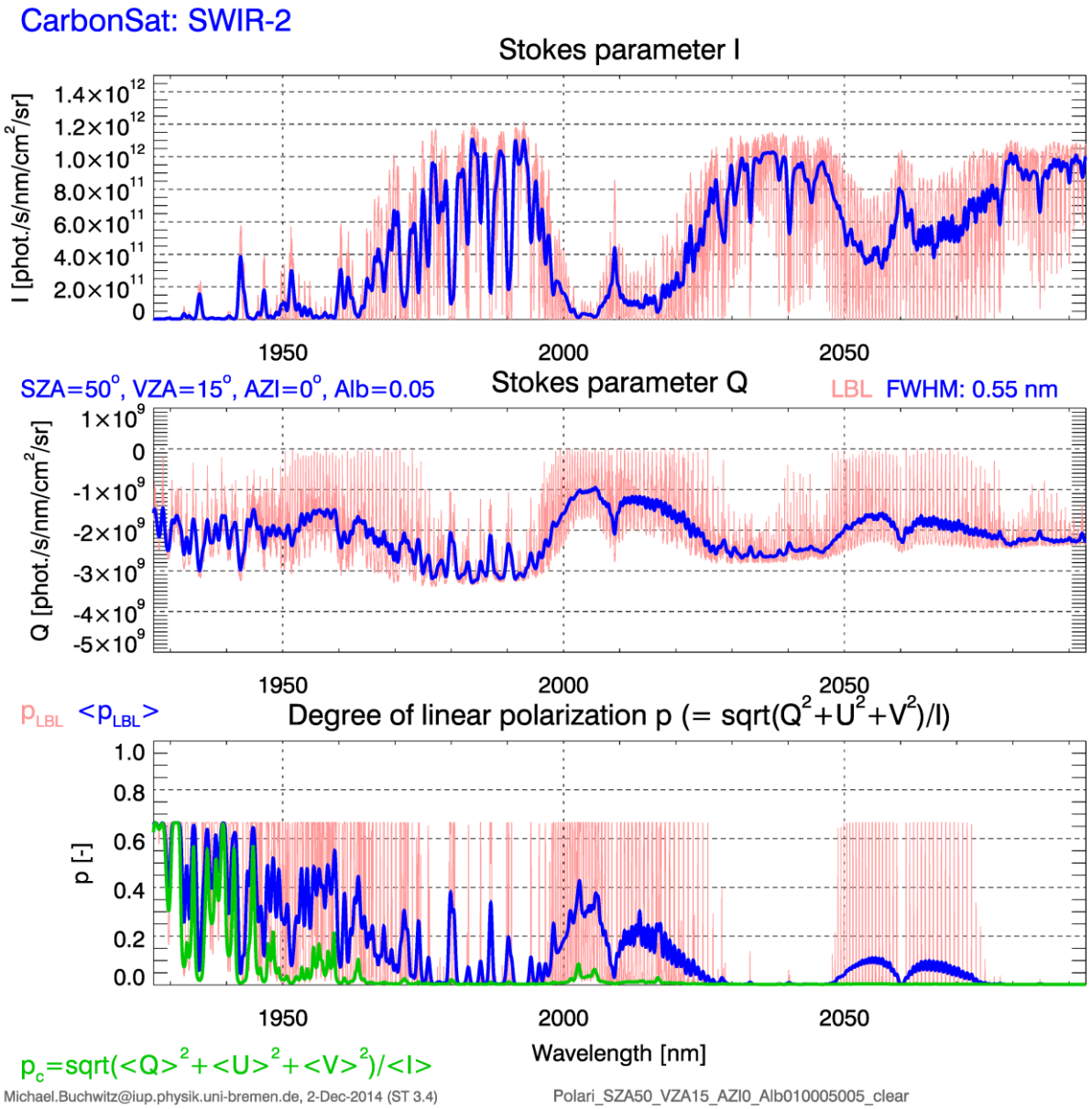

Figure 45: As **Figure 43** but for the CarbonSat SWIR-2 band.

8.2.3. Polarized reference spectra for polarizing surface

In this section SCIATRAN spectra for scenes with a polarizing surface are presented.

Figure 46 shows radiance spectra with polarization and the degree of linear polarization for the CarbonSat NIR band as computed with the RTM SCIATRAN v3.4. The scenario is similar as the one for SZA 70^o described in **Sect. 8.2.2**, except for the surface reflection properties. Here, for surface reflection, a polarizing BRDF for a vegetation surface has been used.

The light red lines shown in **Figure 46** correspond to high-resolution monochromatic radiances (computed using a spectral sampling of 0.002 nm for the NIR band) and the blue lines are the spectra at CarbonSat spectral resolution (here: 0.1 nm FWHM).

As for the figures in the previous section, **Figure 46** not only shows the Stokes vector elements I and Q (radiance spectra) but also the Degree Of linear Polarization (DOP). As in the previous section, convolved DOP (at CarbonSat) has been computed using two different formulas (note that Stokes elements U and V are 0.0):

- $<p_{LBL}> := <(\sqrt{Q^2})/I> = <|Q|/I>$, where p_{LBL} is the monochromatic DOP and < > denotes convolution with the CarbonSat ISFR (Instrument Spectral Response Function).
- $p_c := <\sqrt{Q^2}>/<I> = <|Q|>/<I>$.

As already noted in the previous section, for CarbonSat the relevant spectra are those denoted p_c (green curve).

Spectra for similar conditions have been computed independently by SRON as shown in **Figure 47**. As can be seen, the SRON radiance and DOP spectra (here p_c is shown) for VZA = $+15^o$ (blue curves) are “similar” as the corresponding spectra shown in **Figure 46**. They are however not identical as different models and parameters for the vegetation BRDF have been used. As a consequence, DOP is smaller for the SRON spectra.

Figure 48 and **Figure 49** show the corresponding SCIATRAN spectra for

- the SWIR-1 band (spectral sampling: 0.008 nm) and
- the SWIR-2 band (spectral sampling: 0.02 nm), respectively.

The (monochromatic) Stokes vector radiance spectra have been made available for ESA for CarbonSat related purposes.

They are stored on the IUP CSL1L2 ftp server:

Main directory for all reference spectra described in this section:

- RefSpec/Radiances_polarization/ RefSpec_Polarization_2Dec2014/

Sub-directory for this scenario:

- SZA70_VZA150_AZI000_ VegBRDF_clear/

For each band (NIR, SWIR-1, SWIR-2) a high-resolution (monochromatic) nadir radiance spectrum is provided:

- rad_pol_sza70_brdf_nir.dat
- rad_pol_sza70_brdf_sw1.dat
- rad_pol_sza70_brdf_sw2.dat

In addition a solar irradiance spectrum is provided for each band:

- irrad_nir.dat
- irrad_sw1.dat
- irrad_sw2.dat

They are stored in sub-directory:

- SolarIrradiance/

The files are ASCII files with a header followed by a table of data with 5 columns: wavelength [nm] and the Stokes radiance components I, Q, U, V in [photons/s/nm/cm^2/sr].

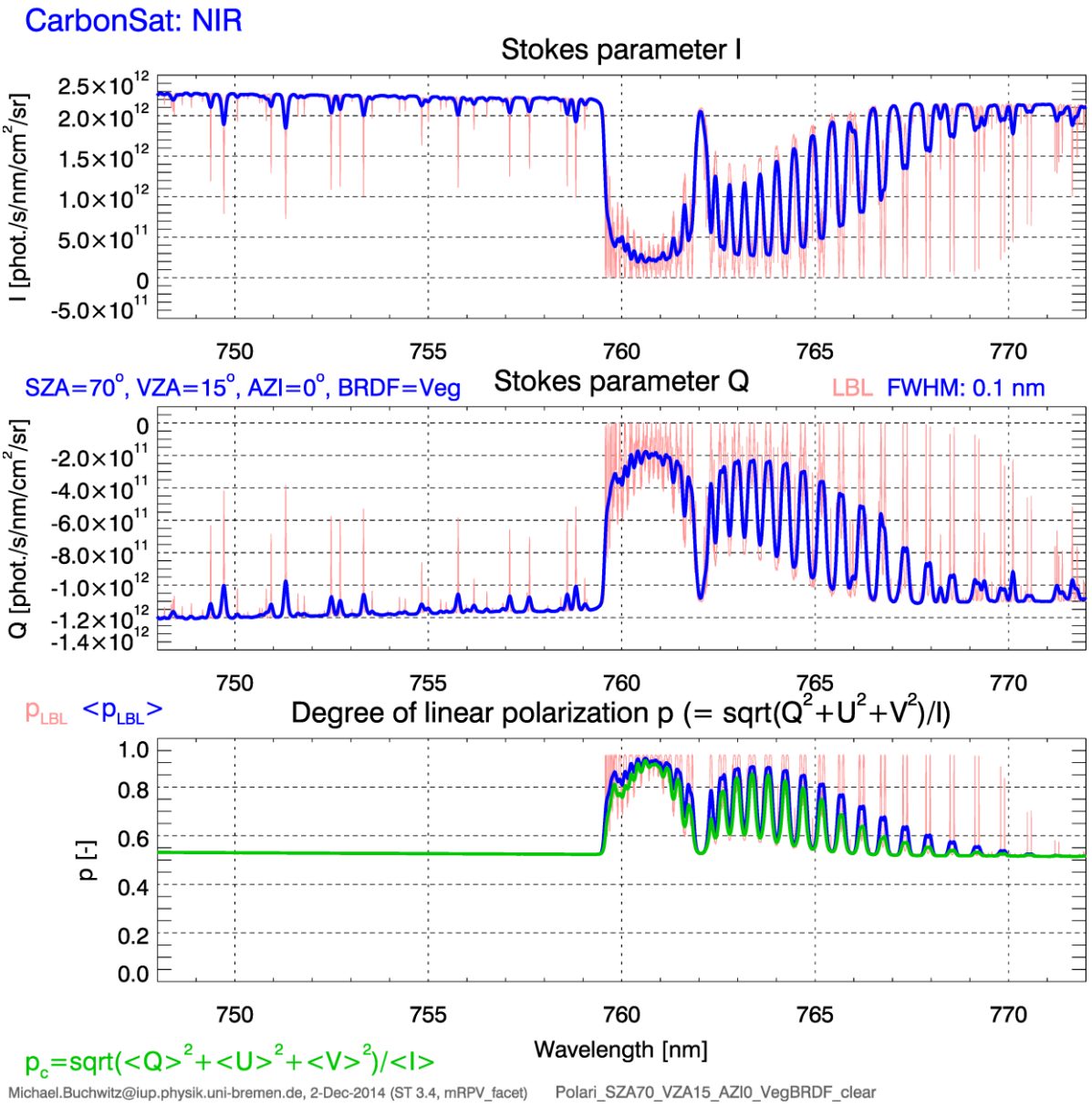

Figure 46: CarbonSat radiance spectra and degree of linear polarization (DOP): Top: Stokes parameter *I* (= total radiance), middle: Stokes parameter *Q* (= linear polarized radiance), and bottom: corresponding degree of linear polarization *p* computed via $p = |Q|/I$ (as $U = V = 0$). Scenario: SZA 70°, relative azimuth angle (AZI) 0° (= looking to the sun), Viewing Zenith Angle (VZA) 15° and surface reflection via polarized BRDF for vegetation ("wet grass", SCIATRAN v3.3 "mRPV_facet" model (with parameter a=0.014)). The light red lines correspond to high-resolution monochromatic radiances (computed using a spectral sampling of 0.002 nm) and the blue lines are the spectra at CarbonSat spectral resolution (here: 0.1 nm FWHM). Spectral sampling: 0.002 nm. The green curve shows the DOP curve which is relevant for CarbonSat ($p_c = <|Q|>/<I>$).

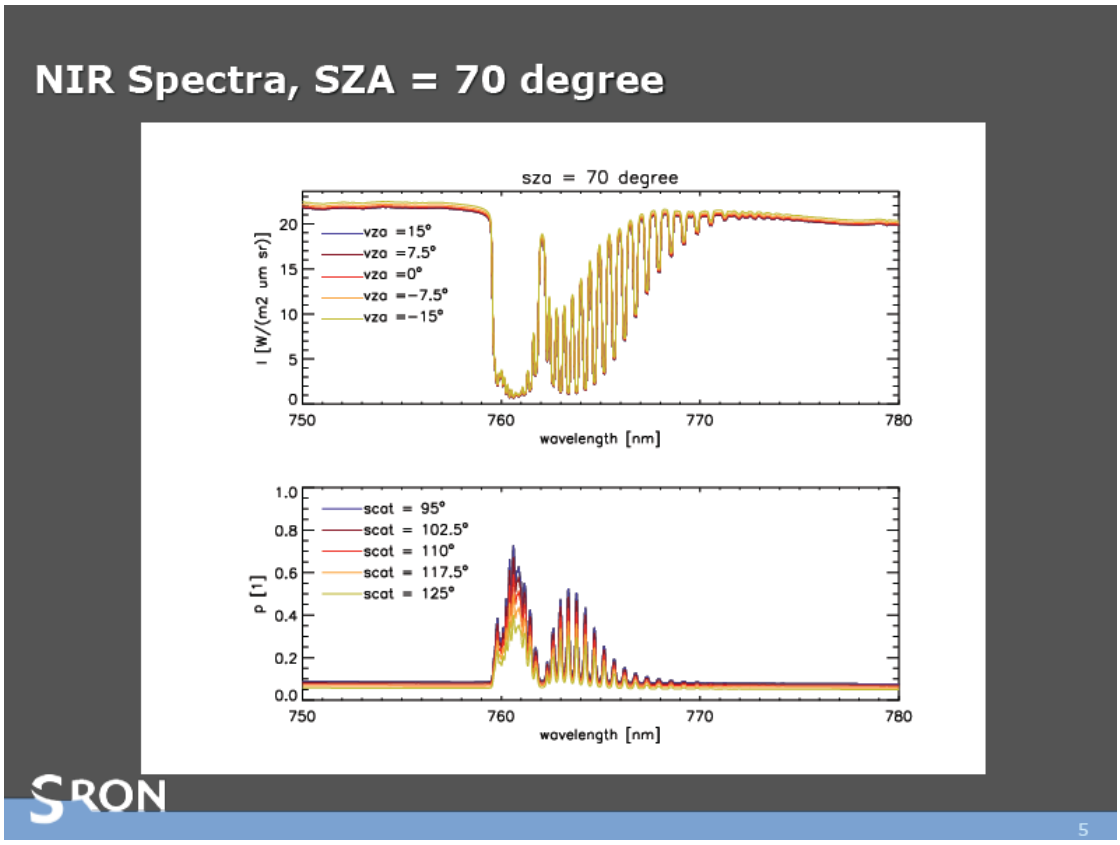

Figure 47: CarbonSat NIR radiance (top) and degree of linear polarization (bottom) as computed by SRON (Jochen Landgraf, "CarbonSat Polarization Spectra" (presentation pdf file), 31 March 2014) for several VZA (and corresponding scattering angles "scat") and a SZA of 70^o. The surface reflection comprises Lambertian (albedo 0.1 in NIR) and non-Lambertian (vegetation BRDF with polarization) components. The spectral resolution FWHM is 0.1 nm. As can be seen, the degree of linear polarization (p_c = <|Q|>/<I>) is slightly larger than 0.6 in the centre of the O_2-A band (~761 nm) for VZA = +15^o (or scattering angle 95^o; blue curve).

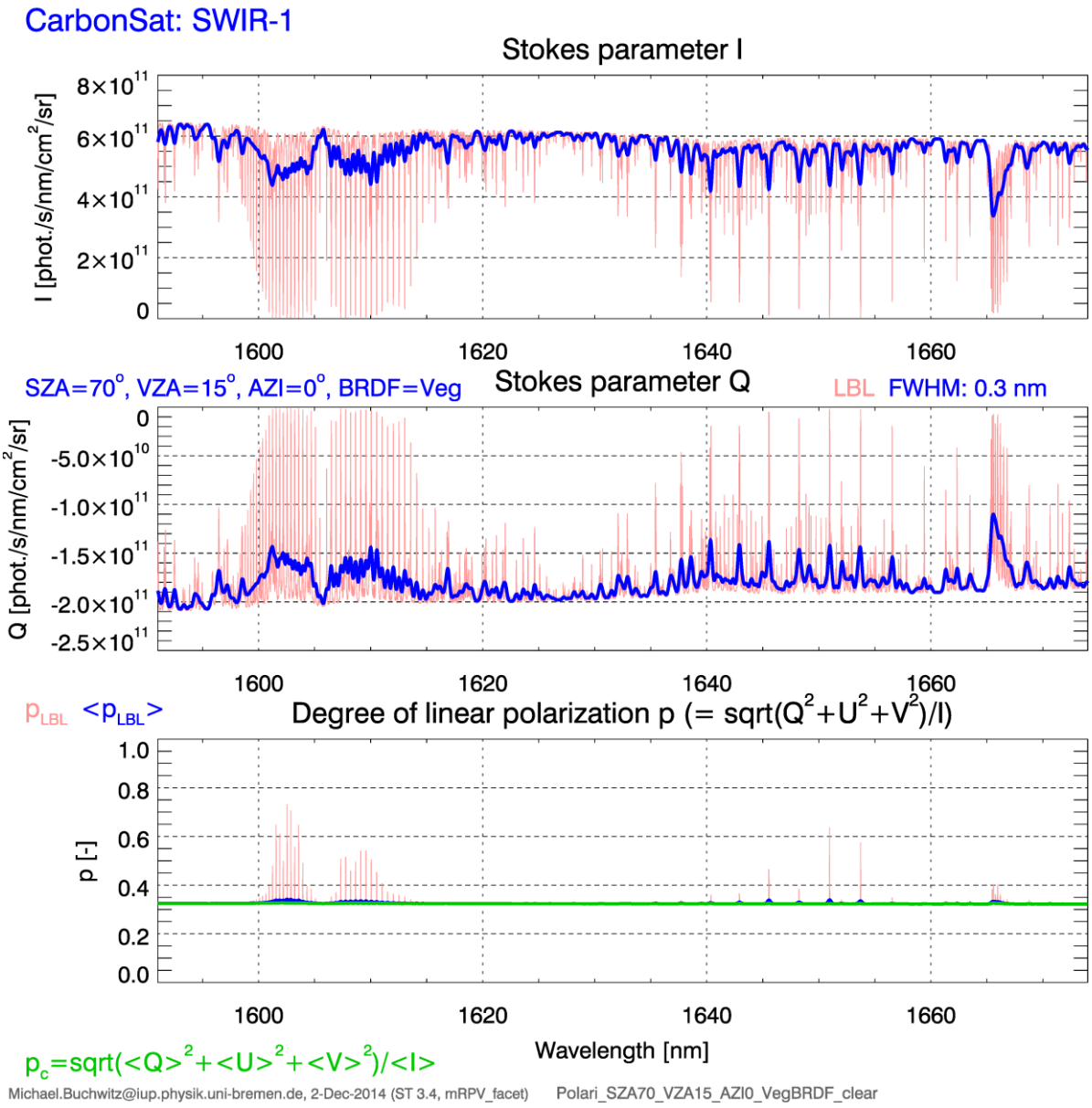

Figure 48: As **Figure 46** but for the SWIR-1 band (spectral sampling: 0.008 nm).

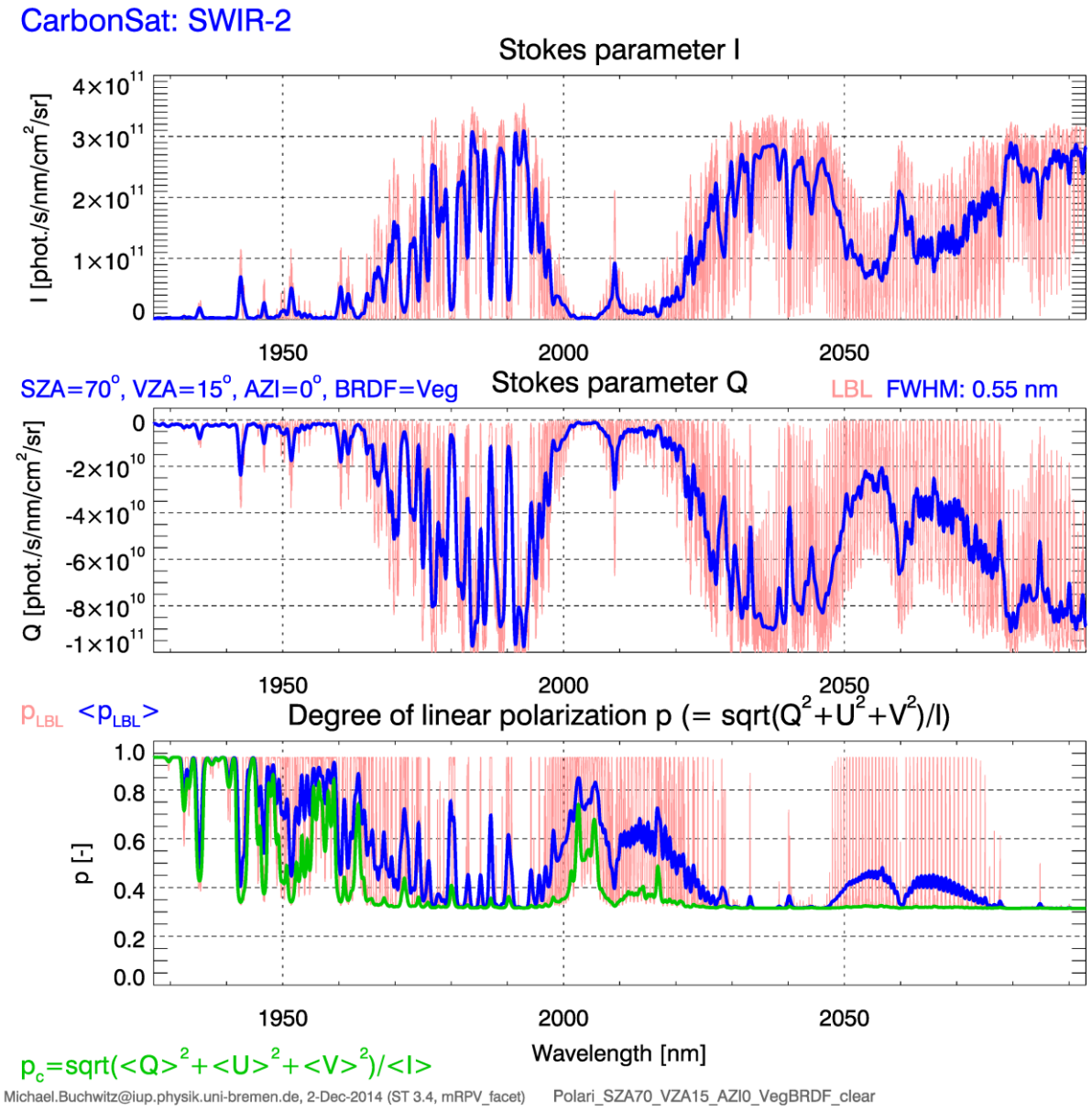

Figure 49: As **Figure 46** but for the SWIR-2 band (spectral sampling: 0.02 nm).

Figure 50 -
Figure 52 show the corresponding spectra for SZA = 50°. They are stored in sub-directory for this scenario:

- SZA50_VZA150_AZI000_ VegBRDF_clear /

For each band (NIR, SWIR-1, SWIR-2) a high-resolution (monochromatic) nadir radiance spectrum is provided:

- rad_pol_sza50_brdf_nir.dat
- rad_pol_sza50_brdf_sw1.dat
- rad_pol_sza50_brdf_sw2.dat

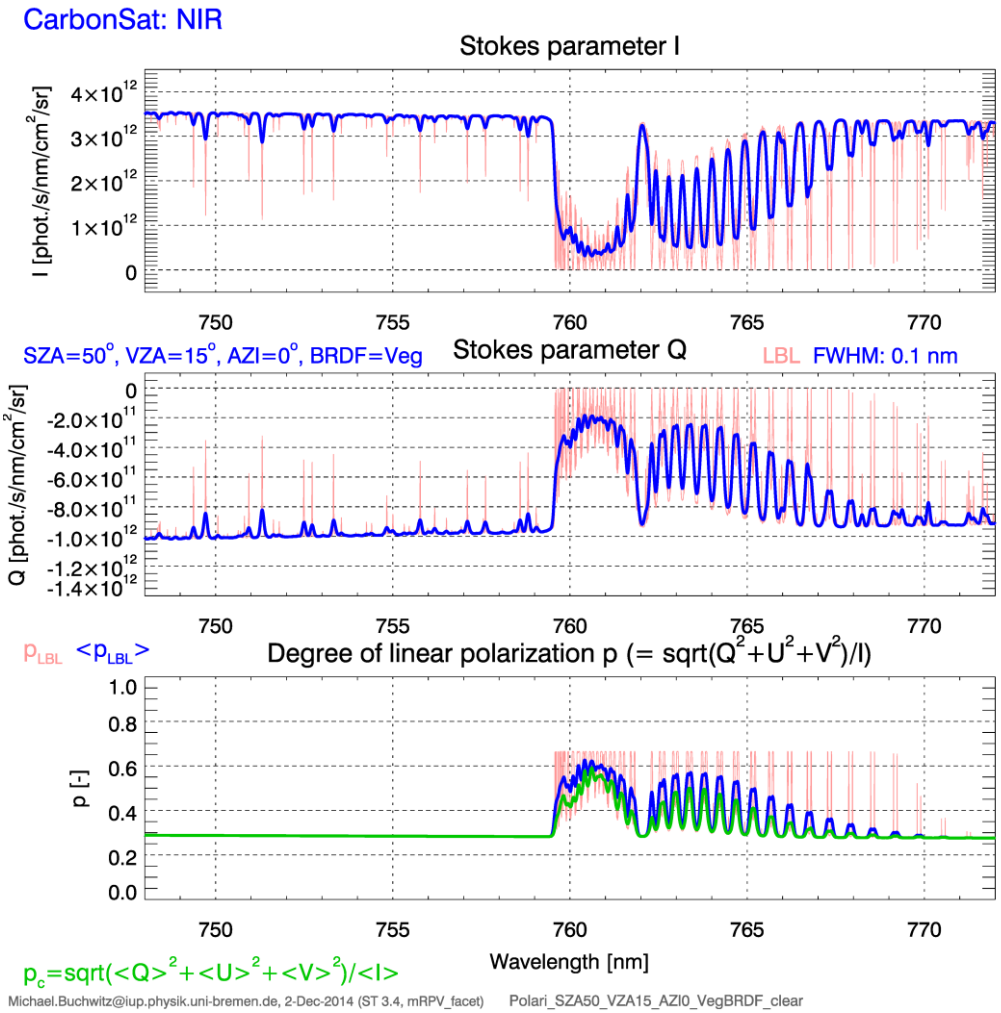

Figure 50: As **Figure 46** but for SZA 50°.

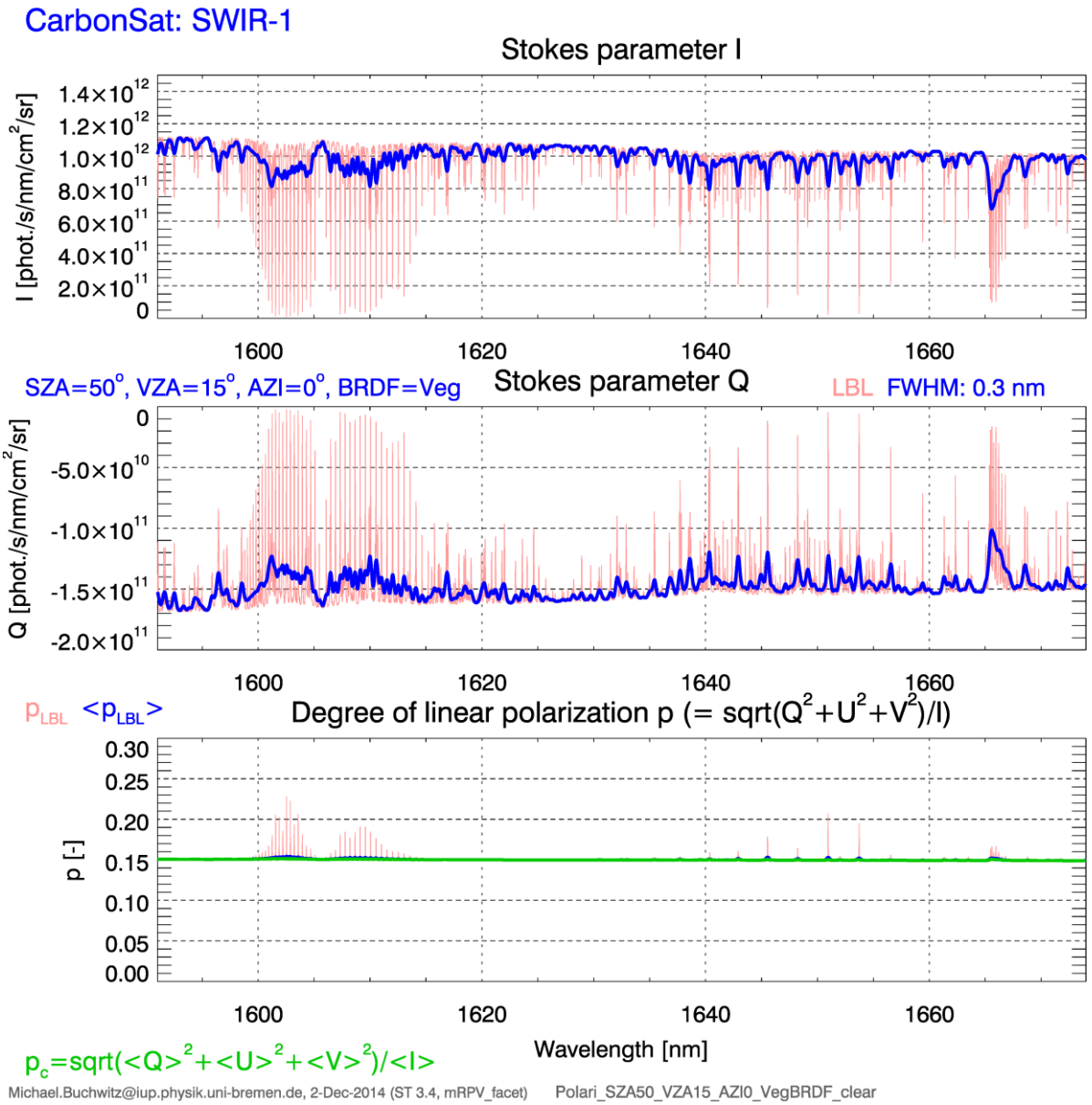

Figure 51: As **Figure 48** but for SZA 50°.

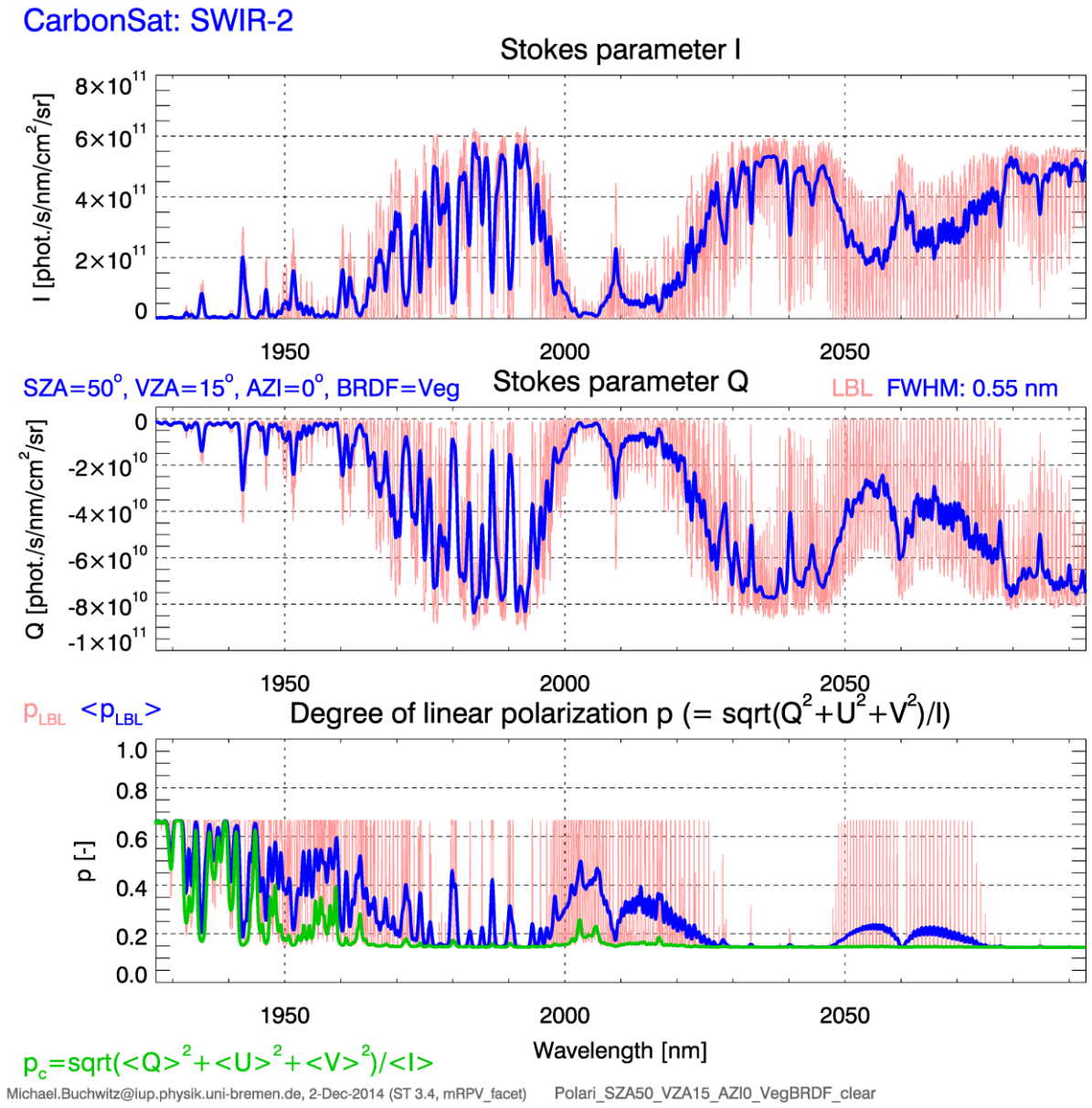

Figure 52: As **Figure 49** but for SZA 50°.

8.3. Reference spectra for out-of-band straylight assessments

On request by ESA nadir radiance and corresponding solar irradiance reference spectra have been generated for out-of-band straylight assessments.

Key parameters for of the corresponding scenarios are listed in **Table 6**.

These reference spectra have been made available for ESA on 13-Feb-2015. They have been stored for ESA access on the IUP ftp server in sub-directory RefSpec/Radiance_OutofBandDtraylight/RefSpec_OutOfBandStraylight_v1/.

An overview about these spectra is presented in **Figure 53 – Figure 56**.
The used spectral sampling is 0.005 nm.

Scenario	ID	SZA	Surface albedo	
			260-1400 nm	1400-2490 nm
Tropical Bright with Water cloud	**TBW**	0^o	0.7	0.2
Tropical Dark	**TRD**	0^o	0.1	0.05

Table 6: Definition of scenarios for out-of-band straylight assessments.

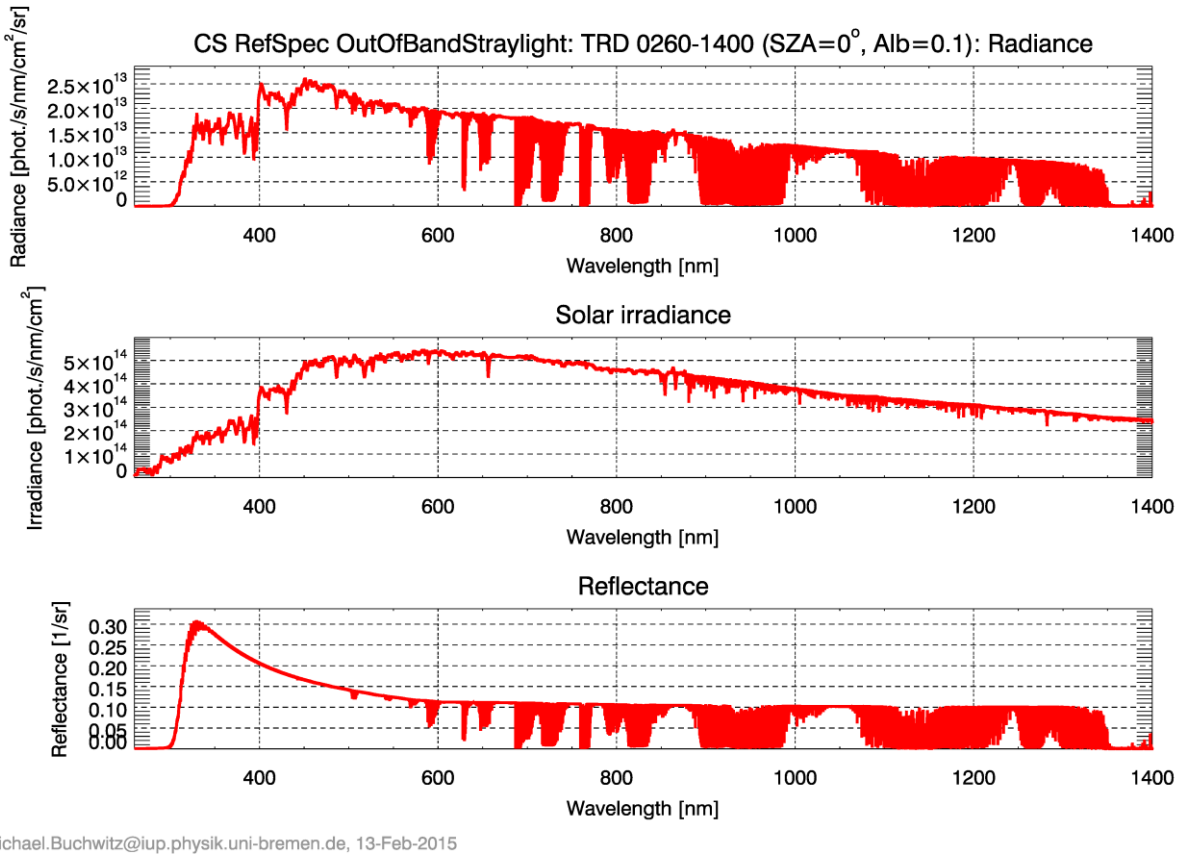

Figure 53: Reference spectra for scenario TRD wavelength range 260 -1400 nm.

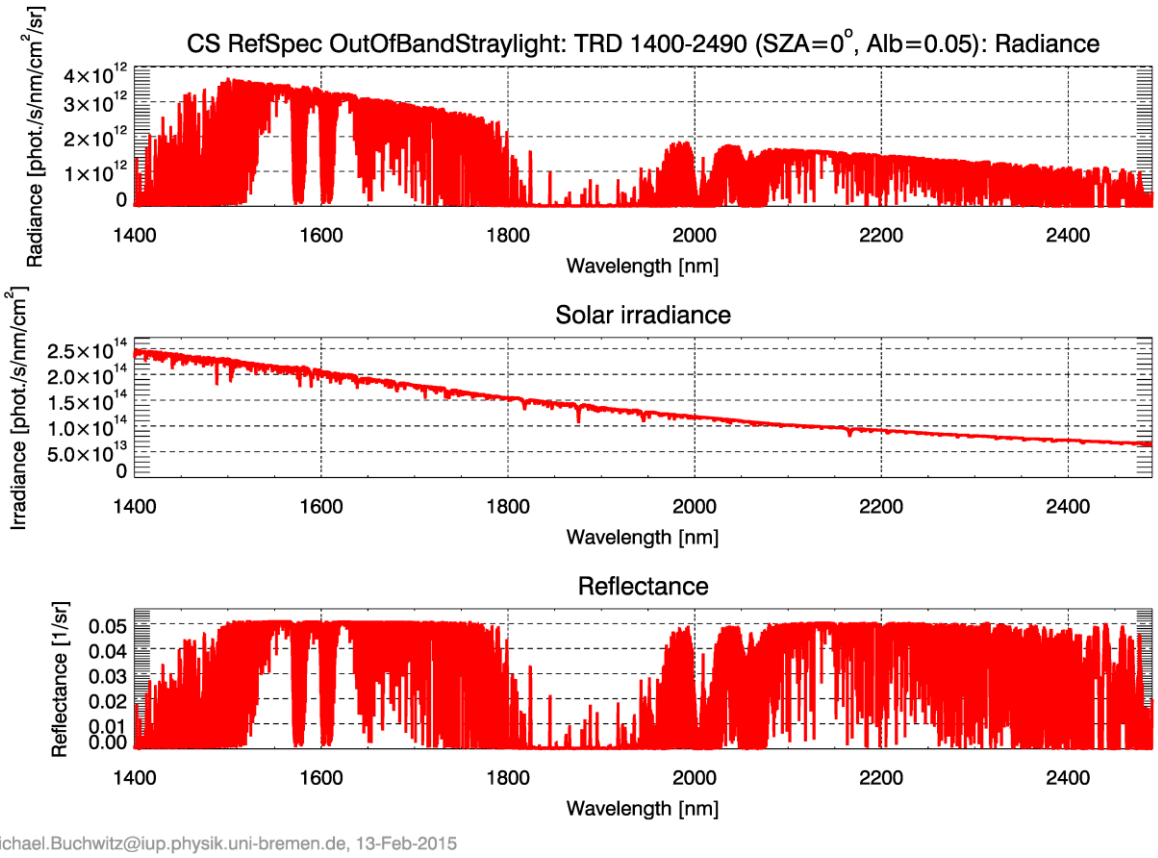

Figure 54: Reference spectra for scenario TRD wavelength range 1400 - 2490 nm.

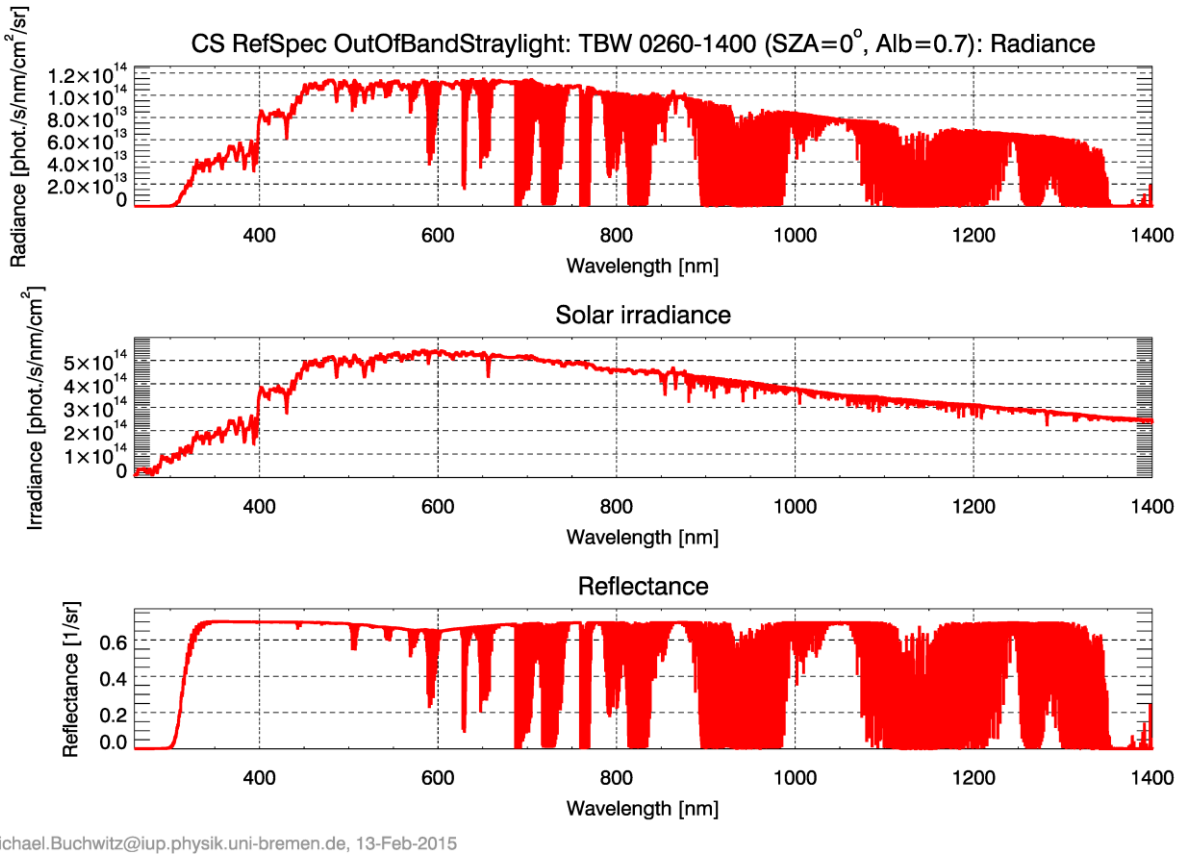

Figure 55: Reference spectra for scenario TBW wavelength range 260 -1400 nm.

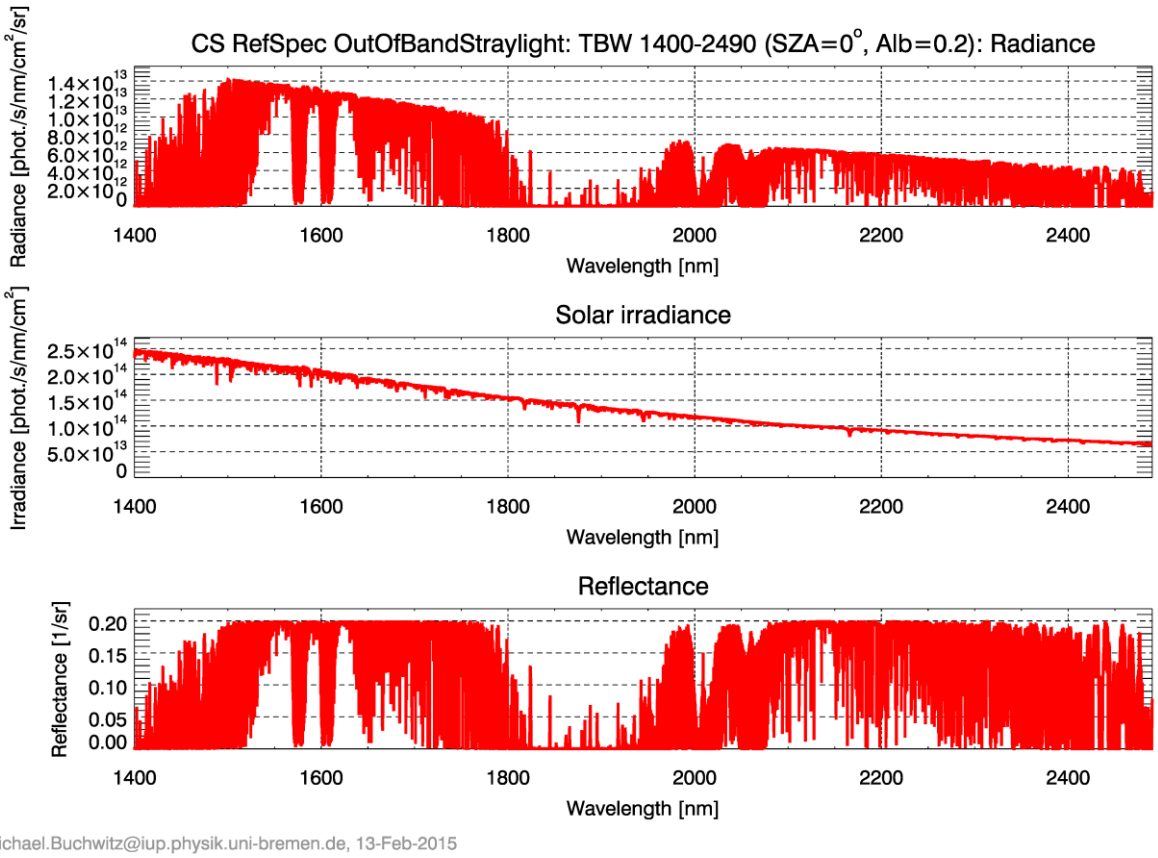

Figure 56: Reference spectra for scenario TBW wavelength range 1400 -2490 nm.

9. Radiometric requirements ZLO, RxRA/RSRA, ARA

In this section, detailed simulations and assessment results are presented and discussed which are related to various instrument related radiometric requirements, namely

- zero-level-offset (ZLO),
- spatial and spectral radiometric accuracy (RxRA and RSRA) and
- absolute radiometric accuracy (ARA),

as given in the CarbonSat MRD v1.2 **/CS MRD v1.2, 2013/**.

For each of the addressed requirements it has been assessed to what extent the requirements can be relaxed or need to be tightened taking into account the L2 error budget presented in **Sect. 4**.

These assessments have been made primarily via simulated retrievals using the CarbonSat simulation framework described in **Sect. 5**.

9.1. Radiometric requirements: Overview

Several radiometric requirements are listed in the CarbonSat Mission Requirements Document (MRD) version 1.2 **/CS MRD v1.2, 2013/**. Several of them had also been addressed in the predecessor study **/CS L1L2-I-Study FR/.** Therefore only certain aspects are covered by this document.

The main purpose is to further consolidate some of the mission requirements as given in MRDv1.2.

Here an overview about important MRDv1.2 radiometric requirements. Most of them are addressed in the following sections (note: T = Threshold (= minimum) requirement; p2p = peak-to-peak):

- Absolute Radiometric Accuracy (**ARA**): MR-OBS-165
  - Reflectance error < 2% NIR, < 3% SWIR

- Relative Radiometric Accuracy (**RRA**): MR-OBS-170
  - Between band reflectance error: < 2% (T) p2p

- Effective Spectral Radiometric Accuracy (**ESRA**): MR-OBS-185
  - „spectral features“ requirement; via „Gain matrices“ (GMs)
  - Errors < 0.2 ppm for XCO_2 and < 2 ppb for XCH_4

- Relative Spectral Radiometric Accuracy (**RSRA**): MR-OBS-180
  - Within band reflectance error: < 0.25% (T) p2p

- Relative Spatial Radiometric Accuracy (**RxRA**): MR-OBS-190
  - Reflectance error within swath: < 0.25%

- Additive offsets: Zero-Level-Offsets (**ZLO**): MR-OBS-200
  - NIR: < 4.2×10^9 phot/s/nm/cm^2/sr
  - SW1: < 4.3×10^9 phot/s/nm/cm^2/sr
  - SW2: < 5.3×10^8 phot/s/nm/cm^2/sr

In the following sub-section the various radiometric requirements are discussed.

9.2. Radiometric requirements: Additive offsets (ZLO)

The additive offset, or zero-level-baseline or Zero-Level-Offset (ZLO) requirement (ZLO) is the following:

MR-OBS-200 from MRDv1.2 **/CS MRD v1.2, 2013/:**

As unknown small additive offsets on the radiance have a severe impact on XCH_4, XCO_2 and retrievals /Lev2009/, there is a need to define the offset correction accuracy.

MR-OBS-200	The offset (zero-level baseline) correction accuracy under dark conditions (in photons/s/nm/cm²/sr) of the radiance shall be known to • 4.2×10^9 in NIR, • 4.3×10^9 in SWIR-1, • 5.3×10^8 in SWIR-2. NB radiance values correspond to percentages of the maximum radiance level in each band taken from the DR-min-75 scenario (see Tables 4.5); i.e., 0.15%, 0.5%, 0.14%, respectively.

In this section it has been investigated if this requirements can be relaxed, e.g., by selecting larger radiance values than given above.

This aspect has been addressed using simulated retrievals using various approaches as described below.

9.2.1. TRD and TRM GM results with and without ZLO as state vector elements

XCO_2 and XCH_4 biases have been computed using the v2 and v3 GMs for the scenarios TRD and TRM (see **Sect. 8.1**). The results are shown in **Table 7** (for v2) and **Table 8** (for v3).

As shown in **Table 7**, most of the biases are less than the required maximum errors. However, some of the XCH_4 biases can exceed the requirement for additive offsets (red values) for v2, where ZLO has not been added as state vector elements to BESD/C. Note that offsets have only been added to the bands marked by "**#**". The offsets are band dependent and correspond to the values listed in MRDv1.2 (these values are listed in **Table 7**).

For v3, where ZLO has been added as state vector elements to BESD/C, the errors are much reduced (see **Table 8** compared to **Table 7**). All errors are well below the required values. From this point of view it is therefore recommended to add ZLO state vector elements to BESD/C. However, this cannot be concluded only from the limited number of scenarios presented in this section.

In order to answer the question if stable XCO_2 and XCH_4 retrievals are possible even in the presence of clouds and aerosols if ZLO is added as state vector elements to BESD/C, a series of additional "crash test" retrievals have been performed using full iterative BESD/C retrievals using a number of scenarios for different cloud and aerosol conditions. The corresponding results are presented in **Sect. 9.2.3**.

However, before the "crash test" retrieval results are presented additional retrievals are presented using (again) linear error analysis (i.e., via GMs) but for a much larger number of scenarios. The corresponding results are presented in the following **Sect. 9.2.2**.

GMs: TRD & TRM (v2): Additive errors

Constant additive offset per band: e.g., **ZLO**

Scenario	Spectral error Δy			XCO_2 error [ppm]	XCH_4 error [ppb]
	NIR	SWIR-1	SWIR-2		
TRD	#	0	0	0.000	+0.102
TRM	#	0	0	+0.003	-0.120
TRD	0	#	0	-0.037	-3.195
TRM	0	#	0	-0.007	-0.366
TRD	0	0	#	-0.109	+0.061
TRM	0	0	#	-0.065	-0.285
TRD	0	#	#	-0.146	-3.134
TRD	#	#	0	-0.038	-3.093
TRD	#	#	#	-0.147	-3.032
Required for additive offset:				< 0.2 ppm	< 2 ppb

#: (Max.) **Additive error** according to MRDv1.2 MR-OBS-200:

- NIR: 4.2 x 10^9 photons/s/nm/cm^2/sr
- SWIR-1: 4.3 x 10^9 photons/s/nm/cm^2/sr
- SWIR-2: 5.3 x 10^8 photons/s/nm/cm^2/sr

Note: GMs computed via BESD/C without any correction for offsets, e.g., without ZLO added as state vector element(s); e.g., SWIR-2: 2x10^9 (= x3.8) would require some correction, e.g, adding ZLO to state vector

Table 7: ZLO related XCO_2 and XCH_4 biases computed with the TRD and TRD GMs v2 (without ZLO as state vector element). As can be seen, for some of the scenarios the XCH_4 bias (shown in red) exceeds the requirement.

GMs: TRD & TRM (v3): Additive errors

Constant additive offset per band: e.g., **ZLO**

Scenario	Spectral error Δy			XCO_2 error [ppm]	XCH_4 error [ppb]
	NIR	SWIR-1	SWIR-2		
TRD	#	0	0	-0.001	**-0.001**
TRM	#	0	0	**0.000**	**-0.001**
TRD	0	#	0	**-0.011**	**-0.658**
TRM	0	#	0	**0.000**	**-0.013**
TRD	0	0	#	**-0.002**	**-0.005**
TRM	0	0	#	**0.000**	**0.000**
TRD	0	#	#	**-0.014**	**-0.668**
TRD	#	#	0	**-0.012**	**-0.659**
TRD	#	#	#	**-0.014**	**-0.664**
Required for additive offset:				< 0.2 ppm	< 2 ppb

#: (Max.) **Additive error** according to MRDv1.2 MR-OBS-200:

- NIR: 4.2×10^9 photons/s/nm/cm^2/sr
- SWIR-1: 4.3×10^9 photons/s/nm/cm^2/sr
- SWIR-2: 5.3×10^8 photons/s/nm/cm^2/sr

Green: Improved wrt previous v2

Note: GMs computed via BESD/C with „offset correction" by adding ZLO to state vector

Table 8: ZLO related XCO_2 and XCH_4 biases computed with the TRD and TRD GMs v3 (i.e., with ZLO as state vector element). As can be seen, the biases are much smaller compared to the v2 results shown in **Table 7**.

9.2.2. Additive offsets: GM approach using “900 scenarios”

In this section additional error analysis results are presented using the 900 scenarios shown in **Figure 57**.

The retrievals have been performed using linear error analysis using the GM approach. No correction has been applied to deal with additive offsets, i.e., ZLO has not been added to the BESD/C state vector.

The XCO_2 and XCH_4 results for all 900 scenarios are shown in **Table 9**. As can be seen, most of the biases are smaller than the required maximum bias for additive offsets if the SZA is 50^o or less. For a SZA of 75^o, the biases can exceed the required maximum bias (note that for high SZA one finds that typically all sensitivities are larger and therefore this is not a particular feature of additive offsets). However, large biases due to additive offsets can be significantly reduced if a correction is applied, e.g., by adding ZLO to the BESD/C state vector, as indicated in the previous section. To further investigate this, additional simulations have been carried out and the results are presented in the following section.

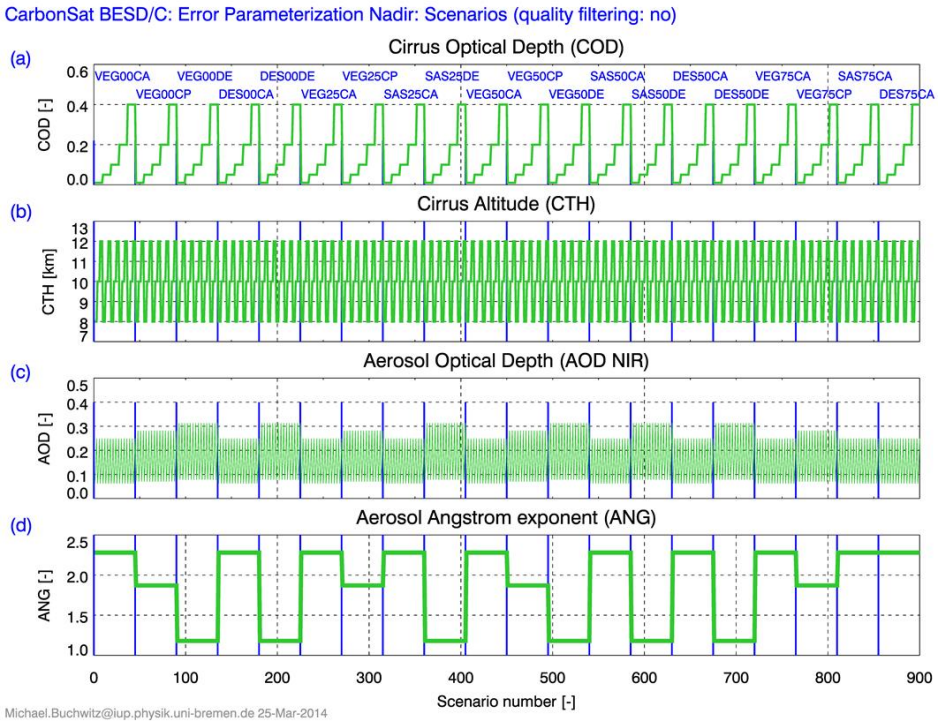

Figure 57: Definition of “900 scenarios” used to assess additive offsets using the GM approach. The blue text at the top indicates the chosen surface albedo (VEG = vegetation, SAS = sand/soil, DES = desert), the selected SZA (00=0^o, 25=25^o, etc.) and the chosen aerosol type (CA = Continental Average, CP = Continental Polluted, DE = Desert **/Hess et al., 1998/**). Other parameters which vary are COD, CTH and AOD (also shown at the bottom is the aerosol Angstrom exponent, which corresponds to the chosen aerosol type).

Additive offsets: Errors for „900 scenarios“

Assessment via linear error analysis (GM approach); no correction algorithm applied

SZA: 0° – 50° (N = 720)

ZLO error (#) added to band:	XCO_2 error [ppm]	XCH_4 error [ppb]
NIR	+0.00 +/- 0.01	0.00 +/- 0.01
SW1	-0.05 +/- 0.04	-0.05 +/- 0.04
SW2	-0.03 +/- 0.07	-0.03 +/- 0.07
NIR+SW1	-0.05 +/- 0.04	-0.05 +/- 0.04
SW1+SW2	-0.08 +/- 0.09	-0.08 +/- 0.09
NIR+SW2	-0.03 +/- 0.07	-0.03 +/- 0.07
NIR+SW1+SW2	-0.08 +/- 0.08	-0.08 +/- 0.08
Required:	< 0.2 ppm	< 2 ppb

SZA: 75° (N = 180)

ZLO error (#) added to band:	XCO_2 error [ppm]	XCH_4 error [ppb]
NIR	-0.15 +/- 0.08	-0.64 +/- 0.30
SW1	-0.11 +/- 0.11	-2.11 +/- 1.44
SW2	-0.49 +/- 0.32	+2.62 +/- 1.55
NIR+SW1	-0.26 +/- 0.19	-2.75 +/- 1.69
SW1+SW2	+0.38 +/- 0.21	+0.51 +/- 0.43
NIR+SW2	+0.34 +/- 0.24	+1.98 +/- 1.31
NIR+SW1+SW2	+0.23 +/- 0.14	-0.13 +/- 0.45
Required:	< 0.2 ppm	< 2 ppb

#: Max. additive error according to MRDv1.2 MR-OBS-200:

- NIR: 4.2×10^9 photons/s/nm/cm^2/sr
- SWIR-1: 4.3×10^9 photons/s/nm/cm^2/sr
- SWIR-2: 5.3×10^8 photons/s/nm/cm^2/sr

Table 9: XCO_2 and XCH_4 biases for all 900 scenarios evaluated to quantify the impact of additive offset errors on the radiance (the chosen radiance offsets are listed above and correspond to the values given for MR-OBS-200 in MRDv1.2).

9.2.3. Additive offsets: Full iterative BESD/C retrievals ("crash test")

Here full iterative BESD/C retrieval results are shown to confirm that ZLO can be added as state vector elements (= 3 additional parameters, see ZLONIR, ZLOSW1 and ZLOSW2 Jacobians in **Figure 58**).

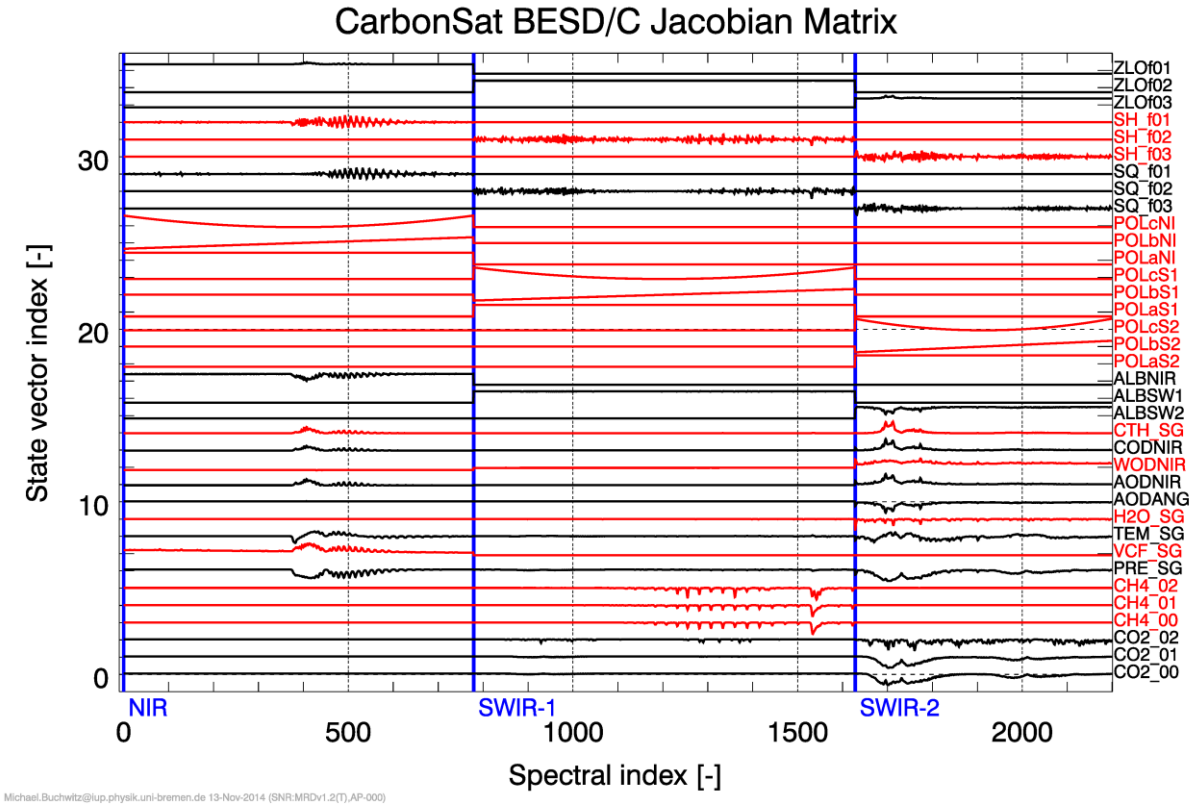

Figure 58: As **Figure 5** but with ZLO Jacobians (top three curves denoted ZLOf01 (for NIR band), ZLOf02 (SWIR-1) and ZLOf03 (SWIR-2)).

Approach:

- Full iterative BESD/C retrieval with full pre-processing (to obtain albedo, VCF/SIF, and COD *a priori* & first guess values)

Expectation:

- Large Level 2 biases (e.g., due to correlation of ZLO with other Jacobians, e.g., the COD Jacobian)
- Much slower or even no convergence.

Two assessments have been carried out:

- Assessment 1 (A1) and
- Assessment 2 (A2)

Each assessment corresponds to a different combination of the investigated offset values. The results for the two assessments are shown in the following.

Assessment 1 (A1):

Added offsets (using relaxed, i.e., larger values than specified in MRDv1.2):

- NIR: MRDv1.2 **x2** = 8.4×10^9 photons/s/nm/cm^2/sr
- SW1: MRDv1.2 **x2** = 8.6×10^9 photons/s/nm/cm^2/sr
- SW2 B&C: MRDv1.2 **x3.8** = 2.0×10^9 photons/s/nm/cm^2/sr

Offset correction via BESD/C:

- ZLO added as state vector elements for all 3 bands (= 3 additional fit parameters)

Scenarios:

- VEG50 (= vegetation albedo, SZA 50^o), 45 combinations of COD, CTH, AOD
- VEG75 (= vegetation albedo, SZA 75^o), 45 combinations of COD, CTH, AOD

The results are shown in **Figure 59 - Figure 63** and summarized in **Table 10**.

As can be seen, simulated retrievals have been performed with and without perturbing the radiance spectra by additive offsets and retrievals have been performed with and without adding ZLO state vector elements to BESD/C.

As summarized in **Table 10**, the results clearly show that if ZLO is added as state vector elements stable retrievals are possible without any significant degradation of precision and accuracy of the retrieved XCO_2 and XCH_4. Precision degradation is approx. 10% (2-14% depending on scenario) and accuracy degradation is zero (sometimes accuracy is even a bit better if ZLO is added to BESD/C) Furthermore, no convergence issues have been identified (not shown here).

It therefore seems possible to relax MR-OBS-200 from MRDv1.2 **/CS MRD v1.2, 2013/** by the values listed above, i.e.:

- NIR: MRDv1.2 **x2** = 8.4x10^{9} photons/s/nm/cm^{2}/sr
- SW1: MRDv1.2 **x2** = 8.6x10^{9} photons/s/nm/cm^{2}/sr
- SW2 B&C: MRDv1.2 **x3.8** = 2.0x10^{9} photons/s/nm/cm^{2}/sr

As will be shown in the following sub-section, the value for the SWIR-2A band can even be further relaxed to 1.0x10^{10} photons/s/nm/cm^{2}/sr.

Scenario	Additive error ?	ZLO in state vector ?	XCO_2 [ppm]		XCH_4 [ppm]	
			Bias	Precision	Bias	Precision
VEG50	N	N	0.25+/-0.31	1.11+/-0.12	0.41+/-2.05	8.88+/-1.28
VEG50	Y	N	0.12+/-0.41	1.11+/-0.12	-2.17+/-2.34	8.92+/-1.30
VEG50	Y	Y	0.34+/-0.28	1.16+/-0.12	1.19+/-1.37	10.04+/-0.85
VEG75	N	N	-0.55+/-1.49	2.17+/-0.63	-4.98+/-4.84	14.69+/-4.15
VEG75	Y	Y	0.42+/-1.05	2.47+/-0.62	-0.27+/-3.28	16.80+/-3.78

Table 10: Summary ZLO “crash test” retrieval results. Each of the five lines corresponds to one of the five figures **Figure 59** - **Figure 63**, where more details are given.

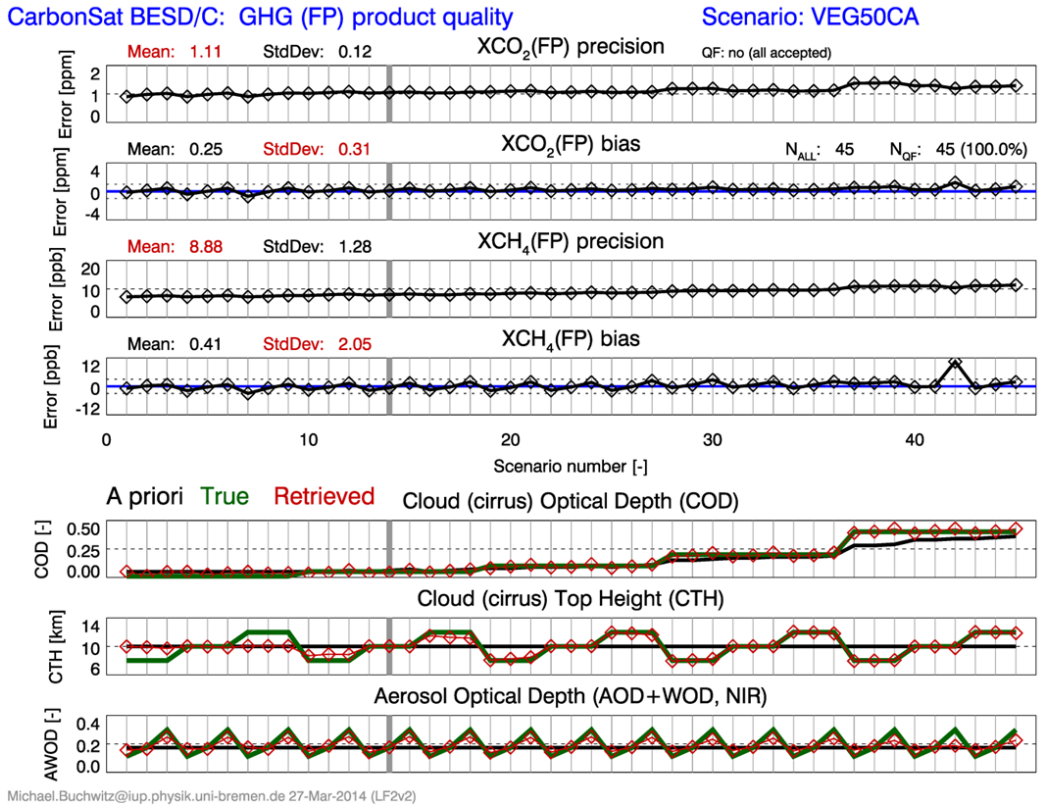

Figure 59: ZLO crash test results for scenario VEG50. Shown are XCO_2 and XCH_4 precision and bias (top 4 panels) and COD, CTH and AOD (bottom 3 panels) for 45 scenarios as defined by different combinations of COD, CTH and AOD. This figure shows the "reference retrieval" without offset error and without ZLO as state vector elements added to BESD/C. For better comparison with the following figures the key parameters are: Scenario: VEG50, offset error: no, ZLO added to BESD/C: no.

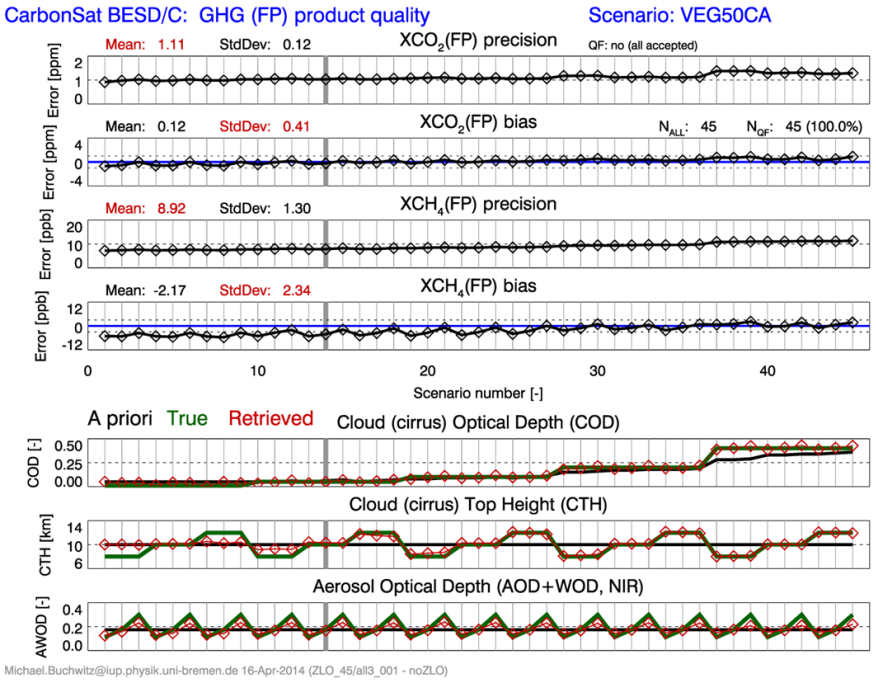

Figure 60: As **Figure 59** but for: Scenario: VEG50, offset error: yes, ZLO added to BESD/C: no.

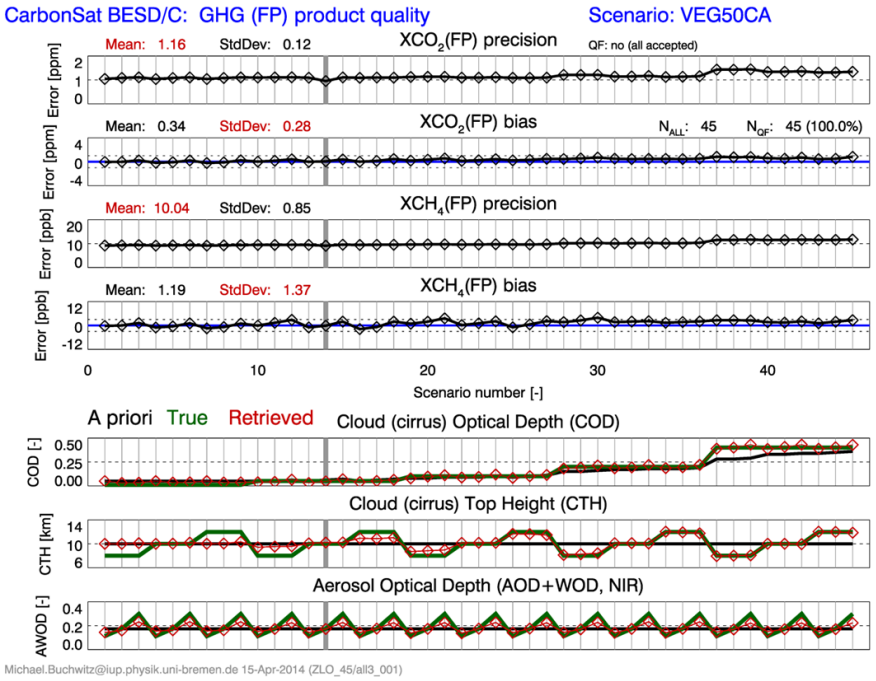

Figure 61: As **Figure 59** but for: Scenario: VEG50, offset error: yes, ZLO added to BESD/C: yes.

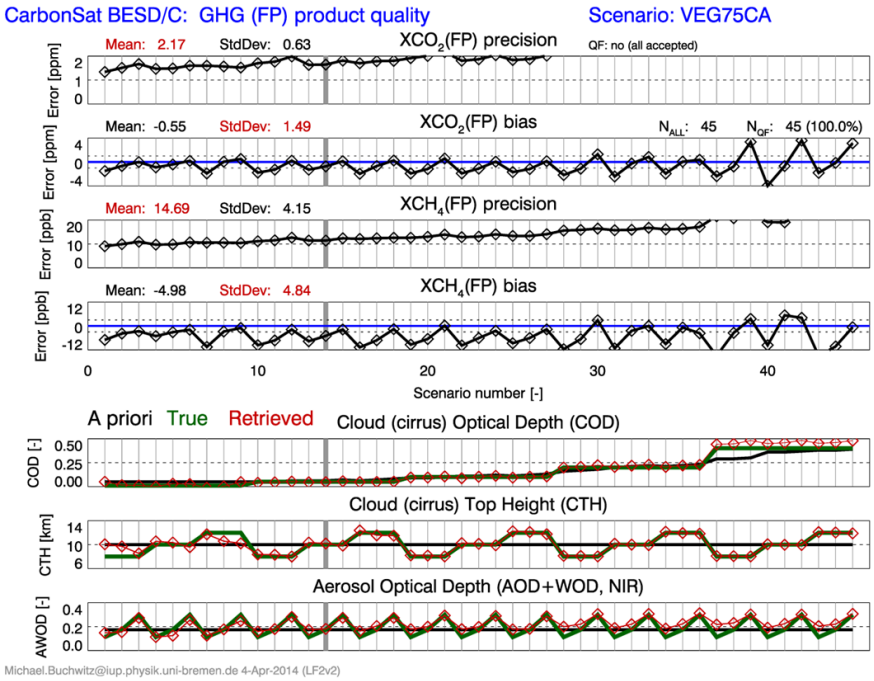

Figure 62: As **Figure 59** but for: Scenario: VEG75, offset error: no, ZLO added to BESD/C: no.

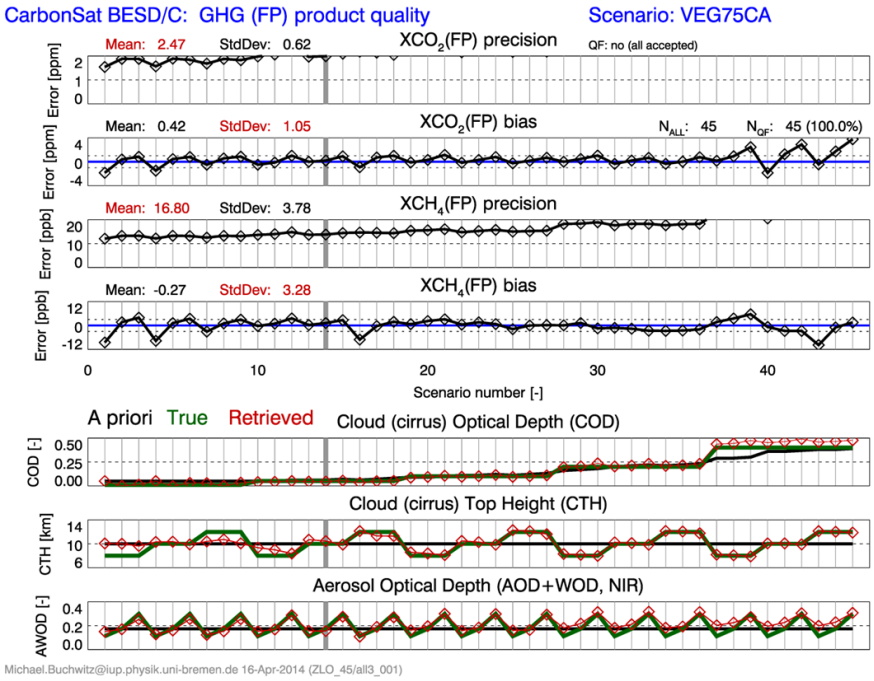

Figure 63: As **Figure 59** but for: Scenario: VEG75, offset error: yes, ZLO added to BESD/C: yes.

Assessment 2 (A2):

Furthermore, it has also been investigated if the following offsets would be acceptable:

- NIR: MRDv1.2 **x3.6** = $15x10^9$ photons/s/nm/cm^2/sr (additional relaxation)
- SW1: MRDv1.2 **x0.7** = $3x10^9$ photons/s/nm/cm^2/sr (stricter than before)
- SW2 B&C: MRDv1.2 **x3.8** = $2.0x10^9$ photons/s/nm/cm^2/sr (same as before)

The results of this assessment are shown in the following.

Assessment A2 has been carried out with a slightly different SNR model compared to assessment A1. For A1 the SNR model described in **/Buchwitz et al., 2013a/** whereas for assessment A2 the threshold SNR requirement as formulated in **/CS MRD v1.2, 2013/** has been used. The letter results in higher SNR in the continuum but in lower SNR in deep absorption lines.

Overall, in terms of XCO_2 and XCH_4 retrieval errors, both SNR models are essentially equivalent as can be seen from **Figure 64** and **Figure 65**.

A summary of the previous A1 and new A2 results are shown in **Figure 66** and **Figure 67**.

Detailed A2 results are shown in **Figure 68** - **Figure 71**.

A comparison of the A2 with the A1 results show that they are quite similar. Therefore, the conclusions which have been drawn for A1 are also valid for A2. The concusions are summarized along with recommendations in **Sect. 9.2.5**.

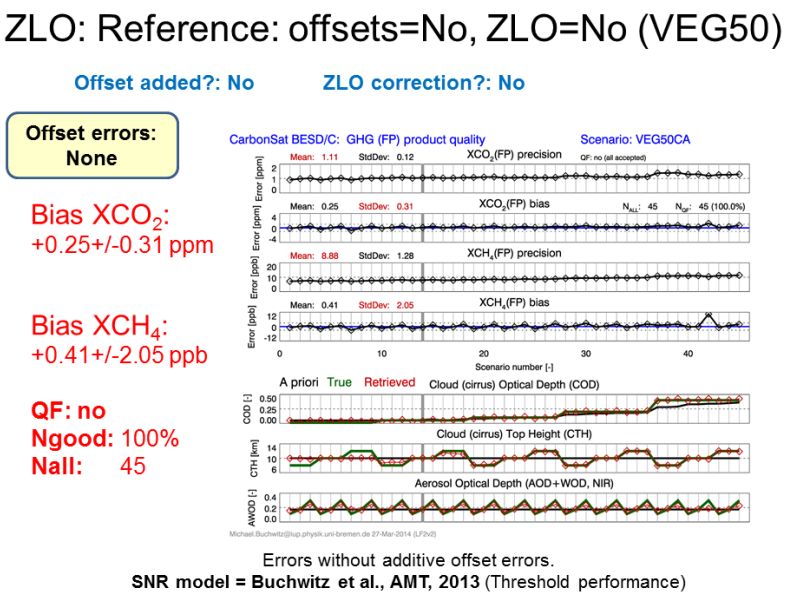

Figure 64: Retrieval results using the SNR model described in **/Buchwitz et al., 2013a/** (threshold performance) used for assessment A1.

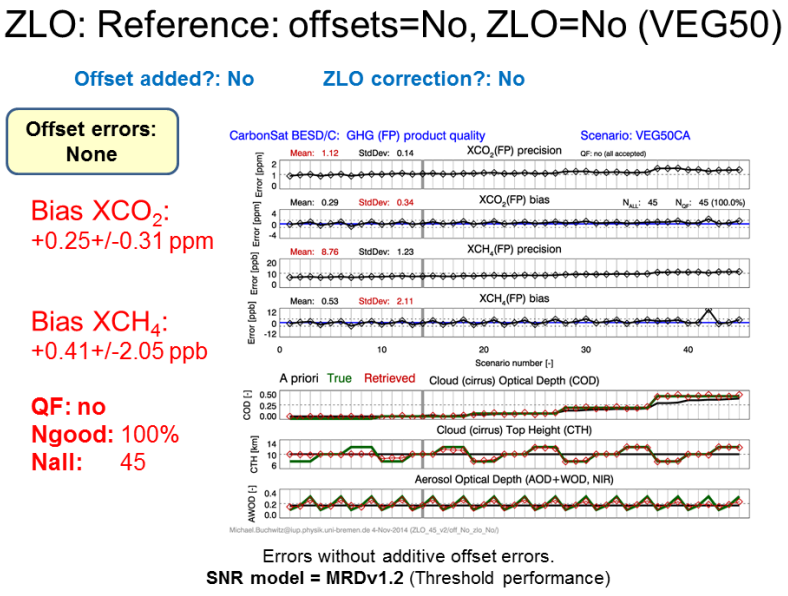

Figure 65: As **Figure 64** but using the SNR model described in **/CS MRD v1.2, 2013a/** (threshold performance). This SNR model is used for assessment A2.

ZLO crash test results: Summary A1 results

Scenario (added offsets In 10^9 phot/s/...: NIR / SW1 / SW2)	Correction ? (via adding ZLO to BESD/C)	XCO_2 [ppm]		XCH_4 [ppb]	
		Bias	Precision	Bias	Precision
VEG50:					
No offsets	N	0.25+/-0.31	1.11+/-0.12	0.41+/-2.05	8.88+/-1.28
With offsets (+8.4 / +8.6 / +2)	**N**	**0.12+/-0.41**	**1.11+/-0.12**	**-2.17+/-2.34**	**8.92+/-1.30**
With offsets (+8.4 / +8.6 / +2)	**Y**	**0.34+/-0.28**	**1.16+/-0.12**	**1.19+/-1.37**	**10.04+/-0.85**
VEG75:					
No offsets	N	-0.55+/-1.49	2.17+/-0.63	-4.98+/-4.84	14.69+/-4.15
With offsets (+8.4 / +8.6 / +2)	**Y**	**0.42+/-1.05**	**2.47+/-0.62**	**-0.27+/-3.28**	**16.80+/-3.78**

Offset errors: A1

Figure 66: Summary of the A1 results.

ZLO crash test results: Summary A2 results

Scenario (added offsets In 10^9 phot/s/...: NIR / SW1 / SW2)	Correction ? (via adding ZLO to BESD/C)	XCO_2 [ppm]		XCH_4 [ppb]	
		Bias	Precision	Bias	Precision
VEG50:					
No offsets	N	0.29+/-0.34	1.12+/-0.14	0.53+/-2.11	8.76+/-1.23
With offsets (+15 / +3 / +2)	**N**	**0.30+/-0.40**	**1.13+/-0.13**	**0.60+/-2.31**	**8.78+/-1.22**
With offsets (+15 / +3 / +2)	**Y**	**0.41+/-0.34**	**1.18+/-0.13**	**1.80+/-2.05**	**9.82+/-0.82**
With offsets (+15 / +3 / -2)	**N**	**0.08+/-0.33**	**1.13+/-0.13**	**-2.20+/-2.17**	**8.78+/-1.21**
With offsets (+15 / +3 / -2)	**Y**	**0.33+/-0.29**	**1.18+/-0.13**	**1.44+/-1.98**	**9.82+/-0.82**

Offset errors: A2

Figure 67: Summary of the A2 results.

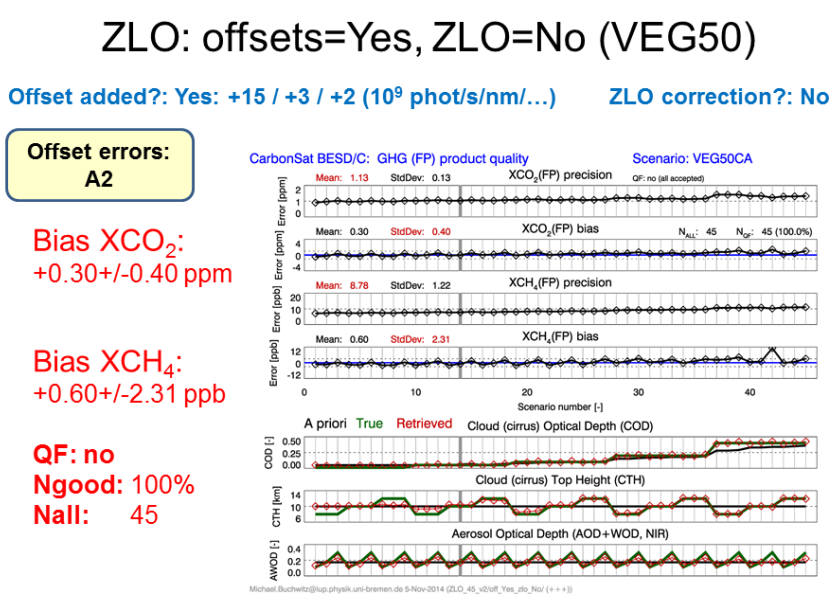

Figure 68: Detailed A2 results for scenario: Offsets in 10^9 phot/s/nm/cm^2/sr: NIR= +15, SWIR-1: +3, SWIR-2B&C: +2. ZLO added to BESD/C: no.

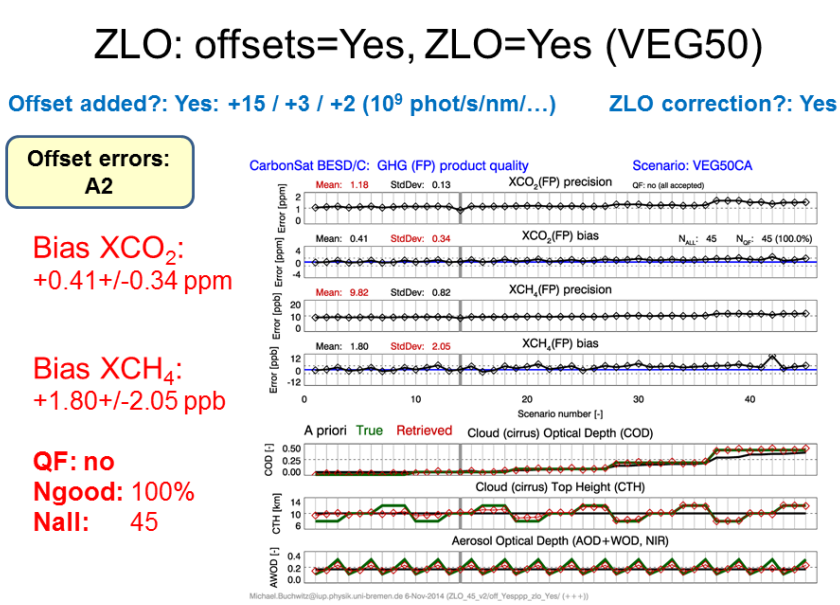

Figure 69: Detailed A2 results for scenario: Offsets in 10^9 phot/s/nm/cm^2/sr: NIR= +15, SWIR-1: +3, SWIR-2B&C: +2. ZLO added to BESD/C: yes.

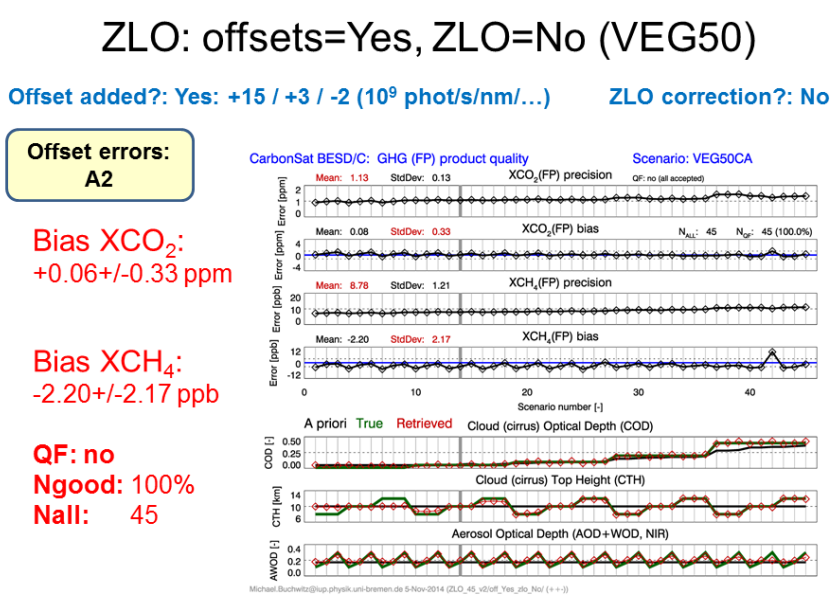

Figure 70: Detailed A2 results for scenario: Offsets in 10^9 phot/s/nm/cm^2/sr: NIR= +15, SWIR-1: +3, SWIR-2B&C: -2. ZLO added to BESD/C: no.

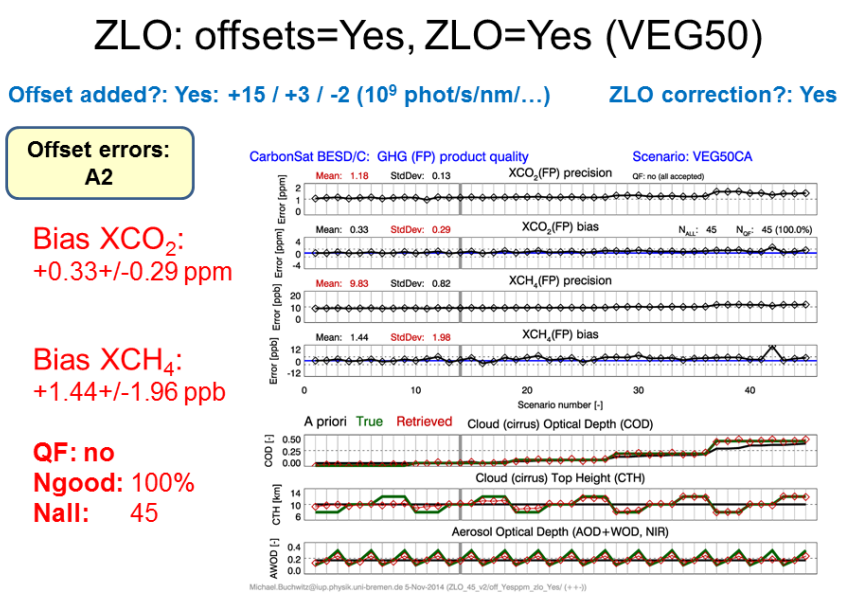

Figure 71: Detailed A2 results for scenario: Offsets in 10^9 phot/s/nm/cm^2/sr: NIR= +15, SWIR-1: +3, SWIR-2B&C: -2. ZLO added to BESD/C: yes.

9.2.4. Use of SWIR-2A for cirrus screening and corresponding ZLO requirement

As a first step, a simple algorithm has been implemented to use the SWIR-2A spectral region (1925 – 1990 nm) to get (improved) information on cirrus clouds.

Using simulations it has been found that to a very good approximation the radiance around the 1939 nm spectral region – a region with very strong water vapour absorption – depends linearly on the cirrus optical depth (COD): The radiance is essentially zero if no cirrus clouds are present (COD = 0.0) and the radiance is approximately 1.85×10^{11} photons/s/nm/cm^2/sr for COD = 0.2.

Based on these findings a Pre-Processing (PP) algorithm has been implemented (as already explained in **Sect. 6**) in BESD/C to obtain *a priori* and first guess values for state vector element COD using this formula:

$$COD_{\,a\ priori} = 0.2 \times RAD / (1.85 \times 10^{11})$$

where RAD is the measured radiance (in photons/s/nm/cm^2/sr) at 1939 nm.

The required accuracy for COD retrieval in this spectral regions is approximately $\Delta COD = 0.02$, which corresponds to $\Delta RAD = 1.85 \times 10^{10}$ photons/s/nm/cm^2/sr.

As a consequence, the ZLO requirement for SWIR-2A can be relaxed to approx. 1×10^{10} photons/s/nm/cm^2/sr.

For comparison: **Guerlet et al., 2013/** also used this spectral region (in the framework if GOSAT XCO_2 retrievals) used as a threshold for cirrus detection 5×10^{10} photons/s/nm/cm^2/sr.

Also interesting in this context is the comparison with the expected noise of the CarbonSat observations. As shown in **Figure 72**, the radiance at 1939 nm is typically (here: VEG50 scenario) 5×10^{10} photons/s/nm/cm^2/sr and the (threshold performance) SNR is about 20. This means that the noise is typically 0.25×10^{10} photons/s/nm/cm^2/sr, i.e., a factor of four smaller than the proposed new ZLO requirement of 1×10^{10} photons/s/nm/cm^2/sr.

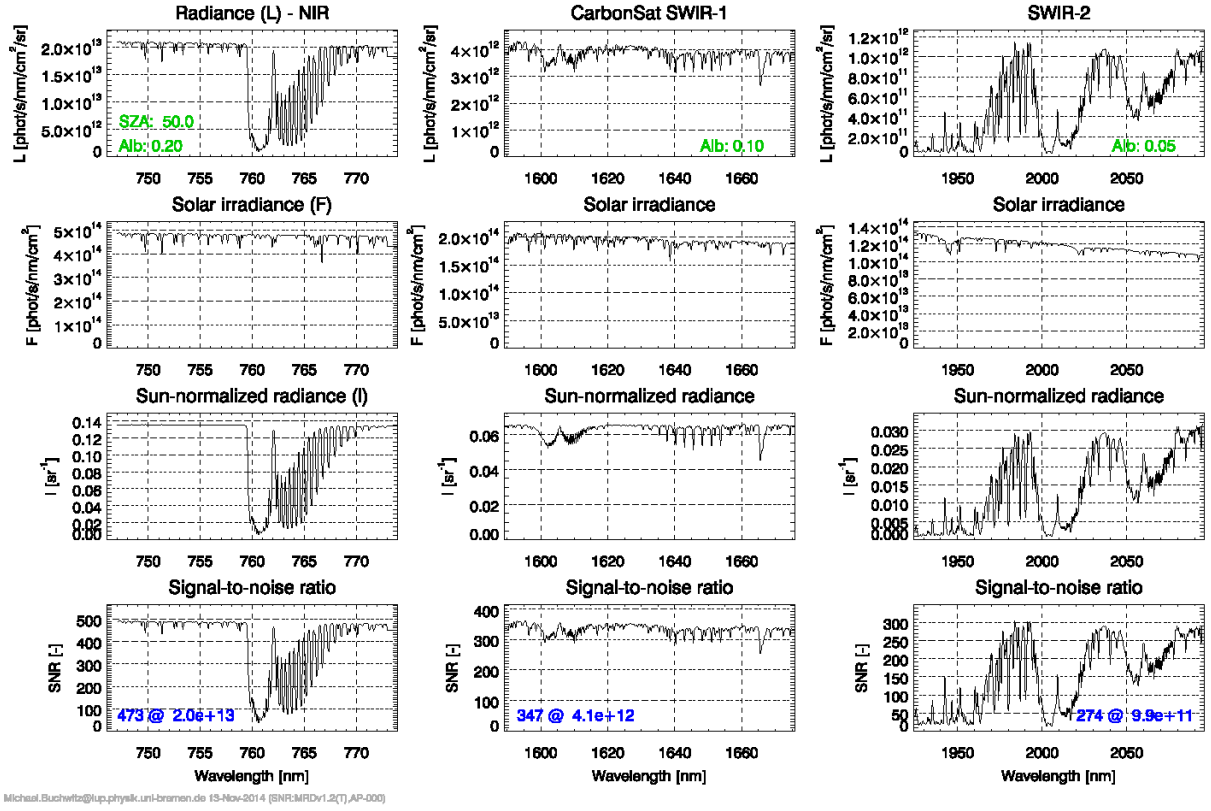

Figure 72: As **Figure 3** but showing the entire spectral range covered by SWIR-2.

9.2.5. Summary: Possible relaxation of additive offset requirement

Simulated retrievals have been performed to find out to what extent the MRDv1.2 ***/CS MRD v1.2, 2013/*** additive offset requirement MR-OBS-200 can be relaxed.

The analysis presented here shows that - if necessary - the requirement can be relaxed by replacing the three radiance values as listed in MR-OBS-200 for the three bands using the values listed here in **Table 11**.

However, it needs to be noted that the results have been obtained assuming constant offsets per band, i.e., neglecting any spectral dependence within a given band. This assumption is likely very optimistic.

Band	MRDv1.2 radiance offsets	Relaxation factor	Relaxed radiance offsets	Comment
NIR	4.2×10^{9}	2	8.4×10^{9}	
SWIR-1	4.3×10^{9}	2	8.6×10^{9}	
SWIR-2 **SWIR-2A**	5.3×10^{8} -	3.8 3.8 x 5 = 17.5	2.0×10^{9} 10×10^{9}	SWIR-2A&B No SWIR-2A (1925-1990 nm) req. in MRDv1.2

Table 11: Required offset (zero-level-baseline) correction accuracy in photons/s/nm/cm^2/sr as given in MR-OBS-200 of MRDv1.2 ***/CS MRD v1.2, 2013/*** and recommended values should it be necessary to relax this requirement.

Alternative the offsets are listed in **Table 12**. Here the relaxation in the NIR is larger but the required maximum offset in SWIR-1 is even stricter than in MRDv1.2.

Band	MRDv1.2 radiance offsets	Relaxation factor	Relaxed radiance offsets	Comment
NIR	4.2×10^{9}	3.6	15×10^{9}	
SWIR-1	4.3×10^{9}	0.7	3×10^{9}	Stricter than for MRDv1.2
SWIR-2 **SWIR-2A**	5.3×10^{8} -	3.8 3.8 x 5 = 17.5	2.0×10^{9} 10×10^{9}	SWIR-2A&B No SWIR-2A (1925-1990 nm) req. in MRDv1.2

Table 12: As **Table 11** but for the offsets assessed via assessment 2 (A2).

The results presented above are valid for CarbonSat nadir mode observations.

UoL has reported retrieval biases for CarbonSat glint mode observations using linear error analysis and without adding ZLO as state vector element to the retrieval algorithm. Scaling their results gives the following XCO_2 biases (peak to peak range):

- MRDv1.2 NIR offset $4.9x10^9$ phot./s/nm/cm^2/sr: +/- 0.1 ppm
- NIR offset $8.4x10^9$ phot./s/nm/cm^2/sr: +/- 0.2 ppm
- NIR offset $15x10^9$ phot./s/nm/cm^2/sr: +/- 0.36 ppm

According to the glint mode error budget, 0.2 ppm (1 sigma) is the maximum permited XCO_2 bias for additive offset errors. From this one can conclude that offsets larger than $15x10^9$ phot./s/nm/cm^2/sr in the NIR should clearly be avoided.

Concerning NIR offsets and VDCF / SIF retrieval:

Note also that for CarbonSat the VCF / SIF single measurement precision is about 0.3 mW/m^2/nm/sr = $10x10^{10}$ phot./s/nm/cm^2/sr = $100x10^9$ phot./s/nm/cm^2/sr at 755 nm. This means that $15x10^9$ phot./s/nm/cm^2/sr is approximately 1/7-th of the presision, i.e., is still significantly smaller than the precision, which is good. But this also shows that the NIR offset should not be larger than $15x10^9$ phot./s/nm/cm^2/sr.

Note also that **/Frankenberg et al., 2012/** has shown that an approximately 1 mW/m^2/nm/sr VCF / SIF signal or additive offset (if not accounted for) may lead to an XCO_2 bias of approximately 1 ppm. This means that offsets should not be larger than 0.2 mW/m^2/nm/sr = $6x10^9$ phot./s/nm/cm^2/sr to restrict XCO_2 bias to below 0.2 ppm. Note that $6x10^9$ phot./s/nm/cm^2/sr is smaller than the $15x10^9$ phot./s/nm/cm^2/sr offset discussed here but one has to note that the results presented in **/Frankenberg et al., 2012/** are not directly applicable to CarbonSat because they are valid for an instrument with higher spectral resolution. Nevertheless, these results also indicate that offsets higher than $15x10^9$ phot./s/nm/cm^2/sr should be avoided in the NIR for CarbonSat.

9.3. Radiometric requirements: Multiplicative errors RxRA and RSRA

9.3.1. General remarks

There are several error sources which can be characterized as multiplicative radiometric errors:

- Multiplicative / absolute errors are covered by the ARA requirement (see, e.g., **Sect. 9.7** and **Sect. 18.1**).
- Multiplicative / relative errors are assumed to consist of 3 major components:
    - ESRA (see **Sect. 9.5**): Errors which introduce spectral features are covered by the ESRA requirement; ESRA includes polarization related errors (see **Sect. 17**), straylight (see, e.g., **Sect. 8.3**), non-linearity (see **Sect. 13**) and diffuser specles); to quantify ESRA related errors gain matrix reference spectra have been generated and delivered to ESA (see **Sect. 8**)
    - Errors related to Relative spatial Radiometric Accuracy (RxRA) (see **Sect. 9.3.2**)
    - Errors related to Relative spectral Radiometric Accuracy (RSRA) see **Sect. 9.3.2**)

Assuming that the “Multiplicative / relative” error components are uncorrelated, their overall contribution to the overall “Multiplicative / relative” XCO_2 and XCH_4 errors can be obtained by adding the components via Root-Sum-Square (RSS). In line with the overall uncertainty as given in the error budget (see **Sect. 4**), the following uncertainty contributions are assumed (and used in the context of this document):

Overall uncertainty XCO_2: 0.45 ppm

Components:

- ESRA: 0.4 ppm
- RSRA: 0.2 ppm
- RxRA: 0.1 ppm

Overall uncertainty XCH_4: 4.5 ppb

Components:

- ESRA: 4.4 ppb
- RSRA: 1.0 ppb
- RxRA: 0.6 ppb

Retrieval simulations related to RxRA and RSRA are discussed in the following **Sect. 9.3.2**.

9.3.2. Relative spectal and spatial radiometric accuracy (RSRA and RxRA)

The MRDv1.2 **/CS MRD v1.2, 2013/** requirements for RSRA and RxRA are:

Relative Spectral Radiometric Accuray (**RSRA**): MR-OBS-180:

MR-OBS-180	The relative spectral radiometric accuracy (RSRA) of the reflectance measurement over any spectral range **within each band** shall be known better than (peak-to-peak) 0.05% (G) / 0.25% (T) relative to the background level. NB relative radiometric accuracy is the ratio between two spectral points.

MR-OBS-180 is applicable to polarised scenes with a degree of linear polarisation of 100% (TBC) with any polarisation direction and to homogeneous cloud-free scenes.

Relative Spatial Radiometric Accuray (**RxRA**): MR-OBS-190:

MR-OBS-190	The relative spatial radiometric accuracy of the reflectance measurements within a swath shall be better than 0.25%.

As spectral features are covered via the ESRA requirement (see **Sect. 9.5**) and additive radiometric errors are covered via the offset requirement (see **Sect. 9.2**), assessments have been performed focusing on multiplicative errors without spectral features.

For RxRA the effect of constant (= same factor for all bands) spectral radiance errors has been investigated. This is in-line with the assumption that this error is primarily caused by (across-track) gain variations. This assumption and the selected approach (see below) is similar as the approach which as has been used for RxRA related Sentinel-5 (S-5) methane assessments conducted in the (parallel) S-5 SWIR ESA study.

For RSRA the effect of multiplicative factors has been investigated using errors which are different for the three different bands and may vary “smoothly” within each band.

In particular it has been investigated if:

- RSRA: Is 0.25% (see MR-OBS-180 above) really needed or can this be relaxed, e.g., by replacing 0.25% by 0.5% ?
- RxRA: Is 0.25% (see MR-OBS-190 above) really needed or can this be relaxed, e.g., by replacing 0.25% by 0.5% ?

Chosen approach to assess this:

- Via simulated retrievals using the simulation framework introduced in **Sect. 5**. Here the radiance spectra have been perturbed by multiplication with various factors (as described above) and BESD/C retrievals have been performed using the erroneous radiances as input. The biases caused by RSRA and RxRA related errors have been obtained by computing "retrieved minus true" XCO_2 and XCH_4 values as explained in **Sect. 5**.

Results for RxRA are shown in **Table 13** - **Table 14** and **Figure 73**:

Table 13 shows RxRA related XCO_2 biases in rows 1-4 with final results in rows 3-4 as highlighted by red rectangle:

Row 1 (= "IUP: None (#)") shows "XCO_2 reference biases" as obtained when no RxRA error is present. As can be seen, the errors are not zero, but, for example, 0.12 ppm for SZA = 50^o. This is because the error analysis has not been performed via linear error analysis (i.e., via GMs), as in this case the errors will be very close to zero even if RxRA errors are present. This is because the BESD/C 3-band OE retrieval algorithm is quite insensitive to (constant) multiplicative errors. Therefore it was necessary to perform full iterative BESD/C retrievals including Pre-Processing (PP). However, the BESD/C PP algorithms are still quite simple and preliminary. In any case some error will be caused by this and row 1 shows how large these errors are for the version of BESD/C as used for this assessment.

Therefore, in order to quantify / isolate RxRA errors, two retrievals have been performed: one without error (as just discussed) and one with RxRA error present.

Row 2 (see "0.5/0.5/0.5") lists the XCO_2 errors if an RxRA error is present. "0.5/0.5/0.5" indicates that the same multiplicative radiance error of 0.5% (or factor 1.005) has been applied to the radiance of all three bands. As can be seen, the XCO_2 error for SZA = 50^o is now 0.13 ppm, but this includes the PP related error (see above).

To isolate the RxRA error, the difference of the biases listed in Row 2 and Row 1 are computed and displayed in Row 3 (see "IUP (via Δ) 3 bands 0.5%"). For example for SZA = 50^o the RxRA error is 0.01 ppm.

The RxRA errors as estimated by IUP-UB using the “difference method” just explained and listed in Row 3 are compared with errors computed independently by the University of Leicester (UoL) in the pre-decessor study **/CS L1L2-I-Study FR/**. The UoL error estimates are listed in Row 4 (see “UoL 3 bands 0.5%”). As can be seen, the RxRA errors as estimated by IUP-UB and UoL are quite similar, at least for high and low SZA. For mid-range SZAs, the UoL values are higher. Nevertheless, all errors are below 0.1 ppm and this is less than the maximum “permitted” error for multiplicative relative errors according to the error budget, which is 0.2 ppm. In this context one also has to note that RxRA is not the only contribution to multiplicative relative errors.

Table 14 shows the corresponding RxRA errors for XCH_4 biases. As shown by the comparison of the IUP-UB and UoL derived errors (1st red rectangle), the independently derived errors agree also reasonably well and they are all below 0.25 ppb, which is much less than the maximum “permitted” error for this error source. Again one has to note that RxRA is not the only contribution to multiplicative relative errors.

Figure 73 shows a graphical representation of the RxRA errors just discussed as black curves.

From the results presented it is concluded that a relaxation of the RxRA requirement is possible by replacing 0.25% by 0.5% in MR-OBS-190 (see above).

Results for RSRA are also shown in **Table 13** - **Table 14** and **Figure 73**:

Table 13 shows RSRA related XCO_2 biases the rows after Row 4: The difference to the RxRA results already discussed is than here an error of 0.5% has only been applied per band (e.g., “0.5/0.0/0.0” means that the error is only present in the NIR band and no error is present in the SWIR-2 and SWIR-2 bands; i.e., the given order corresponds to NIR/SWIR-1/SWIR-2). Again the IUP-UB and UoL errors are compared (see values listed in red rectangles). Again the agreement between the two independent error estimates is quite good. All errors are below 0.2 ppm, which equal to the “permitted” error for this error source. The same conclusions are valid for methane (**Table 14**). Note also the graphical representation of the RSRA errors in **Figure 73**.

For RSRA additional simulations have been carried out assuming that the multiplicative errors are not constant per band but vary linearly per band. The results are shown in **Table 15** for XCO_2, in **Table 16** for XCH_4 and are graphically represented in **Figure 74**. The conclusions are very similar as the ones already obtained for RSRA, i.e., the errors are mostly (well) below the required maximum error.

From the results presented it is concluded that a relaxation of the RSRA requirement is possible by replacing 0.25% by 0.5% in MR-OBS-180 (see above).

RxRA and RSRA: XCO_2 bias

XCO_2 bias [ppm] Albedo: VEG

Error [%] (*) NIR / SW1 / SW2	Solar zenith angle [deg]				
	5	25	50	60	70
IUP: None (#)	0.08	0.20	0.12	-0.01	-0.13
0.5 / 0.5 / 0.5	0.17	0.21	0.13	0.01	-0.11
IUP (via Δ) 3 bands 0.5%:	0.09	0.01	0.01	0.02	0.02
UoL 3 bands 0.5%:	0.09	0.09	0.08	0.06	0.03
0.5 / 0 / 0	0.18	0.23	0.15	0.03	-0.11
IUP (via Δ) NIR 0.5%:	0.10	0.04	0.03	0.03	0.02
UoL NIR 0.5%:	0.18	0.20	0.17	0.13	0.06
0 / 0.5 / 0	0.06	0.18	0.09	-0.03	-0.37
IUP (via Δ) SW1 0.5%:	-0.01	-0.01	-0.03	-0.02	-0.24
UoL SW1 0.5%:	-0.04	-0.04	-0.05	-0.07	-0.13
0 / 0 / 0.5	0.07	0.20	0.11	0.00	-0.11
IUP (via Δ) SW2 0.5%:	-0.00	-0.00	-0.00	0.01	0.03
UoL SW2 0.5%:	-0.06	-0.07	-0.04	-0.01	0.09
Requirement: RxRA: < 0.1 ppm; RSRA: < 0.2 ppm					

RxRA: 0.5 / 0.5 / 0.5; IUP (via Δ) 3 bands 0.5%: / UoL 3 bands 0.5%:

RSRA: 0.5 / 0 / 0; IUP (via Δ) NIR 0.5%: / UoL NIR 0.5%: / 0 / 0.5 / 0; IUP (via Δ) SW1 0.5%: / UoL SW1 0.5%: / 0 / 0 / 0.5; IUP (via Δ) SW2 0.5%: / UoL SW2 0.5%:

(*) Error: Constant relative radiance error per band (#) IUP: Primarily due to pre-processing related errors

Only values in RED rectangle relevant = Bias with – without RxRA/RSRA error

Table 13: Multiplicative radiometric errors: XCO_2 biases.

RxRA and RSRA: XCH_4 bias

XCH_4 bias [ppb] Albedo: VEG

Error [%] (*) NIR / SW1 / SW2	Solar zenith angle [deg]				
	5	25	50	60	70
None (#)	-1.01	0.25	-0.57	-1.68	-2.62
0.5 / 0.5 / 0.5	-0.77	0.19	-0.62	-1.71	-2.52
IUP (via Δ) 3 bands 0.5%:	0.24	-0.06	-0.50	-0.02	0.10
UoL 3 bands 0.5%:	0.10	0.13	0.13	0.10	0.05
0.5 / 0 / 0	-0.63	0.38	-0.46	-1.54	-2.47
IUP (via Δ) NIR 0.5%:	0.38	0.12	0.12	0.14	0.14
UoL NIR 0.5%:	0.30	0.40	0.40	0.35	0.20
0 / 0.5 / 0	-1.22	0.06	-0.85	-1.97	-3.89
IUP (via Δ) SW1 0.5%:	-0.20	-0.19	-0.27	-0.28	-1.28
UoL SW1 0.5%:	-0.45	-0.50	-0.50	-0.60	-0.90
0 / 0 / 0.5	-0.95	0.28	-0.52	-1.58	-2.35
IUP (via Δ) SW2 0.5%:	0.06	0.02	0.05	0.11	0.27
UoL SW2 0.5%:	0.25	0.20	0.20	0.35	0.80
Requirement: RxRA: < 0.6 ppb; RSRA: < 1.0 ppb					

RxRA: 0.5 / 0.5 / 0.5; IUP (via Δ) 3 bands 0.5%: / UoL 3 bands 0.5%:

RSRA: 0.5 / 0 / 0; IUP (via Δ) NIR 0.5%: / UoL NIR 0.5%: / 0 / 0.5 / 0; IUP (via Δ) SW1 0.5%: / UoL SW1 0.5%: / 0 / 0 / 0.5; IUP (via Δ) SW2 0.5%: / UoL SW2 0.5%:

(*) Error: Constant relative radiance error per band (#) IUP: Primarily due to pre-processing related errors

Only values in RED rectangle relevant = Bias with – without RxRA/RSRA error

Table 14: As **Table 13** but for XCH_4.

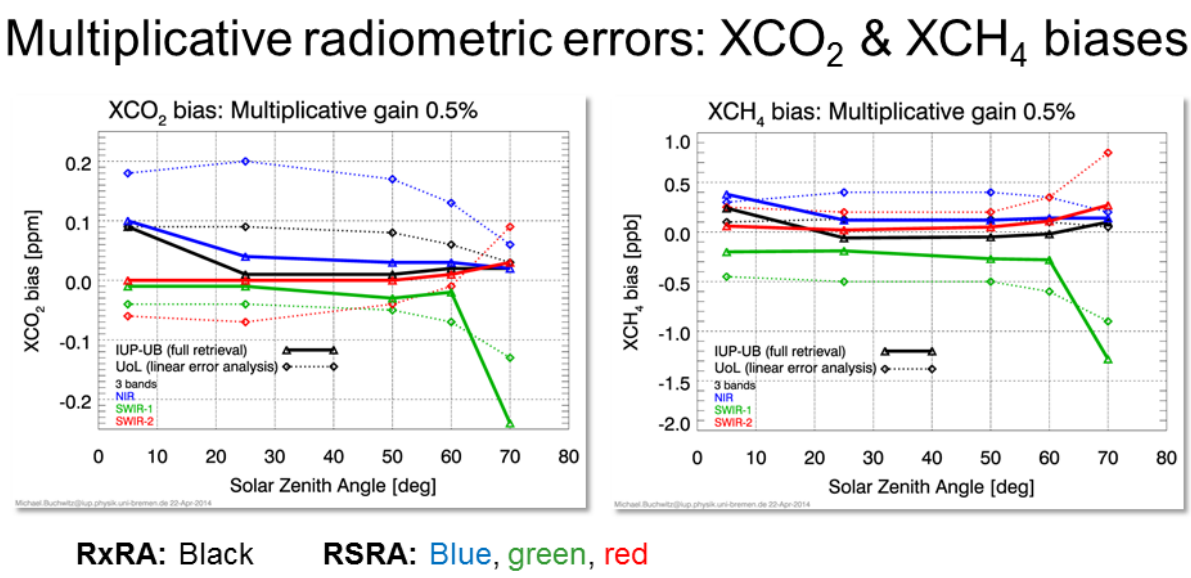

Figure 73: XCO_2 and XCH_4 biases due to multiplicative radiometric errors RxRA and RSRA.

RSRA linear (slope) error: XCO_2 bias

XCO_2 bias [ppm] Albedo: VEG

Slope error [%] NIR / SW1 / SW2	Solar zenith angle [deg]				
	5	25	50	60	70
None (#)	0.08	0.20	0.12	-0.01	-0.13
0.5 / 0.5 / 0.5	0.14	0.20	0.10	-0.01	-0.33
IUP (via Δ) 3 bands 0.5%:	0.06	0.00	-0.02	0.00	-0.20
0.5 / 0 / 0	0.09	0.21	0.11	-0.01	-0.34
IUP (via Δ) NIR 0.5%:	0.01	0.01	0.00	0.00	-0.21
0 / 0.5 / 0	0.07	0.20	0.11	-0.01	0.13
IUP (via Δ) SW1 0.5%:	0.00	0.00	-0.01	-0.01	0.00
0 / 0 / 0.5	0.08	0.19	0.11	0.00	-0.32
IUP (via Δ) SW2 0.5%:	0.00	-0.01	-0.01	0.00	-0.18
Requirement: RSRA: 0.2 ppm					

(*) Error: Constant relative radiance error per band (#) IUP: Primarily due to pre-processing related errors

Only values in RED rectangle relevant = Bias with – without RSRA error

Table 15: XCO_2 biases due to linear ("slope") error (RSRA).

RSRA linear (slope) error: XCH_4 bias

XCH_4 bias [ppb] Albedo: VEG

Slope error [%] NIR / SW1 / SW2	Solar zenith angle [deg]				
	5	25	50	60	70
None (#)	-1.01	0.25	-0.57	-1.68	-2.62
0.5 / 0.5 / 0.5	-0.81	0.22	-0.55	-1.63	-3.57
IUP (via Δ) 3 bands 0.5%:	0.20	-0.03	0.03	0.05	-0.95
0.5 / 0 / 0	-0.99	0.28	-0.60	-1.71	-3.60
IUP (via Δ) NIR 0.5%:	0.03	0.02	-0.02	-0.02	-0.98
0 / 0.5 / 0	-1.07	0.20	-0.69	-1.75	-2.62
IUP (via Δ) SW1 0.5%:	-0.05	-0.05	-0.11	-0.07	0.00
0 / 0 / 0.5	-0.98	0.23	-0.43	-1.55	-3.41
IUP (via Δ) SW2 0.5%:	0.04	-0.02	0.15	0.13	-0.80
Requirement: RSRA: < 1 ppb					

(*) Error: Constant relative radiance error per band (#) IUP: Primarily due to pre-processing related errors

Only values in RED rectangle relevant = Bias with – without RSRA error

Table 16: As **Table 15** but for XCH_4.

RSRA: Biases due to linear („slope“) errors

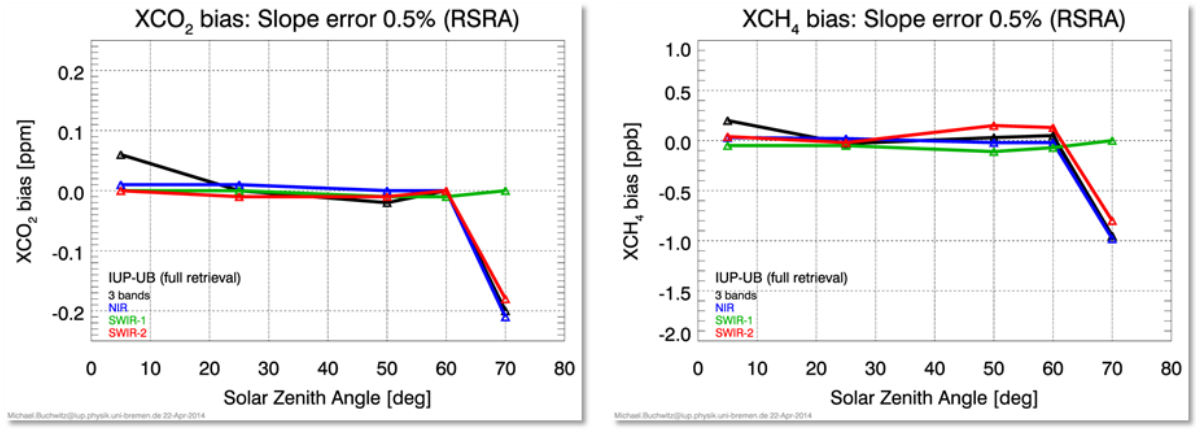

Figure 74: XCO_2 and XCH_4 biases due to linear (“slope”) error (RSRA).

9.3.3. Summary: Possible relaxation of RSRA and RxRA requirements

Simulated retrievals have been performed to find out to what extent the MRDv1.2 ***/CS MRD v1.2, 2013/*** RSRA (MR-OBS-180) and RxRA (MR-OBS-190) requirements can be relaxed.

The analysis presented here shows that - if necessary - the requirement can be relaxed by replacing as follows:

- RSRA: 0.25% (T) can be relaxed to 0.5% (T)
- RxRA: 0.25% (T) can be relaxed to 0.5% (T)

9.4. Radiometric requirements: Maximum degree of linear polarisation (DOP)

In the context of requirements related to polarization it is relevant to know what the expected maximum Degree of (linear) Polarization (DOP) for CarbonSat radiances is.

Using different scenarios, a table of maximum DOP values has been compiled, see **Table 17**, based on the detailed SCIATRAN RTM simulations results presented in **Sect. 8.2**.

As can be seen, DOP can reach 40% in the NIR band for the following scenario:

- SZA 50^o
- VZA 15^o and looking towards the sun (i.e., azimuth angle AZI = 0^o for SCIATRAN)
- (note that the above angles correspond to a scattering angle of 115^o)
- clear sky (i.e., no aerosols or clouds)
- a Lambertian vegetation surface with a quite low albedo of 0.1 (note: the lower the albedo, the higher the DOP)

For the same scenario but SZA 70^o (scattering angle 95^o) maximum DOP is 80%, i.e., higher than for SZA 50^o, as the scattering angle is closer to 90^o, where DOP due to Rayleigh scattering has its maximum values (note that the Lambertian surface is depolarizing).

If the surface is polarizing, DOP can reach 90% for SZA 70^o according to IUP simulations but “only” 60% according to SRON simulations. The reasons for this discrepancy are different assumptions and RT modelling approaches related to the question of how to best model a realistic / typical polarizing vegetation BRDF.

Because it is not entirely clear how to best model an appropriate polarizing vegetation BRDF and because the different modelling approaches result in a quite large spread of the resulting DOP values, it is recommended to determine the maximum DOP values not from the most extreme of the scenarios listed in **Table 17** (i.e., from the IUP simulations for SZA 70^o and using a polarizing surface) but using the SZA 50^o scenario with polarizing surface, where in the NIR the maximum DOP as computed with SCIATRAN is already larger than the DOP as computed by SRON using the SRON RTM.

Using a scenario with polarizing surface is preferred compared to a depolarizing Lambertian surface to be on the save side also for the weak absorption bands SWIR-1 and SWIR-2C (see **Table 17**).

Also listed in **Table 17** are "recommended maximum DOP" values for each band. For the reasons explained above, they are based on the SZA 50° scenario with a polarizing surface.

SZA	Band					Scenario
	NIR	SWIR-1	SWIR-2			
			A	B	C	
	747-773 nm	1590-1675 nm	1925-1990 nm	1990-2043 nm	2043-2095 nm	
50	40%	1%	65%	10%	1%	IUP-UB: Lambertian surface with albedo: 0.1 / 0.05 / 0.05 AZI=0°, VZA=15° See **Sect. 8.2.2**
70	80%	2%	100%	50%	2%	
50 (*)	65%	15%	65%	25%	15%	IUP-UB: Polarizing surface: Pol. Vegetation BRDF AZI=0°, VZA=15° See **Sect. 8.2.3**
70	90% (SRON: 60% for different BRDF)	35%	100%	75%	35%	
Recommended maximum DOP:						
(*) Reference scenario	65%	15%	65%	25%	15%	See main text for details
	60%	30%				Simplified alternative (#)

Table 17: Maximum Degree Of (linear) Polarization (DOP in percent, see computation of p_c described in **Section 8.2**) to be expected for CarbonSat nadir mode observations over land for different scenarios per spectral band. The maximum DOP values have been derived from the simulations and corresponding figures shown in **Section 8.2**. Also listed are recommended maximum DOP values per band. (#) Note that SWIR-2A is (currently) "only" used for cirrus pre-processing (and for this not the entire SWIR-2A band is used) but not for full XCO_2 and XCH_4 3-band retrieval.

9.5. Radiometric requirements: Effective Spectral Radiometric Accuracy (ESRA)

This requirement deals with erroneous “spectral features”. This important aspect is primarily addressed via the Gain Matrix (GM) approach already explained.

The GMs can be used to map Level 1 errors onto Level 2 errors. Within this study GMs have been used to address several requirements, most of them also related to error sources causing erroneous spectral features.

How exactly various instrument related erroneous spectral features will “look like” is currently not well known as the instrument design is still being optimized.

To consider this aspect – also for instrument optimization and performance assessments during instrument design development - several GMs have been generated and delivered to ESA (e.g., **Sect. 8.1**).

These GMs will be used by industry and ESA during instrument design / optimization. They permit to compute Level 2 errors. Requirements for the maximum permitted Level 2 errors have been formulated in the MRD **/CS MRD v1.2, 2013/**.

The (delivered) GMs are used to compare the expected performance with the required performance. This is an activity carried out by ESA and industry and therefore not presented and discussed in this section (but for other requirements at various places in this document).

9.6. Radiometric requirements: Heterogeneous scenes (Pseudo-Noise (PN))

Simulated retrievals for heterogeneous scenes have already been performed and discussed in the predecessor study **/CS L1L2-I-Study FR/**.

The results of that activity can be summarized as follows (see **/CS L1L2-I-Study FR/** for details):

IUP-UB has conducted an initial analysis to quantify XCO_2 and XCH_4 errors due to Pseudo Noise (PN) arising from inhomogeneous slit illumination in case of inhomogeneous ground pixels.

The analysis is based on “PN error spectra” as provided by ESA. This data set contains PN error spectra for 7 scenarios (denoted IH0 to IH6, see **/CS L1L2-I-Study FR/** for details).

These PN error spectra have been used to generate “perturbed” simulated CarbonSat radiance spectra. BESD/C has been applied to these perturbed spectra to retrieve XCO_2 and XCH_4. Systematic errors have been computed by “retrieved – true”, where true is the true XCO_2 and XCH_4 from the model atmosphere (it has been verified that for unperturbed spectra, the retrieved values are equal to the true values).

Based on the limited number of scenarios studied initially, it has been found that error can be quite large if no correction method is applied. However, using a spectral SHIFT correction (as part of the BESD/C retrieval method), it has been found that the errors can be significantly reduced.

However, based on an analysis of ~1400 additional scenarios, it has been found that biases can be quite large even with SHIFT and SQUEZZE correction. The largest biases found were 1.3 ppm for XCO_2 and 9 ppb for XCH_4.

However - at least to some extent - these biases will vary from ground pixel to ground pixel and are therefore essentially „noise“ rather than spatio-temporally coherent biases on the relevant spatio-temporal scales. If this assumption is true, the impact is essentially a random error contribution and not a systematic error contribution. For the worst case errors mentioned above and assuming that PN results in a pure random error, the estimated retrieval precision degradation is as follows:

- XCO_2 precision degradation: 1 ppm (T) -> 1.6 ppm ($=\sqrt{(1.0^2+1.3^2)}$)
- XCH_4 precision degradation: 10 ppb (T) -> 13.5 ppb ($(=\sqrt{(10^2+9^2)}$)

The precision degradation is therefore expected not to be entirely negligible.

To what extent PN also results in systematic errors and to what extent this error source impacts on the quality of the inferred CO_2 and CH_4 emissions (fluxes) has not yet been assessed. A first step to address this is presented in the following section.

9.6.1. Gain matrices for heterogeneous scene analysis

In order to perform additional investigations related to PN using the fast GM approach it has been investigated if GMs for scenes with arbitrary "intermediate albedos" (corresponding to inhomogeneous scenes) can be obtained via linear combination of a scene for low albedo ("w00") and a scene of high albedo ("w10") (representing).

Scene ID	Weight w (for TRB)	Albedo			Comment
		NIR	SWIR-1	SWIR-2	
w00	**0.0**	0.10	0.05	0.05	TRD scenario
w02	**0.2**	0.24	0.18	0.16	TRB*w + TRD*(1-w)
w04	**0.4**	0.38	0.31	0.27	-"-
w06	**0.6**	0.52	0.44	0.38	-"-
w08	**0.8**	0.66	0.57	0.49	-"-
w10	**1.0**	0.80	0.70	0.60	TRB scenario

Table 18: Six scenes with different albedo defined for PN related studies using GMs. TRD = Tropical Dark; TRB = Tropical Bright.

The results are shown in **Figure 75** -
Figure 77. As can be seen, the "interpolation errors" are quite high (**Figure 76** and **Figure** 77). Therefore this method has not been used for PN related studies. However, it cannot be excluded that interpolation errors can be much reduced in order to use this method for the assessment of PB, but this needs to be further investigated.

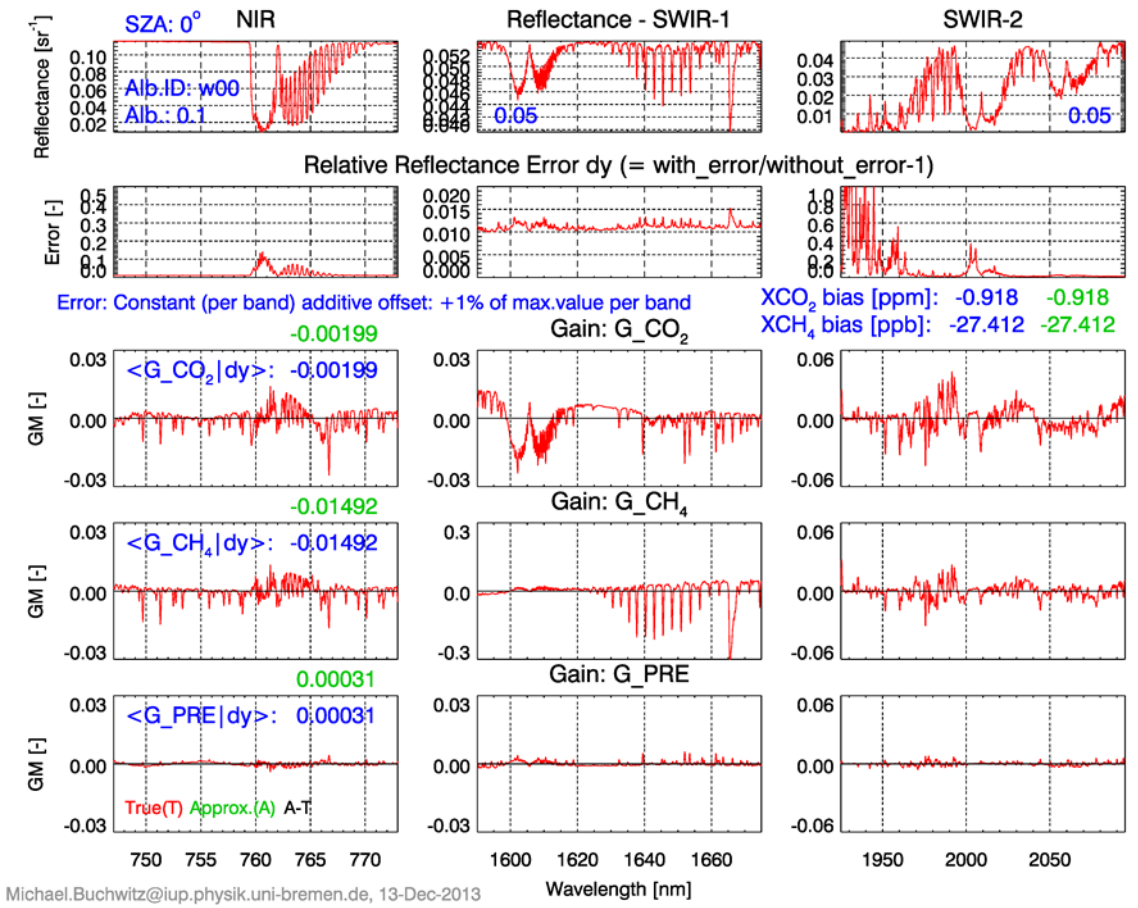

Figure 75: Reference result (scenario w00 = 0% bright (TRB) = 100% dark (TRD)) for PN related study using GMs. Two retrieval results are shown, one using the correct GM for the selected scenario providing the “true biases” (shown in blue) and one using the interpolated GM providing the biases computed via linear combination the TRB and TRD GMs (biases shown in green). Here both approaches give the same result (blue = green) as the selected scenario corresponds to one of the extreme cases (here TRD).

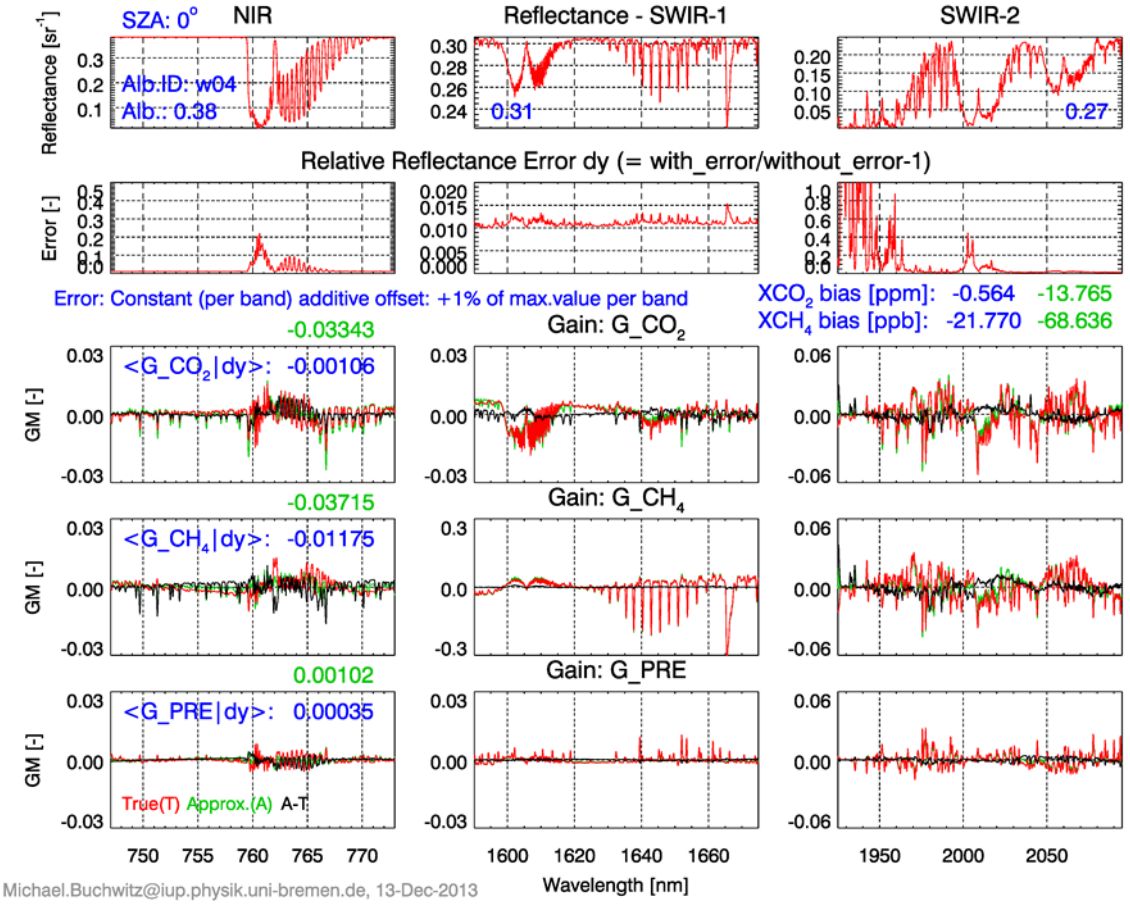

Figure 76: As **Figure 75** but for scenario w04 = 40% bright (TRB) = 60% dark (TRD). As can be seen, here the biases obtained via interpolation (green) significantly differ from the true (blue) biases.

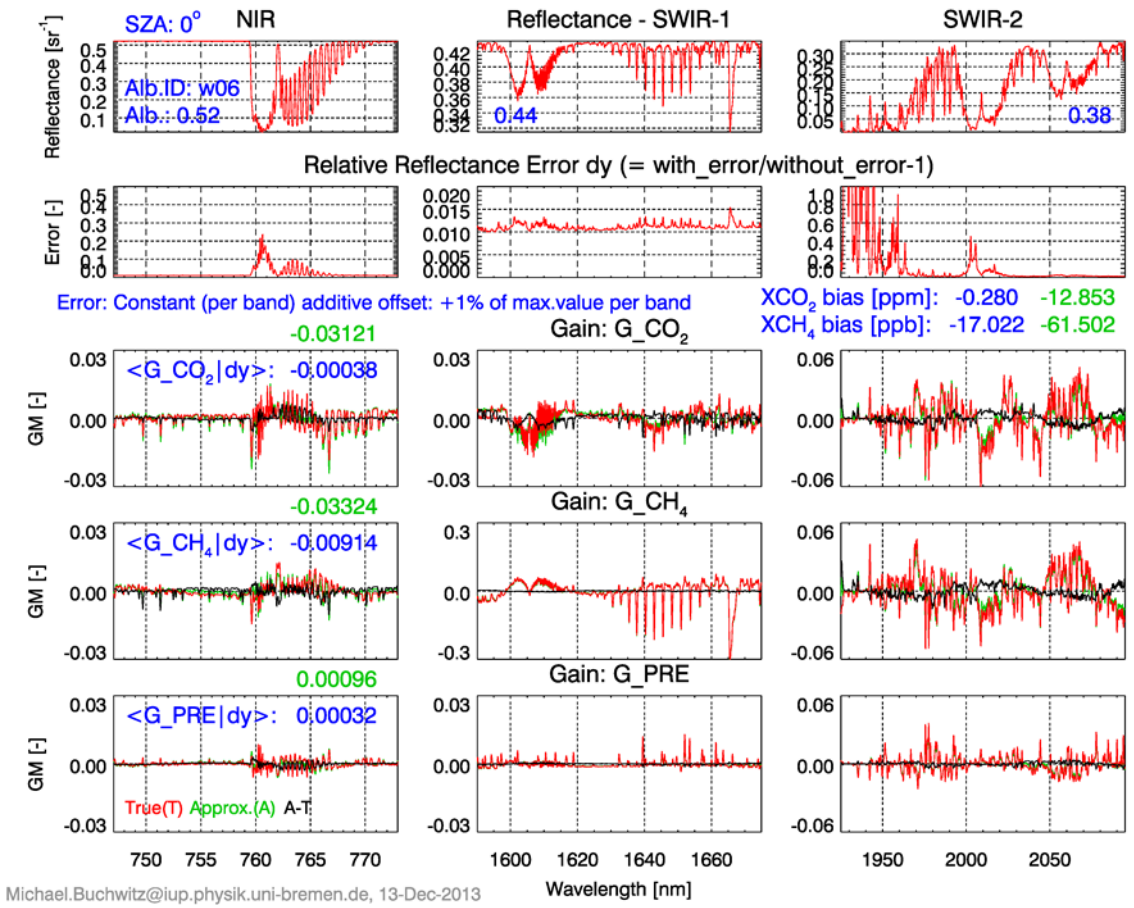

Figure 77: As **Figure 75** but for scenario w06 = 60% bright (TRB) = 40% dark (TRD). As can be seen, also here the biases obtained via interpolation (green) significantly differ from the true (blue) biases.

9.6.2. Assessment based on artificial scenes

Artificial scenes have been defined to compute perturbed ISRFs due to scene heterogeneity. **Figure 78** shows one example for a fairly inhomogeneous scene (likely close to a worst case scenario). The same approach has been used for realistic scenes (see **Sect. 9.6.3**).

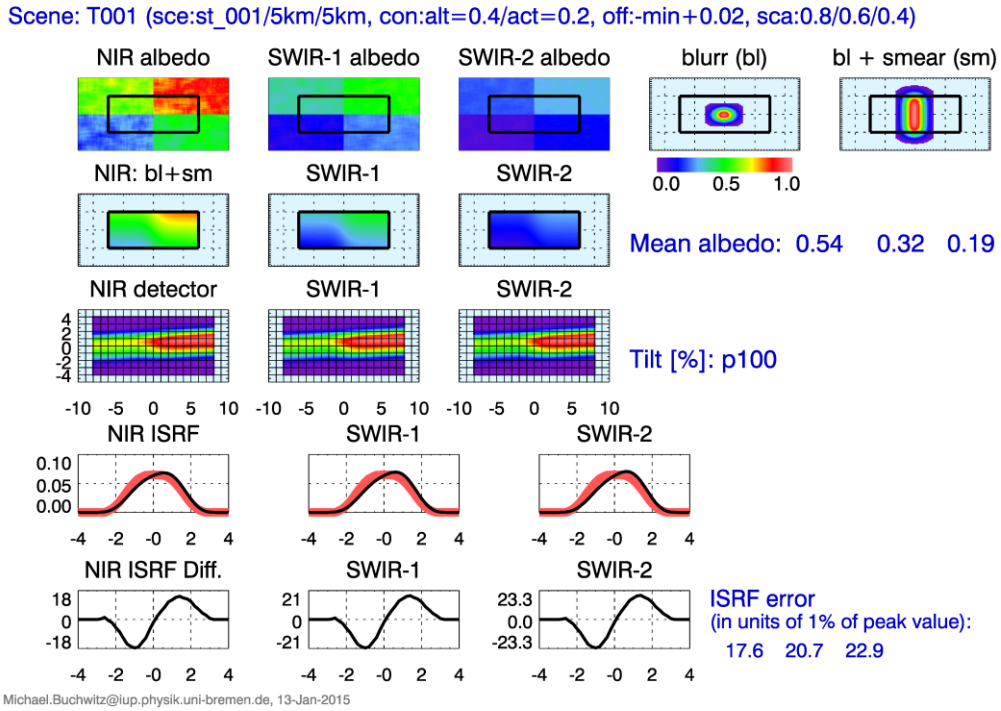

Figure 78: Illustration of computation of erroneous ISRFs due to an artificial inhomogeneous scene. The spatially resolved (assumed) albedos in the NIR, SWIR-1 and SWIR-2 bands are shown in the top row. The black-rimmed rectangle indicates an area of 2 km along-track (here: horizontal, i.e., left-right) times 3 km across-track (here: vertical). The scene as observed by CarbonSat is essentially blurred and smeared (due to the along-track motion of the spacecraft (~7 km/s) during the integration time (~0.3 s)), see top right. The resulting blurred and smeared scene as effectively observed in the three bands is shown in the second row. The third row shows for each band how a single wavelength is mapped onto the detector (each square denotes a single detector pixel and the x and y coordinates are in detector pixel units). Note that here it also has been assumed that the slit is tilted w.r.t. to the detector. The resulting ISRFs are shown in the fourths row. The red lines indicate the unperturbed ISRFs corresponding to homogeneous scenes and the black lines are the perturbed ISRFs corresponding to the assumed inhomogeneous scenes (the x coordinate is again in detector pixel units). The bottom row shows the differences between the inhomogeneous and the homogeneous ISRFs in units of 1% of the maximum of the unperturbed ISRF (the corresponding maximum errors are listed on the right hand side; note that 17.6 means that the (maximum) error of the NIR ISRF is 17.6% of the maximum value of the unperturbed ISRF).

The perturbed ISRFs shown in **Figure 78** have been used in combination with the gain matrix method to compute XCO_2 and XCH_4 biases for different albedos and assuming a solar zenith angle of 50°. The results are shown in **Table 19**.

As can be seen, the maximum biases are 15.4 ppm for XCO_2 and 53.3 ppb for XCH_4. These biases correspond to ISRF errors of ~20% (see caption **Table 19**).

Assuming a maximum ISRF error of 2% (requirement for ISRF errors due to inhomogeneous scenes), the biases would be 10 times smaller than the biases listed in **Table 19**, i.e., the maximum bias would be 1.5 ppm for XCO_2 and 5 ppb for XCH_4.

Assuming that these values, i.e., 1.5 ppm for XCO_2 and 5 ppb for XCH_4, are worst case (single observation) biases due to pseudo-noise (quasi random error due to quasi random variability of scenes) they may be interpreted as additional 2-sigma precision contributions. They would therefore add 0.8 ppm (for XCO_2) or 3 ppb (for XCH_4) to the 1-sigma retrieval precision and would therefore degrade the precision as follows:

- XCO_2 precision degradation ~30%: 1 ppm -> 1.3 ppm ($=\sqrt{(1.0^2+0.8^2)}$)
- XCH_4 precision degradation ~7%: 8 ppb -> 8.5 ppb ($(=\sqrt{(8^2+3^2)}$)

The precision degradation due to ISRF errors caused by inhomogeneous scenes is therefore considered acceptable if a 2% ISRF error requirement due to scene heterogeneity would be met.

No	Albedo			Bias	
	NIR	SWIR-1	SWIR-2	XCO_2 [ppm]	XCH_4 [ppb]
1	0.2	0.2	0.2	1.1	-10.0
2	0	0.2	0.2	1.4	-9.4
3	0.2	0	0.2	0.3	30.1
4	0.2	0.2	0	4.9	2.1
5	1	0.2	0.2	11.9	36.5
6	0.2	1	0.2	0.8	36.5
7	0.2	0.2	1	1.1	36.5
8	1	1	1	15.4	53.3

Table 19: XCO_2 and XCH_4 bias for various surface albedos due erroneous ISRFs (see **Figure 78**) caused by a highly inhomogeneous scene. The used (asymmetric) ISRFs have ISRF errors of 17.6% (NIR), 20.7% (SWIR-1) and 22.5% (SWIR-2) in terms of the maximum value of the unperturbed ISRF.

9.6.3. Assessment based on AVIRIS scenes

For the results shown in this section a similar assessment has been carried out as presented in the previous section but using realistic scenes.

For this purpose AVIRIS (Airborne Visible / Infrared Imaging Spectrometer, http://aviris.jpl.nasa.gov/) measurements have been used. ESA has provided IUP with AVIRIS radiances for several scenes. Two scenes have been selected for the results shown in this section:

- A city scene using AVIRIS data at and around Washington, D. C., see **Figure 79**.
- A somewhat more homogeneous scene in California, see **Figure 80**.

The AVIRIS radiances L_i corresponding to the three CarbonSat spectral bands NIR, SWIR-1 and SWIR-2, have been converted to surface albedo via

$$Albedo_i = L_i / F_i \times (\pi/\cos(SZA)),$$

where F_i is solar irradiance in band i and SZA is the solar zenith angle, which is assumed to be 50^o for the results shown in the following. The albedo conversion has been carried out as this is a relevant parameter for the RT simulations carried out for the results presented in this section.

Figure 81 shows as an example a result for the Washington scene for a single CarbonSat ground pixel located directly above Washington. The scene inhomogeneity results in an ISRF which differs from the homogeneous case as shown in the bottom panels. The resulting ISRF errors in units of 1% percent of the peak value of the homogeneous ISRF are 2.2, 2.9 and 7.2 in this case for the NIR, SWIR-1 and SWIR-2 bands, respectively.

The corresponding XCO_2 and XCH_4 biases have been estimated using gain matrices, i.e., using linear error analysis and using an interpolation scheme applied to precomputed radiance spectra and gain matrices for various scenarios in terms of surface albedos in the three CarbonSat spectral bands.

To obtain statistically robust results the location of the CarbonSat ground pixel has been shifted around the location shown in **Figure 81** and for each location ISRF errors and corresponding XCO_2 and XCH_4 biases have been obtained and a similar analysis has been carried out for the California scene (**Figure 82** shows one example).

The results can be summarized as mean +/- standard deviation of the following quantities:

Washington scene results “as is”:

Maximum ISRF error:	7.7 +/- 4.9
Mean +/- StdDev of XCO_2 bias:	0.13 +/- 1.16 ppm
Mean +/- StdDev of XCH_4 bias:	-0.97 +/- 6.03 ppb

California scene results “as is”:

Maximum ISRF error:	6.0 +/- 5.4
Mean +/- StdDev of XCO_2 bias:	0.17 +/- 0.31 ppm
Mean +/- StdDev of XCH_4 bias:	-1.65 +/- 2.72 ppb

The most relevant bias quantity is the standard deviation (StdDev), as this corresponds to the Pseudo Noise (PN) introduced by varying biases due to scene inhomogeneity. The obtained standard deviations can be compared with the required (“permitted”) random error due to “Heterogeneous scenes / Pseudo Noise (PN)” as listed in the error budget (**Table 1**).

The standard deviations are, as expected, largest for the Washington scene, namely ~1.2 ppm for XCO_2 and ~6 ppb for XCH_4, which exceeds the requirement by a factor of 4 for XCO_2 and 2.5 for XCH_4. This shows that XCO_2 is the driver for improving this situation.

For XCO_2 the mean value of the ISRF error is approx. 8 (= 8% of the peak value of the homogeneous ISRF) for the Washington scene. If the ISRF errors would be reduced by a factor of 4 (e.g., by implementing a “spatial scrambler” / “slit homogenizer”), than the error listed above are reduced to:

Washington scene results for “ISRF errors reduced by a factor of 4”:

StdDev of XCO_2 bias:	0.29 ppm
StdDev of XCH_4 bias:	1.50 ppb

These errors are smaller than the errors listed for “Heterogeneous scenes / Pseudo Noise (PN)” in the error budget (**Table 1**), which are:

XCO_2 error:	~0.3 ppm
XCH_4 error:	~2.6 ppb

These errors are therefore “acceptable” but likely require the implementation of a correction or mitigation method such as a “slit homogenizer”.

Similar but somewhat larger errors are obtained if the correction/mitigation method limits the ISRF error to 2% but has no effect on the ISRF if the error is below 2%:

Washington scene results for “ISRF errors limited to 2% but only for bands where 2% is exceeded”:

StdDev of XCO_2 bias: 0.47 ppm
StdDev of XCH_4 bias: 2.51 ppb

As can be seen, in this case the error budget value for XCO_2 is slightly exceeded.

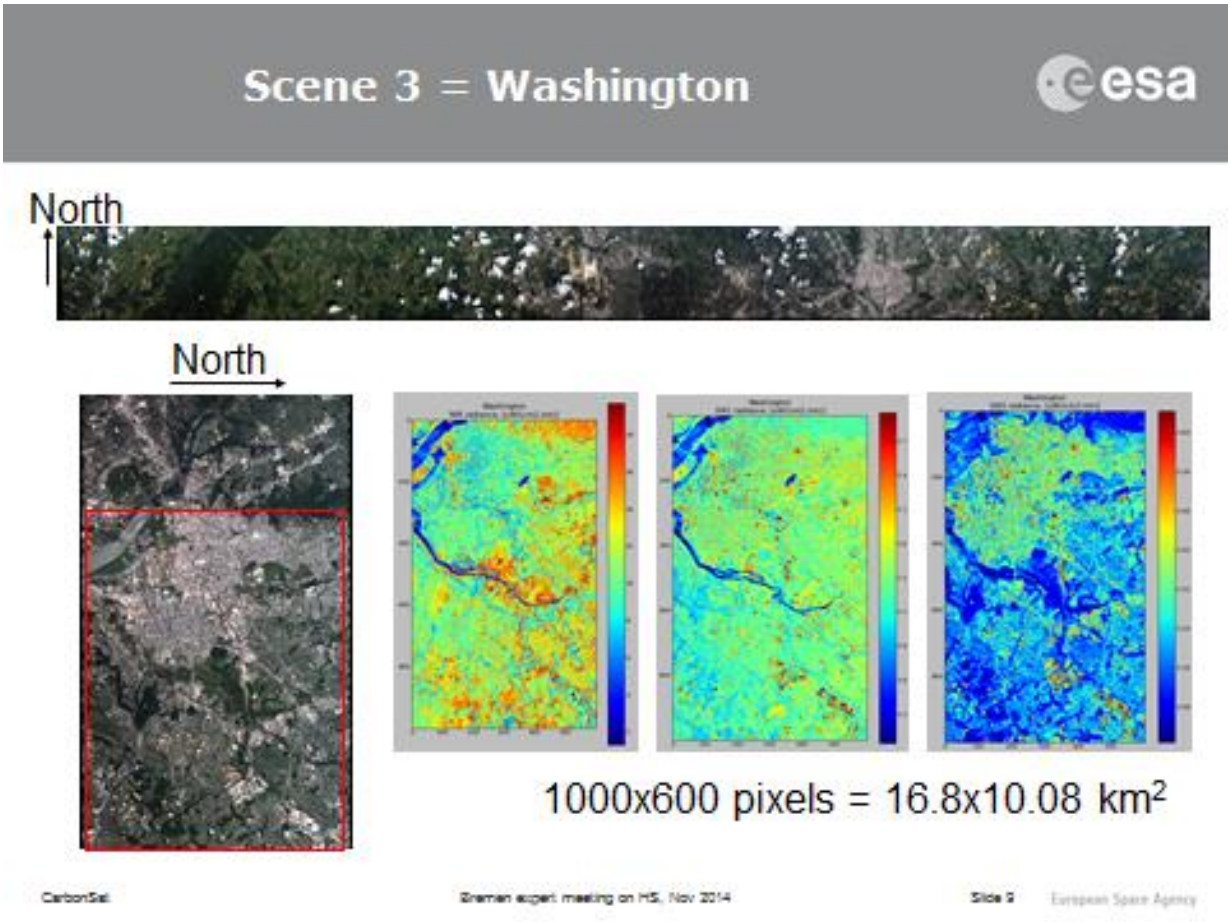

Figure 79: AVIRIS Washington scene as chosen for CarbonSat heterogeneous scene (Pseudo Noise (PN)) analysis (from: J. Caron, ESA/ESTEC).

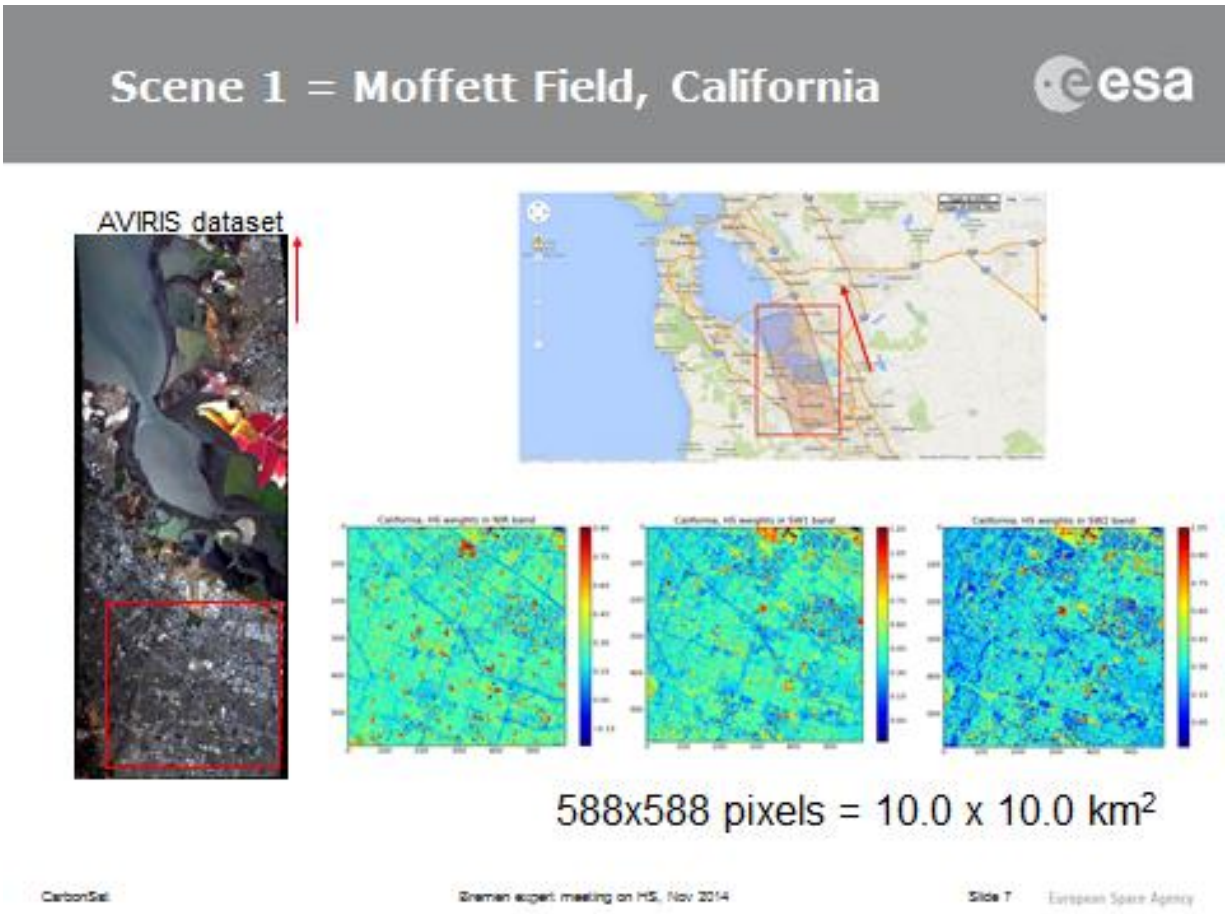

Figure 80: AVIRIS California scene as chosen for CarbonSat heterogeneous scene (Pseudo Noise (PN)) analysis (from: J. Caron, ESA/ESTEC).

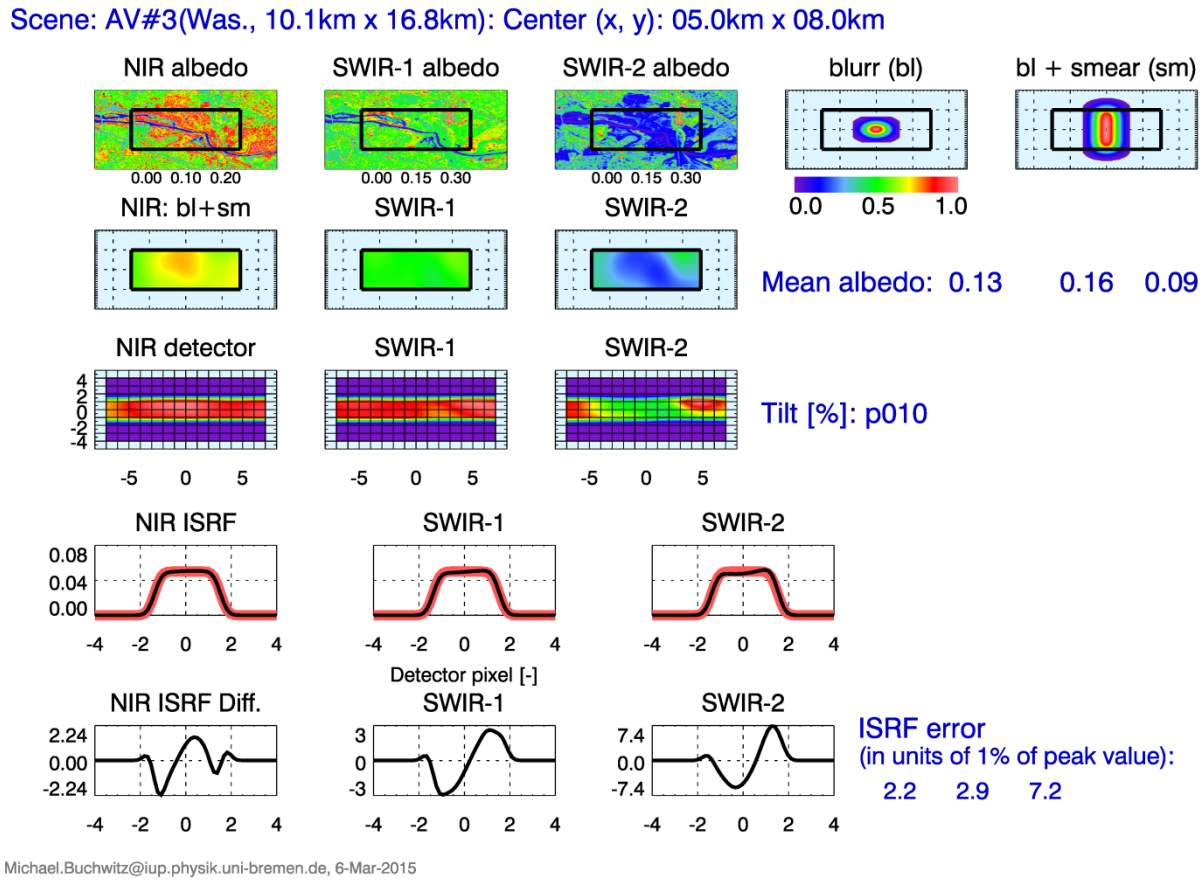

Figure 81: As **Figure 78** but using AVIRIS high spatial resolution measurements around Washington D.C. (see also **Figure 79**). Note that these simulations have been carried out assuming that no corrections (such as a slit homogenizer) have been implemented.

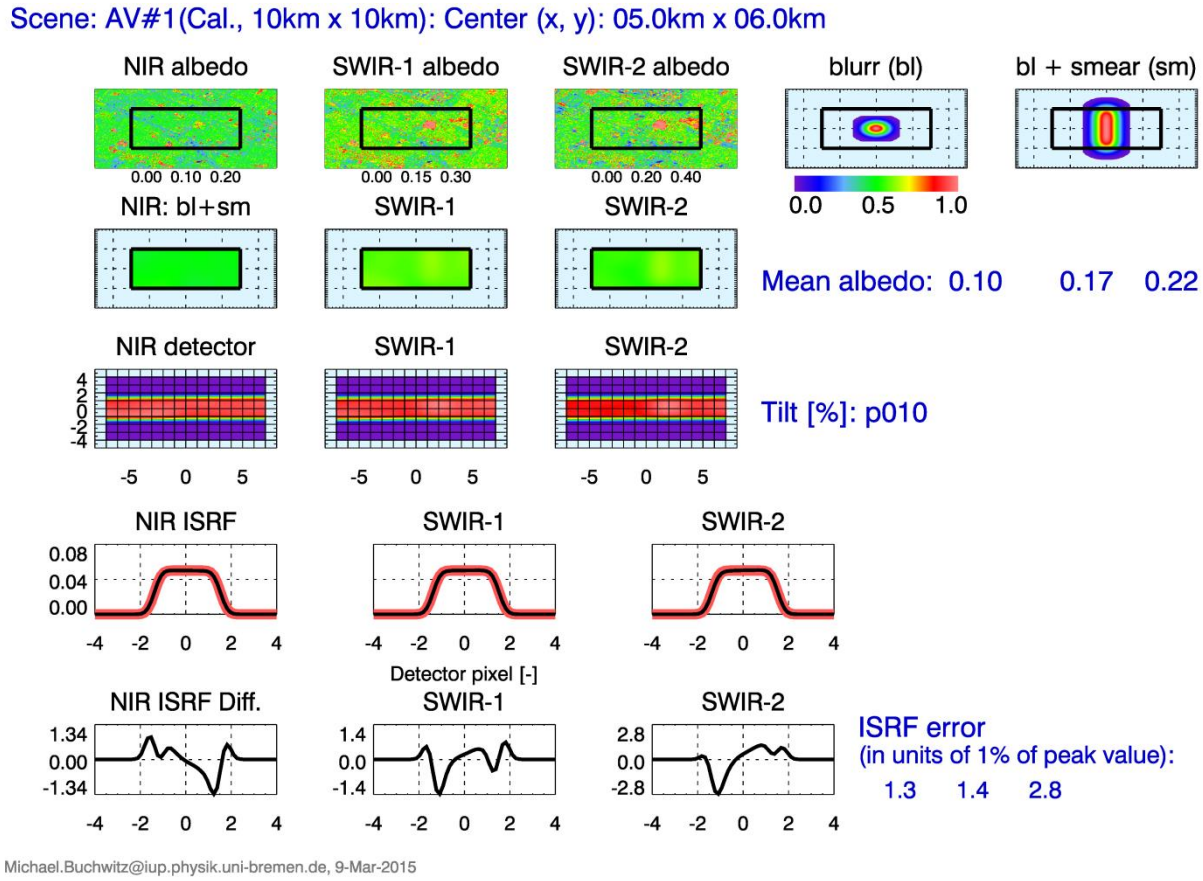

Figure 82: As **Figure 78** but using AVIRIS high spatial resolution measurements in California (see also **Figure 80**).

9.6.4. Summary and conclusions

ISRF errors due to inhomogeneous scenes have been computed and corresponding XCO_2 and XCH_4 errors have been estimated using simulated retrievals based on the gain matrix method, i.e., via linear error analysis. The assessments have been carried out using simplified artificial inhomogeneous scenes but also realistic inhomogeneous scenes using real high-spatial resolution AVIRIS aircraft radiance observations.

Due to the variable nature of inhomogeneous scenes (change from one ground pixel to the next) this error source primarily contributes to the XCO_2 and XCH_4 random errors (“precision”) and is therefore also referred to as Pseudo Noise (PN).

It has been found that the impact is largest for XCO_2, as expected, primarily because the XCO_2 error requirement is more demanding compared to the XCH_4 requirement.

If one considers a precision degradation due to ISRF errors of 0.3 ppm for XCO_2 as acceptable, which is in-line with the error budget (**Table 1**), where a random error of 0.3 ppm is allocated for this error source, than the simulations using artificial scenes indicate that this can be met if the ISRF error due to inhomogeneous scenes is less than 2% of the maximum value of the unperturbed ISRF.

Similar conclusions have been drawn based on the analysis of real data using high spatial resolution AVIRIS radiances. Here it has been found that ISRF errors for the scenes investigated are typically 8% (maximum values in at least one of the three bands) for a challenging city scene resulting in a standard deviation of the XCO_2 bias of 1.2 ppm. If it would be possible, e.g., by implementing a “spatial scrambler” / “slit homogenizer”, to reduce ISRF errors to 2%, i.e., by factor of at least 4, this would reduce the XCO_2 errors from 1.2 ppm to below 0.3 ppm, which would be in-line with the error budget (**Table 1**). The XCH_4 errors would be reduced to 1.5 ppb, which is also in-line with the error budget.

Note that for the results shown here it has been neglected that the ISRF may also vary within each band. Band-to-band variations have been considered for the results presented here but not variations within each band.

Nevertheless, based on the results presented in this section it is concluded that the XCO_2 and XCH_4 errors will be smaller or similar as the values allocated for this error source in the error budget (**Table 1**) if the (additional) ISFR error due to inhomogeneous scenes / Pseudo Noise (PN) is less than 2% of the maximum value of the unperturbed ISRF.

9.7. Radiometric requirements: Absolute radiometric accuracy (ARA)

The required absolute radiometric accuracy of the reflectance measurements is "better than 2%" in the NIR band according to **/CS MRD v1.2, 2013/** and "better than 3%" in the SWIR-1 and SWIR-2 bands (requirement MR-OBS-165).

Here it has been investigated if the NIR requirements can be relaxed using the same requirement as also used for the other two bands, i.e., also requiring "better than 3%" for the NIR band.

Sufficient radiometric accuracy is required by the current version of the BESD/C algorithm primarily to obtain a good estimate of the surface albedo via a pre-processing scheme. The current albedo retrieval pre-processing scheme is based on retrieving surface albedo in the NIR band from the continuum radiance or reflectance around 755 nm.

The radiance or reflectance at 755 nm is (for a given SZA, etc.) not only affected by surface albedo but also by, for example, aerosols and cirrus clouds. Using "900 scenarios" defined for estimating errors due to clouds and aerosols, the variability of the radiance / reflectance at 755 nm due to aerosols and cirrus has been estimated.

For example for vegetation albedo and a SZA of 50^o, it has been found that the radiance varies by +/- 3.3% (1-sigma) due to variability of aerosols and cirrus. At least for the current albedo retrieval pre-processing scheme, which neglects variability due to aerosols and cirrus clouds, this results in a (relative) albedo error on the same order. For a SZA of 25^o, the variability of the radiance is lower (+/- 1.7%).For a SZA of 75^o, the variability of the radiance is higher (+/- 8.2%).

It therefore concluded that the albedo retrieval error is typically dominated or at least significantly affected by the variability of aerosols and clouds and not by errors related to absolute radiometric accuracy (ARA), if ARA is better than approx. 3%.

A related question is what the sensitivity of XCO_2 and XCH_4 errors to surface albedo errors is. This has been addressed by performing (full iterative) BESD/C retrievals but using a surface albedo which is perturbed in each band by a certain percentage. The results are shown in **Table 20**. As can be seen, an albedo error of 2% in the NIR results in an XCO_2 bias of 0.05 ppm and an XCH_4 bias of 0.42 ppb for the VEG50 scenario. This shows that albedo errors of a few percent are acceptable.

It is therefore concluded that the requirement MR-OBS-165 in **/CS MRD v1.2, 2013/** can be relaxed from 2% to 3% for the NIR band.

Biases due to surface albedo errors

Scenario: VEG50 (albedo: NIR:0.2 / SW1:0.1 / SW2:0.05)

Albedo error			XCO_2 error [ppm]		XCH_4 error [ppb]	
NIR	SWIR-1	SWIR-2	Bias	Precision	Bias	Precision
0%	0%	0%	-0.01	1.09	0.07	9.25
1%	0%	0%	0.02	1.09	0.18	9.25
2%	0%	0%	0.05	1.09	0.42	9.22
10%	0%	0%	0.56	1.10	2.13	9.29
0%	1%	0%	-0.03	0.86	-0.34	8.56
0%	2%	0%	-0.06	1.09	-0.39	9.24
0%	10%	0%	-0.24	1.09	-2.12	9.21
0%	0%	1%	-0.03	1.09	0.01	9.25
0%	0%	2%	-0.04	0.95	-0.17	8.91
0%	0%	10%	-0.15	1.09	-0.72	9.29

Table 20: Biases due to surface albedo errors.

10. Instrument Spectral Response Function (ISRF) – homogeneous scenes

An initial assessment of XCO_2 and XCH_4 errors due to errors of the Instrument Spectral Response Function (ISRF) for homogeneous scenes has been carried out in the framework of the predecessor study **/CS L1L2-I-Study FR/**. It has been shown using worst case assumptions that errors can be as large as about ~1 ppm for XCO_2 and ~5-10 ppb for XCH_4. It is however not clear how likely the worst case assumptions are and what the characteristics of the resulting XCO_2 and XCH_4 errors are. If the ISRF error would be constant, than it likely will be relatively easy to correct for this error to a significant extent. But even if the errors listed above are not constant and if they are a realistic estimate for peak-to-peak errors, this would mean that a 1-sigma error would very likely be 4 or more times smaller (assuming peak-to-peak corresponds to 4-sigma), i.e., ~0.2 ppm for XCO_2 and ~1-2 ppb for XCH_4, which is close to the errors listed **Table 1** for this error sources. Note that errors due to inhomogeneous scenes causing “Pseudo Noise” (PN) have to be excluded here as this aspect is covered separately (see **Sect. 9.6**). It is therefore concluded that the values listed in **Table 1** for this error source are good estimates.

11. Integrated energy (IE) and spatial under-/oversampling: impact on point source emission estimates (IUP-UB)

11.1. Introduction

The system energy distribution function (SEDF) describes the spatial sensitivity with respect to the observed ground scene (see **/CS MRD v1.2, 2013/** for exact definition). When the SEDF is not perfectly known this has consequences for the quantitative interpretation of the inferred XCO_2 and XCH_4 data.

This section deals with the impact of the SEDF shape and the insufficient knowledge thereof with respect to point source emission rate estimates using a Gaussian plume inversion approach as used in **/Krings et al., 2011, 2013/**. This method is not ideal to assess the impact of the SEDF shape or the spatial sampling distance (SSD) itself on the inversion result. If forward model and inversion use the same SEDF and SSD, there will be no bias in the inversion. However, under-/oversampling can impact the precision. This will be addressed in Sections 11.5 and 11.6.

11.2. Assessment method

To analyse the impact of an imperfectly known SEDF, CarbonSat retrieval results of XCO_2 in the vicinity of a coal fired power plant with yearly emissions of 24 $MtCO_2$ (similar to power plant Jänschwalde in eastern Germany) are simulated using various SEDFs. The simulated XCO_2 data is subsequently inverted using the Gaussian plume fitting techniques from **/Krings et al., 2011, 2013/** assuming a specific SEDF that differs from the one selected for simulating the data. The bias in emission rate estimate is then interpreted as systematic error based on the imperfectly known SEDF. Further atmospheric and geometric parameters for the simulation are wind speed (u = 4.5 m/s) and atmospheric stability (moderately unstable).

As base function for the SEDF a two dimensional centred generalized normal distribution has been chosen, which allows shapes with varying width and steepness:

$$SEDF = \left(\frac{\beta}{2\alpha\Gamma(1/\beta)}\right)^2 e^{-(|x|/\alpha)^\beta-(|y|/\alpha)^\beta}$$

with parameters β, α and the Gamma function Γ. The parameter β mainly controls the steepness of the flanks while α controls the width. The parameters x and y denote the horizontal distance from the centre point given in kilometres. While in this chapter and chapter 11.3 the SEDF is assumed symmetric, i.e. with the identical parameters α and β for along and across track direction as shown in the equation above, the parameters are set individually for the different directions in chapters 11.4, 11.5 and 11.6.

In a first approach the parameter α was chosen so that the FWHM equals 2 km. Cross sections (y = 0) of the associated SEDFs with varying parameter β are shown in **Figure 83**. The same functions as contour plot are shown in **Figure 84** with contour levels of 0.05, 0.1 and 0.2. Data simulated with these SEDFS were than inverted using a rectangular SEDF with FWHM of 2 km.

In a second approach the parameter α was varied so that the FWHM ranges between 1.6 km and 2.4 km (see **Figure 85** and **Figure 86**). The parameter β was held constant (β = 3). The associated simulated data were inverted using a generalized normal distribution with β = 3 and FWHM = 2 km. Varying the FWHM while still assuming a spatial sampling distance of 2 km also leads to an under-/oversampling effect.

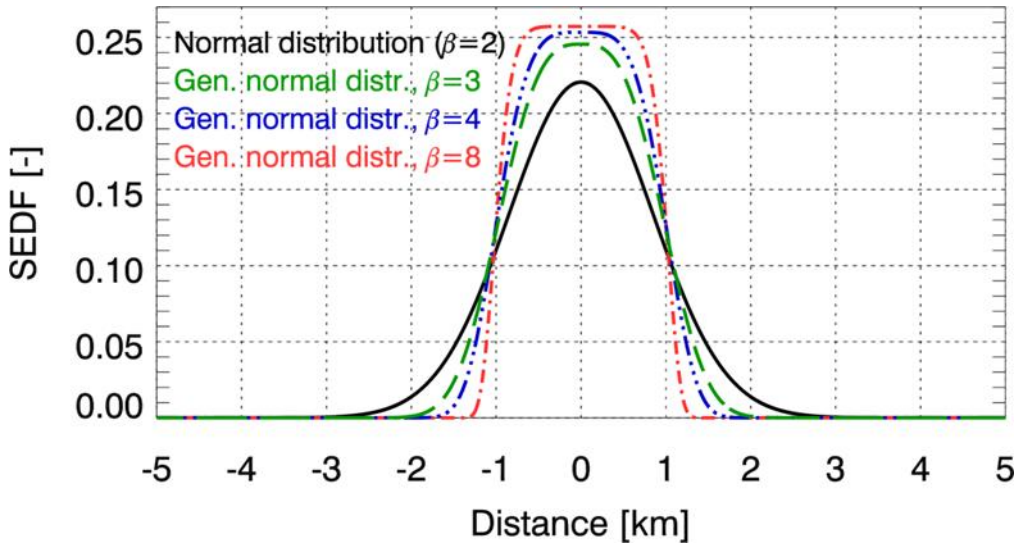

Figure 83: Cross section of the system energy distribution functions with varying parameter β and constant FWHM of 2 km.

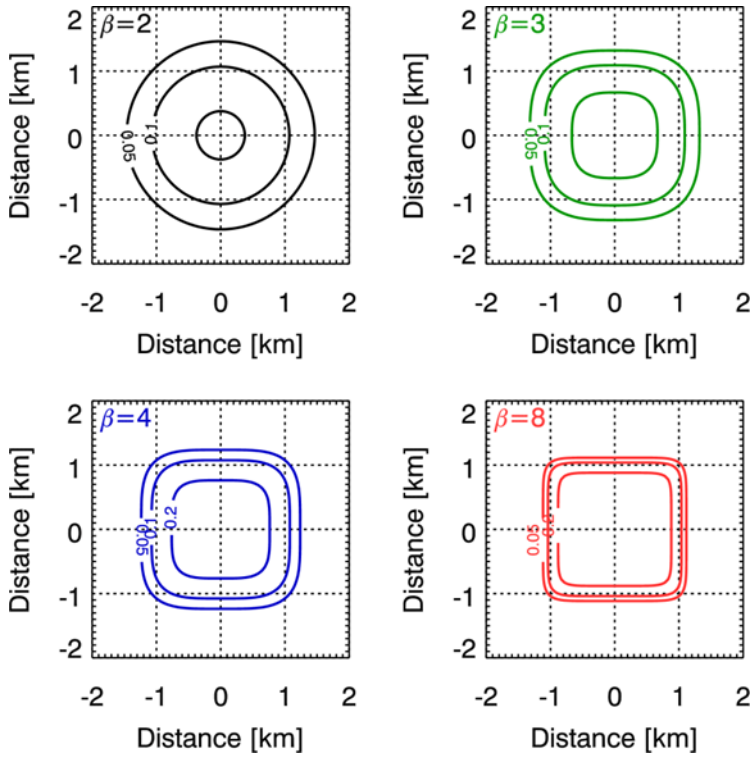

Figure 84: Contour plot of system energy distribution functions shown in **Figure 83**. Contour lines denote the 0.05, 0.1 and 0.2 levels.

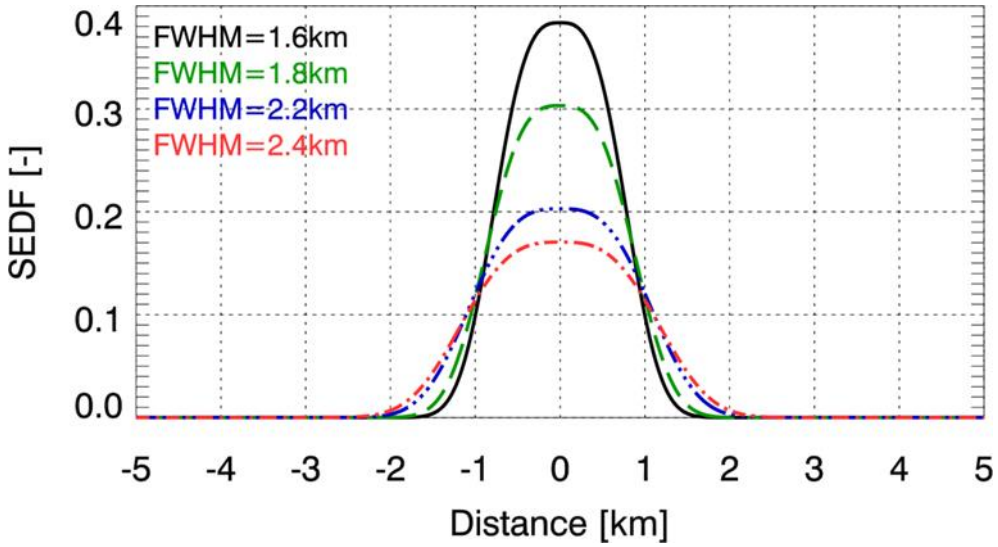

Figure 85: Cross section of the system energy distribution functions with varying parameter α so that the FWHM ranges between 1.6 km and 2.4 km. The parameter β was held constant (β = 3).

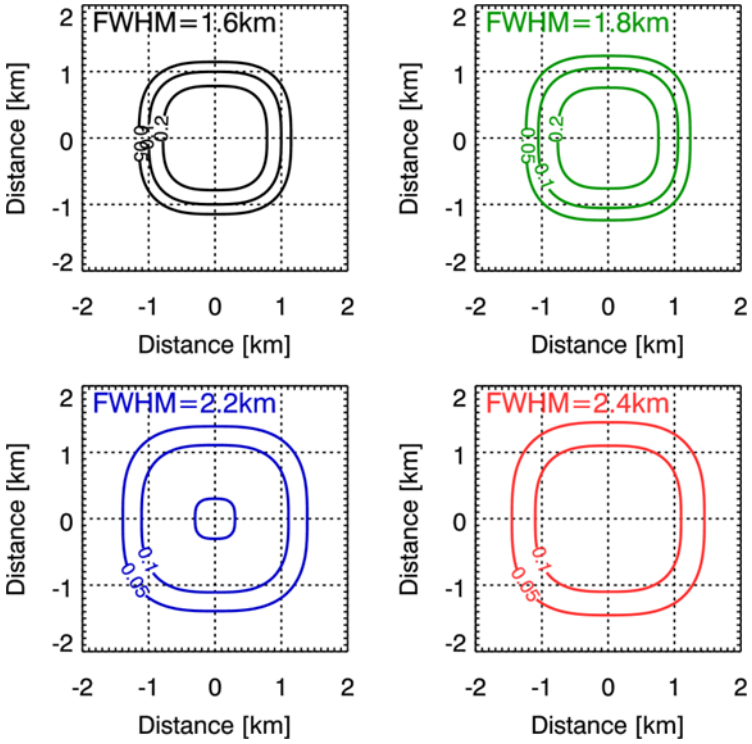

Figure 86: Contour plot of system energy distribution functions shown in **Figure 85**. Contour lines denote the 0.05, 0.1 and 0.2 levels.

11.3. Assessment results for impact of SEDF knowledge

The system integrated energy (SIE) of the system energy distribution functions with varying shape parameter β are shown in **Table 21** for 1.5 times, 2 times and 1 times the along and across track spatial resolution. In this case the spatial resolution was assumed to be 2 km x 2 km. Note that the actual spatial resolution as defined in ***/CS MRD v1.2, 2013/*** (70% of system integrated energy) slightly differs. The normal distribution with a FWHM of 2 km does not meet the requirement regarding the system integrated energy but is treated here for comparison.

Table 21: System integrated energy (SIE) for the system energy distribution functions with varying parameter **β**. The spatial resolution was assumed to be 2 km x 2 km.

System energy distribution function	SIE in 1.0 (along track) by 1.0 (across track) times the spatial resolution	SIE in 1.5 (along track) by 1.5 (across track) times the spatial resolution	SbIE in 2.0 (along track) by 2.0 (across track) times the spatial resolution
Normal distribution (β=2)	57.9%	85.1%	96.3%
Generalized normal distribution (β=3)	72.0%	96.7%	99.9%
Generalized normal distribution (β=4)	79.2%	99.5%	100%
Generalized normal distribution (β=8)	90.0%	100%	100%
Requirement	**Larger than 70%**	**Larger than 90%**	**Larger than 99%**

The simulated data for the various SEDFs are shown in **Figure 87**. The visual appearance of the CO_2 plume structure is very similar for all cases. Variations are better identified in the differences for observed ground scenes relative to simulated data using a rectangular SEDF as shown in **Figure 88**. The differences decrease with increasing parameter β because the SEDFs get closer to a rectangular shape. Maximum differences in XCO_2 are found for a normal distribution with less than 0.2%. For β = 8 differences are below 0.025%.

The inversion results of the simulated data using the varying SEDF but assuming for the analysis a rectangular SEDF with a FWHM of 2 km are shown in **Table 22**. The systematic errors are in the range of a few percent. Highest error in this comparison originates from the case with the normal distribution, which however does not meet the requirement for the system integrated energy.

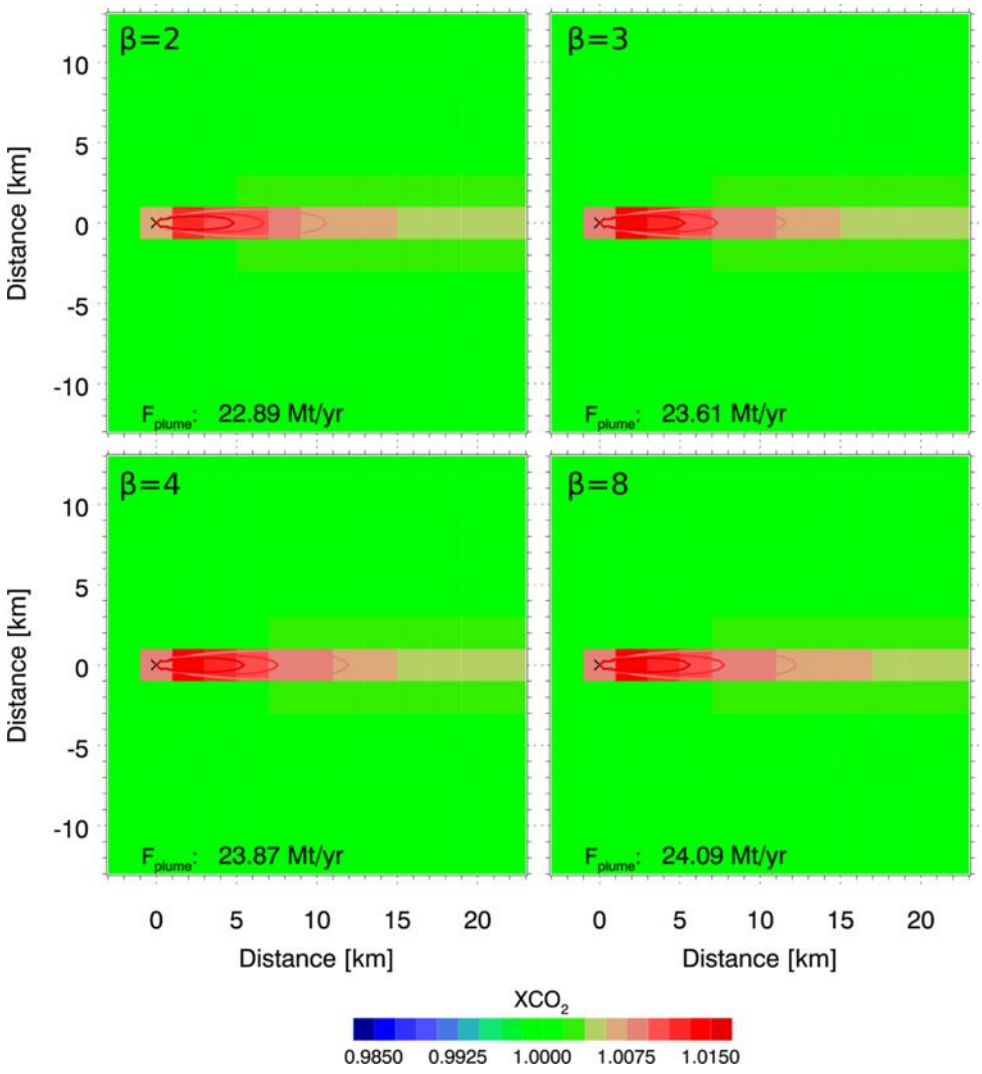

Figure 87: Simulated XCO_2 data based on SEDFs with varying parameter β. The absolute inversion results in $MtCO_2/yr$ are also given in the figures.

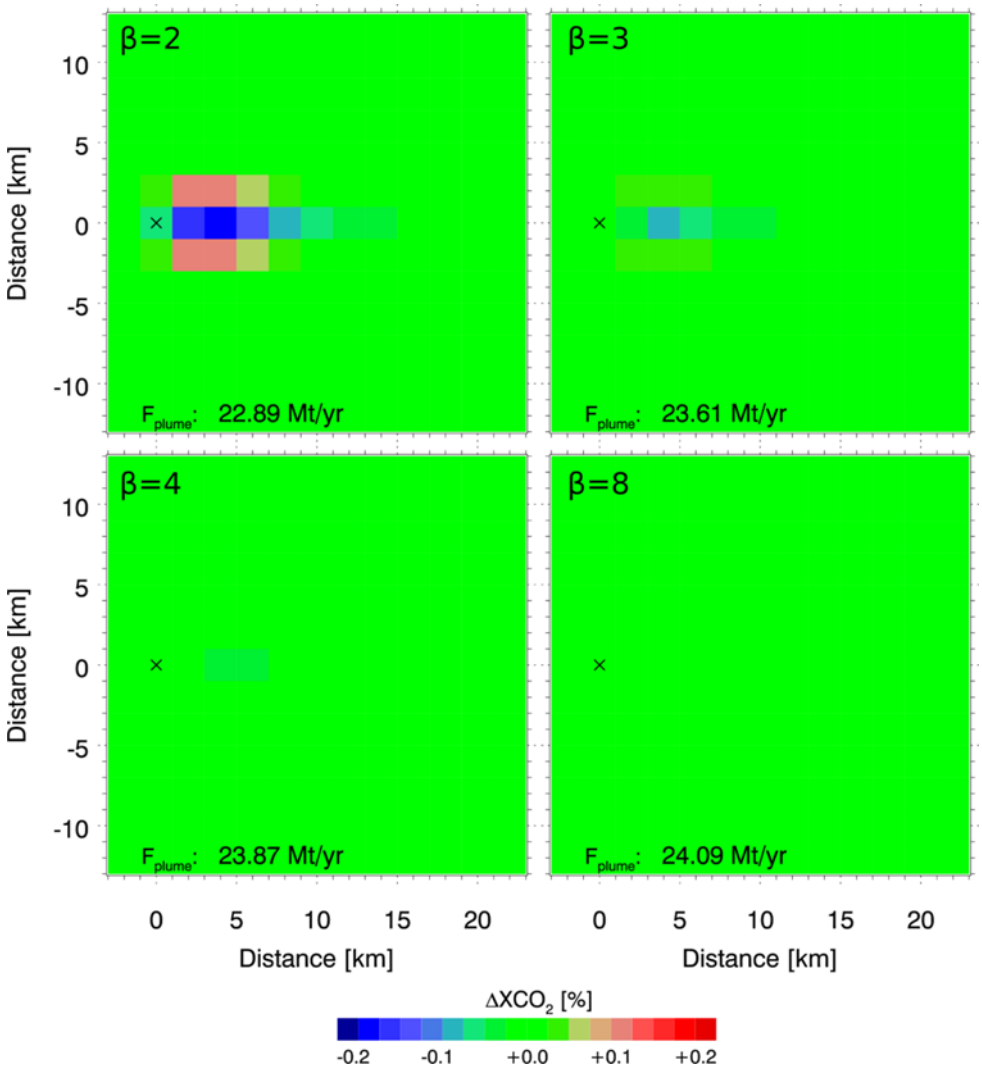

Figure 88: Differences of simulated data using SEDFs with varying parameter β relative to data simulated with a rectangular SEDF. The absolute inversion results are also shown.

Table 22: Inversion results for varying system energy distribution functions assuming in the analysis a rectangular SEDF.

System energy distribution function for simulation	Assumed system energy distribution function for inversion	Inversion bias
Normal distribution (β=2)	Rectangular	-4.6%
Generalized normal distribution (β=3)		-1.6%
Generalized normal distribution (β=4)		-0.5%
Generalized normal distribution (β=8)		+0.4%

In the second approach the FWHM of a SEDF with parameter β = 3 was varied from 1.6 km to 2.4 km. The system integrated energies of the SEDFs are shown in **Table 23**. The SEDF with FWHM = 2.4 km does not meet the SIE requirement. The simulated data shown as differences to the baseline SEDF with β = 3 and FWHM = 2.0 km is shown in **Figure 89**. Maximum differences are about ±0.25% for individual ground scene XCO_2 values.

When inverting the simulated data using the baseline SEDF (β = 3 and FWHM = 2.0 km) the resulting systematic bias of a few percent is similar to the variations of the first approach, except for the extreme cases of FWHM = 1.6 km and FWHM = 2.4 km. Note that the last one would not meet the requirement on the system integrated energy. When the shape function is perfectly known and used for simulation and inversion the systematic error is zero.

Table 23: System integrated energy (SIE) for the system energy distribution functions with varying FWHM. The parameter β was 3.

System energy disribution function (β=3)	SIE in 1.0 (along track) by 1.0 (across track) times the spatial resolution	SIE in 1.5 (along track) by 1.5 (across track) times the spatial resolution	SIE in 2.0 (along track) by 2.0 (across track) times the spatial resolution
FWHM = 1.6 km	88.6%	99.8%	100%
FWHM = 1.8 km	80.5%	98.8%	100%
FWHM = 2.0 km	72.0%	96.7%	100%
FWHM = 2.2 km	63.9%	93.2%	99.6%
FWHM = 2.4 km	56.5%	88.6%	98.8%
Requirement	**Larger than 70%**	**Larger than 90%**	**Larger than 99%**

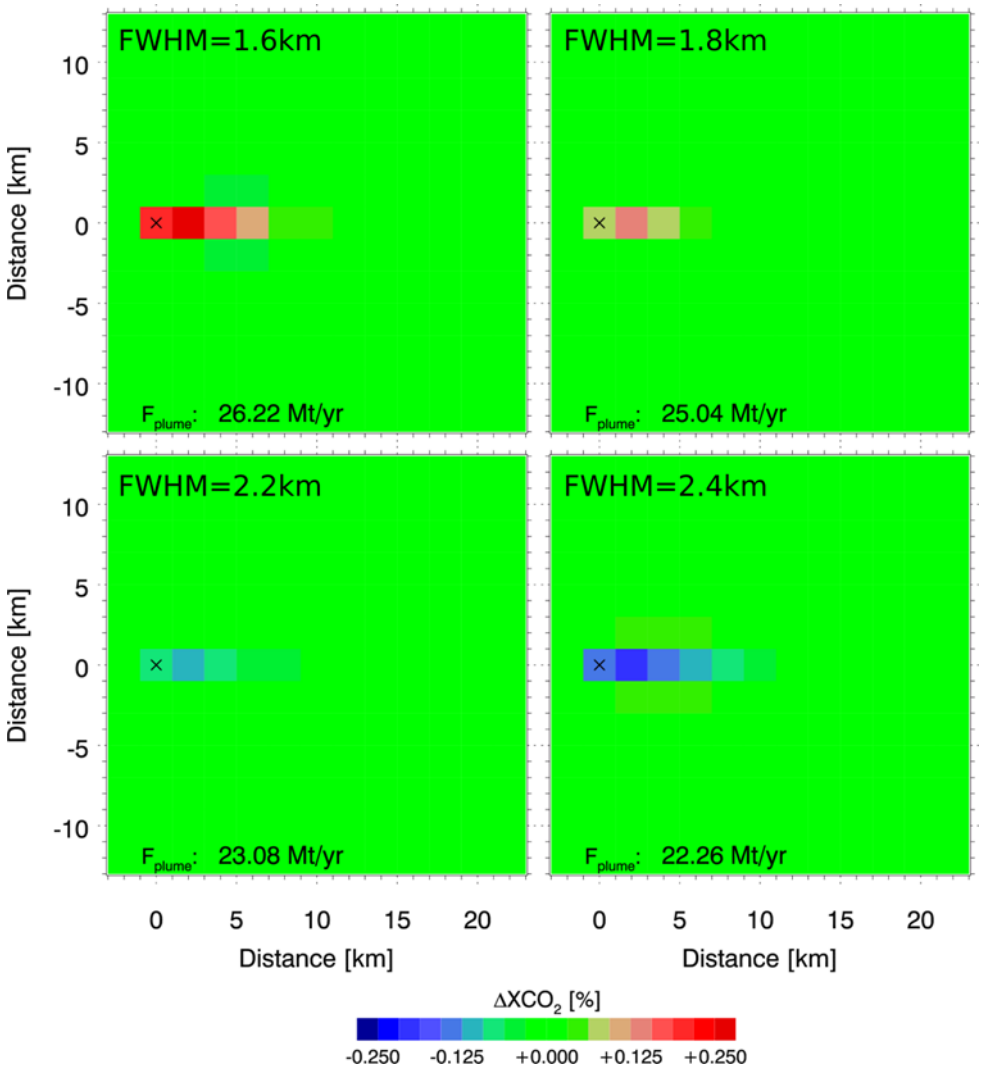

Figure 89: Differences of simulated data using SEDFs with varying FWHM relative to data simulated with a SEDF of FWHM = 2.0 km. In all cases the shape parameter β was set to 3. The absolute inversion results are also shown.

Table 24: Inversion results for varying system energy distribution functions assuming as SEDF in the analysis a generalized normal distribution with FWHM = 2 km and β = 3.

System energy distribution function for simulation (β=3)	Assumed system energy distribution function for inversion	Inversion bias
FWHM = 1.6 km	β = 3 FWHM = 2 km	+9.3%
FWHM = 1.8 km		+4.3%
FWHM = 2.0 km		+/- 0%
FWHM = 2.2 km		-3.8%
FWHM = 2.4 km		-7.3%

11.4. Assessment results for independently varied SEDF in along and across track direction

Similar to the more general approach in the previous chapter, the SEDF of the inversion model can be varied independently for along track (ALT) and across track (ACT) direction using as a starting point an SEDF that is an approximation of industry concept 1 (see Figure 90). Thereby the across track direction is parallel to the wind direction. For the along track direction (perpendicular to wind direction) the error is again in the order of a few percent, similar to before, while there is only very low sensitivity for SEDF knowledge errors in across track direction (parallel to wind direction).

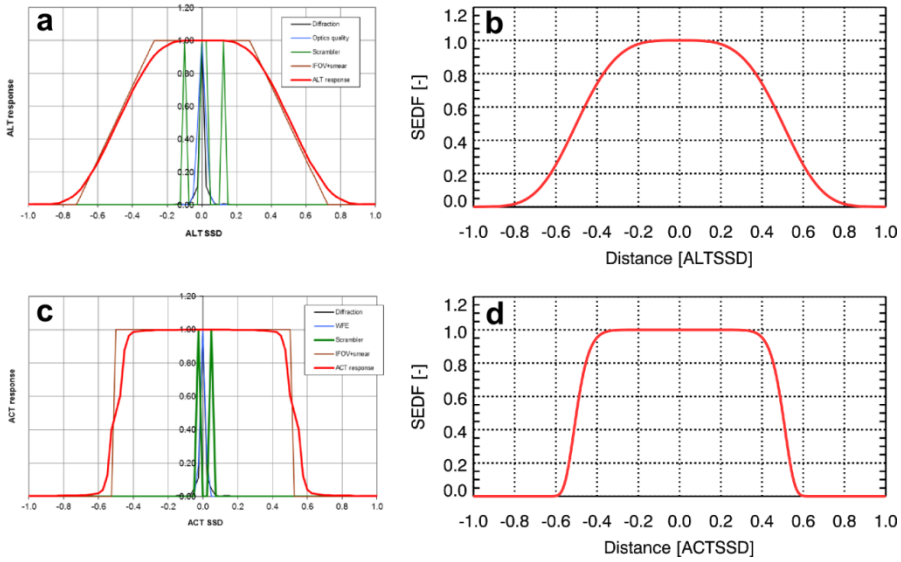

Figure 90: Comparison between the industry concept 1 for the SEDF in along track (a) and across track direction (c) with the adaptation in the simple model used here for along track (b) and across track direction (d). Thereby the SEDF was approximated using in along track direction a FWHM of 2km and β=3.75 and in across direction FWHM=3km and β=12. Hence the ground scene is non-square.

Table 25: Inversion bias for SEDF variations in along track (ALT, left) and across track (ACT, right). The shape parameters β (top) and FWHM (bottom) were modified independently. Here, the across track direction is parallel to wind direction.

ALT (perpendicular to wind)

Δβ	Inversion bias
-2.0	-4.9%
-1.0	-1.3%
+1.0	+0.6%
+2.0	+0.9%

ACT (parallel to wind)

Δβ	Inversion bias
-10.0	-0.6%
-8.0	-0.1%
-4.0	+/- 0.0%
+4.0	+/- 0.0%

ΔFWHM	Inversion bias
-300m	+5.9%
-200m	+3.7%
-100m	+1.8%
+100m	-1.7%
+200m	-3.2%
+300m	-4.6%

ΔFWHM	Inversion bias
-300m	+0.1%
-200m	+/-0.0%
-100m	+/-0.0%
+100m	+/-0.0%
+200m	+/-0.0%
+300m	-0.1%

11.5. Spatial sampling distance (SSD) and emission rate precision

While the spatial sampling distance itself does not introduce a bias in the inferred emission rate if applied consistently in the simulated data and the inversion, it can result in a modified precision.

As can be seen in **Figure 91**, enlarging the SSD can lead to an undersampling of the simulated CO_2 plume. Vice versa, when the SSD is reduced while the SEDF is constant, an oversampling can be introduced. Oversampling conditions will generally improve the precision while undersampling leads to a deteriorated precision due to less coverage of the area of interest.

Assuming an SEDF shape for along track and across track direction that matches closely the industry concept 1 (see **Sect. 11.4**) and assuming further the FWHM of 2 km x 3 km and a XCO_2 precision of 1 ppm (0.25%), the precisions for various SSDs are shown in **Table 26**. The precision for simulated data from single overpasses thereby varies about +/-2% around the mean of 11.6% when varying the SSD by +/-400 m in across track and along track direction.

Depending on the degree of undersampling, reduced coverage could also lead to missing smaller sources of CO_2 or CH_4, so that gapless measurements are more favourable.

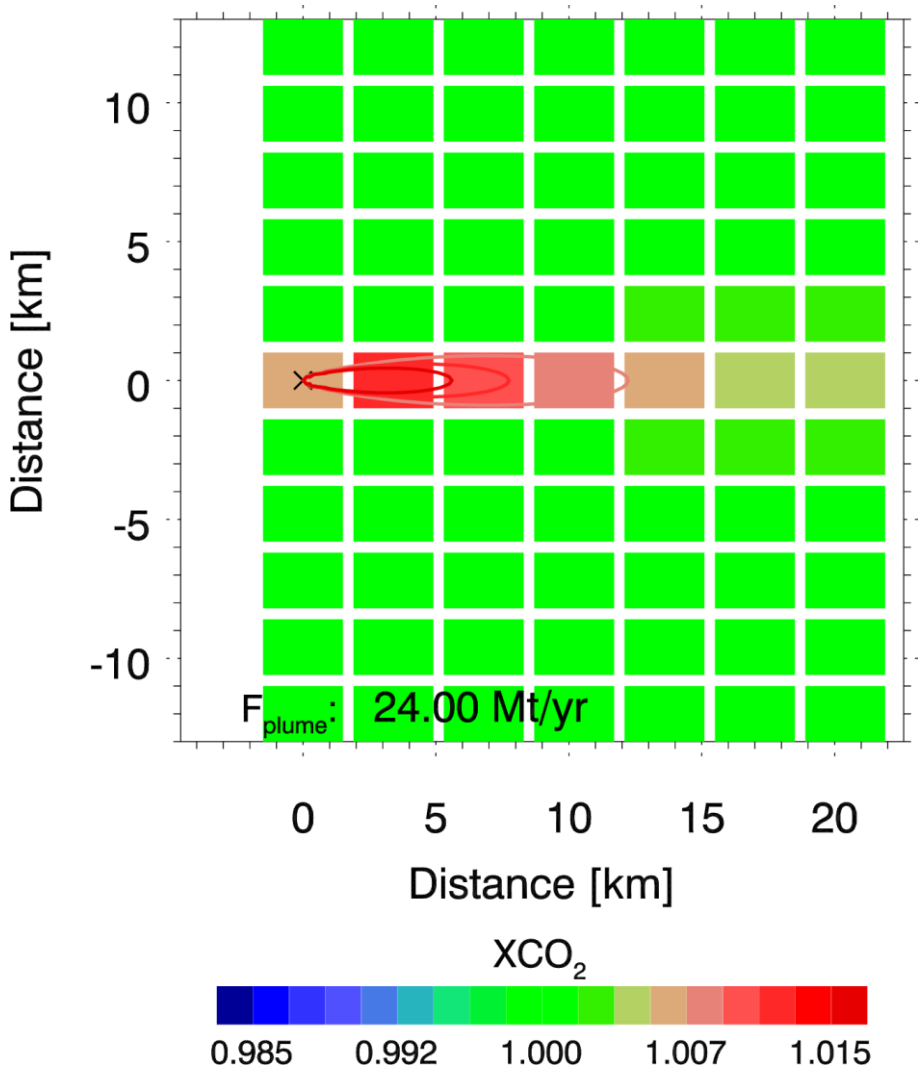

Figure 91: Simulated data with a spatial sampling distance (SSD) that does exceed the FWHM of the SEDF leading to an undersampling of the CO_2 plume.

Table 26: Inversion precision for varying SSD using simulated data from a single overpass.

Spatial sampling distance (ALT x ACT)	Emission rate precision
1.6 km x 2.6 km	9.8%
1.7 km x 2.7 km	10.2%
1.8 km x 2.8 km	10.8%
1.9 km x 2.9 km	11.2%
2.0 km x 3.0 km	11.6%
2.1 km x 3.1 km	12.3%
2.2 km x 3.2 km	12.7%
2.3 km x 3.3 km	13.1%
2.4 km x 3.4 km	13.4%

11.6. Spatial resolution and emission rate precision

Similar to the previous chapter, also the spatial resolution (defined by the 70% integrated energy level of the SEDF) can be varied while the SSD is kept constant at 2km x 3km (ALT x ACT). For this the parameter α of the generalized normal distribution was varied independently for the ALT and ACT directions which results in a modified spatial resolution and FWHM (see **Table 27**). The shape parameter β was held constant at 3.75 (ALT) and 12.0 (ACT) respectively as in the previous chapter approximating the industry concept 1.

Again, if assuming the knowledge of the SEDF as perfect, there is no systematic error that can be assessed with the present method. Only the impact on precision can be modelled.

By definition 70% of the system integrated energy originates from the pixel with dimensions given by the spatial resolution (SR). If for the given SEDF the spatial resolution equals, for example, 1.7 km x 2.7 km, then information originates to 70% from an area of 1.7 km x 2.7 km, to 85% from an area of 2. 0km x 3.0 km, to 95% from an area of 2.2 km x 3.3 km, and to 99% from an area of 3.0 km x 4.5 km.

Table 27: Parameters for the scenarios with varying spatial resolution (SR). The spatial sampling distance (SSD) was thereby constant at 2km x 3km (ALT x ACT) and the parameter β was 3.75 (ALT) and 12.0 (ACT) respectively.

ALT			ACT		
FWHM [km]	α [km]	SR [km]	FWHM [km]	α [km]	SR [km]
2.0	1.1025358	1.68	3.0	1.5463917	2.68
2.142	1.1812884	1.8	3.134	1.6156331	2.8
2.262	1.2469155	1.9	3.246	1.6733343	2.9
2.38	1.3125427	2.0	3.358	1.7310354	3.0
2.5	1.3781698	2.1	3.47	1.7887366	3.1
2.618	1.4437970	2.2	3.582	1.8464378	3.2
2.738	1.5094241	2.3	3.694	1.9041390	3.3

Table 28: Precision of the inverted emission rate for different spatial resolution but constant SSD.

Spatial resolution (ALT x ACT)	Precision of inversion result
1.7 km x 2.7 km	11.6%
1.8 km x 2.8 km	11.7%
1.9 km x 2.9 km	11.9%
2.0 km x 3.0 km	12.0%
2.1 km x 3.1 km	12.1%
2.2 km x 3.2 km	12.2%
2.3 km x 3.3 km	12.3%

The results for the precision of the inverted emission rate using the plume model inversion are listed in **Table 28**. Generally, there appears to be a rather low dependence of the inversion precision with respect to the spatial resolution within the investigated range from 1.7km x 2.7km to 2.3km x 3.3km.

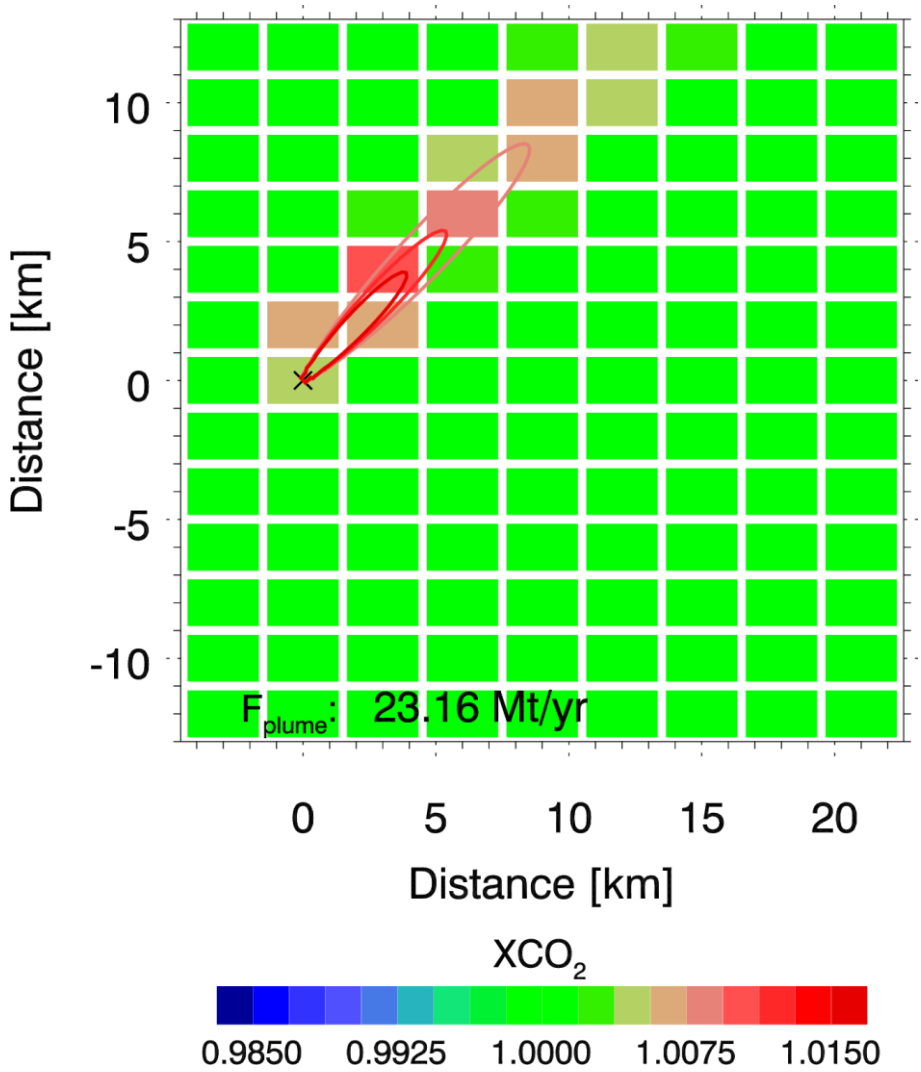

Figure 92: Simulated data with a spatial resolution (SR) that is smaller than the spatial sampling distance (SSD). In addition, the source location for the simulation was moved 400m in positive y-direction, while for the inversion the source location was assumed at the coordinate origin. This leads to a bias that is dependent on the spatial resolution.

In a different scenario, the source location was assumed to be wrong by 400m accounting for example representing a geolocation error. For the simulation, the source location was shifted by 400m in positive y-direction from the origin of the coordinate system, while for the inversion the source was still assumed to be located at the centre of the coordinate system. Furthermore the wind direction was assumed to be 45° relative to the y-direction (ALT direction) compared to 90° as in the other scenarios (see **Figure 92**).

This results in a bias for the emission rate estimate that additionally to the precision is listed in **Table 29**. In this scenario, the precision is hardly influenced by the spatial resolution. However, as can be expected the bias decreases with larger spatial resolution, when the exact source location becomes less relevant.

Table 29: Random and systematic error for the emission rate estimate assuming different spatial resolution and a source location that is wrong by 400m (e.g. due to a geolocation error).

Spatial resolution (ALT x ACT)	Precision of inversion result	Bias of inversion result
1.7 km x 2.7 km	12.0%	-3.5%
1.8 km x 2.8 km	12.0%	-2.9%
1.9 km x 2.9 km	11.9%	-2.5%
2.0 km x 3.0 km	12.0%	-2.2%
2.1 km x 3.1 km	12.0%	-2.0%
2.2 km x 3.2 km	12.0%	-1.9%
2.3 km x 3.3 km	12.0%	-1.9%

11.7. Summary and conclusions

The instrument sensitivity within a single ground scene is described by the system energy distribution function (SEDF). For point sources of CO_2 or CH_4, imperfect knowledge of the SEDF can lead to systematic biases in the inferred emission rate.

To assess the impact on plume inversion methods as used in **/Krings et al., 2011, 2013/** CarbonSat data was simulated using different SEDFs varying in shape and width. The FWHM was varied between 1.6 km and 2.4 km using a generalized normal distribution function, which was also varied in shape by modifying the shape parameter β. The simulated data were then inverted to emission rates using a fixed SEDF that did not agree with the SEDF which was used to simulate the data. This method aims at assessing the error due to insufficient knowledge of the SEDF (not on the actual shape or FWHM).

The systematic biases in the emission rate estimate resulting from this mismatch between actual and assumed SEDF were generally in the order of a few percent. The better known the SEDF is, the lower the systematic error will be. Assuming that the error on the FWHM will likely be below 5% the integrated energy impact will not drive the error budget for the flux inversion.

Also the choice of the spatial sampling distance (SSD) was investigated by assessing the impact on the precision of the inferred emission rate. When varying the SSD by +/-400 m from the FWHM of the SEDF, the precision varies by about +/-2% around a mean of 11.6% for a FWHM of (2 km x 3 km). Since the simulation and inversion model are consistent (i.e. the knowledge on SR, SSD, SEDF, etc. is assumed to be perfect), there is no resulting bias on the estimated emissions.

Furthermore, the spatial resolution (SR) was varied while the SSD was kept constant. Depending on the investigated scenario the precision may slightly improve with smaller ground pixels. The impact of a geolocation error reduces with increasing pixel size for the analysed spatial resolutions of 1.7 km x 2.7 km to 2.3 km x 3.3 km.

It has to be noted, that these assessments were performed under idealized conditions only taking into account the Gaussian plume model inversion. For example the geolocation error is significantly less relevant for a mass budget approach which can also be applied to CarbonSat data (demonstrated for MAMAP airborne data by **/Krings et al., 2011, 2013/** and for SCIAMACHY data by **/Schneising et al., 2014b/**).

12. Spatial co-registration (SRON)

Focus: Assessment of the requirement for spatial co-registration elevation effects

12.1. Requirements and assessment approach

For the CarbonSat mission, the requirement on spatial co-registration between the different bands of the spectrometer (inter-band co-registration) is formulated as follows (**/CS MRD v1.2, 2013/**):

MR- OBS-060	The spatial co-registration between all channels of the NIR and SWIR-1 bands shall be equal to or better than 0.1 (G) / 0.15 (T) times the spatial resolution in nadir mode. The spatial co-registration between all channels of the NIR and SWIR-2 bands shall be equal to or better than 0.1 (G) / 0.15 (T) times the spatial resolution in nadir mode. The spatial co-registration between all channels of the SWIR-1 and SWIR-2 bands shall be equal to or better than 0.2 (G) / 0.3 (T) times the spatial resolution in nadir mode. NB spatial mis-registration shall be interpreted as a combination of along- and across-track directions.

Spatial co-registration is defined as maximum equivalent ground distance between the centres of a pair of spatial samples acquired in two spectral bands and related to the same target on Earth. The stringent co-registration requirement is motivated by corresponding requirements on the CO_2 and CH_4 level-2 product as stated in **/CS MRD v1.2, 2013/**. Overall, for temporal and spatial co-registration a maximum CO_2 and CH_4 error of 0.5 ppm (~0.1 %) and 2 ppb (~0.1 %) is assigned in the total error budget (see **Section 4**).

In the previous CarbonSat requirement support study **/CS L1L2-I-Study FR/**, we identified two main sources for co-registration error due to the spatial heterogeneity of the observed scene:

- Spatial variability of cirrus optical properties
- Spatial variability of surface elevation

The presence of optically thin cirrus clouds affects the accuracy of the retrieved greenhouse gas columns for spatial mis-registration between different spectral bands. In this case, the cirrus coverage varies between different spectral bands of the instrument if they are misaligned. For this situation, no physical model of cirrus scattering can be developed which describes the observed spectral variation of cirrus properties. In the previous study **/CS L1L2-I-Study FR/**, we estimated that

mis-registration has to be 10% or smaller to keep the maximum CH_4 and CO_2 retrieval error below 0.1%. [1] The study thus supports the present MRD.

In case of spatially varying surface elevation, different spectral bands probe a different amount of air mass. Because the exact pointing of the instrument on the spatial scale of the co-registration requirements cannot be provided (the geolocation knowledge threshold requirement is < 400 m **/CS MRD v1.2, 2013/**, see MR-OBS-040), this effect cannot be accounted for in the retrieval and has to be considered as a potential contribution to the CarbonSat CO_2 and CH_4 error budget.

The aim of this study is to quantify this effect using simulated measurements. For this purpose, we consider a region over China for which sub-pixel information on elevation is required. This information is inferred from the SRTM3 data set (SRTM = Shuttle Radar Topography Mission), which contains global coverage from 56 degrees south latitude to 60 degrees north latitude in 1 degree by 1 degree blocks with an approximate resolution of 90 meters by 90 meters.

12.2. The China ensemble

To test the CH_4 and CO_2 retrieval performance, we consider measurement simulations over China which a distinct variation in surface height. Because of the focus of this study on elevation variability, we consider a constant model atmosphere bounded below by a varying surface height inferred from the SRTM3 data set.
The Shuttle Radar Topography Mission (SRTM) is an international research effort to generate the most complete high-resolution digital topographic database of Earth prior to the release of the ASTER GDEM in 2009. SRTM consisted of a specially modified radar system that flew on board the Space Shuttle Endeavour during the 11-day STS-99 mission in February 2000, based on the older Spaceborne Imaging Radar-C/X-band Synthetic Aperture Radar (SIR-C/X-SAR), previously used on the Shuttle in 1994. The data are slightly biased with the canopy height of the observed scene due to the sensitivity of the used sensors. However, for the purpose of this study this shortcoming of the data set can be considered even as an advantage because of similar sensitivity of the CarbonSat sensor.

Figure 93 shows the mean surface elevation over China averaged over a 2x2 km^2 pixel size. It illustrates the dataset with a diverse topography going from sea surface level up to 4500 m above sea level with a lot of small-scale variations. **Figure 94** shows the corresponding surface elevation variation within each ground pixel, represented by the standard deviation of the SRTM3 data. Here, values can exceed 200 m for rough terrain. With the employed data set, we can consider also the effect

[1] This error of 0.1% relates to **Table 1** of this document (error budget). The listed errors of 0.5 ppm and 2 ppb for XCO_2 and XCH_4 both reflect a 0.1% error.

of a spatial pixel displacement on the mean surface elevation. **Figure 95** presents the different in the mean surface elevation due to a western displacement of the scene by 200 m.

Comparing **Figure 94** and **Figure 95**, we see that for flat terrain indicated by small variation of the internal elevation a displacement of the pixel changes only marginally the mean elevation, as expected. This correlations suggests to use the pixel internal surface elevation as a data quality filter to mitigate CO_2 and CH_4 errors due to spatial co-registration errors. To visualize this effect for the entire ensemble, we consider the probability density function (PDF) of the difference in the mean surface height due to the pixel displacement. The PDF for non-filtered data shows clear wings, which indicates that for a significant number of pixels, the mean surface height changes with more than 5 m because of the displacement. Applying a data filter based on the pixel internal variation of surface elevation reduces the wings considerably.[2] Filtering on the standard deviation of the internal pixel variation <40 m removes all contribution with a mean surface elevation > 10 m, whereas for a more strict filter with a standard deviation <20 m the mean surface elevation changes by less than 5 m due to the pixel displacement. This illustrates clearly the use of the filter to mitigate errors due to spatial mis-registration of the different CarbonSat bands. Later, we will show the filter effect on CH_4 and CO_2 retrievals.

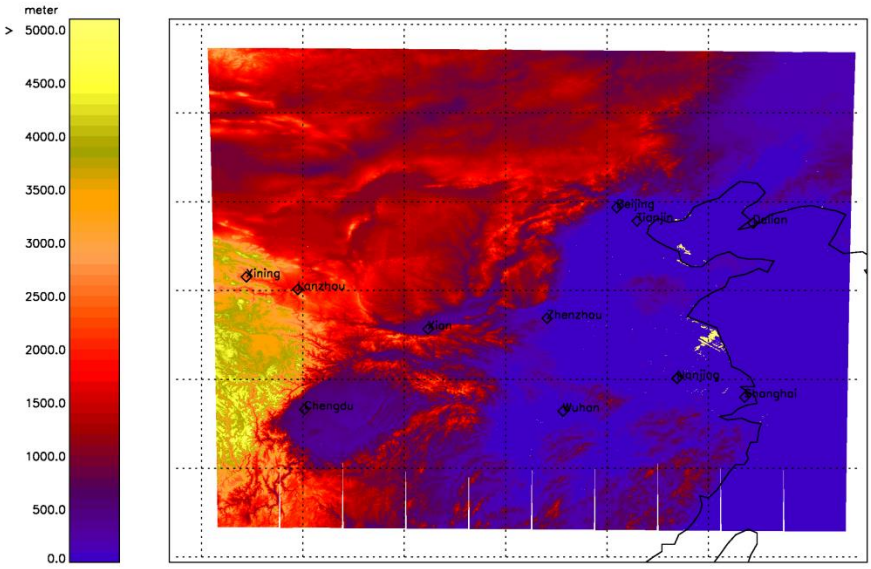

Figure 93: SRTM3 surface elevation averaged on CarbonSat nadir sub-satellite pixels with a pixel size of approximated 2 x 2 km^2 pixel size. The scale is about 3500 x 2000 km.

[2] This is standard practice. (See e.g. Detmers, R, et al., (2014), ESA Climate Change Initiative (CCI) Product User Guide (PUG) for the RemoTeC XCH4 Full Physics GOSAT Data Products for the Essential Climate Variable (ECV), Greenhouse Gases (GHG), Version 2)

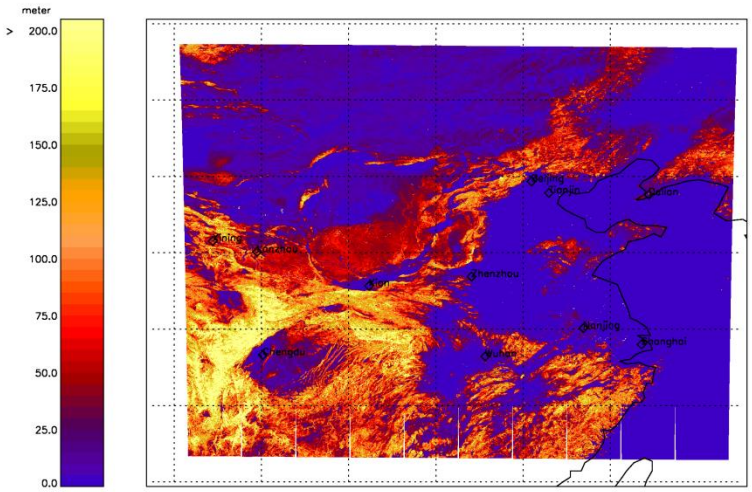

Figure 94: Standard deviation of the pixel internal elevation.

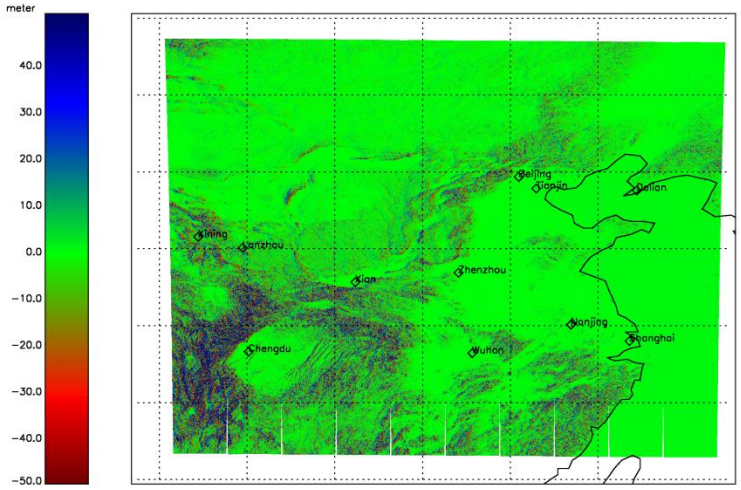

Figure 95: Mean elevation difference due to a longitudinal pixel displacement by 200 m.

Finally, we consider the effect of different directions of the displacement. **Figure 108** shows that the PDF for the difference in mean surface height changes only little for different direction of the displacement. Thus on spatial scales of the entire data ensemble, it is sufficient to consider displacement on one direction only, which eases the data analysis significantly.

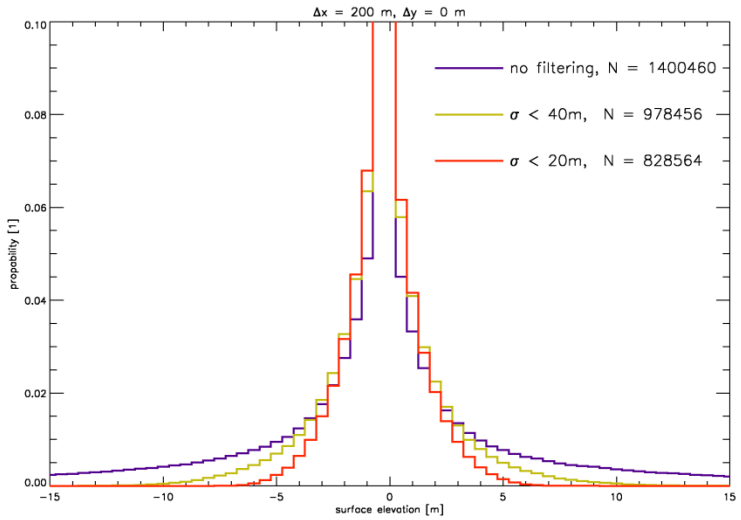

Figure 96: Surface elevation PDF for a longitudinal displacement of Δx=+200 m using different filters for the internal pixel variation. The blue line indicates the non-filters dataset, the orange and red line represents the effect of a filtering for the pixel internal elevation differences with a standard deviation σ<20m and <40m, respectively.

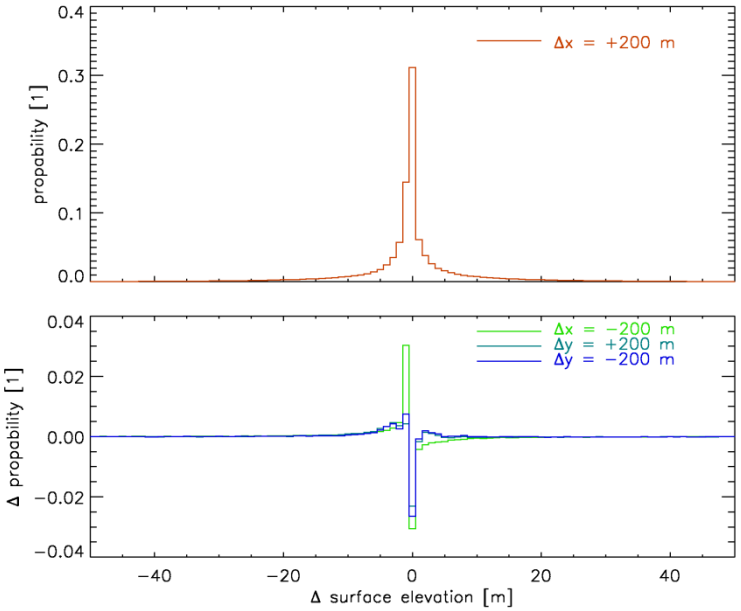

Figure 97: Probability density function (PDF) for a longitudinal pixel displacement of Δx=+200m (upper panel) and PDF differences for longitudinal displacement Δx=-200m and latitudinal displacements Δy=±200m.

12.3. RemoTeC simulations for (extra) retrieval errors due to elevation co-registration errors.

To estimate the retrieval error due to the difference in surface elevation Δz_{surf} seen by the CarbonSat spectral bands, CarbonSat measurements could be simulated with different surface heights for the different spectral band for any specific data point. Considering all potential co-registration errors and the number of data points, this would result in a huge amount of simulations. We therefore investigated the retrieval error in CO_2 and CH_4 column density as a function of Δz_{surf} for a few generic scenarios and subsequently projected it to the spatial distribution of surface elevation. For this purpose, we generated synthetic CarbonSat spectra with specified values of Δz_{surf} due to spatial mis-registration per retrieval window.

We calculated synthetic CarbonSat spectra for the instrument settings stated in **Table 30**. This calculation required input for aerosol properties, surface albedo, and SZA. Here we use a horizontally homogenous aerosol layer covering the entire scene with an optical thickness of 0.1, situated either at 500 or 8000 m altitude, an albedo of 0.05 and a SZA of 30°.

Band	**O_2 A**	**SWIR-1a**	**SWIR-1b**	**SWIR-2**
Spectral range [cm^{-1}]	**12920 – 13195**	**6170 – 6277.5**	**6045 – 6138**	**4806 – 4896**
Spectral range [nm]	**758.9-774.0**	**1593.0-1620.8**	**1629.2-1654.3**	**2042.5-2080.7**
Spectral resolution FWHM [cm^{-1}]	1.7	1.1	1.1	1.3

Table 30: Assumed CarbonSat observation windows for the simulations presented in this chapter.

We simulated the retrievals for differences in surface elevation seen by the CarbonSat spectral bands for -100 m to +100 m. Both CO_2 and CH_4 are fairly well mixed throughout the Troposphere (roughly CO_2 at about 400 ppm, CH_4 at about 2000 ppb.), so this yields - order of magnitude - about 1% column difference for each 100 m elevation difference. (It was of course calculated much more precisely, based on the exact modelled atmosphere). We assumed that the SWIR-1a and SWIR-1b were always perfectly aligned to each other, and treated them as one single band. The results of these simulations showed a more or less linear relation between Δz_{surf} and the extra retrieval errors for CH_4 and CO_2 due to elevation co-registration errors of the different bands. We therefore parameterized these relations as linear functions. The corresponding slopes are listed in **Table 31** and **Table 32** for the situations where the aerosol layer is situated at 500 m and 8000 m respectively.

Affected Band	**O_2 A**	**SWIR-1**	**SWIR-2**
Extra retrieval error for CH_4 due to Δz_{surf} in [% / m]	0.012	-0.013	0.00026
Extra retrieval error for CO_2 due to Δz_{surf} in [% / m]	0.017	-0.0061	-0.0096

Table 31: Extra retrieval errors in [%] per Δ-elevation [m] (aerosol layer situated at 500 m).

Affected Band	**O_2 A**	**SWIR-1**	**SWIR-2**
Extra retrieval error for CH_4 due to Δz_{surf} in [% / m]	0.011	-0.019	0.010
Extra retrieval error for CO_2 due to Δz_{surf} in [% / m]	0.018	-0.020	-0.0078

Table 32: Extra retrieval errors in [%] per Δ-elevation [m] (aerosol layer situated at 8000 m).

12.4. The RemoTeC simulations related to the China Ensemble

The extra retrieval errors per Δz_{surf} (as listed in **Table 31** and **Table 32**) were related to the China ensemble by combining them with the China surface elevation PDFs for longitudinal displacement of Δx=+100 m, Δx=+200 m, Δx=+300 m ,and Δx=+400 m (see

Figure 96 for the 200 m case). This yielded China Ensemble PDFs for the extra retrieval errors due to elevation co-registration errors, for several spatial mis-alignements of the different spectral bands. Furthermore different filters were applied based on the internal pixel variation. In **Figure 98** and **Figure 99** the results are shown for a longitudinal displacement of 200 m (which amounts to 10% of the 2 km footprint of the instrument) and for the aerosol layer situated at 500 m and 8000 m respectively.

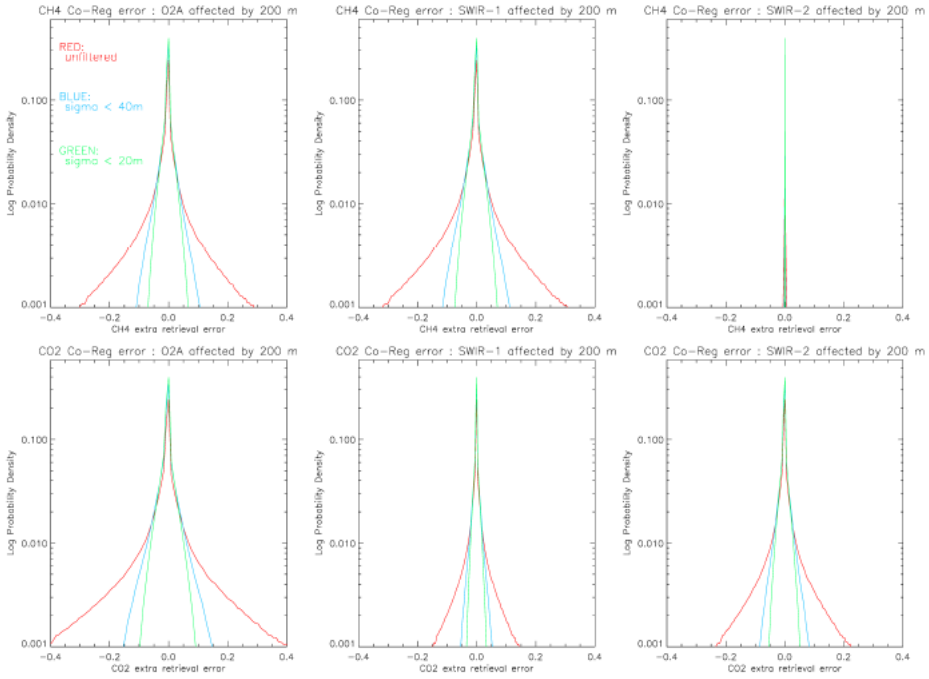

Figure 98*: Probability density functions (PDFs) of the extra retrieval errors (in [%]) for a longitudinal pixel displacement of Δx=+200m in the China Ensemble (please note the logarithmic scale). Here the aerosol layer is situated at 500 m. From left to right the panels show the results for different affected bands (O2A, SWIR-1, and SWIR-2). Top row:* **CH_4,** *bottom row:* **CO_2**. *The red line represents the non-filtered dataset, the blue and green lines represent the effect of a filtering for the pixel internal elevation differences with a standard deviation σ<20m and <40m, respectively.*

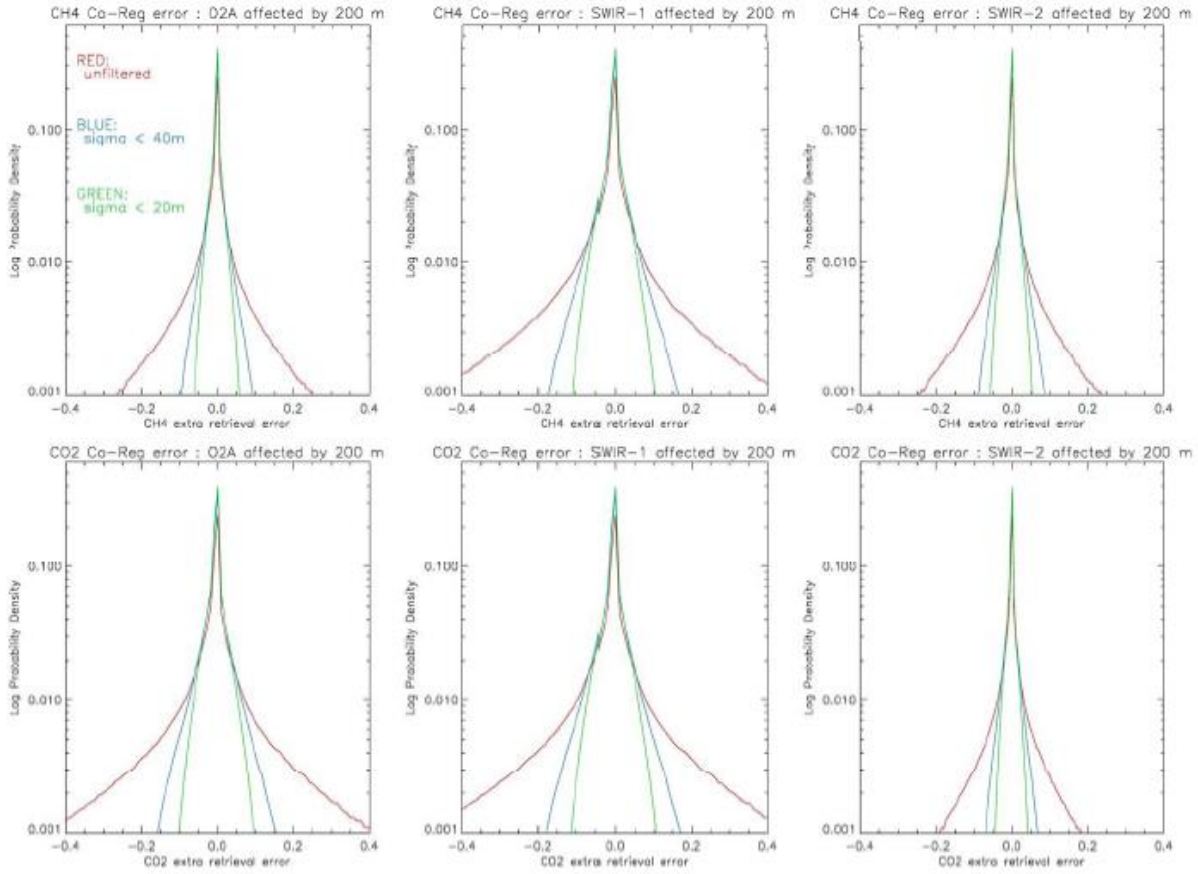

Figure 99: Probability density functions (PDFs) of the extra retrieval errors (in [%]) for a longitudinal pixel displacement of Δx=+200m in the China Ensemble (please note the logarithmic scale). Here the aerosol layer is situated at 8000 m. From left to right the panels show the results for different affected bands (O2A, SWIR-1, and SWIR-2). Top row: **CH_4**, bottom row: **CO_2**. The red line represents the non-filtered dataset, the blue and green lines represent the effect of a filtering for the pixel internal elevation differences with a standard deviation σ<20m and <40m, respectively.

In **Figure 98** and **Figure 99** the PDFs of the extra retrieval errors were shown for a longitudinal displacement of 200 m of the pixels in the China ensemble. As mentioned, simulations were also done for displacements of 100, 300, and 400 m. Each of the resulting PDFs can to a certain extend be characterized by calculating the mean absolute value of the percentage error. In Figure 8 these mean errors are plotted as a function of longitudinal displacement for the unfiltered case (corresponding to the red curves in **Figure 98** and **Figure 99**).

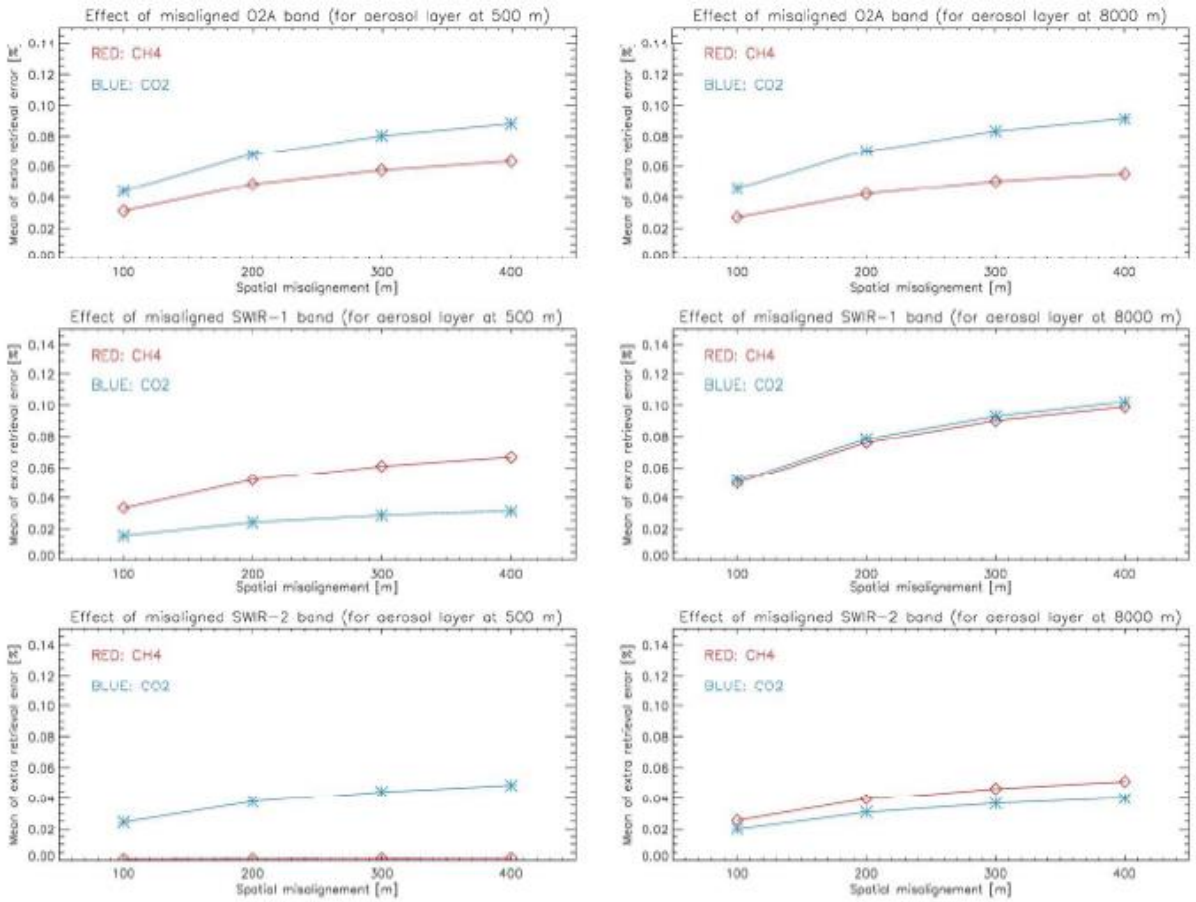

Figure 100: The mean absolute value of the extra retrieval error (in [%]) for the China ensemble as a function of the spatial mis-alignement. No filtering was applied to the dataset. The left panels give the results for an aerosol layer situated at 500 m, the right panels for an aerosol layer at 8000 m. The three rows of panels represent a mis-alignened O2A band, a mis-alignened SWIR-1 band and a mis-alignened SWIR-2 band respectively. The red lines show the extra errors in the CH_4 retrieval, the blue lines those for CO_2.

12.5. CO_2 emission plume detection of a coal power plant

In this section, we study the effect of spatial mis-registration on the detection of an exhaust CO_2 plume of a typical coal powerplant, where we relate the corresponding retrieval error to the total expected retrieval error budget of the CarbonSat column measurements. For this purpose, we first evaluate the roughness of the terrain at 33 coal plants in China looking at the change of the mean elevation height of a CarbonSat ground pixel due to lateral shift of 200m. Based on the analysis shown in **Figure 101***, we* selected *Gung'an* (30°31′41″N, 106°49′34″E) as a typical example of a coal power plant, which adjoins two mountain ridges in the East. To simulate enhanced CO_2 column concentrations due the emission of the power station, we apply the plume model of **/Krings et al. 2011/**. We assumed a background CO_2 column of 6.0 [$kgCO_2$ / m^2] and - for easy comparison - a CO_2 emission flux of 1.5e6 [g/s], which is indicative of a 1 GW powerplant. (In reality the Guang'an power plant has a capacity of approximately 2.4 GW). We assumed a wind speed of 4 [m/s] and an atmospheric stability factor of 200.

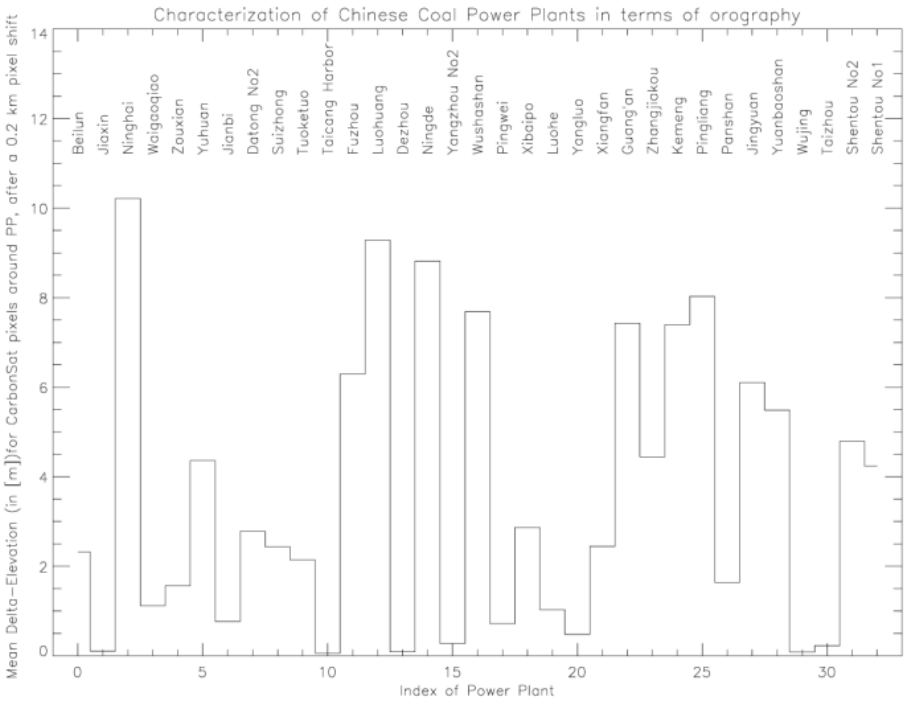

Figure 101: A characterization of 33 Chinese coal power plants by the orography of their surroundings. The y-axis indicates the mean difference in elevation [m] of a CarbonSat pixel [2 x 2 km] when it is shifted 200 m westward.

Figure 102 shows the CO_2 field sampled on a 2x2 km^2 CarbonSat pixel size. The panel represents an area of 25 x 10 pixels, or about 50 x 20 km^2.

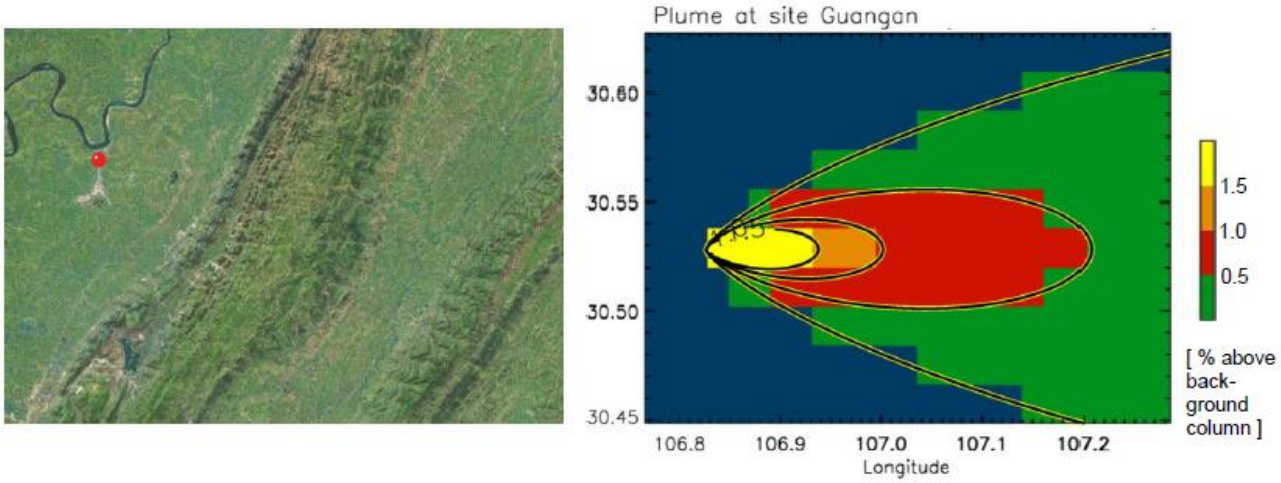

Figure 102: Left panel: Relief around Guang'an, China (30°31′41″N, 106°49′34″E) Right panel: CO_2 total column density field sampled on 2x2 km^2 CarbonSat ground pixels in the area near 1 GW coal powerplant (Guang'an), for a wind speed of 4 [m/s], and an atmospheric stability factor of 200. For illustration purposes, the contours of the modelled plume are superimposed on the CarbonSat pixels (see also the plume model of **/Krings et al. 2011/**).

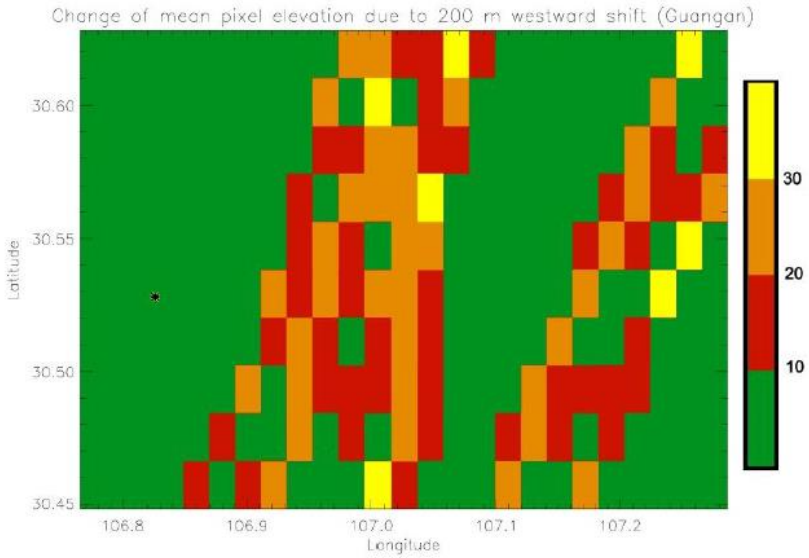

Figure 103: The change of the mean CarbonSat pixel elevation [m] due to a westward shift of these pixels of 200 m. The spatial domain is the same as in **Figure 102**.

Our analysis contains three steps: First we look at the effect of the *mean* elevation per pixel when the pixel is shifted 200 m westward, simulating a co-registration error effect. Second, we relate this co-registration elevation effect to the resulting extra retrieval error. Finally we relate this resulting extra retrieval error to the CarbonSat CO_2 measurement of the presence of a plume, thus giving an indication of how these local effects may influence the plume detection.

The co-registation error analysis of the plume simulation is presented in **Figure 104**. It shows the change of mean CarbonSat pixel elevation due to a westward shift of 200 m. The absolute difference in mean elevation ranges from 0 m up to more than 20 m (orange pixels), and in some extreme cases exceeds 30 m (yellow pixels). The location of the power plant itself is indicated by the black spot in the West of the area.

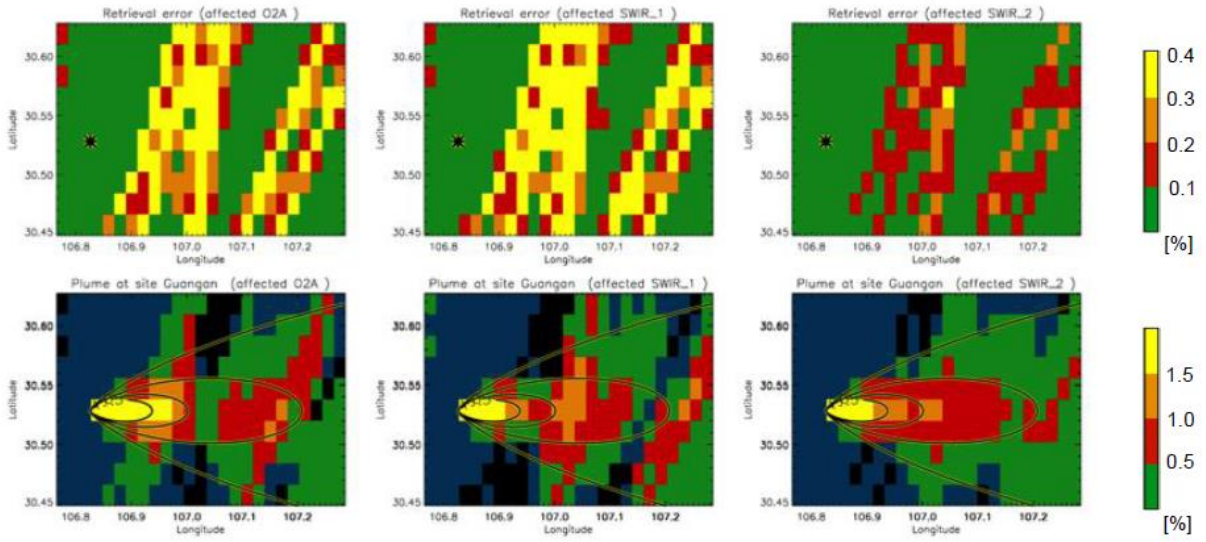

Figure 104: The top panels show the (simulated) influence of a spatial coregistration elevation error on the extra CarbonSat CO_2 retrieval error in the area near 1 GW coal powerplant (Guang'an, indicated by the black dot). The second row panels show the retrieved column values, expressed as a percentual deviation of the background value, assuming that a plume is present and that the spatial coregistration elevation error is the only source of retrieval. For illustration purposes, the contours of the modelled plume are superimposed on the CarbonSat pixels. The panels represent the same area as in **Figure 102**.

The first row panels of **Figure 104** show the orography effect on the extra CO_2 retrieval error due to a 200 m spatial misregistration of the NIR, SWIR-1 and SWIR-2 spectral band of CarbonSat. For this purpose, we used the lookup table approach as described above for an optically thin scattering layer at 8000 m altitude. Even for this mountainous area the extra retrieval error for each CarbonSat pixel is relatively small, mostly staying within 0.3% and never exceeding 0.4 %.

The second row panels of **Figure 104** show the CO_2 column of the power plant plume as a percentage of the background column ***i****ncluding* the extra co-registration errors due to the 200 m spatial misregistration of the NIR, SWIR-1 and SWIR-2 spectral band of CarbonSat. For this purpose the modelled plume was integrated per CarbonSat pixel. Again, the results are given, from left to right, for a misalignement of each of the three spectral windows with respect to the other two.

The situation plotted in **Figure 104** represents a worst-case scenario: A wind speed of 4 [m/s] is rather large. Smaller wind speeds would make the plume 'thicker' and thus more easily detectable. Furthermore, the assumed CO_2 emission is typical for a 1 GW power plant, while most power plants have higher emissions, making plume detection easier, since the plume concentration scale nearly linear with the capacity of the power plant. Finally, we have chosen a power plant, which is surrounded by a rather unfavourable orography. Also we have placed the modelled scattering layer at 8000 m, a situation for which the coregistration error is larger than when this layer would have been placed at 500 m. To estimate the importance of the spatial misregistration for the accuracy and detectability of the emission strengths of the power plant, a dedicated source inversion has to be performed based on the plume fields in **Figure 104**. This goes beyond the scope of this investigation.

12.6. Conclusions

We estimated that mis-registration error on CarbonSat CO_2 and CH_4 column retrieval due to differences in surface elevation for inter-band co-registration errors between 5-20 % of the instrument footprint, or 100-400 m, respectively. Here, pixel elevation is estimated from the SRTM3 data set. CH_4 and CO_2 retrievals are performed using the RemoTeC model for simulated CarbonSat measurements.

Based on two model atmospheres with a boundary layer aerosol and an elevated scattering layer, the mean retrieval error on the retrieved CH_4 and CO_2 total column is estimated over China. Overall, for CH_4 the mean co-registration error does not exceed 0.03% (0.5 ppb) for goal instrument performance and 0.05% (0.9 ppb) for threshold performance. For CO_2, the mean co-registration errors are a little higher but do not exceed 0.05 % (goal) and 0.07 % (threshold). These numbers are based on Table 1, which lists the overall error budgets. The contribution for spatio-temporal co-registration errors must be interpreted as a combination of the cirrus induced errors and the elevation induced errors.

On smaller spatial scales, retrieval errors can exceed these values. However, we have shown that the pixel internal elevation variability can be used as an effective data filter to reject most critical scenes. Errors due to spatial mis-registration of bands can be interpreted as a pseudo-noise contribution and so the assigned total co-registration error of about 0.1% of the CarbonSat error budget can be distributed between the two relevant error sources, i.e., spatial variability of cirrus and surface elevation, in a statistical manner. This yields a maximum of 0.07 % for the maximum co-registration errors due to surface elevation differences between different bands. Thus, we conclude that the CarbonSat inter-band co-registration requirement is supported by the error analysis of this study.

Additionally, we performed a case study for the effect of co-registration errors on local plume events due to CO_2 emissions of a coal plant in China. We considered a 1 GW power plant at 30°31′41″N, 106°49′34″E for a local wind speed of 4 m/s. For western wind the CO_2 plume is superimposed by co-registration errors of up to 0.4%. The effect of these errors on the detectability of the emission strength of the power plant by CarbonSat is subject of another work package.

13. Non-linearity: Impact on Level 2

13.1. Introduction

Residual calibration errors due to non-linearities will result in biases of the retrieved XCO_2 and XCH_4. These biases have been estimated using simulated retrievals via the BESD/C retrieval gain matrix approach.

To achieve this, a certain radiance dependence of the non-linearity and a certain error amplitude has been assumed. Some of the investigated dependencies are broadly in line with the dependencies shown in **/Caron et al., 2014/**.

13.2. Assessment method

BESD/C retrieval gain matrices have been computed for a number of scenarios covering several SZAs and assuming a surface albedo corresponding to vegetation.

The XCO_2 and XCH_4 biases have been computed using these gains and reflectance errors caused by non-linearity (NL).

How large the non-linearity related errors for CarbonSat are and what the radiance dependencies could be, is currently not known. Therefore, a certain amplitude and shape (= radiance dependence) has been assumed for the results shown here. The biases have been computed for a non-linearity relative error (peak-to-peak) of “1%”. It may assumed that the biases scale with the assumed amplitude of the error, i.e., the biases are expected to be a factor of 2 smaller the amplitude is a factor of 2 smaller.

It is expected that NL related errors may be large at low radiance levels **/Caron et al., 2014/**. Therefore, and to reduce the degree of freedom, we here assume the following: We assumed that the NL error is zero if the radiance level is equal to Radiance level DR-max-0 values as specified in **/CS MRD v1.2, 2013/.** These maximum radiance levels are:

- NIR radiance: 8.2×10^{13} photons/s/nm/cm^2/sr corresponding to a scene with surface albedo 0.5 and SZA 0^o.
- SWIR-1: 2.6×10^{13} photons/s/nm/cm^2/sr (albedo: 0.4, SZA 0^o)
- SWIR-2: 1.4×10^{13} photons/s/nm/cm^2/sr (albedo: 0.4, SZA 0^o)

In line with **/Caron et al., 2014/** we assume that mostly the “relative gain error” is important. The NL errors are therefore specified as relative reflectance (or radiance) error as a function of the normalized radiance, where the radiance in each band has been normalized by its corresponding DR-max-0 value.

For the radiance dependence of the NL error we have investigated the following three functions (amp is the error amplitude = 0.01 = 1% for the results shown here):

- PX2(amp) = $(amp/0.5)^2$ * (radiance/ DR-max-0 -0.5)^2 (see **Figure 105**)
- MX2(amp) = -PX2(amp) (see **Figure 106**)
- P10(amp) = amp * (radiance/ DR-max-0 -1.0) ^{10} (see **Figure 107**)

Note:

- We assume that the NL error is the same for all wavelengths (detector pixels or, more precisely, spectral resolution elements) in a given band. This may be a worst case assumption in terms of retrieval biases as this prevents compensation of errors.

The results are presented in the following sub-section.

13.3. Assessment results

Figure 105 shows a typical result of the XCO_2 and XCH_4 bias computation using the assumed non-linearity error for error function PX2 assuming a 1% error amplitude "amp". The results shown are valid for vegetation albedo, SZA 50^o and it is assumed that the NL error has the same dependence of the normalized radiance in each band with the same amplitude. The XCO_2 and XCH_4 biases have been computed using the BESD/C retrieval gain matrix approach and the used gain vectors are also shown in **Figure 105**. As can be seen, the biases are -0.48 ppm for XCO_2 and 1.98 ppb for XCH_4.

Figure 106 shows the corresponding results for NL error function MX2 and **Figure 107** for error function P10. As can be seen and as expected, the biases differ somewhat depending on which NL error function is used.

Figure 108 - **Figure 113** show the results for several SZAs and different combinations w.r.t. which band is affected by the NL error. As can be seen, the biases depend somewhat on the SZA, on the assumed error function and on which band is affected by the NL error.

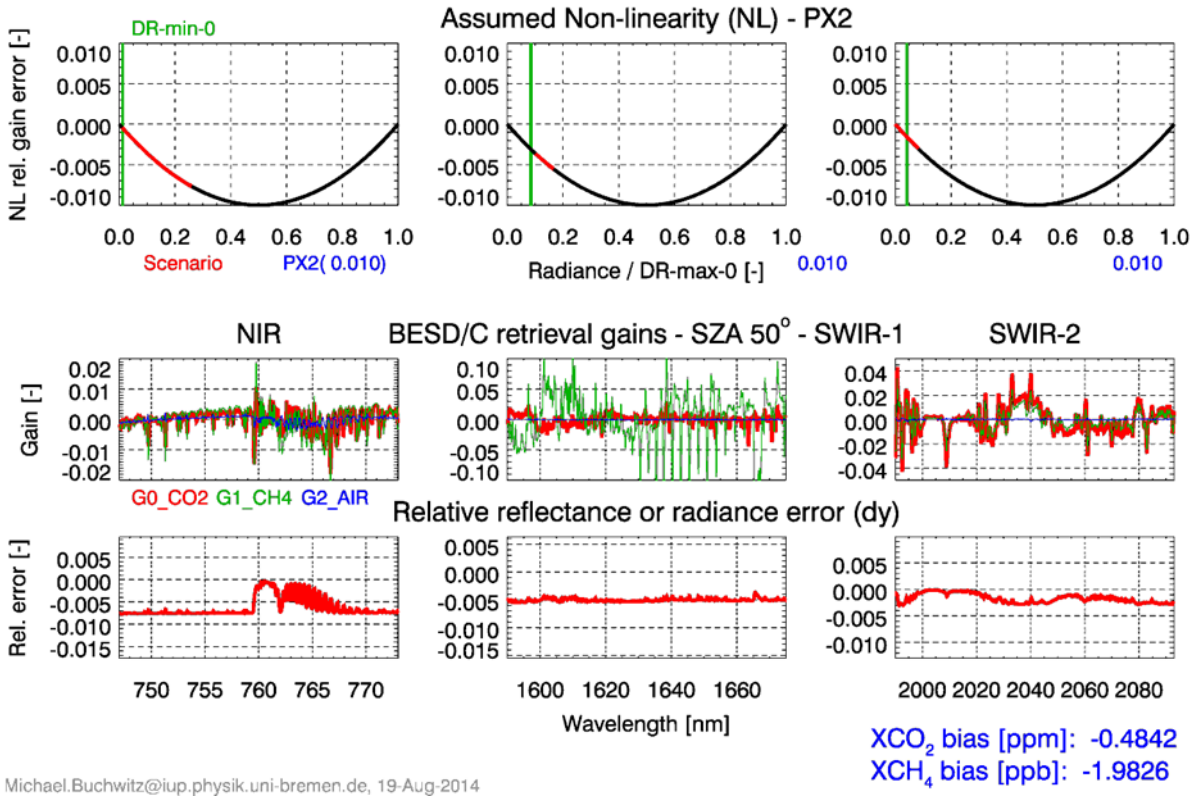

Figure 105: Computation of XCO_2 and XCH_4 biases due to non-linearity for error function PX2 (see main text). Top: Assumed non-linearity ("relative gain error") shown as black curve. The x-axis shows the radiance normalized to the band dependent maximum radiance level DR-max-0 according to **/CS MRD v1.2, 2013/**. The assumed error amplitude is 1% in all three bands. The overplotted red curve corresponds to the radiance range covered by the investigated scenario, which corresponds to SZA 50° and vegetation albedo. Middle: Corresponding BESD/C gain vectors. Bottom: Corresponding relative reflectance or radiance error. The resulting XCO_2 and XCH_4 biases are listed in the bottom right.

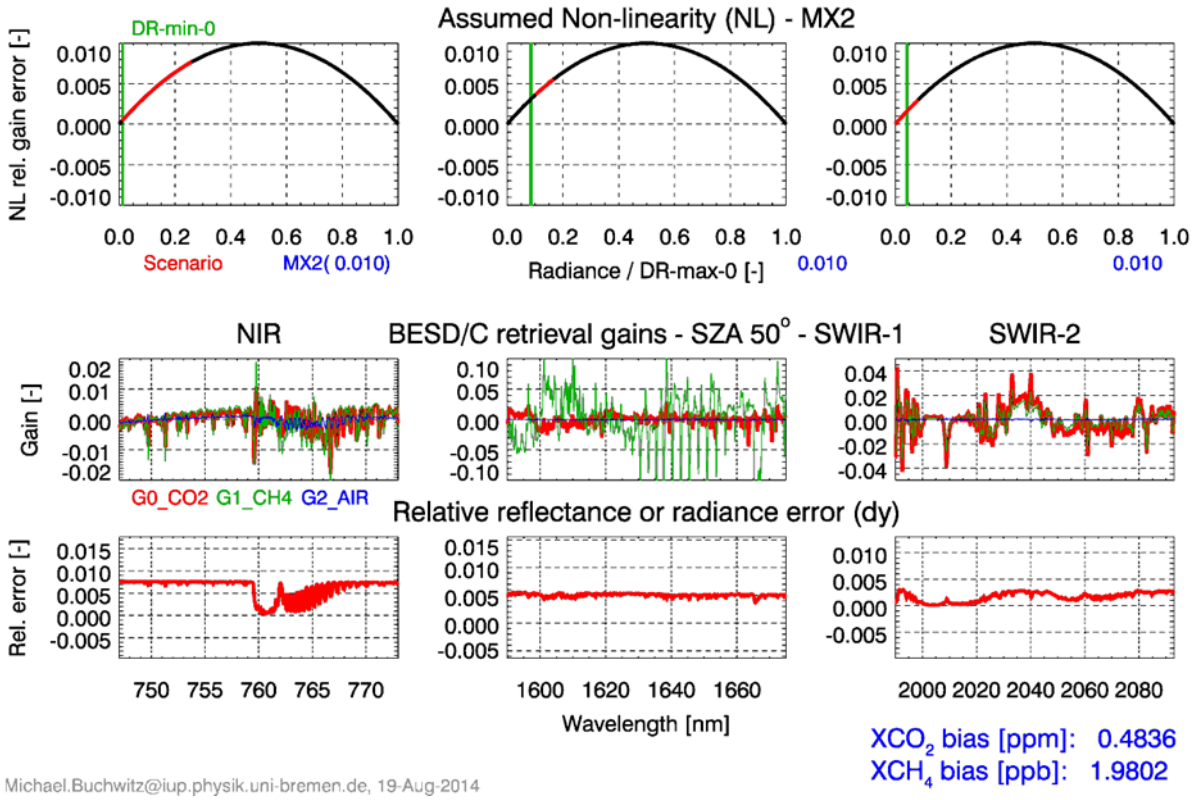

Figure 106: As
Figure 105 but for NL error function MX2.

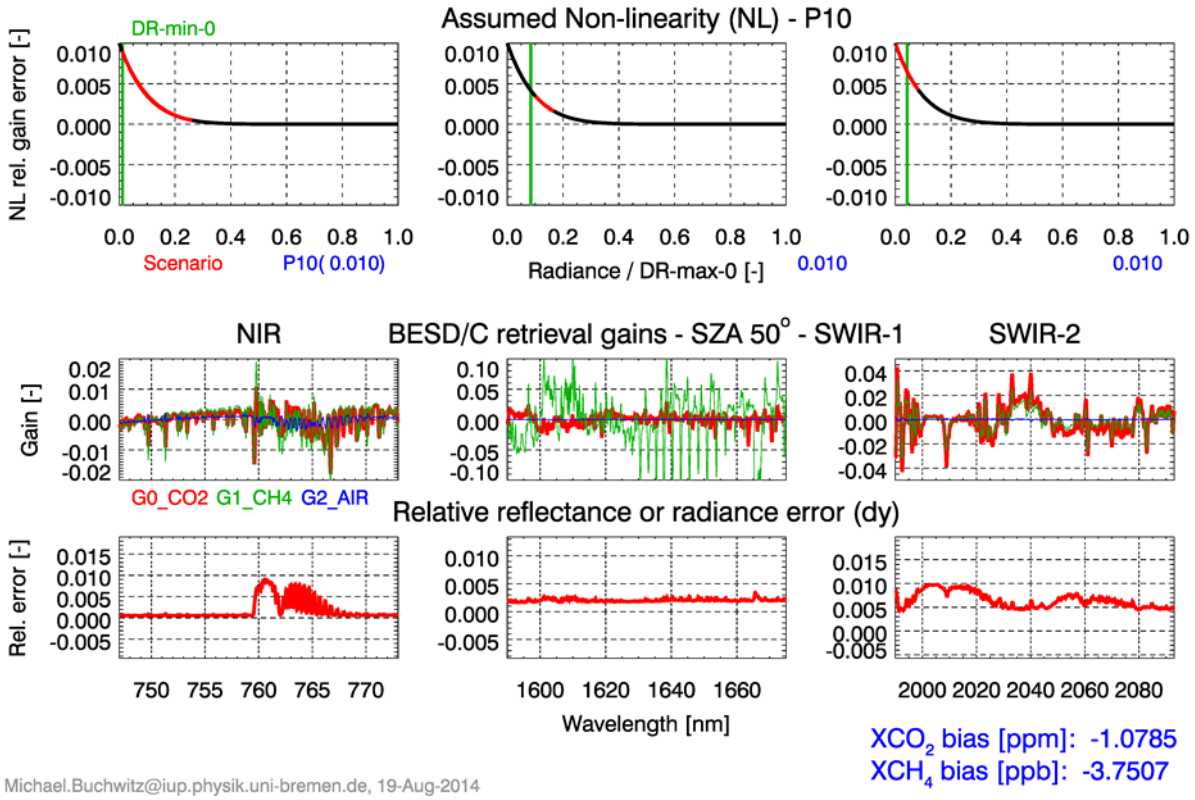

Figure 107: As
Figure 105 but for NL error function P10.

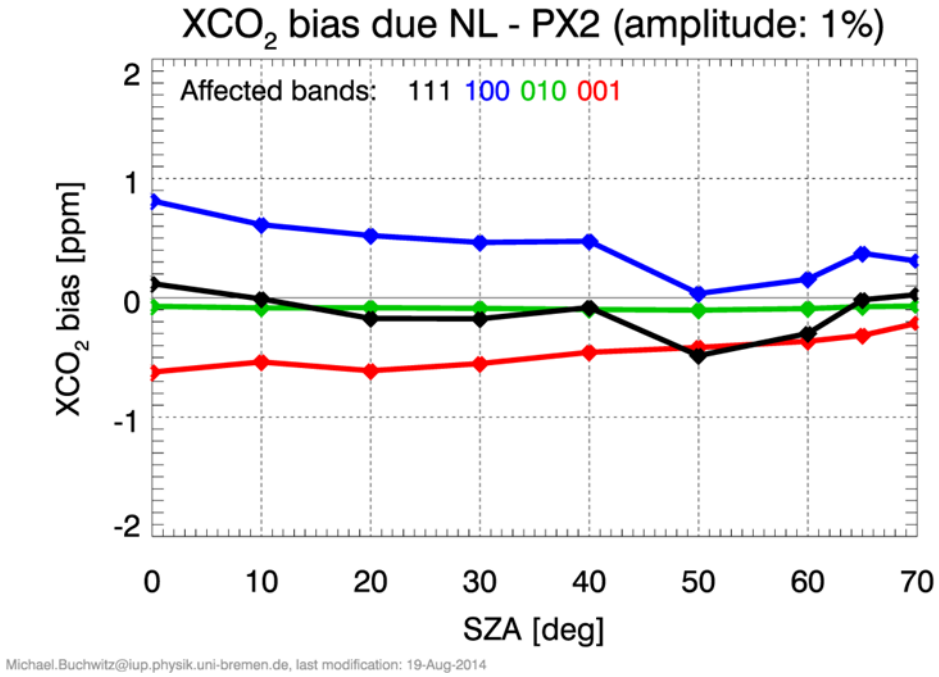

Figure 108: XCO_2 bias for NL error function PX2 for NL errors in all three bands ("111") or only in single bands (100: only NIR affected; 010: only SWIR-1; 001: only SWIR-2).

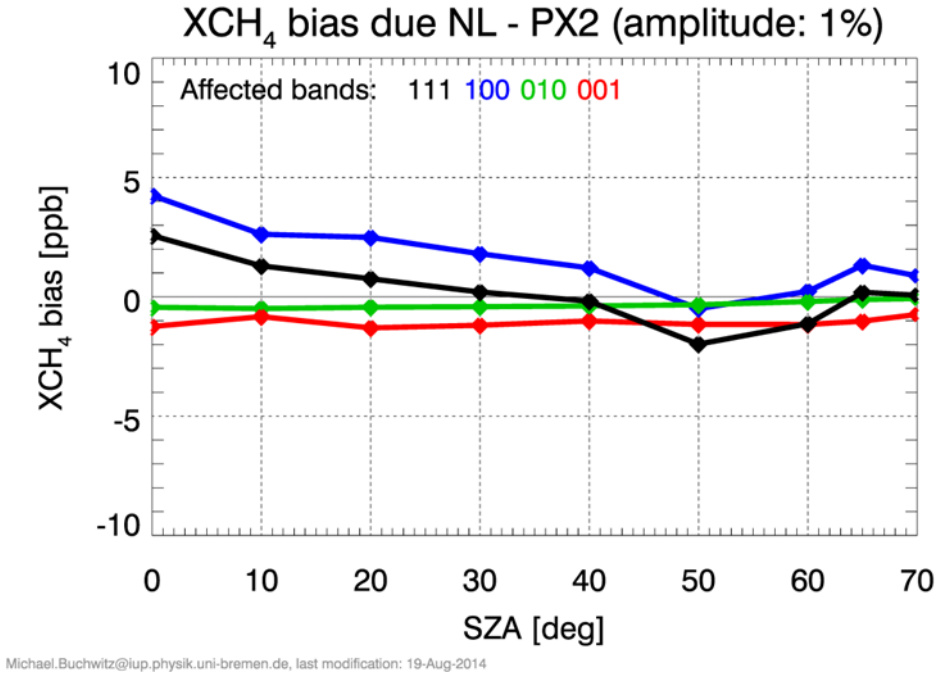

Figure 109: XCH_4 bias for NL error function PX2 for NL errors in all three bands ("111") or only in single bands (100: only NIR affected; 010: only SWIR-1; 001: only SWIR-2).

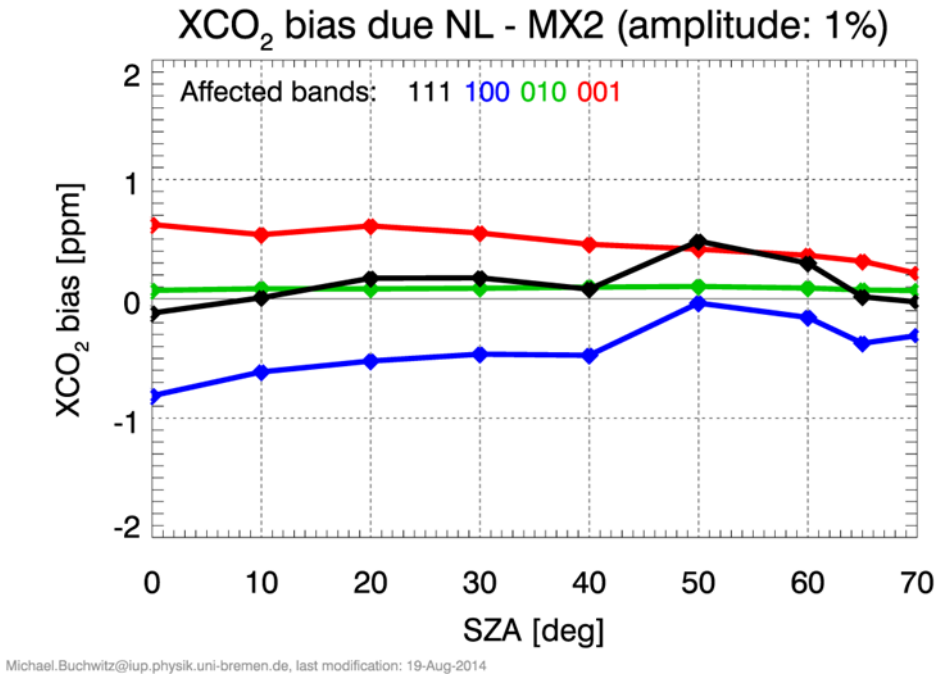

Figure 110: As **Figure 108** but for NL error function MX2.

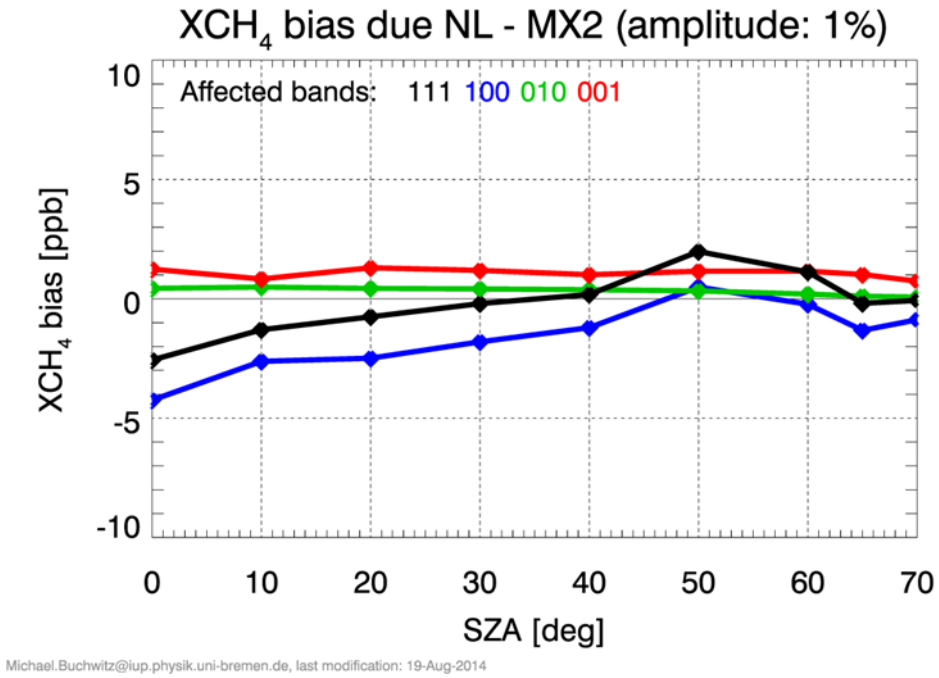

Figure 111: As **Figure 109** but for NL error function MX2.

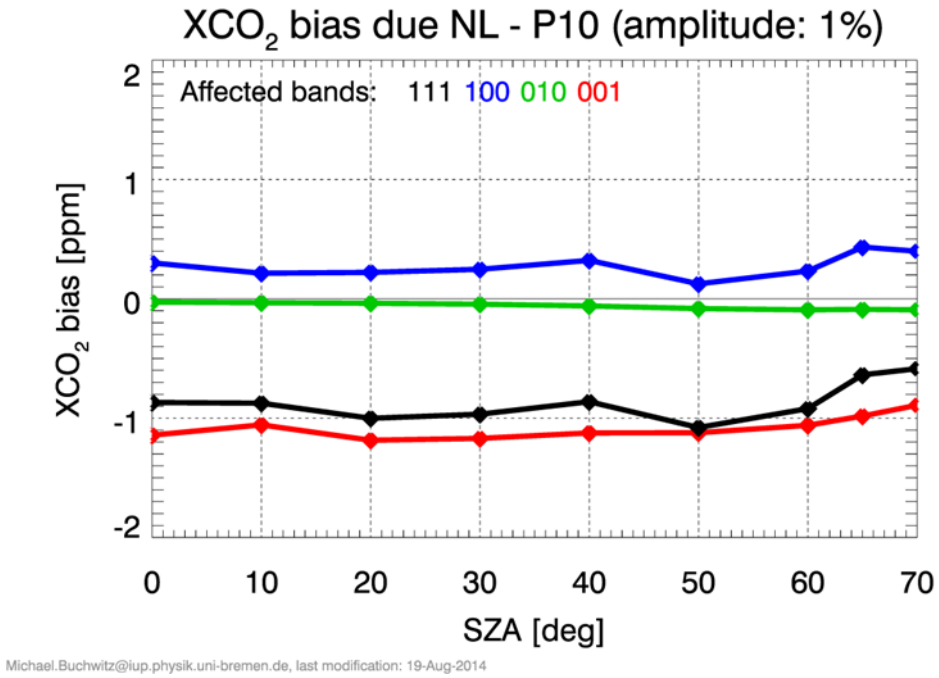

Figure 112: As **Figure 108** but for NL error function MX2.

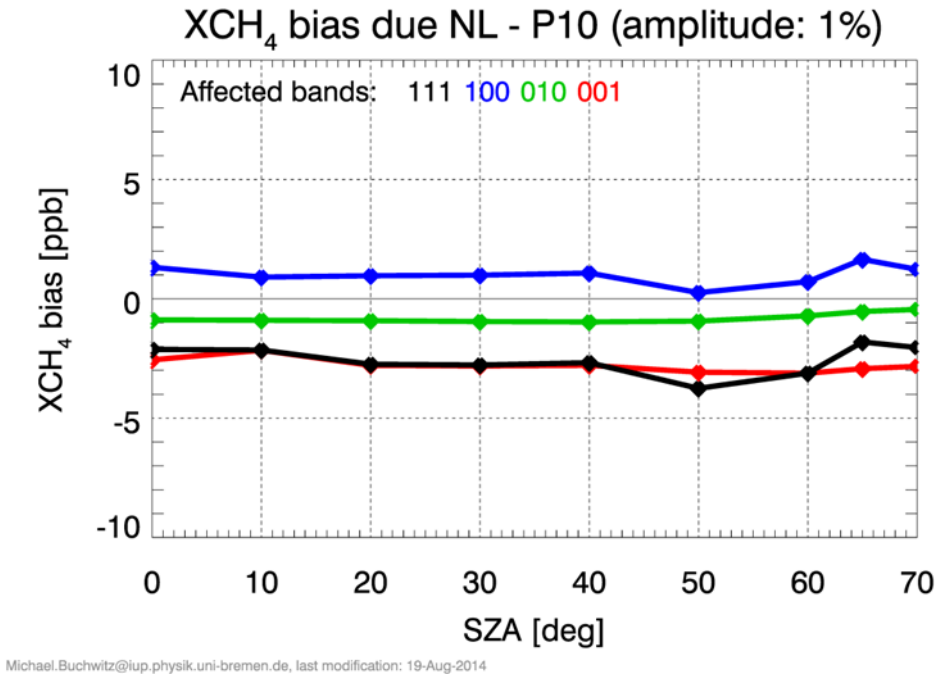

Figure 113: As **Figure 109** but for NL error function MX2.

13.4. Summary and conclusions

XCO_2 and XCH_4 biases have been computed assuming certain radiance dependencies of the non-linearity (NL) error obtained from information provided by ESA.

Furthermore it is assumed that the peak-to-peak amplitude of the NL error is 1% in the “full radiance” range (from zero to the band dependent maximum value DR-max-0 as specified in MRDv1.2).

The XCO_2 and XCH_4 biases have been computed assuming three NL error functions, several SZAs and several combinations on which bands are affected.

Overall it has been found that the XCO_2 bias is typically a few tenths of a ppm (up to approx. 1 ppm) and the XCH_4 bias is typically a few ppb.

However, these values depend on the assumption used w.r.t. the assumed amplitude and radiance dependence of the NL error and it is unclear how large NL related errors will be for the real instrument. Probably the most important simplification is that the same NL error (i.e., error as a function of radiance) has been assumed for all detector pixels (wavelengths).

The results shown here therefore can only give a rough indication on how XCO_2 and XCH_4 biases can be affected by NL related errors. More reliable error estimates can be performed if more knowledge on the NL errors will be available.

14. Dynamic range minimum: Impact on Level 2

In **/CS MRD v1.2, 2013/** several radiance levels are specified such as radiance level DR-min-0, which is the lowest radiance level for which most requirements as listed in **/CS MRD v1.2, 2013/** are applicable.

If the radiance is below the (band dependent) level DR-min-0, the required CarbonSat performance is not specified.

The DR-min-0 values **/CS MRD v1.2, 2013/** are:

- NIR radiance: $1x10^{12}$ photons/s/nm/cm^2/sr corresponding to a scene with surface albedo 0.1 and SZA 0^o.
- SWIR-1: $2.2x10^{12}$ photons/s/nm/cm^2/sr (albedo: 0.05, SZA 0^o)
- SWIR-2: $6x10^{11}$ photons/s/nm/cm^2/sr (albedo: 0.05, SZA 0^o)

As the performance of radiances below DR-min-0 is not specified one either has to use assumptions on how (worse) the performance could be for radiances below this level or to entirely exclude the corresponding detector pixels from the retrieval. At this point in time, this would result in probably meaningless speculation or at least in results which are very difficult to interpret. Therefore Level 2 issues related to radiance levels below DR-min-0 have not been investigated in the context of this study.

It has however been identified that non-linearities are expected to be critical, especially for low signals **/Caron et al., 2014/**. This aspect has been investigated and the results have been shown in **Section 13**.

15. Dynamic range maximum: Impact on Level 2

15.1. Introduction

In **/CS MRD v1.2, 2013/** several radiance levels are specified such as radiance level DR-max-0, which is the upper radiance level for which most requirements as listed in **/CS MRD v1.2, 2013/** are applicable.

If the radiance exceeds the (band dependent) level DR-max-0, the required CarbonSat performance is not specified. For radiance levels significantly higher, even saturation may occur, which will result in “useless” measurements.

DR-max-0 has been defined to achieve a “best compromise” between sufficiently large “detector filling” (i.e., good signal-to-noise ratio and good radiometric performance) and avoidance of saturation for the most relevant observations, which are essentially conflicting requirements. As a consequence, good performance is ensured for most situations. However, it is not ensured that good performance or even avoidance of saturation is guaranteed under all conditions, e.g., for (very) high albedo scenes and low SZAs.

The DR-max-0 values **/CS MRD v1.2, 2013/** are the following:

- NIR radiance: 8.2×10^{13} photons/s/nm/cm^2/sr corresponding to a scene with surface albedo 0.5 and SZA 0^o.
- SWIR-1: 2.6×10^{13} photons/s/nm/cm^2/sr (albedo: 0.4, SZA 0^o)
- SWIR-2: 1.4×10^{13} photons/s/nm/cm^2/sr (albedo: 0.4, SZA 0^o)

In the following it is described under which conditions it can be expected that these radiance levels are exceeded.

15.2. Assessment method

To assess under which conditions the band dependent radiance level DR-max-o can be exceeded, the one year data set of simulated CarbonSat observations generated in the parallel LOGOFLUX-II data set (“L2e files”) has been used.

This data set is an updated version of the LOGOFLUX-I data set described in **/Chimot et al., 2014/** and /**Buchwitz et al., 2013a/**. This data set contains for each (sufficiently cloud free) single CarbonSat observation (= 2x3 km^2 ground pixel) detailed information such as time and latitude and longitude of the observation, SZA and the surface albedo in the NIR and SWIR-1 spectral bands (obtained from MODIS satellite data).

This data set has been used to compute band dependent radiance levels using this formula:

$$L = E / PI * \cos(SZA) * A,$$

Where, L is the (desired) radiance, E is the solar irradiance, SZA is SZA and A is surface albedo.
Using this formula permits to estimate the maximum radiance expected in the continuum, i.e., outside of spectral regions where strong absorption due to atmospheric gases occur.

For the band dependent solar irradiance, the following values have been used:

- E(NIR): 4.9×10^{14} photons/s/nm/cm^2
- E(SWIR-1): 2.1×10^{14} photons/s/nm/cm^2
- E(SWIR-2): 1.25×10^{14} photons/s/nm/cm^2 (not used)

The information given in the L2e files has been used to compute the total number of observations in spatial areas of $0.5^o \times 0.5^o$ in a given time period (one month) and the fraction of these observations, where radiance level DR-max-0 is exceeded. The results are shown in the following section.

15.3. Assessment results

Figure 114 shows the fraction of observations where the radiance level DR-max-o is exceeded in the NIR band. The results shown are valid for July and for $0.5^o \times 0.5^o$ spatial intervals. **Figure 115** shows the corresponding results for the SWIR-1 band and **Figure 116** shows the total number of observations (=100%). For these figures only the good, i.e., quality filtered CarbonSat observations over land have been used.

As can be seen, DR-max-0 may be exceeded typically only over desert regions, due to high albedo. As can also be seen, DR-max-0 is exceeded more often in the SWIR-1 band compared to the NIR band. As can be seen from **Figure 116**, the data set has large gaps due to the quality filtering, which removed scenes with too high aerosol optical depth and significant cloud contamination due to (thin) cirrus.

Therefore, also results are shown where the quality filtering as has not been applied: **Figure 117** shows “all” observation as given in the L2e files (note that the L2e files only contain those observations which are relatively cloud free). As can be seen, nearly all regions are covered, except one region over water, where no MODIS data are available. **Figure 118** shows the same quantity as **Figure 114** but for “all” data and **Figure 119** shows the same quantity as **Figure 115** but for “all” data. Note that only data over land are shown because the assessment method is not applicable for (e.g., sun-glint) observations over oceans. Again, DR-max-o is mostly exceeded over deserts and more frequently in the SWIR-1 than in the NIR band.

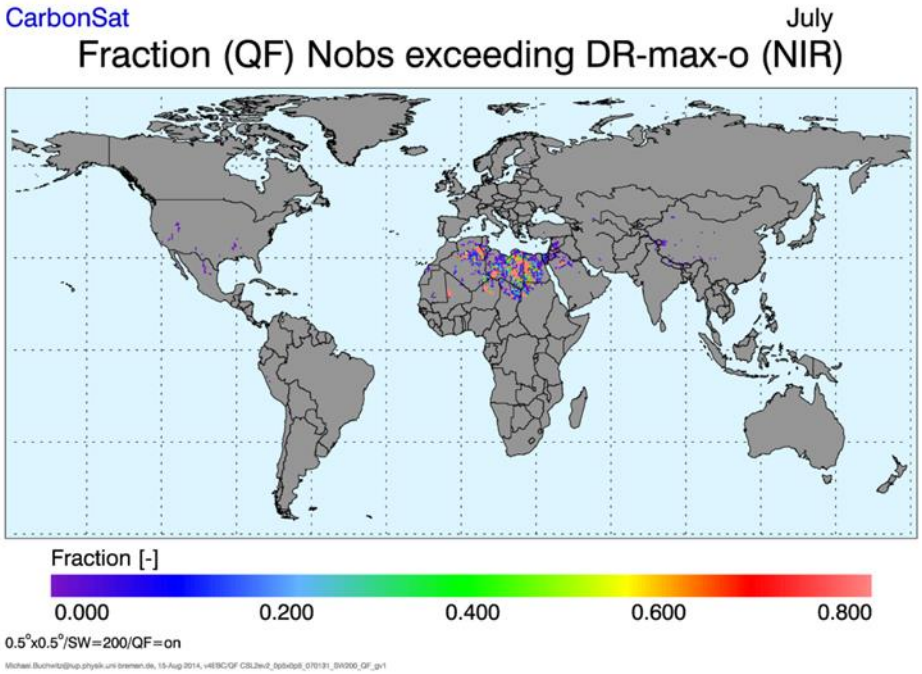

Figure 114: Fraction of the number of quality filtered nadir observations over land exceeding radiance level DR-max0o for the NIR band (= 8.2×10^{13} photons/s/nm/cm^2/sr,corresponding to a scene with surface albedo 0.5, SZA 0^o) as specified in **/CS MRD v1.2, 2013/**. The results shown are valid for July and spatial gridding interval 0.5^o x 0.5^o. For the total number of observations (=100%) see **Figure 116**.

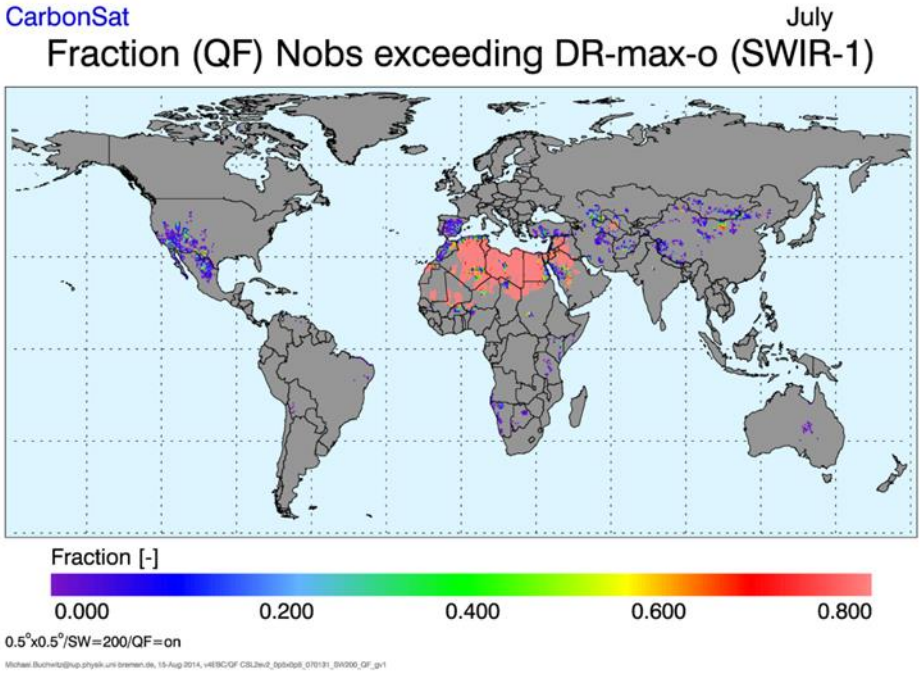

Figure 115: As **Figure 114** but for the SWIR-1 band.Radiance level DR-max-0 for the SWIR-1 band is 2.6×10^{13} photons/s/nm/cm^2/sr,corresponding to a scene with surface albedo 0.4, SZA 0^o **/CS MRD v1.2, 2013/**.

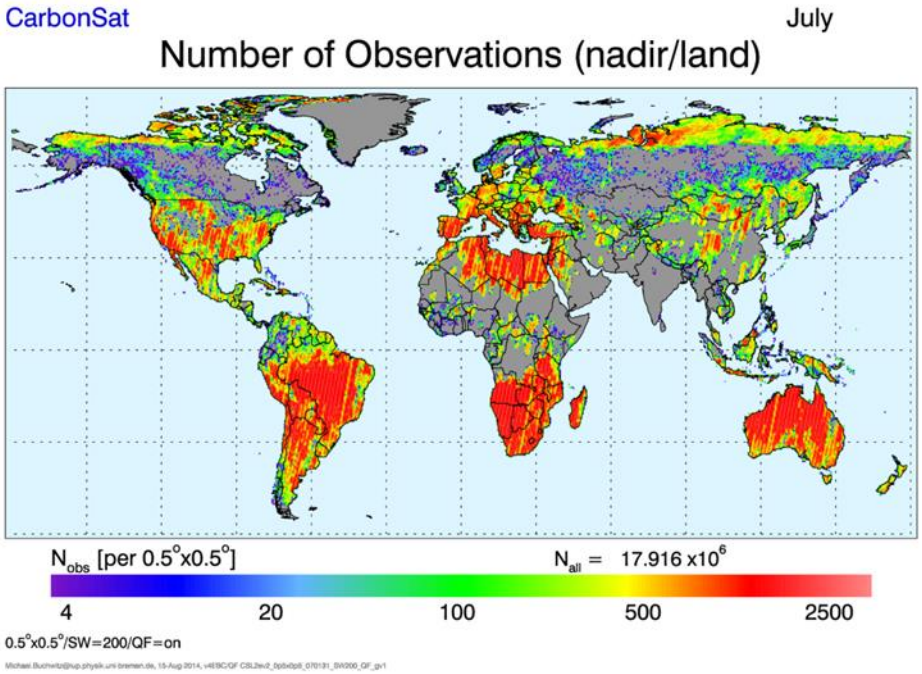

Figure 116: Total number of quality filtered nadir observations over land during July at 0.5^{o}x0.5^{o} resolution.

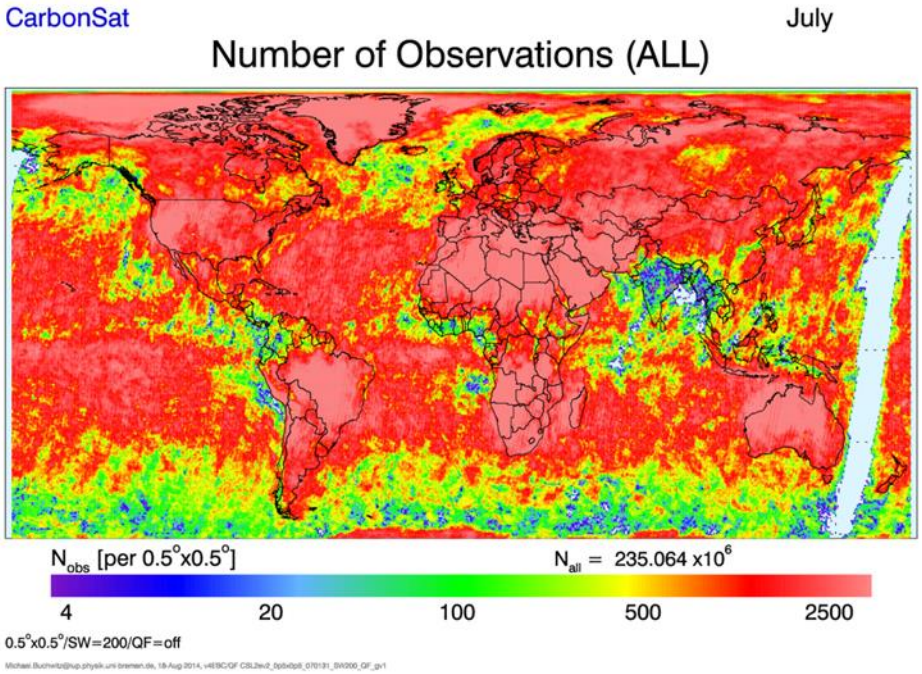

Figure 117: As **Figure 116** but for all observations (= nadir and land and without quality filtering except for cloud cover). Note that the gap on the right originates from not using any observations between 00:00 and 01:00 hours GMT due to non-optimized settings of the gridding program.

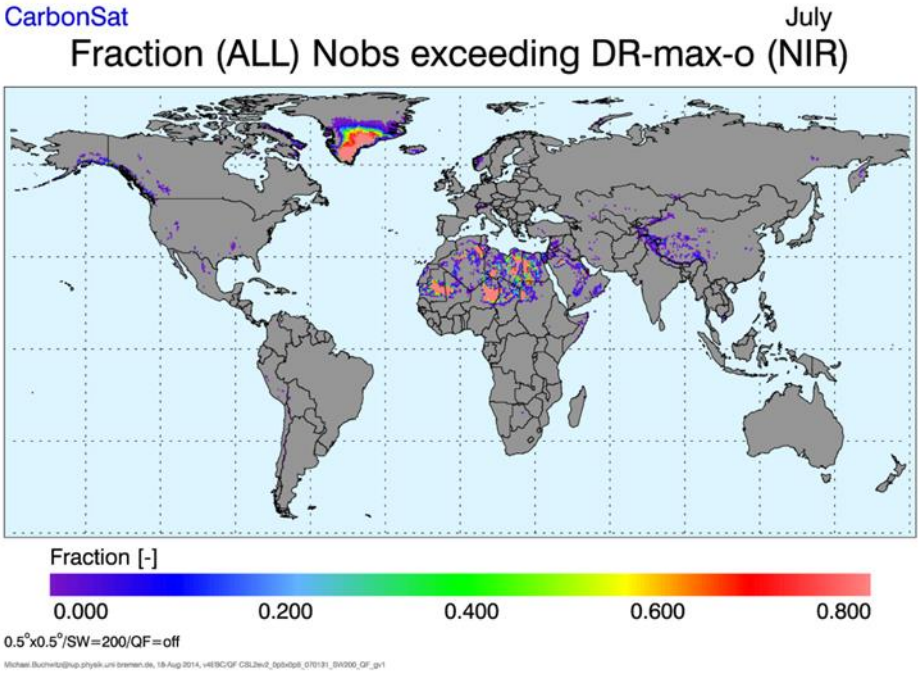

Figure 118: As **Figure 114** but for all nadir observations over land.

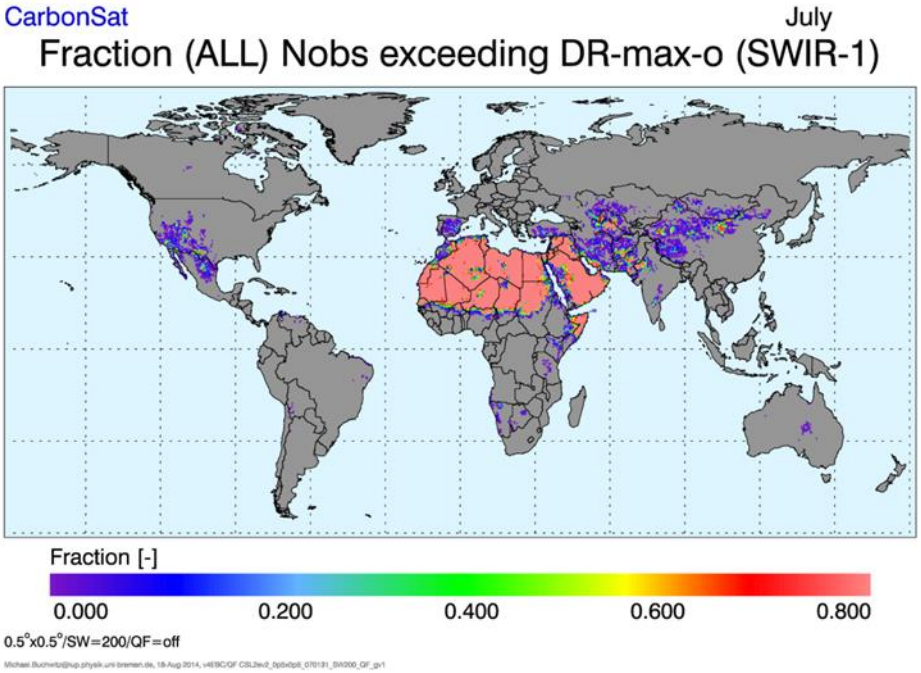

Figure 119: As **Figure 115** but for all nadir observations over land.

15.4. Summary and conclusions

It has been assessed under which conditions the band dependent radiance level "DR-max-o" can be exceeded. DR-max-0 is specified in the MRD **/CS MRD v1.2, 2013/** and defines the maximum radiance level until which all requirements as listed in the MRD are applicable. For radiances larger than DR-max-0, the performance is therefore not specified and even saturation may occur (but typically this requires much higher radiance levels, see **/CS MRD v1.2, 2013/**).

Using a data set of simulated CarbonSat observations (the so-called L2e files /**Buchwitz et al., 2013a/** as generated in the parallel LOGOFLUX-II study) it has been assessed where and how frequent radiance levels DR-max-0 may be exceeded. To achieve this, global maps at 0.5^{o}x0.5^{o} resolution have been generated showing the total number of observations per grid cell and the fraction of observations where DR-max-0 is exceeded.

It has been found the DR-max-0 is exceeded mostly over desert areas (as expected) and that it is exceeded more frequently in the SWIR-1 band compared to the NIR band.

16. Impact of SNR requirements for HSS channels & applications

Some detectors which are currently taken into account as potential detectors for CarbonSat allow spatially and temporally un-destructive oversampled readout (in the following referred to as high spatial sampling (HSS)) simultaneously operated with the regular read out of the (main) instrument. Given an adequate instrument design, this can result in ground pixels with much higher spatial resolution across and/or along track which hold important sub pixel information on, e.g., clouds, aerosols, albedo, and point sources of CO_2 and CH_4. With less light hitting the detector, HSS will have a reduced SNR performance which can partly be compensated by spectral binning.

Table 33 lists the most important HSS channels and their potential applications. The spectral position and width of the HSS channels is shown in **Figure 120**.

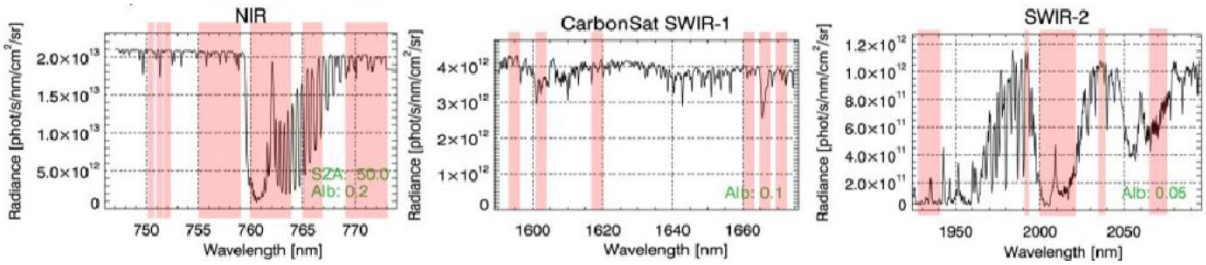

Figure 120: Position of proposed high spatial sampling (HSS) channels.

The most important potential applications for HSS channels are:

i) The detection of sub-pixel cloud/aerosol contamination and microphysical cloud classification and, as a consequence, the reduction of systematic errors in the greenhouse gas retrievals.

ii) Hot spot detection and spatial up-scaling of full physics CO_2 and CH_4 retrieval results particularly at point sources with the aim to improve flux estimates.

iii) Hot spot detection and spatial up-scaling of chlorophyll fluorescence retrievals of the main instruments in regions with large spatial variability at sub-pixel scale.

In the following we will analyse the impact of SNR requirements of the main instruments on the main HSS applications as listed above. Other potential benefits of the HSS channels are the support for co-registration analysis and the detection and analysis of inhomogeneous scenes.

Table 33: List of HSS-channels. Reference SNR values for the HSS channels have been derived from **Figure 2** and **Figure 3**. HSS SNR values have been estimated by multiplication of the reference SNR by $\sqrt{n}$ (see text for more information).

	Centre wavelength [nm]	Band width [nm]	# of binned spectral channels	Reference SNR	HSS SNR	Objective
NIR, FWHM: 0.1nm, spectral oversampling: 3						
HSS-01	750.3	0.3	9	490	1470	Surface albedo / continuum level
HSS-02	751.3	0.3	9	480	1440	Fluorescence from solar Fraunhofer line
HSS-03	752.0	0.3	9	485	1455	Surface albedo / continuum level
HSS-04	757.0	4.0	120	475	5203	Surface albedo / continuum level /clouds
HSS-05	762.0	4.0	120	175	1917	Cirrus detection from saturated O_2 absorption line
HSS-06	766.0	2.0	60	330	2556	Surface pressure from moderate O_2 absorption line with weak temperature dependence
HSS-07	771.0	4.0	120	465	5094	Surface albedo / continuum level /clouds
SWIR-1, FWHM: 0.3nm, spectral oversampling: 3						
HSS-08	1595.4	3.9	39	335	2092	Surface albedo / continuum level /clouds
HSS-09	1602.5	3.0	30	350	1725	CO_2 absorption line
HSS-10	1618.1	3.9	39	330	2061	Surface albedo / continuum level /clouds
HSS-11	1662.0	3.9	39	325	2030	Surface albedo / continuum level /clouds
HSS-12	1666.5	3.0	30	310	1698	CH_4 absorption line
HSS-13	1671.5	3.9	39	320	1998	Surface albedo / continuum level /clouds
SWIR-2, FWHM: 0.55nm, spectral oversampling: 3						
HSS-14	1935.0	11.0	60	30	232	Cirrus detection from saturated H_2O absorption line
HSS-15	1992.0	2.2	12	290	1005	Surface albedo / continuum level /clouds
HSS-16	2010.0	11.0	60	50	387	CO_2 absorption line (strong)
HSS-17	2038.0	5.5	30	280	1534	Surface albedo / continuum level /clouds
HSS-18	2070.0	11.0	60	200	1549	CO_2 absorption line (moderate)

16.1. Cloud detection and microphysical classification

Most of the HSS channels have been selected according to the existing and future satellite instruments MODIS, MTG, and OLCI. Similar band definitions have also been used on former satellite instruments such as AVHRR, SEVIRI, and MERIS (to list only a few) where they have proven their usefulness many times in the past.

The selected HSS channels allow cloud detection on the following bases:

- Clouds are spatially more variable than the cloud free surface (e.g. **/Rossow, 1989/, /Rossow et al., 1993/, /Rossow and Garder, 1993a,b/, /Kriebel et al., 2003/**).
  Channels: HSS-4, 7, 8, 10, 11, 13, 15, 17
- Clouds are bright (e.g. **/Rossow, 1989/, /Rossow et al., 1993/, /Rossow and Garder, 1993a,b/, /Kriebel et al., 2003/, /Ackerman et al., 1998, 2002/**).
  Channels: HSS-4, 7
- Clouds are high and shield O_2-A absorption (e.g**. /Preusker and Lindstrot, 2009/, /Preusker, 1999/**)
  Channels: HSS-4, 5, 6, 7
- Cirrus clouds shield the H_2O absorption which takes place mainly in the lower troposphere (e.g. **/Ackerman et al., 1998, 2002/**)
  Channels: HSS-14

The following microphysical properties can be retrieved with the HSS channels:

- Thermodynamic phase due to differences of absorption coefficients of water and ice at 1.6 µm (e.g. **/King et al., 1992, 1997/**)
  Channels: HSS-7, 8, 10, 11, 13, 15, 17
- Droplet effective radius due to variations of the spectral reflectivity of clouds within the SWIR (e.g. **/Nakajima and King, 1990/, /Schüller et al., 2005/**)
  Channels: HSS-7, 8, 10, 11, 13, 15, 17

The following tables list the relevant MODIS, MTG, and OLCI channels and corresponding HSS channels. In order to assess the usability of the HSS channels, we compare the expected SNR of the HSS channels with the SNR of the corresponding MODIS, MTG, and OLCI channels.

Reference SNR values for the HSS channels have roughly been estimated by visual inspection of **Figure 2** and **Figure 3** and are in so far strictly valid only for the vegetation 50 scenario.

Table 34: Relevant METEOSAT Third Generation (MTG) bands. Calculated from Tab. 3 and the radiometric scaling function for maximal reflectance (page 112) of http://www.eumetsat.int/website/wcm/idc/idcplg?IdcService=GET_FILE&dDocName=PDF_MTG_EURD&RevisionSelectionMethod=LatestReleased&Rendition=Web

MTG band ID	Centre wavelength	SNR	Corresponding HSS band(s)
MTG-4	865	230	HSS-7
MTG-7	1610	300	HSS-8,10,11,12
MTG-8	2250	250	HSS-15,17

Table 35: Relevant MODIS bands. http://modis.gsfc.nasa.gov/about/specifications.php

MODIS band ID	Centre wavelength	SNR	Corresponding HSS band(s)
MODIS-1	645	128	HSS-4
MODIS-2	858.5	201	HSS-7
MODIS-5	1240	74	HSS-14
MODIS-6	1640	275	HSS-8, 10, 11, 13
MODIS-7	2130	110	HSS-15, 17
MODIS-15	748	586	HSS-4

Table 36: Relevant OLCI bands. Tab. 15 of http://esamultimedia.esa.int/docs/GMES/GMES_Sentinel3_MRD_V2.0_update.pdf

OLCI band ID	Centre wavelength	SNR	Corresponding HSS band(s)
OLCI-10	754	673	HSS-4
OLCI-11	761	407	HSS-5, 6
OLCI-12	779	810	HSS-7

In the following, we assume that spectral binning improves SNR by the square root of the number of binned channels n (where n is calculated from the band width w divided by fwhm f and multiplied by the oversampling o).

$$SNR_{HSS} = SNR_{Ref}\sqrt{n} = SNR_{Ref}\sqrt{\frac{w\ o}{f}}$$

This is only valid if the HSS bands cover the same area at ground a (pixel size) as the main instrument which we assume to be $A = 2km \cdot 3km = 6km^2$. The number of photons hitting the detector is assumed to be proportional to the pixel size so that the SNR of the HSS channels at smaller pixel sizes is estimated by:

$$SNR_a = SNR_{HSS}\sqrt{a/A}$$

Figure 121 shows SNR_a with pixel sizes between $0.06\ km^2$ (100 sub pixels) and $6\ km^2$ (no sub pixels) for those HSS channels being most relevant for sub pixel cloud detection and classification. SNR values of the corresponding MODIS, MTG, and OLCI bands always intersect at pixel sizes smaller than about $0.6\ km^2$ and most times smaller than $0.2\ km^2$.

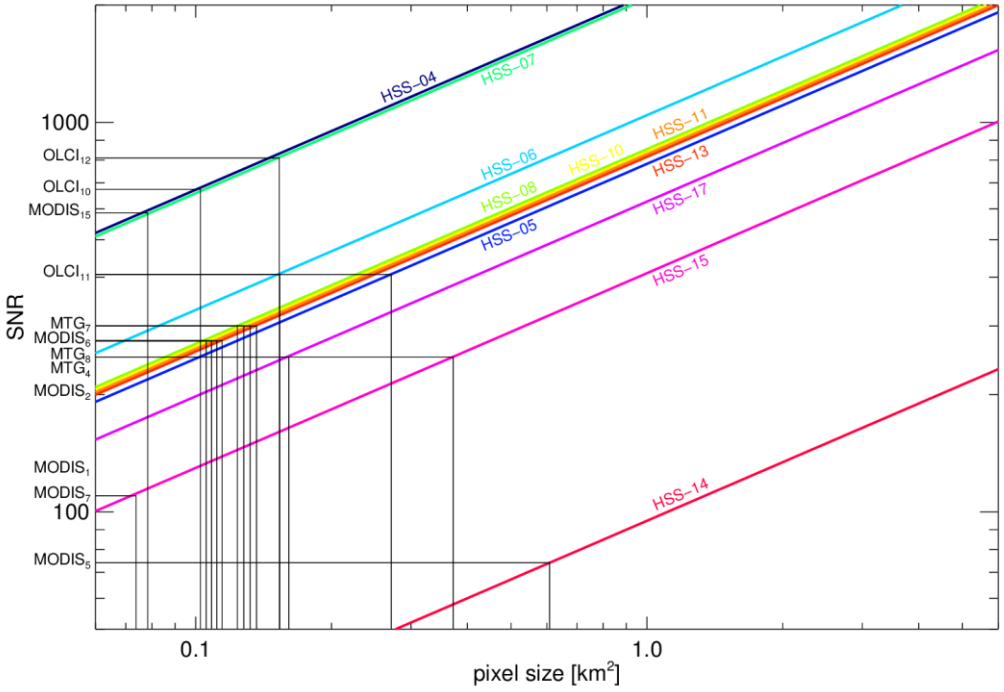

Figure 121: Estimated SNR of the HSS channels at different pixel sizes compared with the SNR of corresponding MODIS, MTG, and OLCI channels.

16.2. Hot spot detection and spatial up-scaling

Spectrally binned HSS channels have also been defined for CO_2 and CH_4 absorption bands and Fraunhofer structures plus corresponding continuum levels. In the following, we will roughly estimate how spectral binning, pixel size, and the SNR of the main instrument influences hot spot detection and spatial up-scaling capabilities.

According to Beer-Lambert's law, the radiance in an absorption band I can be expressed by the radiance without absorption I_0, the concentration c of the absorber (e.g. CO_2) and a constant b.

$$I = I_0 \, e^{-b\,c}$$

Solving for c yields:

$$c = \frac{1}{b}\ln(I_0) - \frac{1}{b}\ln(I)$$

For weak absorbers ($\Delta I = (I_0 - I) \ll I_0$), a first order Taylor approximation at I_0 results in:

$$c \approx \frac{1}{b\,I_0}\Delta I$$

This means, for an absorption band sampled with n spectral channels i of spectral width $\Delta\lambda$, the concentration becomes (to a first order approximation) proportional to the enclosed area between I and I_0 (**Figure 122**).

$$c \sim \sum_n \Delta I_i \, \Delta\lambda$$

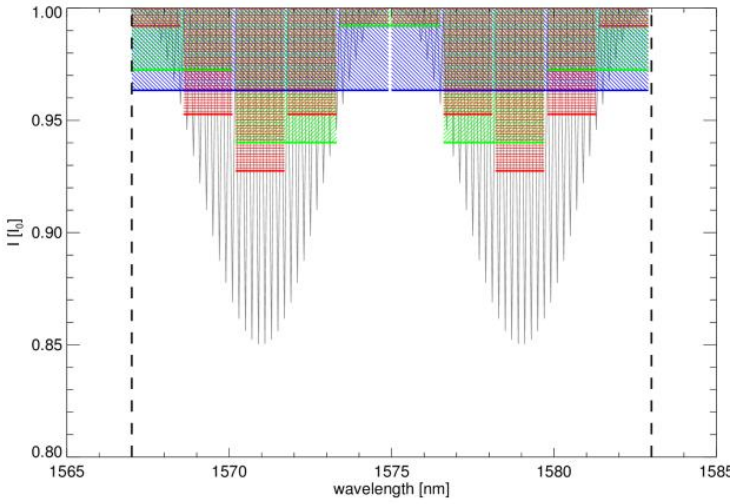

Figure 122: Sketch of an absorption band (black) sensed with spectral channels of varying spectral width (red, green, blue).

Note that the same applies for the retrieval of chlorophyll fluorescence. We are now interested how the noise of the individual measurements, which we assume to be the same for all spectral channels ($\sigma_I = \sigma_{I_0} = const$), translates into noise of the derived concentration σ_c (or chlorophyll fluorescence). According to the last equation, the variance of c becomes:

$$\sigma_c{}^2 = V(c) \sim \Delta\lambda^2 \, n \, \sigma_I{}^2$$

As the noise of the radiance measurements σ_I scales with $\sqrt{1/\Delta\lambda}$, it follows:

$$\sigma_c \sim \sqrt{n \, \Delta\lambda}$$

This means that (to a first order approximation), the noise of the derived concentration is constant and does not depend on the spectral resolution. Nonetheless, the high spectral resolution of the main instrument is essential in order to disentangle changes in concentration, scattering at clouds, temperature shifts, water vapour differences, etc. Spatial up-scaling algorithms using the binned HSS channels will need to make assumptions on the inner-pixel constancy of such effects.

If not only the spectral binning is changed but also the spatial resolution, the noise of the individual HSS measurements becomes:

$$\sigma_a = \sigma_c \sqrt{A/a}$$

In respect to hot spot detection, the simplest case is to assume a flat background field with a pronounced enhancement at a scale smaller than the pixel size of the main instrument so that we can assume that always only one HSS pixel is influenced by the enhancement. The enhancement E_a at HSS pixel size a can then be calculated from the enhancement E_A at the pixel size of the main instrument A:

$$E_a = E_A \, \frac{A}{a}$$

This means that the maximal observed enhancement increases with $1/a$ whilst the noise only increases with $\sqrt{1/a}$ when reducing the HSS pixel size (see **Figure 123** and **Figure 124** for an illustration). Consequently, hot spot detection continuously improves for HSS pixels getting smaller. The effect levels off when the size of the HSS pixels becomes similar or smaller than the size of the enhancement (**Figure 123**, dashed lines). In this case the maximum signal reaches a maximum but the noise continues to increase. Note that this does not mean that smaller HSS pixels would degrade hot spot detection because with decreasing pixel size more and more pixel would measure the maximum signal.

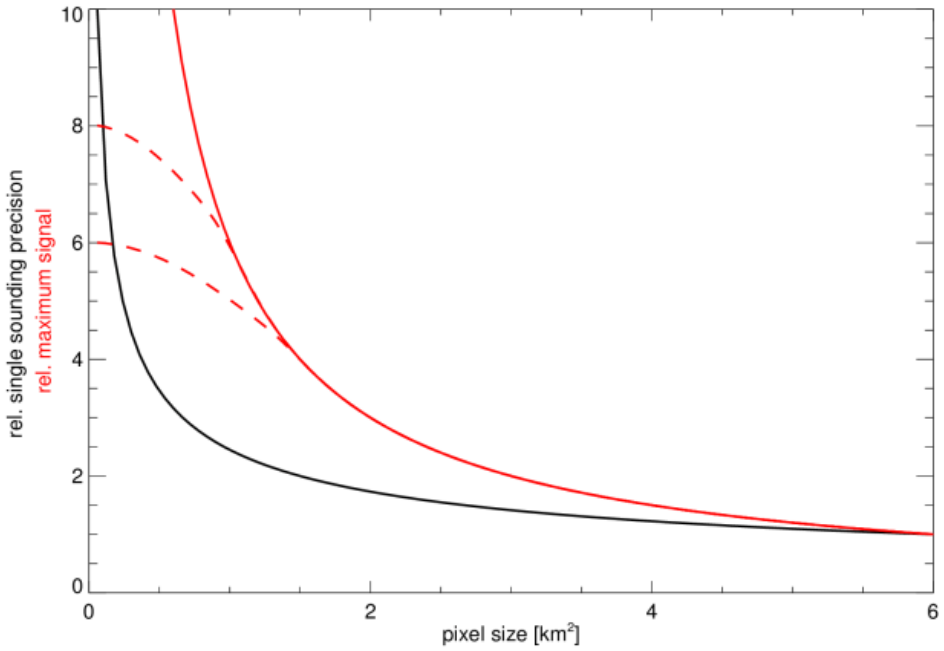

Figure 123: Single sounding precision and maximum signal vs. HSS pixel size for a hypothetic point-target smaller than the HSS pixel size (**solid lines**). The **dashed lines** qualitatively illustrate the expected behaviour when enhancement and pixel size become similar in size.

The just outlined scenario may not be unrealistic for small scale structures in chlorophyll fluorescence. It is probably less realistic for CO_2 or CH_4 sources because even point sources usually produce extended plumes. This means independent of pixel scale, the integrated excess across wind direction is basically constant in wind direction so that the measured maximum enhancement only increases when reducing pixel size across wind direction but not along wind direction. As a result, the maximum signal increases only by $\sqrt{1/a}$ just as the noise (**Figure 125**).

Nevertheless, flux inversions with a Gaussian plume model also suggest an improvement (**Figure 126**). For the performed inversion study, the exact position of the source was assumed to be known. In reality this is not necessarily the case and inversions may further profit from the up-scaled HSS retrievals by being more capable in deriving the location of the source.

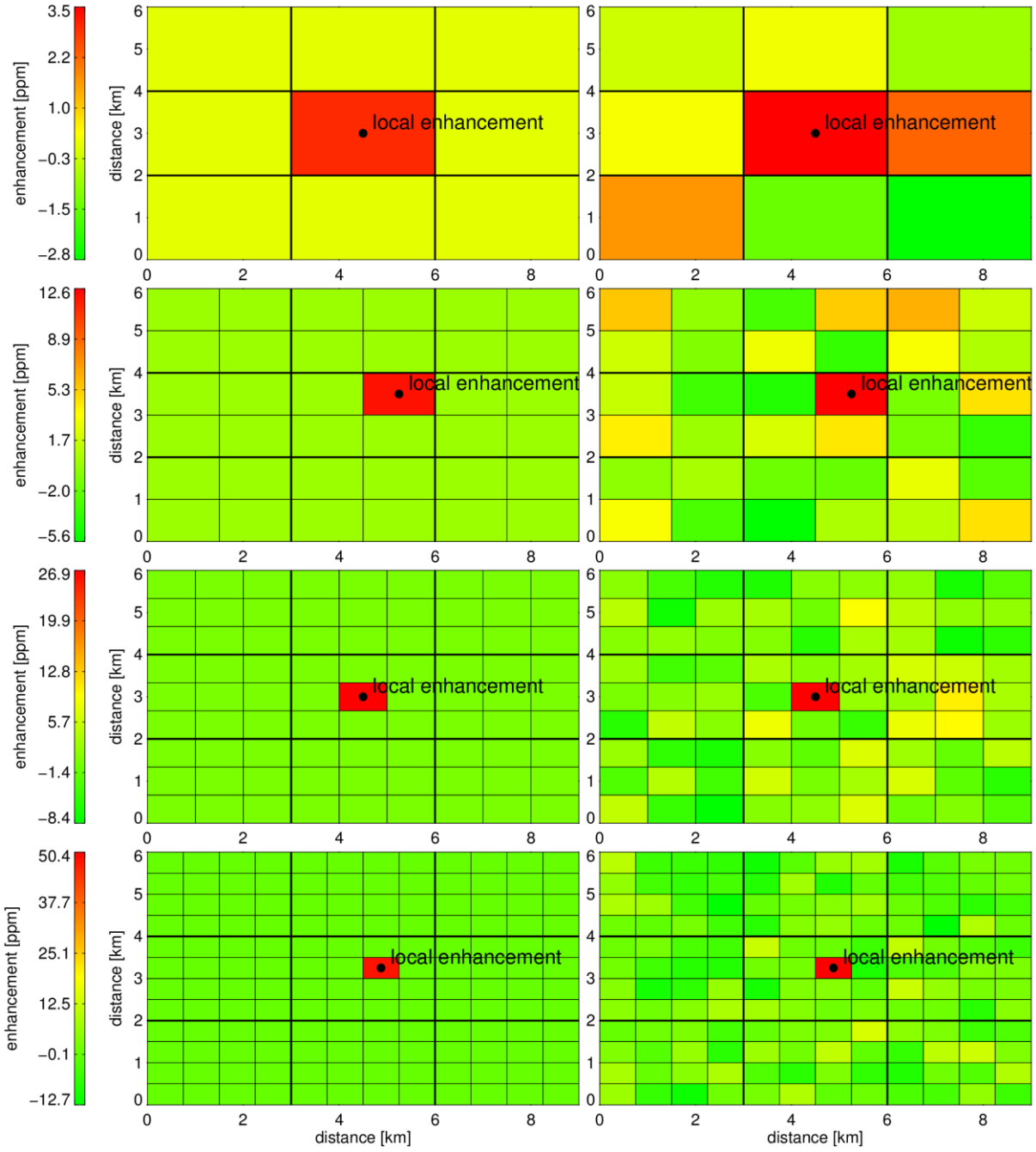

Figure 124: Expected measured enhancement of a hypothetic CO_2 point-target with a strength resulting in an enhancement of 3 ppm relative to background at the resolution of the main instrument (**top**) and at (from **top to bottom**) 4-times, 9-times, and 16-times sub-sampling by the HSS. **left**: without noise. **right**: with 1.5 ppm Gaussian noise.

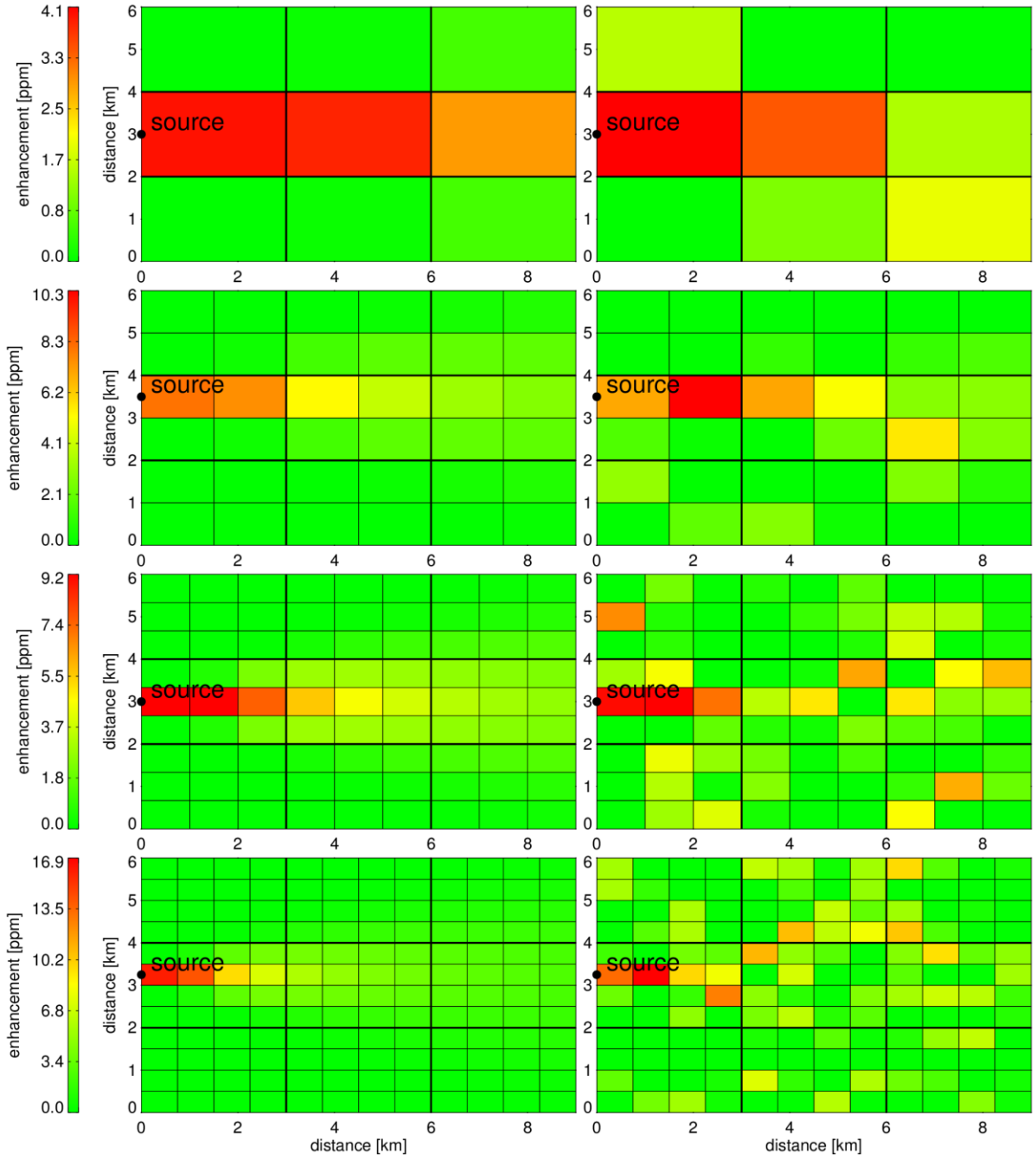

Figure 125: Similar as **Figure 124** but for a CO_2 point source producing a Gaussian plume in wind direction. The maximum enhancement above background at nominal resolution (top, left) is 4.5 ppm. The noise level is 1.5 ppm at nominal resolution.

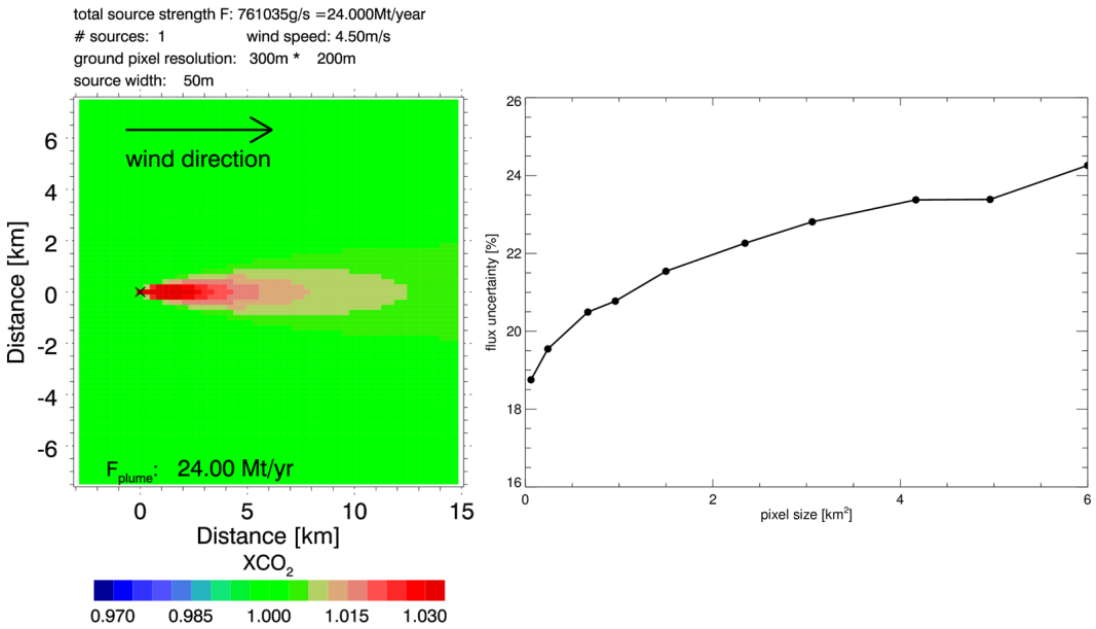

Figure 126: Gaussian plume of a 24Mt/a CO_2 point source (e.g. a power plant) at a wind speed of 4.5 m/s and 200 m x 300 m spatial resolution (**left**). Inversion uncertainty vs. HSS pixel size assuming a single sounding precision of ~2 ppm at 2 km x 3 km nominal resolution (**right**).

16.3. Summary and Conclusions

The comparison of estimated HSS SNR values with SNR estimates for MODIS, MTG, and OLCI suggests that threshold SNR values of the main instrument would likely be sufficient for splitting pixels into 10-30 HSS sub pixels which are suitable for sub pixel cloud detection and classification.

To a first order approximation, the noise of concentration and fluorescence retrievals is invariant for spectral binning (the high spectral resolution of the main instrument is essential for disentangling changes in concentration, scattering at clouds, temperature shifts, water vapour, etc.).

The detection of localised hot spots profits from small HSS pixel sizes because the increase of the enhancement signal over-compensates the increase in single sounding noise. This is especially relevant for fluorescence retrievals.

Hot spot detection of CO_2 and CH_4 profits from small HSS pixels in particular under stable and calm meteorological conditions preventing plume formation. However, quantitative flux inversions are difficult under such conditions.

Under more realistic meteorological conditions, the maximum relative enhancement increases with decreasing pixel size in the same way as the single sounding noise. Nevertheless, flux inversions with a Gaussian plume model also suggest an improvement for smaller pixels. This improvement may be even stronger in cases where the exact source position is not known.

17. Assessment of polarization related errors on Level 2

17.1. Assessments using simulated retrievals (IUP-UB)

In this section polarization related XCO_2 and XCH_4 retrieval errors are quantified using simulated retrievals.

17.1.1. Method and results

In this section it is assessed how large polarization related XCO_2 and XCH_4 biases are if

- (a) no correction is applied, or more precisely, if a fully polarization sensitive instrument is used but only Stokes component *I* is measured and used for retrieval and
- (b) to what extent the biases are reduced assuming (realistic) instrument performance w.r.t. polarization sensitivity using instrument Mueller Matrices.

For this purpose gain matrices have been computed with BESD/C using a range of solar zenith angles and assuming a viewing zenith angle of 15^o and a relative azimuth angle of 0^o (= looking towards the sun) and surface conditions corresponding to a polarizing vegetation surface (with polarizing BRDF).

As a first step the XCO_2 and XCH_4 biases have been computed without applying an instrument Mueller Matrix and without applying any correction to reduce polarization related errors. Detailed results for three SZAs (50^o, 60^o, 70^o) are shown in **Figure 127**, **Figure 129** and **Figure 131**. As can be seen, the biases can be very high and their magnitude typically increases with increasing SZA.

The corresponding results but with an instrument Mueller Matrix applied are shown in **Figure 128**, **Figure 130** and **Figure 132**. The Mueller Matrix (MM) elements (spectra) have been provided by ESA (e-mail J. Caron, 1-Aug-2014). They originate from the industrial consortia working on CarbonSat. The MMs from one of the industrial consortia (ADS) have been used here. In total, 5 MMs have been provided, each corresponding to a certain “Field along slit” (FAS) value.

The results shown in **Figure 128**, **Figure 130** and **Figure 132** are valid for FAS = 0.0 mm. As can be seen, the XCO_2 and XCH_4 biases are reduced to very small values if the MM is taken into account. This is due to the very small magnitude of the corresponding MM elements (shown in the figures), which are essentially scaling factors for the error spectra computed assuming no correction / no MM applied (i.e., as used for **Figure 127**, **Figure 129** and **Figure 131**).

The dramatic reduction of the biases is found for all provided MMs (i.e., for all FAS values) as shown in **Figure 133** and **Figure 134** for XCO_2 and **Figure 135** and **Figure 136** for XCH_4, which summarize the results for all SZA and MMs.

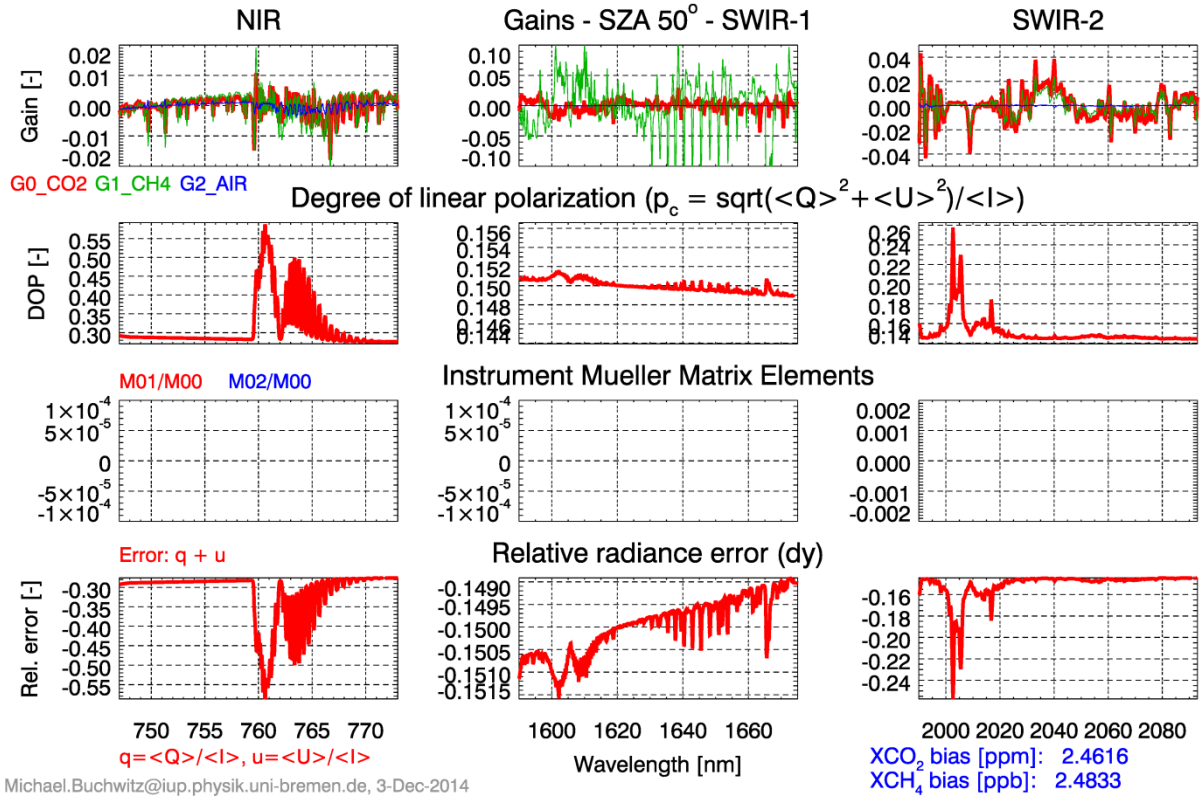

Figure 127: Assessment of XCO_2 and XCH_4 biases due to polarization related spectral errors. Scenario: SZA 50°, viewing zenith angle 15°, relative azimuth angle 0°. The spectral errors have been computed with the SCIATRAN RTM (v3.4) providing polarized radiance spectra of Stokes vectors I, Q, U and V (note that U = V = 0.0 for the conditions used here). Top row: The three gain vectors GO_CO2 (red), G1_CH4 (green) and G2_AIR (blue). 2nd row: Degree of linear polarization (DOP). 3rd row: place holder for instrument Mueller Matrix elements (not used here, therefore empty panels; but used for the corresponding **Figure 128**). Bottom row: Relative radiance error (dy) computed using dy = (<Q>+<U>)/<I> which in this case is equal to <Q>/<I>, i.e., apart from the sign equal to the DOP. The resulting XCO_2 and XCH_4 biases are listed in the bottom right.

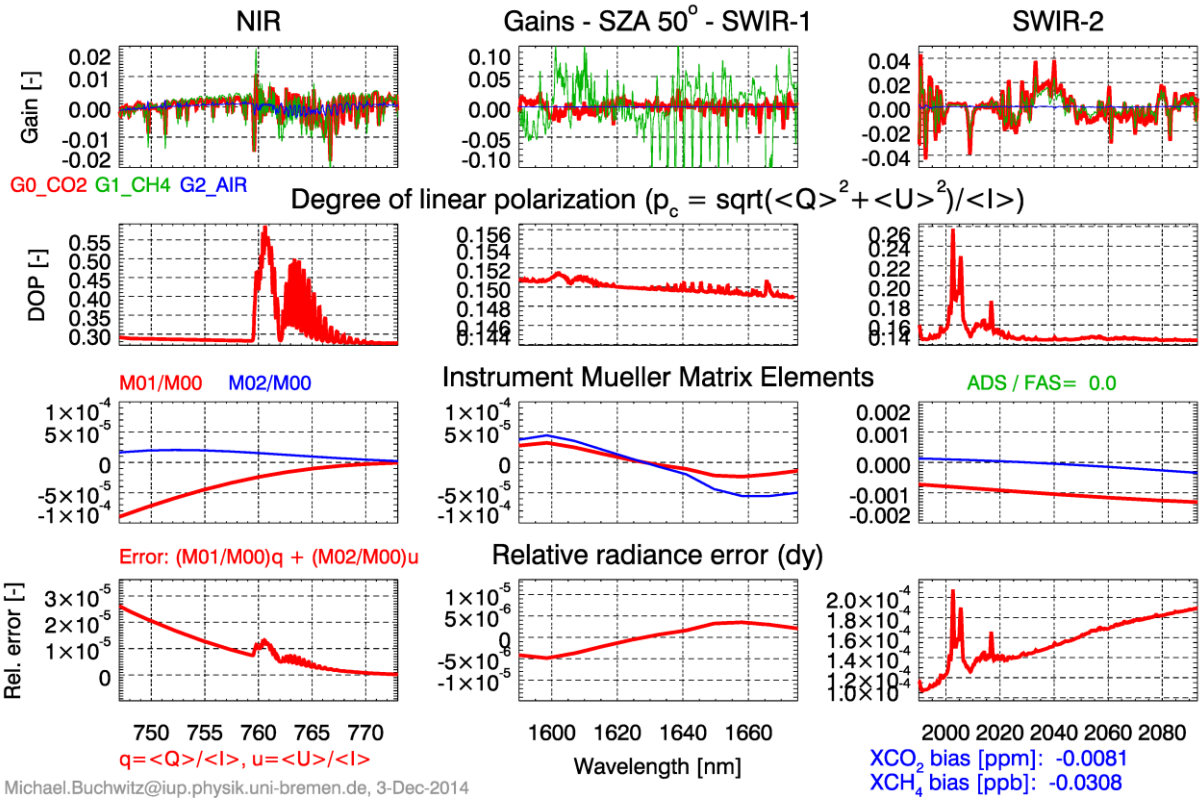

Figure 128: As **Figure 127** but using an instrument Mueller Matrix (provided by ADS; valid for "Field Along Slit" (FAS): 0.0 mm). Here the relative radiance error (dy) has been computed via dy = M_{01}/M_{00}<Q>/<I> + M_{02}/M_{00}<U>/<I>, where M_{ij} are Mueller Matrix elements (spectra). As can be seen by comparing the resulting XCO_2 and XCH_4 biases (bottom right) with the biases shown in **Figure 127**, the biases are dramatically reduced when the Mueller Matrix elements are taken into account for computing the radiance error.

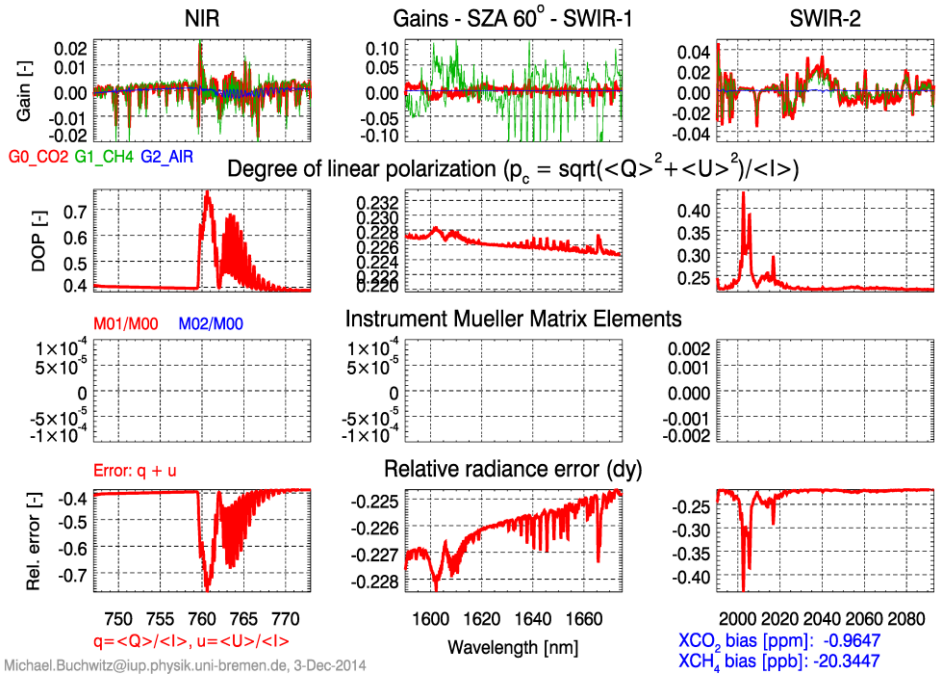

Figure 129: As **Figure 127** but for SZA = 60°.

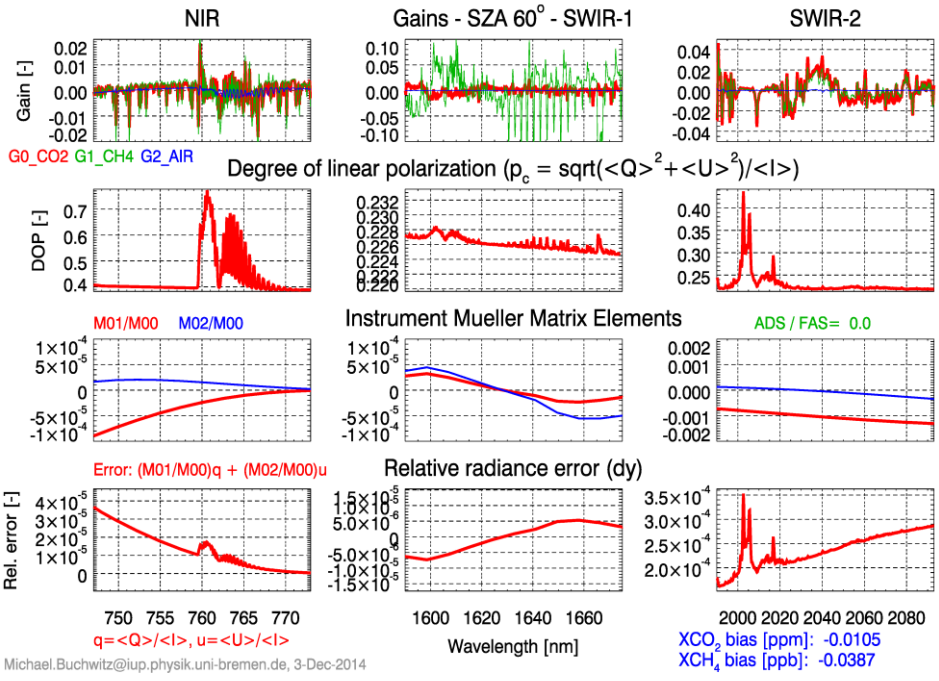

Figure 130: As **Figure 128** but for SZA = 60°.

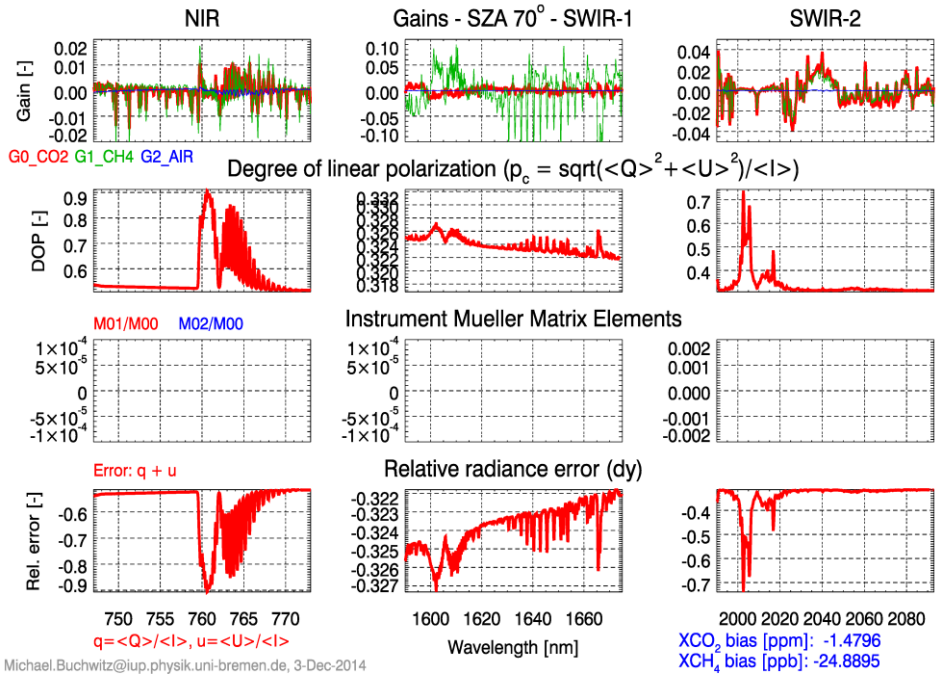

Figure 131: As **Figure 127** but for SZA = 70°.

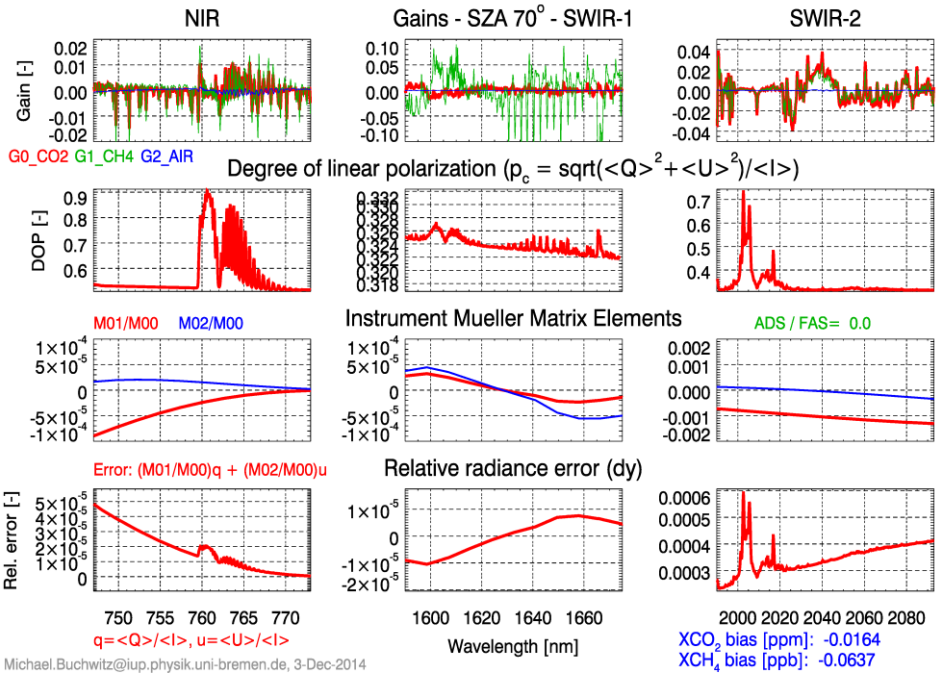

Figure 132: As **Figure 128** but for SZA = 70°.

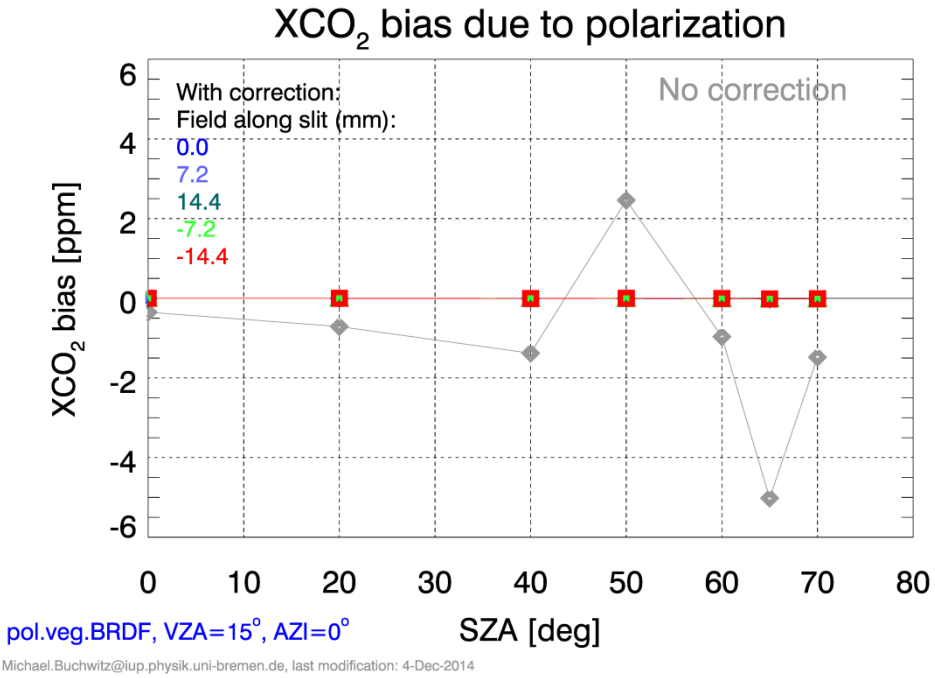

Figure 133: XCO_2 bias without and with correction using instrument Mueller Matrices (for 5 different "Field Along Slit" (FAS) values (in mm)).

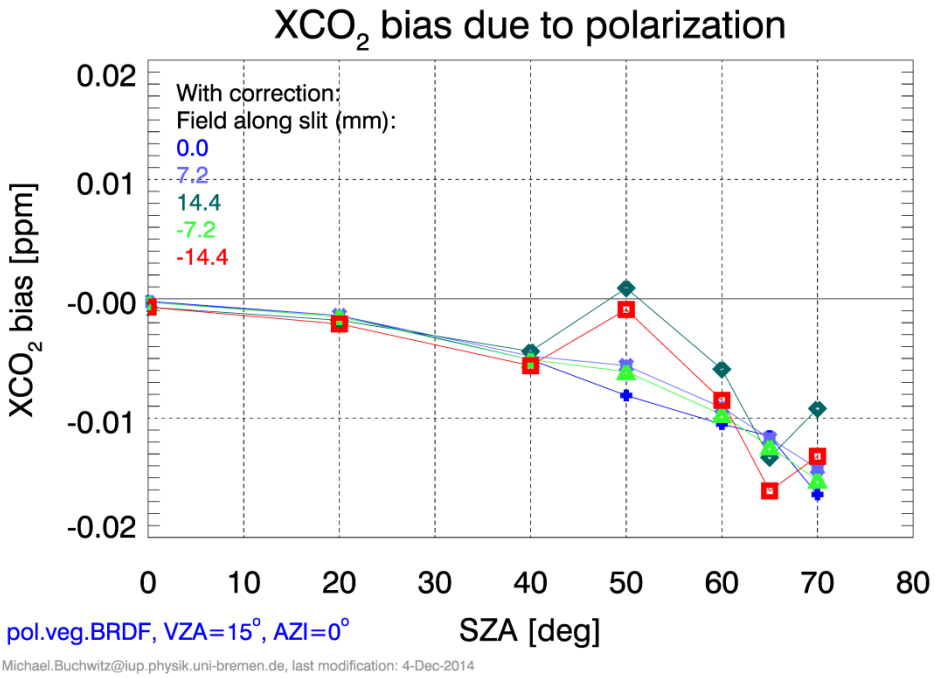

Figure 134: As **Figure 133** but using a smaller y-axis range (y-zoom).

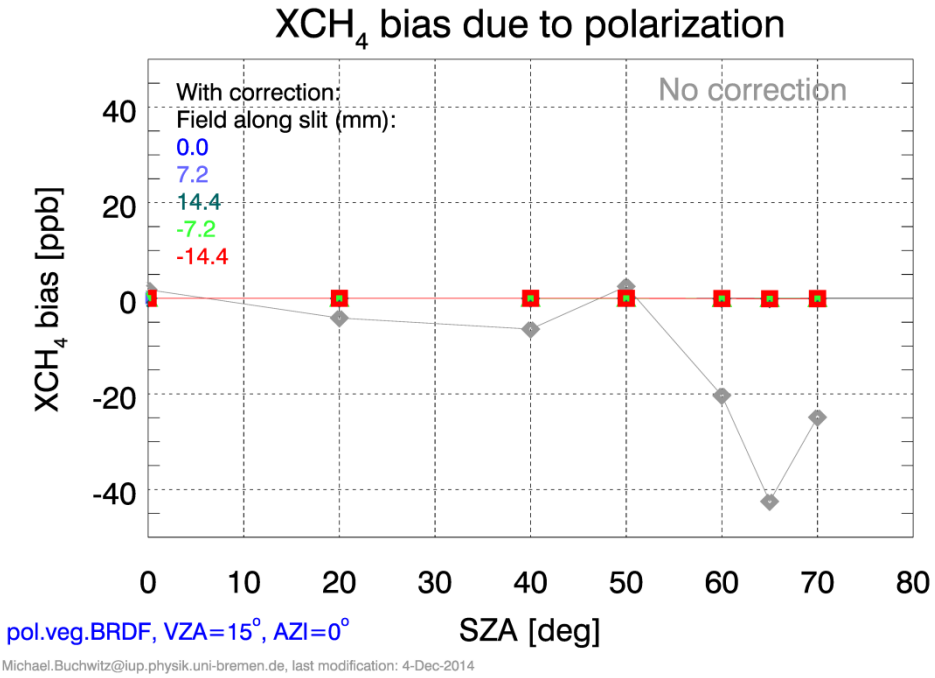

Figure 135: XCH_4 bias without and with correction using instrument Mueller Matrices (for 5 different “Field Along Slit” (FAS) values (in mm)).

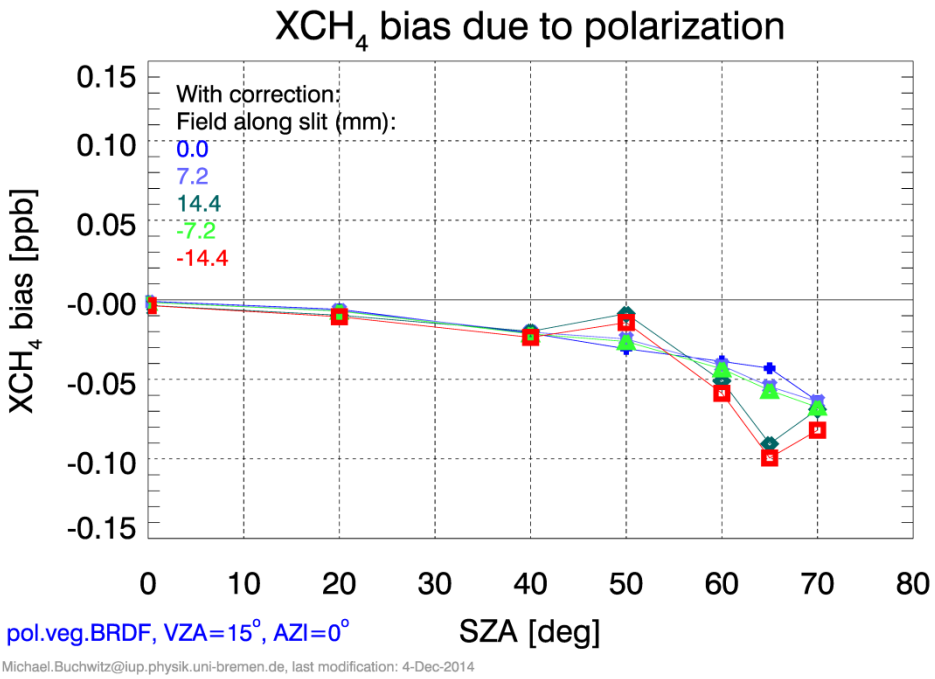

Figure 136: As **Figure 135** but using a smaller y-axis range (y-zoom).

17.1.2. Summary and conclusions

XCO_2 and XCH_4 biases resulting from polarization related radiance errors have been assessed using simulated CarbonSat nadir mode retrievals.

It has been found that the biases can be very large if no correction is applied and a fully polarization sensitive instrument is used. In this case the biases can be as large as several ppm for XCO_2 and several 10 ppb for XCH_4.

For example, the XCO_2 bias is approx. 2.5 ppm for SZA 50^o (see **Figure 127**). In this case the degree of polarization (DOP) is 0.6 (60%) in the NIR band. Note that DOP corresponds to the Polarization Sensitivity (PS) as used in MR-OBS-280 of **/CS MRD v1.2, 2013/**, where it is required that PS is less than 2% (T). If the PS is reduced from 60% to 2% (as required) and assuming that linear error analysis is valid, this would correspond to a XCO_2 bias of 0.083 ppm (= 2.5 ppm / 30), which would be in line with the polarization related error as listed in **Section 4** (error budget total uncertainty for the polarization component of ESRA: < 0.1 ppm (T)).

For XCH_4 the bias can be as large as 25 ppb without correction (e.g., **Figure 131**). In this case DOP is 90% in the NIR band. If the PS reduced from 90% to 2% and assuming that linear error analysis is valid, this would correspond to a XCH_4 bias of ~0.6 ppb (= 25 ppb / 45), which would be in line with the polarization related error as listed in **Section 4** (error budget total uncertainty for the polarization component of ESRA: < 1 ppb (T)).

Polarization related radiance errors have also been computed using several instrument Mueller Matrices as provided by industry. If the radiance errors are computed using these instrument Mueller Matrices, the biases are reduced to below 0.02 ppm for XCO_2 and below 0.15 ppb for XCH_4.

Assuming that the instrument performance as modelled using the provided Mueller Matrices is realistic, it is concluded that polarization related XCO_2 and XCH_4 biases will be quite small. Based on the required / estimated polarization sensitivity and the analysis performed it is concluded that the errors listed in the error budget given in **Section 4** are realistic.

17.2. Assessment using real GOSAT data (SRON)

17.2.1. Introduction

The aim of this study is to verify the CarbonSat requirement on instrument polarization sensitivity using GOSAT RemoTeC retrievals. The CarbonSat requirement is formulated as follows (***/CS MRD v1.2, 2013/***):

> *The light in the NIR reflected by the Earth and the atmosphere can be strongly linearly polarized and earth radiance in the SWIR can also be significantly linearly polarized mainly due to surface reflection. The level of polarisation can reach 100% in deep absorption (sub) bands.*

MR-OBS-280:	*The polarization sensitivity of each spectral channel shall be lower than 0.005 (G) / 0.02 (T).* *NB the degree of polarisation to be considered is up to 100% for the NIR and SWIR-2 bands, and up to 30% for the SWIR-1 band. This shall be met for any fixed polarisation angle between 0 and 180 degrees.*

In this context, polarization sensitivity is defined as (***/CS MRD v1.2, 2013/***):

> "Assuming measurement of a stable, spatially uniform, linearly polarised Lambertian scene, the polarisation sensitivity is defined as **$m = (S_{max} - S_{min}) / (S_{max} + S_{min})$** , where **$S_{max}$** and **$S_{min}$** are the maximum and minimum sample values, respectively, obtained when the polarisation is gradually rotated over 180º."

Caron et al.[3] give an equivalent definition, in a slightly different formulation:

> "Polarization sensitivity is an estimate of the radiometric error due to the absence of knowledge of the polarization state of the measured input signal. It is calculated from the min and max signals measured when the instrument is illuminated with a fully polarized signal that can have any direction."

[3] Polarization scramblers in Earth observing spectrometers: Lessons learned from Sentinel-4 and 5 phases A/B1, www.congrexprojects.com/custom/icso/2012/papers/FP_ICSO-139.pdf

In terms of the measurement simulation as a function of S and P polarized light illuminating the instrument, we may write the measured signal as

$$I_{meas} = (S + P) + m(S - P) \quad (1)$$

where the second term describes the contribution of the measurement due to the polarization sensitivity of the instrument. For the retrieval of CO_2 and CH_4, this term is not considered in the forward simulation and so represents a radiometric error for the retrieval. To stay within the overall CarbonSat error budget, this error must not exceed 0.1 ppm and 1 ppb for CO_2 and CH_4, respectively.

Based on simulated CarbonSat measurements, a maximum polarization sensitivity of 0.02 was derived. The GOSAT instrument provides a unique possibility to confirm this requirement using real measurements. The Fourier Transform Spectrometer measures s- and p-polarized light over the full spectral range of the NIR and SWIR spectral channels, which is used to derive the radiance spectra *I* by

$$I_{meas} = (S + P) \quad (2)$$

The RemoTeC retrieval code uses this radiance signal to infer CO_2 and CH_4 total columns from GOSAT observations.

Modifying the GOSAT measurement using Eq. (1) with a polarization sensitivity *m* adds artificially polarization sensitivity to the GOSAT radiance measurement.

Next, we use the original definition Eq. (2) of the measured radiances in the retrieval and so the effect of instrument polarization sensitivity for real measurements can be estimated. For this purpose, we consider several years of GOSAT measurements, which are co-located with ground-based measurements at twelve TCCON stations. The stations we used are listed in **Table 37**.

Table 37: The TCCON stations where the GOSAT measurements were co-located. The number of processed spectra and the time frames are also listed.

Station	Number of spectra	First date	Last date
Wollongong	1623	22/06/2009	12/12/2012
Tsukuba	169	29/08/2011	27/12/2012
Odankyla	172	30/04/2009	16/09/2012
Parkfalls	1622	25/04/2009	02/09/2011
Orleans	500	29/08/2009	29/12/2012
Lauder	62	26/02/2010	07/06/2013
Lamont	1653	23/04/2009	17/07/2010
Karlsruhe	822	27/04/2010	09/09/2012
Garmisch	803	20/05/2009	08/10/2012
Darwin	1873	23/04/2009	10/12/2012
Bremen	284	23/04/2009	26/03/2012
Bialystok	861	23/04/2009	20/08/2012

For the GOSAT retrievals, we use measurements in the spectral windows specified in

Table 38. Two retrieval runs were carried out, with m having the values m = 0.0 (reference) and m=0.02 (reflecting the requirement *MR-OBS-280*). The differences in the retrieved CH_4 column for both runs provide an estimate for the considered cases.

Table 38: Assumed CarbonSat observation windows for the retrievals presented in this chapter.

Band	O_2 A	SWIR-1a	SWIR-1b	SWIR-2
Spectral range [cm^{-1}]	**12920 – 13195**	**6170 – 6277.5**	**6045 – 6138**	**4806 – 4896**
Spectral resolution FWHM [cm^{-1}]	1.7	1.1	1.1	1.3

17.2.2. Results without CarbonSat Mueller Matrix

The Probability Density Functions (PFDs) of the extra retrieval errors for XCH_4 and XCO_2 are shown in **Figure 137**. The PDFs are largely symmetrical around zero. The mean value of the errors is 0.002% for XCH_4 (0.036 ppb) and 0.0005% for XCO_2 (0.002 ppm).

In almost all cases the extra retrieval error for XCH_4 and XCO_2 is small, with 93% of XCH_4 errors and 94% of XCO_2 errors being within 0.025% (corresponding to 0.1 ppm for XCO_2 and 0.45 ppb for XCH_4).

However, for some retrievals the error caused by the polarization sensitivity can be quite large, exceeding 1% (corresponding to 4 ppm for XCO_2 and 18 ppb for XCH_4) in individual cases.

Integrating the PDFs yields an average of the *absolute* value of the errors of 0.012% for XCH_4 (0.22 ppb) and 0.011% for XCO_2 (0.044 ppm).

The standard deviations of the errors are 0.041% for XCH_4 (0.74 ppb) and 0.040% for XCO_2 (0.16 ppm). These standard deviations do not exceed the maximum errors of 1 ppb (~ 0.06%) for XCH_4 but slightly exceed the maximum error of 0.1 ppm (~ 0.025%) for CO_2 that were assigned within the error budget to the error contribution of polarization sensitivity.

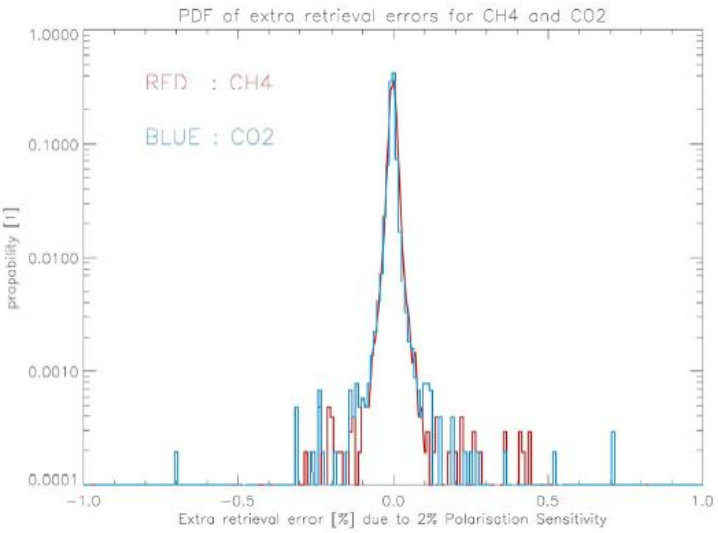

Figure 137: The PDFs of the GOSAT retrieval errors for CH_4 and CO_2 due to an artificially introduced polarization sensitivity m=0.02 of the measurements (please note the logarithmic scale).

Furthermore, the standard deviations of the error distributions varied per station, as has been listed in **Table 39**.

The (absolute) value of the Degree of Polarisation (DoP) in the measurements, averaged over all stations, was 0.12 (NIR), 0.018 (SWIR-1a and SWIR-1b), 0.082 (SWIR-2) in the four windows respectively.

Table 39: The standard deviations of the errors induced by the polarisation sensitivity per station location.

Station	Standard Dev. of CH_4 error [%]	Standard Dev. of CO_2 error [%]
Wollongong	0.041	0.030
Tsukuba	0.076	0.045
Odankyla	0.019	0.033
Parkfalls	0.023	0.029
Orleans	0.046	0.031
Lauder	0.061	0.033
Lamont	0.055	0.042
Karlsruhe	0.043	0.054
Garmisch	0.039	0.042
Darwin	0.025	0.027
Bremen	0.019	0.029
Bialystok	0.048	0.070

17.2.3. Results with CarbonSat Mueller Matrix

In this subsection, we repeated the performance analysis for the CarbonSat polarization sensitivity as presented in the previous section but using a CarbonSat instrument Mueller matrix (made available by ESA; e-mail Bernd Sierk, 26 March 2015) to realistically consider the polarization sensitivity of CarbonSat.

Figure 138 shows the resulting error histograms of the XCH_4 and XCO_2 retrieval errors due to residual polarization-related errors combining the results for 12 TCCON sites (see **Table 37** and **Table 39**). As can be seen, nearly all errors are below 0.1%, i.e., the standard deviation is about 0.05%. 0.05% corresponds to 0.9 ppb for XCH_4 (required: < 1 ppb) and 0.2 ppm for XCO_2 (required: < 0.1 ppm). These results are consistent with the results presented in the previous section as they also indicates that polarization related errors according to this assessment are somewhat smaller (better) than required for XCH_4 but for XCO_2 errors may be somewhat larger (up to a factor of two).

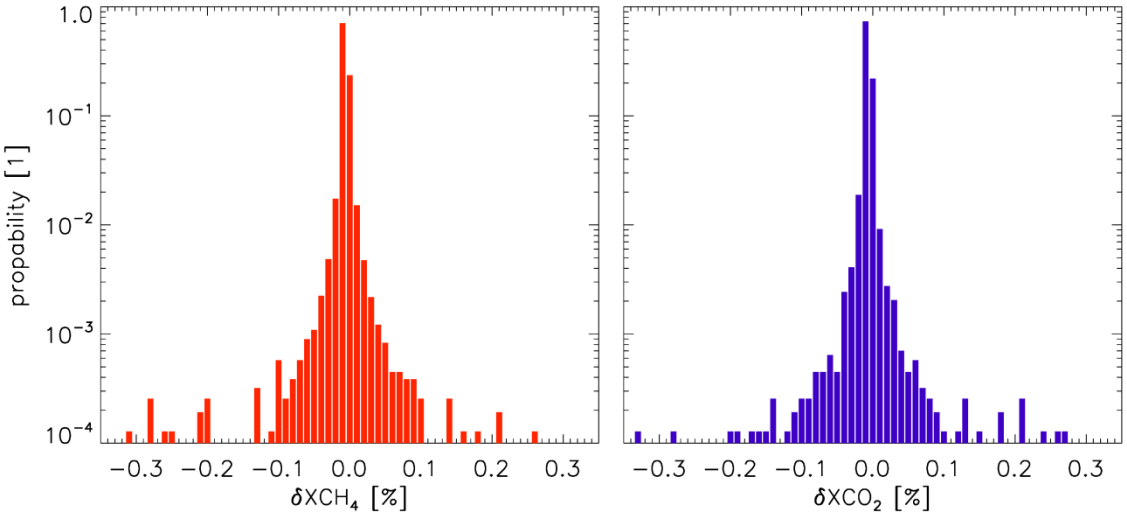

Figure 138: Histograms of the results of the GOSAT error analysis for the CarbonSat instrument polarisation sensitivity based on an industry-provided instrument Mueller matrix combining the results for 12 TCCON sites.

17.2.4. Conclusions

In this study, we have reconsolidated the requirement MR-OBS-280 on the CarbonSat polarization sensitivity using GOSAT measurements.

The Fourier Transform spectrometer GOSAT modulates P and S polarized light separately and so allows us adding artificially polarization sensitivity to the recorded radiance signal.

We showed that for a polarization sensitivity of 2% the induced

- error on XCO_2 is 0.0005% +/- 0.040% (mean +/- standard deviation; 0.002 +/- 0.16 ppm) and the
- error on XCH_4 is 0.0020% +/- 0.041% (0.036 +/- 0.74 ppb).

The station-to-station variability is significant, with standard deviations ranging from 0.019% to 0.076% (XCO_2: 0.97 - 0.3 ppm; XCH_4: 0.34 - 1.37 ppb).

The maximum errors that were assigned within the error budget to the error contribution of polarization sensitivity are 1 ppb (~ 0.06%) for XCH_4 and 0.1 ppm (~ 0.025%) for XCO_2.

The (absolute) value of the Degree of Polarisation (DoP) in the measurements, averaged over all stations, was 0.12 (NIR), 0.018 (SWIR-1a and SWIR-1b), 0.082 (SWIR-2) in the four windows respectively, but it should be kept in mind that the TCCON sites may not cover all possible values of polarization because of the selection criteria for the sites.

Error estimates have also been obtained using an instrument Mueller matrix to realistically consider the polarization sensitivity of CarbonSat. The results confirm the conclusions given above, namely that the requirement for XCH_4 (< 1 ppb) can be met but the requirement for XCO_2 (< 0.1 ppm) is more difficult to achieve as this error could be exceeded by up to a factor of two (i.e., may reach 0.2 ppm).

18. Level 1-2 Pre-Processing (PP) related requirements

The BESD/C retrieval algorithm retrieves three parameters via pre-processing as explained in 5.4:

- Surface albedo in each band
- Cirrus Optical Depth (COD)
- Vegetation Chlorophyll / Solar Induced Fluorescence (VCF / SIF)

In this section instrument related requirements for these pre-processing steps are given.

18.1. Surface albedo

During pre-processing the surface albedo in each band is estimated from nearly transparent spectral regions ("continuum radiance") in each band.

This requires sufficiently good absolute radiometric accuracy (ARA). This aspect is therefore covered in the ARA section in this document, i.e., **Sect. 9.7**.

Note that for most of the results presented in this report a Lambertian surface is assumed for the simulated radiance observations. Also the retrieval method BESD/C used in this report models surface reflection assuming a Lambertian surface in-line with all retrieval algorithms currently used for real (SCIAMACHY, GOSAT, OCO-2) satellite data. This is an approximation and non-Lambertian surface reflection and related XCO_2 and XCH_4 retrieval errors need to be quantified in future CarbonSat-related studies. In case of significant errors it needs to be investigated to what extent the retrieval algorithm can be modified to reduce errors caused by this effect.

18.2. Cirrus Optical Depth (COD)

During pre-processing an estimate of the Cirrus Optical Depth (COD) is obtained via a spectral region covered by band SWIR-2A around 1939 nm as described in **Sect. 5.4** and **Sect. 6.2**.

As can be concluded from the method shown and results explained in **Sect. 6.2**, a radiance error at 1939 nm of $1x10^{10}$ photons/s/nm/cm^2/sr results in a COD error of 0.01, which is already significant for accurate XCO_2 retrieval.

It can therefore be concluded that radiance errors in SWIR-2A need to be less than $1x10^{10}$ photons/s/nm/cm^2/sr.

It has therefore been recommended (see ZLO **Sect. 9.2**) that additive offset errors of the radiance should be less than $1x10^{10}$ photons/s/nm/cm^2/sr in SWIR-2A.

18.3. Vegetation Chlorophyll / Solar Induced Fluorescence (VCF / SIF)

VCF / SIF is retrieved during pre-processing using a small spectral fitting window at 755 nm which covers several clear solar Fraunhofer lines (see **Sect. 5.4** and **/Buchwitz et al., 2013a/**).

The relative radiance response due to VCF / SIF changes is similar as the response to additive radiance offset. Therefore, additive radiance errors should be as small as possible. This has been considered when formulating the zero-level-offset requirement for the NIR band (see **Sect. 9.2.5**).

19. Angle of Polarization (AOP)

On request of ESA it has been assessed to what extent the assumption that the angle of polarization (AoP) is constant for a given scenario across all CarbonSat bands and across all channels within a band.

To assess this, SCIATRAN RT simulations have been carried out.

Figure 139 - Figure 141 show results for a scene with a Lambertian surface albedo 0.05, SZA 58^o, line-of-sight zenith (LOSz) angle 15^o and azimuth angle (AZI) 295^o. As can be seen, the AoP only varies by ~0.2 degree over the entire CarbonSat spectral range.

The same is also true for other angles (**Figure 142 - Figure 144**) and other albedos (not shown here).

It is also expected that this is also true for polarizing surfaces. From what is known about typical surface reflection it appears to be a fair assumption that the polarization properties of surfaces are spectrally smooth. Normally, one calculates the surface polarization using Fresnel reflection (or some modification of it) and so its spectral dependence is governed by the spectral dependence of the refractive index of the surface. **/Litvinov et al., 1999/** uses one fixed value of m = 1.5 to fit RSP surface measurements at different wavelengths. Same does **/Nadal and Breon, 1999/**. Based on this there is not a real indication for a critical dependence of surface polarization on wavelength.

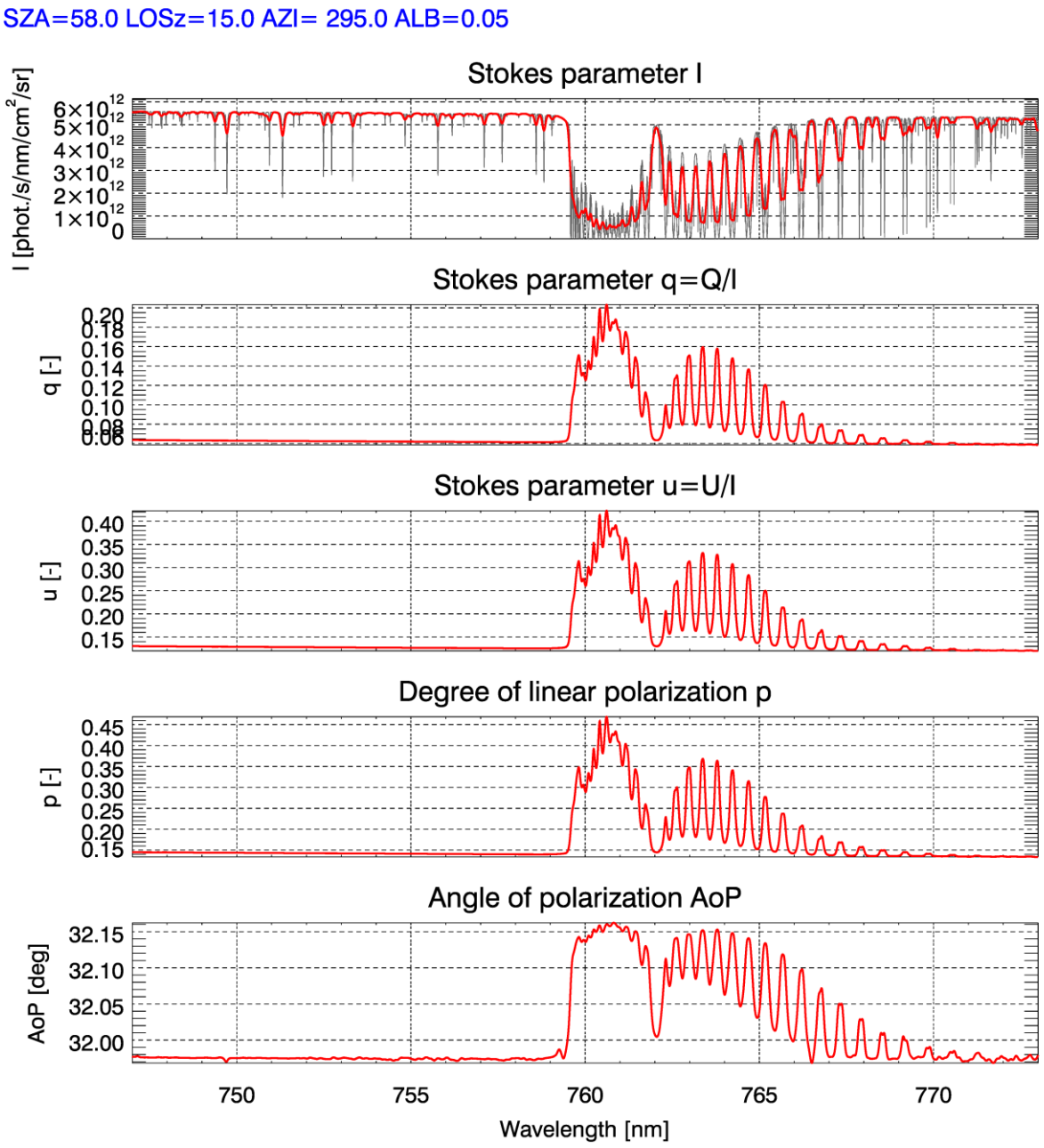

Figure: Michael.Buchwitz@iup.physik.uni-bremen.de, 6-Mar-2015 BAND1_LOS_east_ALBEDO_0.05 (col.: 2)

Figure 139: Stokes parameter spectra for the NIR band including degree of linear polarization (p) and Angle of Polarization (AoP) for a scene with a Lambertian surface albedo 0.05, SZA 58°, line-of-sight zenith (LOSz) angle 15° and azimuth angle (AZI) 295°.

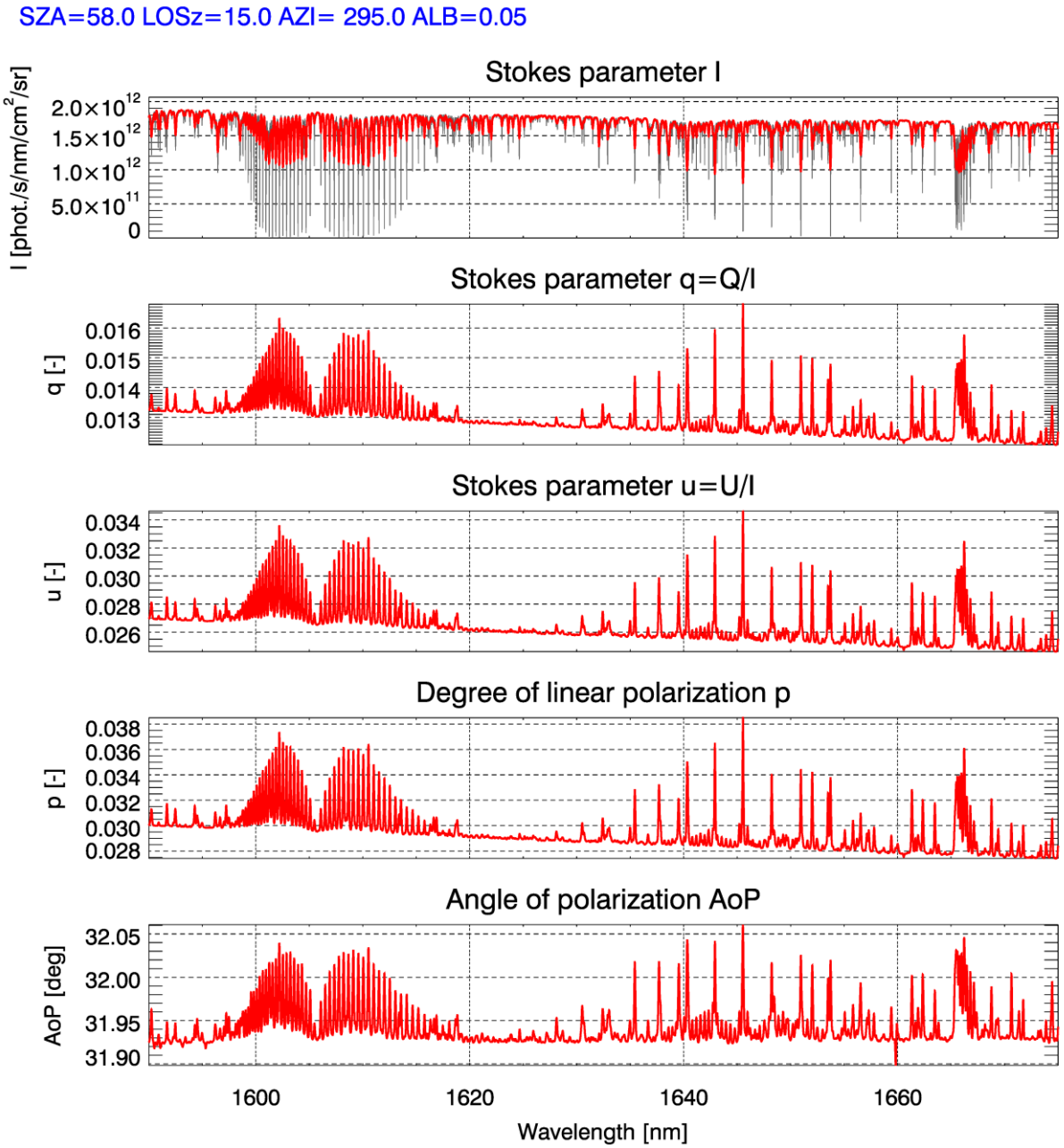

Figure: Michael.Buchwitz@iup.physik.uni-bremen.de, 6-Mar-2015 BAND2_LOS_east_ALBEDO_0.05 (col.: 2)

Figure 140: As **Figure 139** but for the SWIR-1 band.

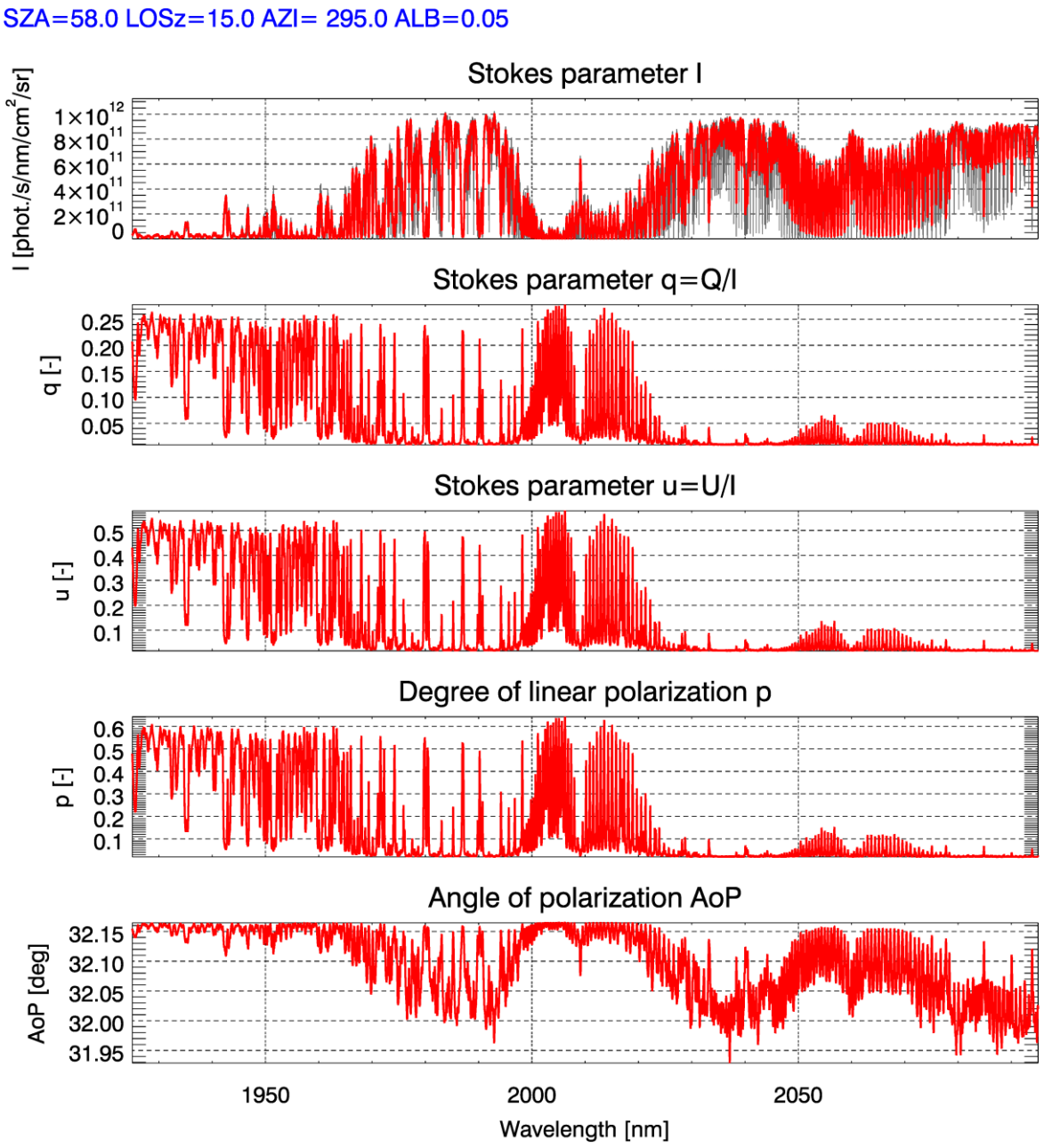

Figure: Michael.Buchwitz@iup.physik.uni-bremen.de, 6-Mar-2015 BAND3_LOS_east_ALBEDO_0.05 (col.: 2)

Figure 141: As **Figure 139** but for the SWIR-2 band.

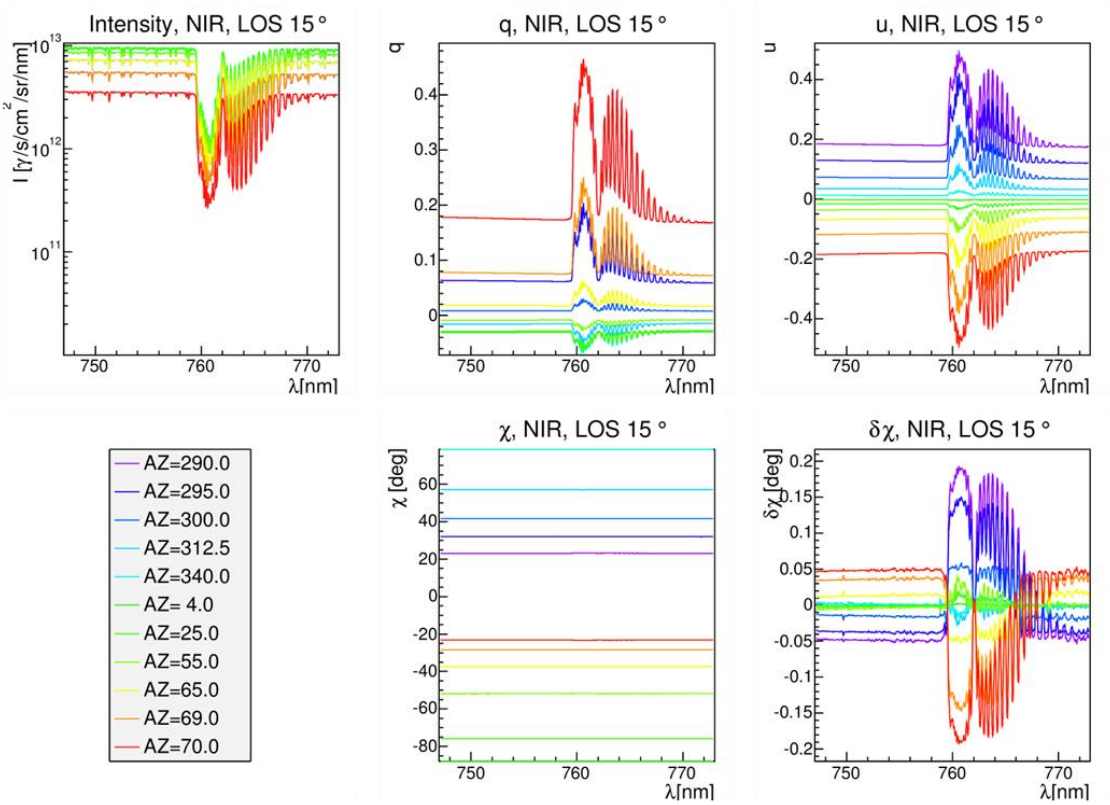

Figure 142: As **Figure 139** but for different SZA and AZI angles.

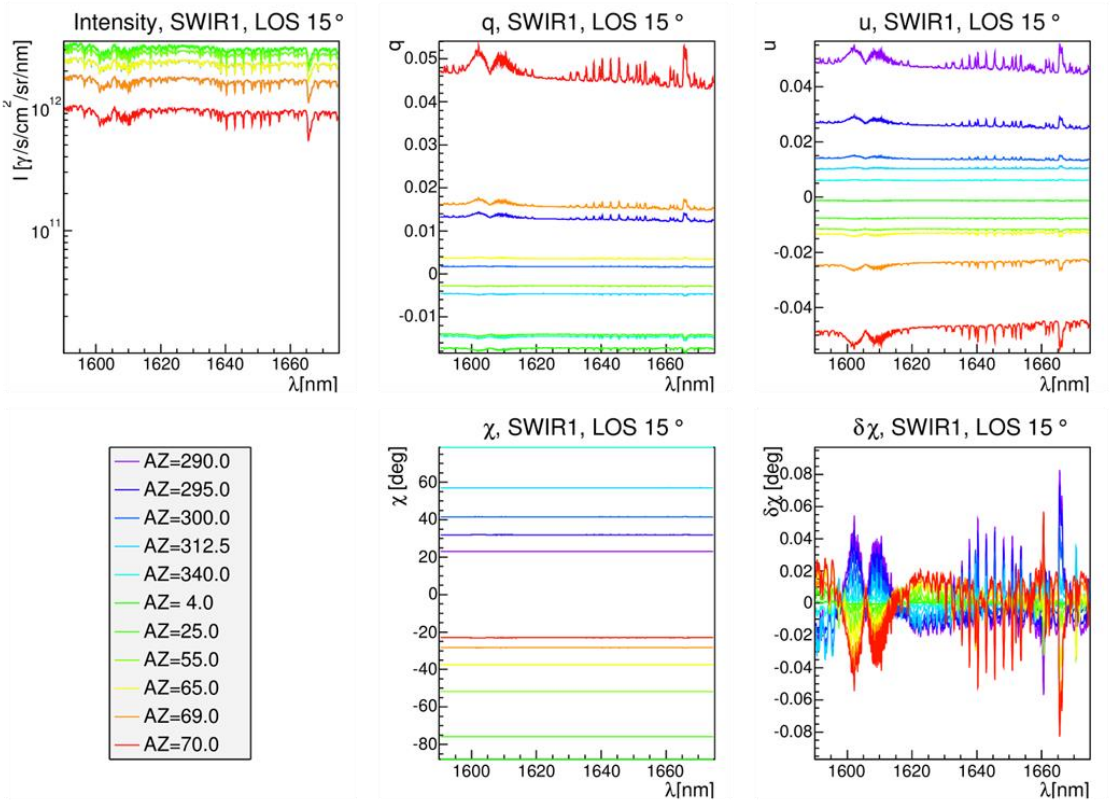

Figure 143: As **Figure 140** but for different SZA and AZI angles.

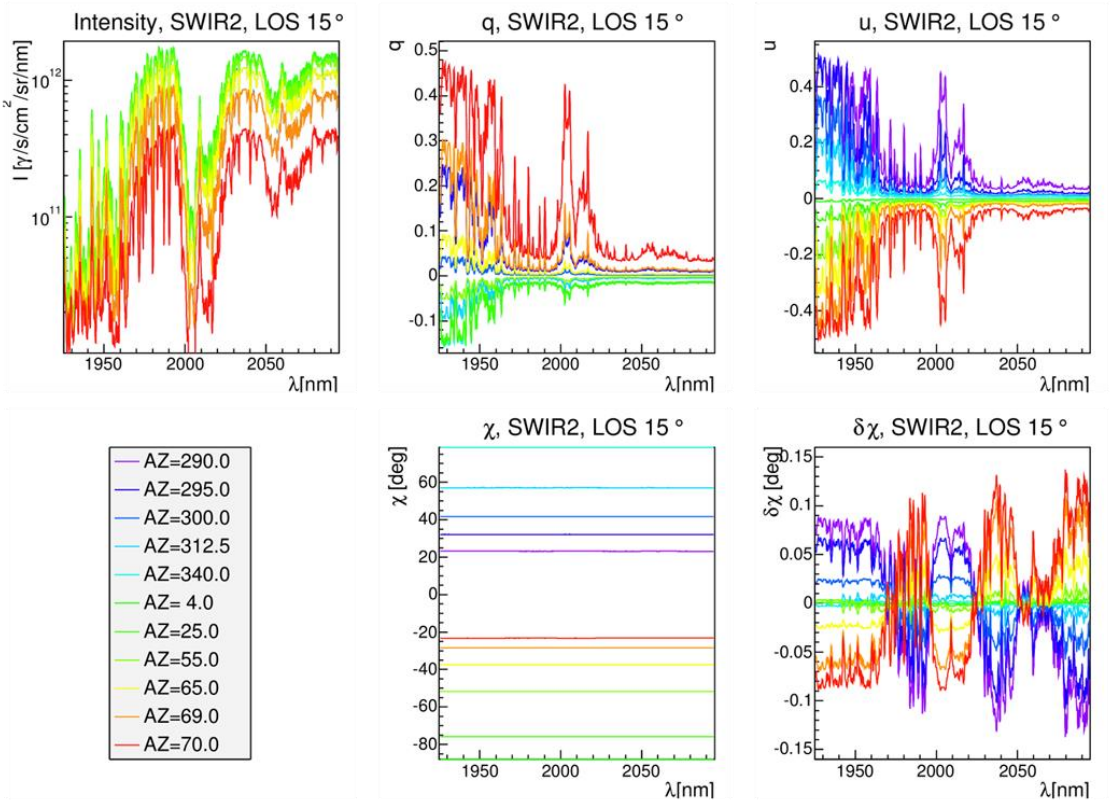

Figure 144: As **Figure 141** but for different SZA and AZI angles.

20. SWIR-2 fitwindow related assessments

On request of ESA it has been investigated if the SWIR-2 fitwindow used for 3-band-retrieval (default: 1990 – 2095 nm = SWIR-2 B and C) can be reduced in particular to exclude regions of strong absorption located in SWIR-2 B (1990 – 2043 nm).

This has been addressed by performing full iterative BESD/C retrievals including pre-processing and quality filtering focussing on 45 cirrus and aerosol scenarios and the VEG50 scenario (vegetation albedo, SZA 50^o) with continental average (CA) aerosol type and varying COD, CTH and AOD.

Figure 145 shows as a reference the results using the default SWIR-2 fitwindow (i.e., using SWIR-2 B and C) for "worst case" reference settings assuming all parameters are unknown (especially VCF/SIF and albedo, which are retreived) and including ZLO as state vector elements.

As the albedo pre-processing retrieval scheme is quite simple and likely preliminary **Figure 146** show results for the same settings but assuming that albedo is well known, i.e., here the true albedo is used instead of the retrieved albedo. As can be seen, the XCO_2 and XCH_4 precisions (random errors) are nearly identical compared to the results shown in **Figure 145** but the biases are somewhat smaller.

Figure 147 used the identical settings as used for **Figure 146** except that only SWIR-2/C (2043 – 2095 nm) has been used as the SWIR-2 fitwindow. As can be seen, the biases get much larger and show a clear correlation with AOD. This shows that - at least for the current version of the BESD/C algorithm - limiting the SWIR-2 fitwindow to the SWIR-2/C range leads to unacceptable results in terms of biases but also in terms of significantly worse XCO_2 precision.

Figure 148 shows the corresponding results when using the 2022 – 2095 nm fitwindow. As can be seen, the bias and precision degradation is still high although somewhat less dramatic compared to the results shown in **Figure 147**.

These results suggest that including the SWIR-2/B range is important in particular as is helps to reduce aerosol related errors. This is confirmed by **Figure 149** where only SWIR-2/B has been used as the SWIR-2 fitwindow. Here the results are very similar as the results obtained for the current default fitwindow shown in **Figure 146**. Except for XCO_2 precision, which is worse for the results shown in **Figure 149**.

In summary it is concluded that the currently used SWIR-2 fitwindow (1990 – 2095 nm = SWIR-2 B and C) should not be reduced in spectral coverage as this results in a significant degradation in terms of larger biases and worse precision. To what extent these conclusions depend on the retrieval algorithm is currently unclear.

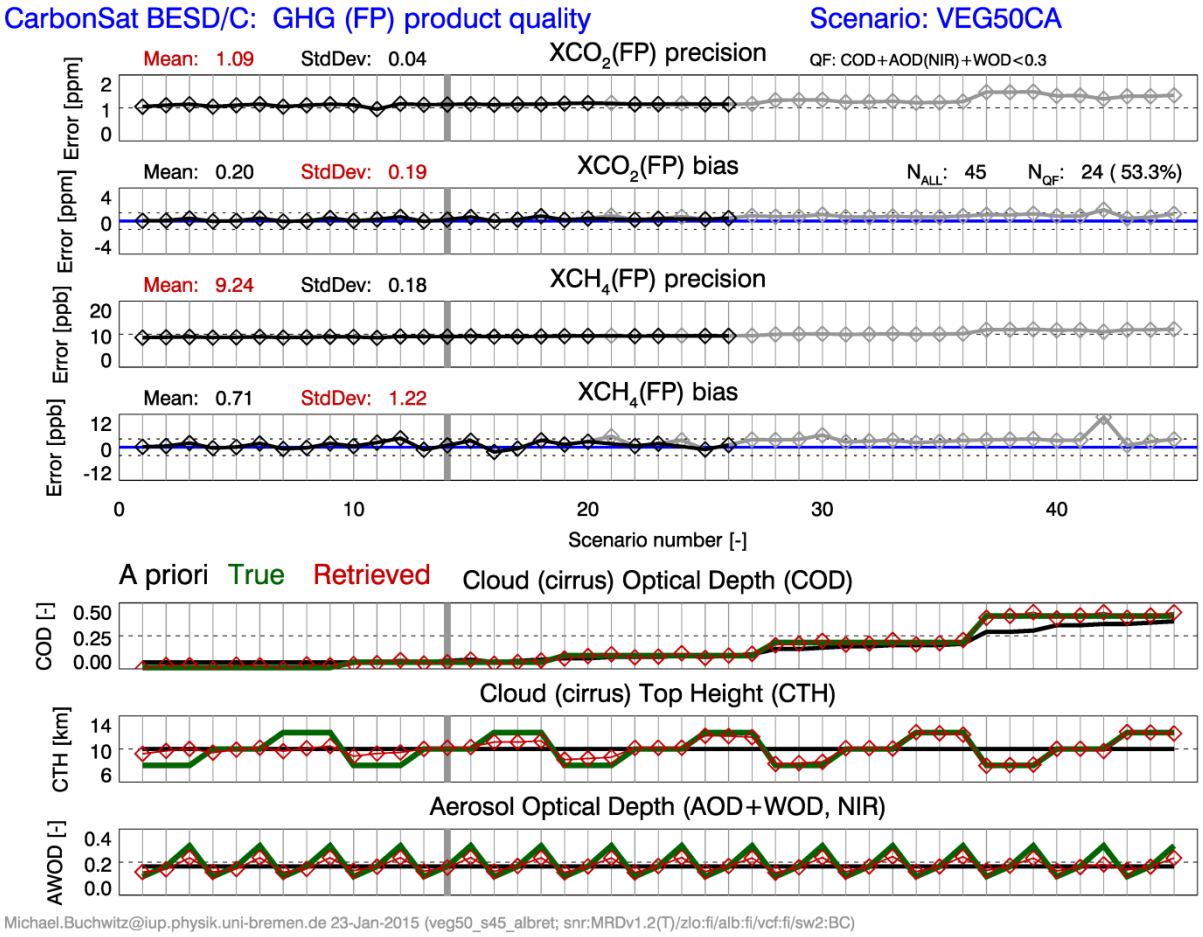

Figure 145: XCO_2 and XCH_4 errors for 45 different cloud and aerosol scenarios (VEG50) for full iterative BESD-C retrievals including ZLO, VCF/SIF and albedo retrieval using the CarbonSat default SWIR-2 fitwindow (SWIR-2 B and C: 1990-2095 nm) for BESD/C 3-band-retrieval.

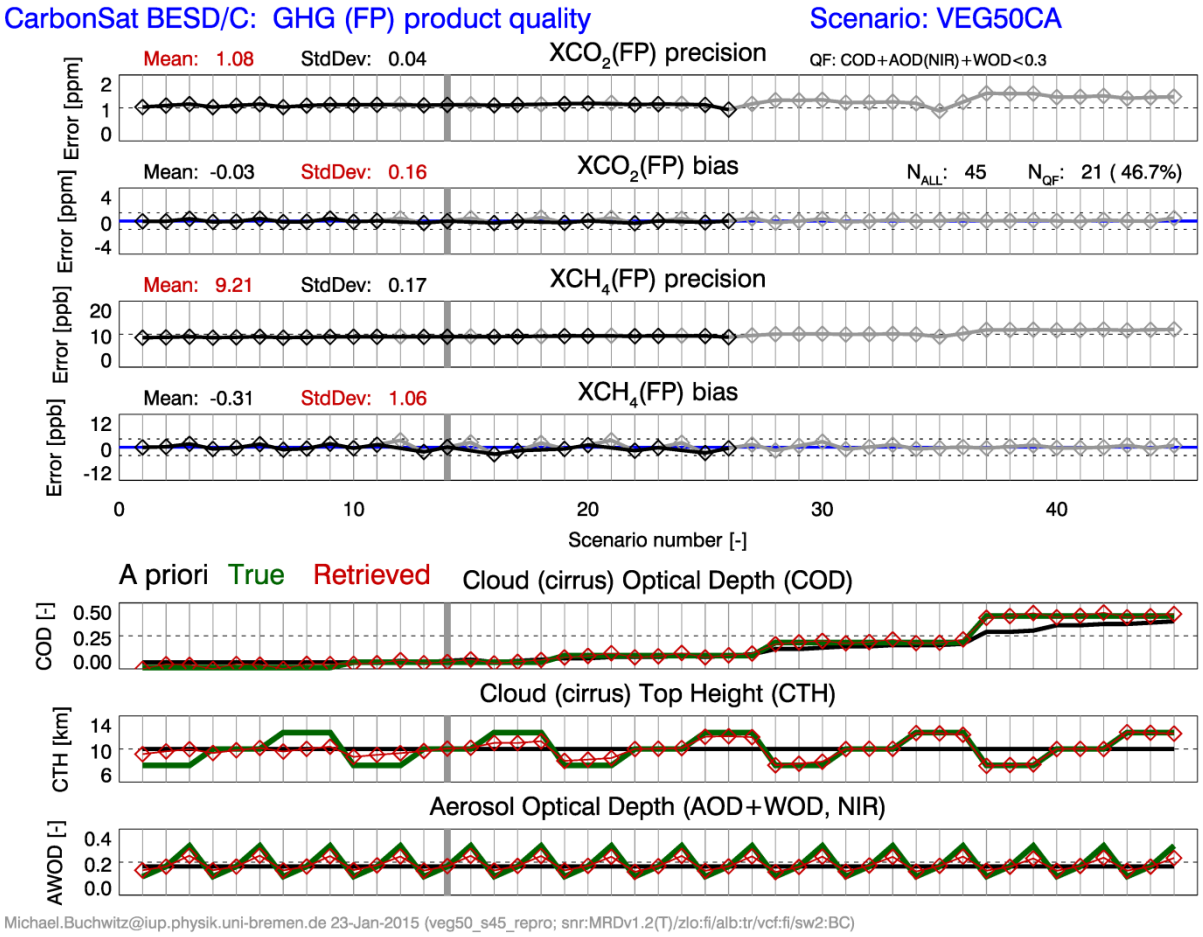

Figure 146: As **Figure 145** but using the true albedo instead of the retrieved albedo.

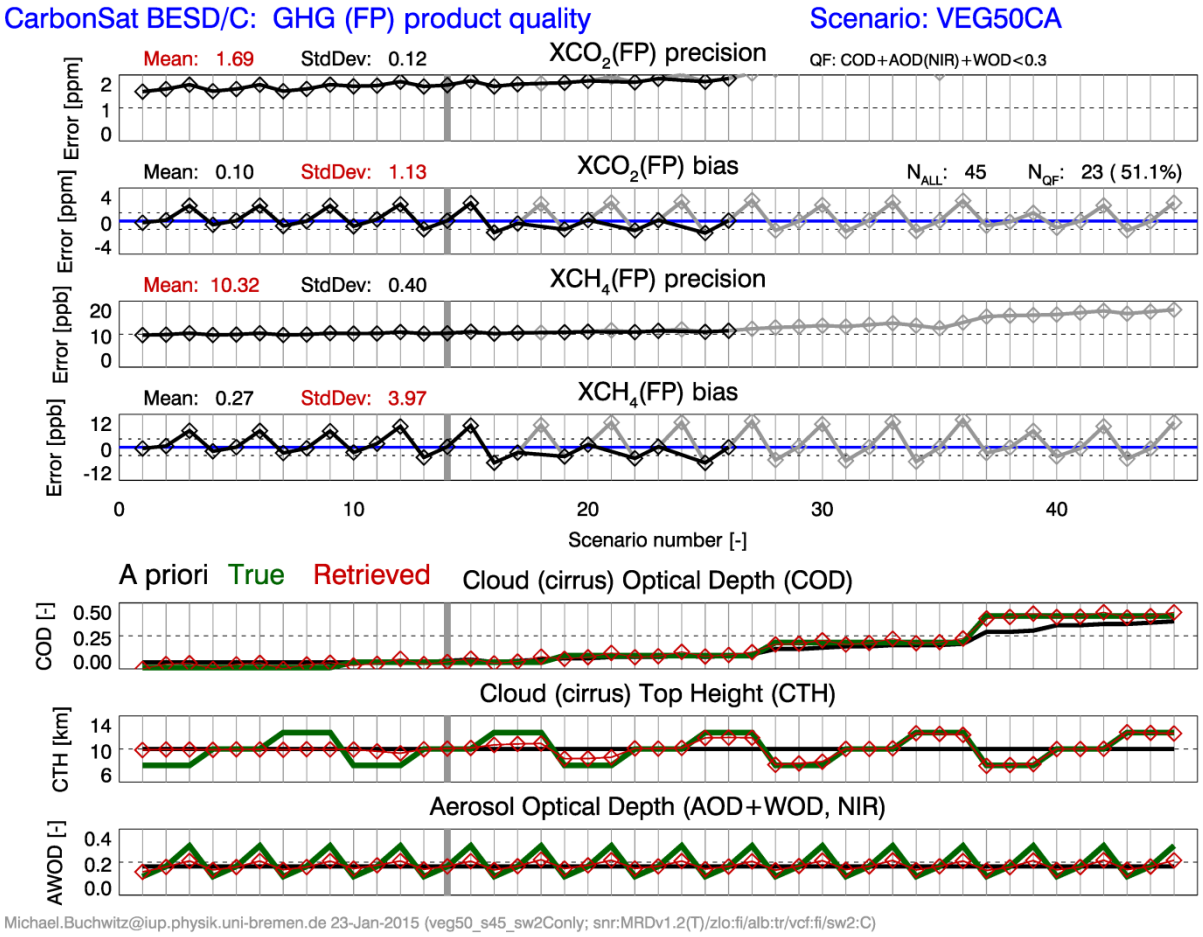

Figure 147: As **Figure 146** but using only SWIR-2 C (2043-2095 nm) instead of the default range (= B and C, i.e., 1990-2095 nm).

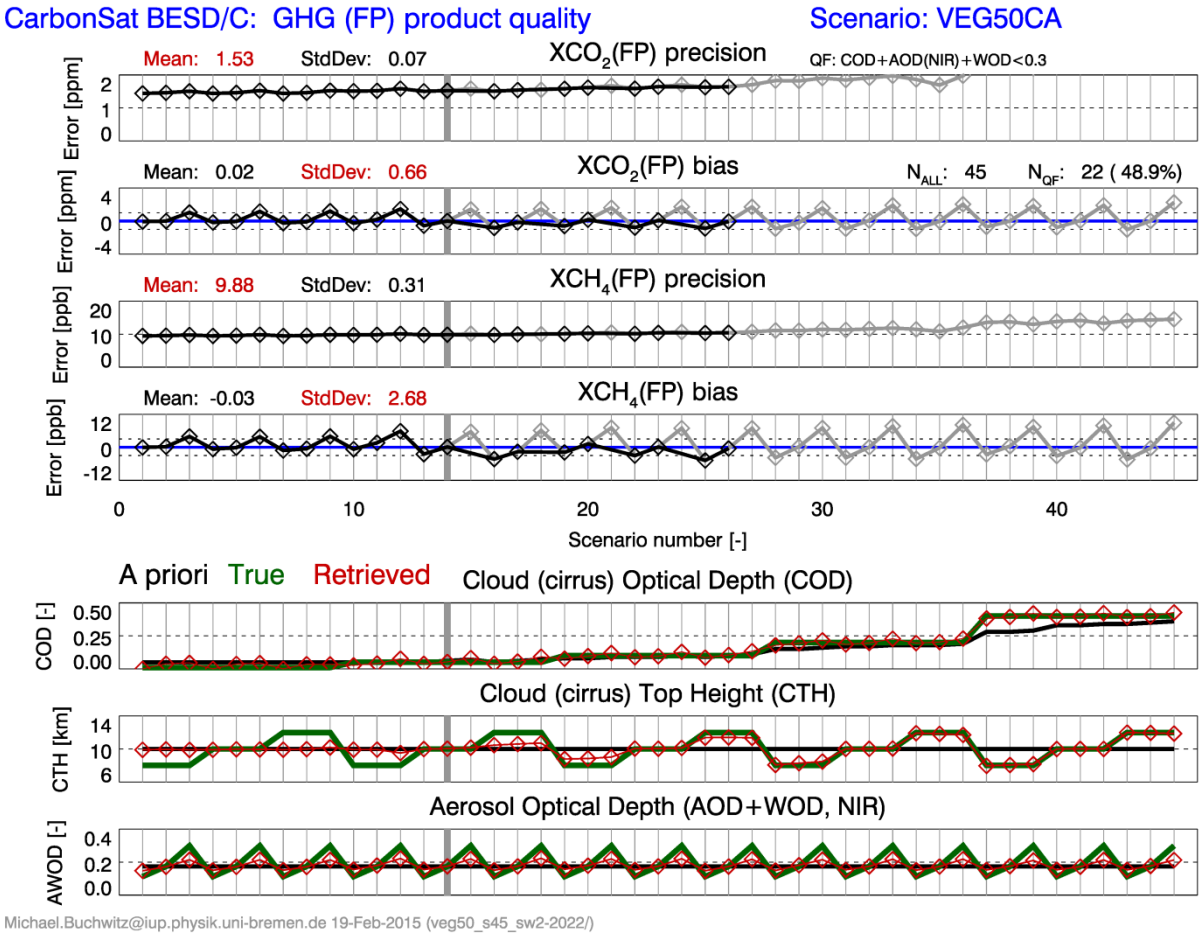

Figure 148: As **Figure 146** but using only SWIR-2 2022-2095 nm instead of the SWIR-2 default range.

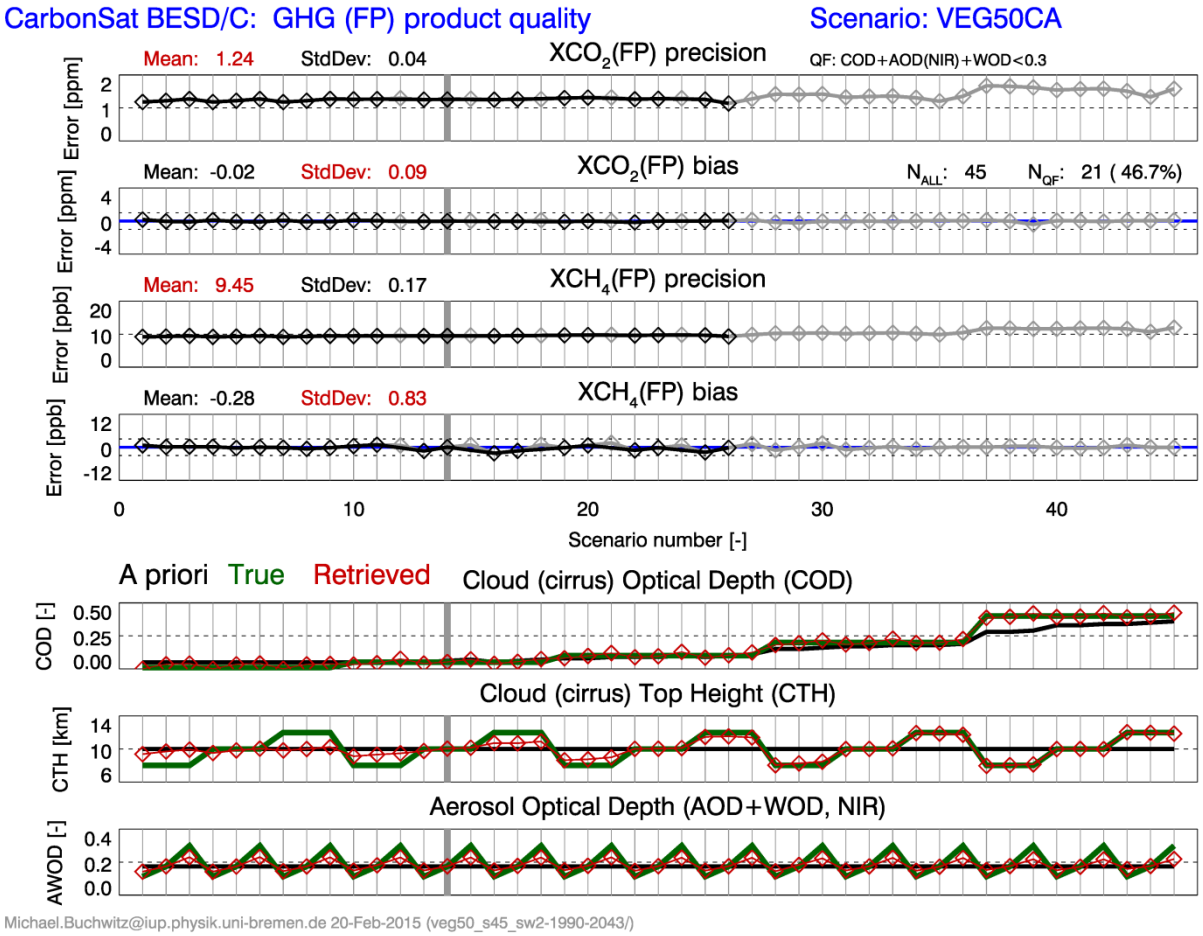

Figure 149: As **Figure 146** but using only SWIR-2 B (1990-2095 nm) instead of the SWIR-2 default range.

21. Acronyms and abbrevations

Acronym	Meaning
AAI	Absorbing Aerosol Index
AK	Averaging Kernel
AOD	Aerosol Optical Depth
ARA	Absolute Radiometric Accuracy
AVIRIS	Airborne Visible / Infrared Imaging Spectrometer
AZI	Azimuth angle
BC	Bias Correction
BESD	Bremen optimal EStimation DOAS
BESD/C	BESD retrieval algorithm for CarbonSat
BL	Boundary Layer
BRDF	Bidirectional Reflectance Distribution Function
CA	Continental Average (aerosol type)
C&A	Clouds and Aerosols
CALIPSO	Cloud-Aerosol Lidar and Infrared Pathfinder *Satellite* Observations
CarbonSat	Carbon Monitoring Satellite
COD	Cloud / cirrus Optical Depth
CA	Continental Polluted (aerosol type)
CS	CarbonSat
CTH	Cloud / cirrus Top Height
DE	Desert (aerosol type)
DES	Desert (surface albedo)
DOAS	Differential Optical Absorption Spectroscopy
DOF	Degrees of Freedom
DOP	Degree of (linear) Polarization
EB	Error Budget
ECMWF	European Centre for Medium Range Weather Forecasts
ENVISAT	Environmental Satellite
ESRA	Effective Spectral Radiometric Accuracy
EVI	Enhanced Vegetation Index
FLEX	Fluorescence Explorer
FLD	Fraunhofer Line Depth
FWHM	Full Width at Half Maximum
GHG	Greenhouse Gas
GOSAT	Greenhouse Gases Observing Satellite
GM	Gain Matrix
GMES	Global Monitoring for Environment and Securitiy
GMM	Gain Matrix Method
GPP	Gross Primary Production
IE	Integrated Energy

ILS	Instrument Line Shape
ISRF	Instrument Spectral Response Function
HSS	High Spatial Sampling
IUP-UB	Institute of Environmental Physics (Institut für Umweltphysik), University of Bremen, Germany
ILS	Instrument Line Shape
L1	Level 1
L2	Level 2
LUT	Look Up Table
MACC	Modelling of Atmospheric Composition and Climate (EU FP7 project)
MAMAP	Methane Airborne Mapper
MODIS	Moderate resolution Imaging Spectrometer
MRD	Mission Requirements Document
NDVI	Normalized Difference Vegetation Index
NIR	Near Infra Red
OCO-2	Orbiting Carbon Observatory 2
OE	Optimal Estimation
OPAC	Optical Properties of Aerosol and Clouds
PDF	Probability Density Function
PN	Pseudo Noise
PP	Pre-Processing
RMSE	Root Mean Square Error
RSRA	Relative Spectral Radiometric Accuracy
RSS	Root Sum Square
RTM	Radiative Transfer Model
RxRA	Relative Spatial Radiometric Accuracy
SAS	Sand/soil (surface albedo)
S-5	Sentinel 5
S-5P	Sentinel 5 Precursor
SCIAMACHY	Scanning Imaging Absorption Spectrometers for Atmospheric Chartography
SCIATRAN	Radiative Transfer Model under development at IUP
SEDF	System Energy Distribution Function
SIE	System Integrated Energy
SIF	Solar-Induced Fluorescence (see also VCF)
SFM	Spectral Fitting Method
SNR	Signal to Noise Ratio
SRTM	Shuttle Radar Topography Mission
SSD	Spatial Sampling Distance
SSI	Spectral Sampling Interval
SSR	Spectral Sampling Ratio
SZA	Solar Zenith Angle
TCCON	Total Carbon Column Observation Network

TOA	Top of atmosphere
TOC	Top of canopy
TRD	Tropical Dark (scenario)
TRM	Tropical Dynamic Range Maximum (scenarios)
UoL	University of Leicester
VEG	Vegetation (surface albedo)
VCF	Vegetation Chlorophyll Fluorescence (see also SIF)
VMR	Volume Mixing Ratio
VZA	Viewing Zenith Angle
ZLO	Zero Level Offset

22. References

/Aben et al., 2007/ Aben, I., Hasekamp, O., Hartmann, W., Uncertainties in the space-based measurements of CO_2 columns due to scattering in the Earth's atmosphere, Journal of Quantitative Spectroscopy & Radiative Transfer, 104, 450–459, 2007.

/Ackerman et al., 1998/ S. A. Ackerman, K. I. Strabala, W. P. Menzel, R. A. Frey, C. C. Moeller, L. E. Gumley: Discriminating clear sky from clouds with MODIS. Journal of Geophysical Research-Atmospheres, vol. 103 (D24), p. 32141-32157

/Ackerman et al., 2002/ S. Ackerman, K. Strabala, P. Menzel, R. Frey, C. Moeller, L. Gumley, B. Baum, S. W. Seeman, H. Zhang Discriminating: Clear Sky from Cloud (Algorithm Theoretical Basis Documents). NASA Goddard Space Flight Center, ATBD-MOD-06, Version 4 (10.01.2002)
http://modis.gsfc.nasa.gov/data/atbd/atbd_mod06.pdf

/Ansmann et al., 1992/ Ansmann, A., Wandinger, U., Riebesell, M., Weitkamp, C., and Michaelis, W., Independent measurement of extinction and backscatter profiles in cirrus clouds by using a combined Raman elastic-backscatter lidar, Appl. Opt., 31, 7113–7131, 1992.

/Boesch et al., 2011/ Boesch, H., D. Baker, B. Connor, D. Crisp, and C. Miller, Global characterization of CO_2 column retrievals from shortwave-infrared satellite observations of the Orbiting Carbon Observatory-2 mission, Remote Sensing, 3 (2), 270-304, 2011.

/Boesch et al., 2006/ Boesch, H., Toon, G. C., Sen, B., Washenfelder, R. A., Wennberg, P. O., Buchwitz, M., de Beek, R., Burrows, J. P., Crisp, D., Christi, M., Connor, B. J., Natraj, V., and Yung, Y. L.: Space-based near-infrared CO_2 measurements: Testing the Orbiting Carbon Observatory retrieval algorithm and validation concept using SCIAMACHY observations over Park Falls, Wisconsin, J. Geophys. Res., 111, D23302, doi:10.1029/2006JD007080, 2006.

/Bovenmann et al., 2010/ Bovensmann, H., Buchwitz, M., Burrows, J. P., Reuter, M., Krings, T., Gerilowski, K., Schneising, O., Heymann, J., Tretner, A., and Erzinger, J., A remote sensing technique for global monitoring of power plant CO_2 emissions from space and related applications, Atmos. Meas. Tech., 3, 781-811, 2010.

/Bovensmann et al., 1999/ Bovensmann, H., J. P. Burrows, M. Buchwitz, J. Frerick, S. Noël, V. V. Rozanov, K. V. Chance, and A. H. P. Goede, SCIAMACHY - Mission objectives and measurement modes, J. Atmos. Sci., 56, (2), 127-150, 1999.

/Buchwitz et al., 2014/ Task 3 Technical Note: Update CarbonSat Level 2 error (L2e) data set, ESA study "LOGOFLUX 2- CarbonSat Earth Explorer 8 Candidate Mission - Inverse Modelling and Mission Performance Study", Draft 1, 13-Aug-2014, 2014.

/Buchwitz et al., 2013a/ Buchwitz, M., M. Reuter, H. Bovensmann, D. Pillai, J. Heymann, O. Schneising, V. Rozanov, T. Krings, J. P. Burrows, H. Boesch, C. Gerbig, Y. Meijer, and A. Loescher, Carbon Monitoring Satellite (CarbonSat): assessment of atmospheric CO_2 and CH_4 retrieval errors by error parameterization, Atmos. Meas. Tech., 6, 3477-3500, 2013.

/Buchwitz et al., 2013b/ Buchwitz, M., M. Reuter, H. Bovensmann, D. Pillai, J. Heymann, O. Schneising, V. Rozanov, T. Krings, J. P. Burrows, H. Boesch, C. Gerbig, Y. Meijer, and A. Loescher, Carbon Monitoring Satellite (CarbonSat): assessment of scattering related atmospheric CO_2 and CH_4 retrieval errors and first results on implications for inferring city CO_2 emissions, Atmos. Meas. Tech. Discuss., 6, 4769-4850, 2013.

/Buchwitz et al., 2013c/ Buchwitz, M., H. Bovensmann, M. Reuter, J. Heymann, O. Schneising, et al., CARBONSAT: ERROR ANALYSIS FOR PRIMARY LEVEL 2 PRODUCTS XCO_2 AND XCH_4 AND SECONDARY PRODUCT VEGETATION CHLOROPHYLL FLUORESCENCE FOR NADIR OBSERVATIONS OVER LAND, ESA Living Planet Symposium, Sept 9-13, 2013, Edinburgh, UK, conference proceedings ESA Special Publication SP-722 (on CD-ROM), 2013.

/Buchwitz et al., 2013d/ Buchwitz, M., M. Reuter, O. Schneising, H. Boesch, S. Guerlet, B. Dils, I. Aben, R. Armante, P. Bergamaschi, T. Blumenstock, H. Bovensmann, D. Brunner, B. Buchmann, J. P. Burrows, A. Butz, A. Chédin, F. Chevallier, C. D. Crevoisier, N. M. Deutscher, C. Frankenberg, F. Hase, O. P. Hasekamp, J. Heymann, T. Kaminski, A. Laeng, G. Lichtenberg, M. De Mazière, S. Noël, J. Notholt, J. Orphal, C. Popp, R. Parker, M. Scholze, R. Sussmann, G. P. Stiller, T. Warneke, C. Zehner, A. Bril, D. Crisp, D. W. T. Griffith, A. Kuze, C. O'Dell, S. Oshchepkov, V. Sherlock, H. Suto, P. Wennberg, D. Wunch, T. Yokota, Y. Yoshida, The Greenhouse Gas Climate Change Initiative (GHG-CCI): comparison and quality assessment of near-surface-sensitive satellite-derived CO2 and CH4 global data sets, *Remote Sensing of Environment*, doi:10.1016/j.rse.2013.04.024, pp. 19, (in press), 2013.

/Buchwitz et al., 2000a/ Buchwitz, M., Rozanov, V. V., and Burrows, J. P.: A correlated-k distribution scheme for overlapping gases suitable for retrieval of atmospheric constituents from moderate resolution radiance measurements in the visible/near-infrared spectral region, J. Geophys. Res., 105, 15247-15262, 2000.

/Buchwitz et al., 2000b/ Buchwitz, M., Rozanov, V. V., and Burrows, J. P.: A near infrared optimized DOAS method for the fast global retrieval of atmospheric CH_4, CO, CO_2, H_2O, and N_2O total column amounts from SCIAMACHY/ENVISAT-1 nadir radiances, J. Geophys. Res., 105, 15231-15246, 2000.

/Buchwitz et al., 2009/ Buchwitz, M., Reuter, M., Schneising, O., Heymann, J., Bovensmann, H., and Burrows, J. P., Towards an improved CO_2 retrieval algorithm for SCIAMACHY on ENVISAT, Proceedings Atmospheric Science Conference, Barcelona, Spain, 7-11 Sept 2009, ESA Special Publication SP-676, 2009.

/Butz et al., 2012/ A. Butz, A. Galli, O. Hasekamp, J. Landgraf, P. Tol, I. Aben, TROPOMI aboard Sentinel-5 Precursor: Prospective performance of CH4 retrievals for aerosol and cirrus loaded atmospheres,,Remote Sensing of Environment, Volume 120, 267-276, 2012

/Butz et al., 2011/ Butz, A., Guerlet, S., Hasekamp, O., Schepers, D., Galli, A., Aben, I., Frankenberg, C., Hartmann, J. M., Tran, H., Kuze, A., Keppel-Aleks, G., Toon, G., Wunch, D., Wennberg, P., Deutscher, N., Griffith, D., Macatangay, R., Messerschmidt, J., Notholt, J., and Warneke, T.: Toward accurate CO_2 and CH_4 observations from GOSAT, Geophys. Res. Lett., 38, L14 812, doi:10.1029/2011GL047888, http://www.agu.org/pubs/crossref/2011/2011GL047888.shtml, 2011.

/Butz et al., 2010/ Butz, A., O. P. Hasekamp, C. Frankenberg, J. Vidot, and I. Aben, CH_4 retrievals from space-based solar backscatter measurements: performance evaluation against simulated aerosol and cirrus loaded scenes, J. Geophys. Res., doi:10.1029/2010JD014514, 2010.

/Butz et al., 2009/ Butz, A., O. P. Hasekamp, C. Frankenberg, I. Aben, Retrievals of atmospheric CO_2 from simulated space-borne measurements of backscattered near-infrared sunlight: accounting for aerosol effects, Appl. Opt., 48, 18, 3322 − 3336, 2009.

/Caron et al., 2014/ Caron, J., Bézy, J.-L., Computing non-linearity from detector characterization data: solution to the problem of large NL values at low signals, ESA presentation, Ref.: IPD-HO-ESA-391, June 2014, 2014.

/Caron et al., 2014b/ Caron, J., Sierk, B., Bézy, J.-L., Loescher, A., Meijer, Y., The CarbonSat Candidate Mission: Radiometric and spectral performance over spatially heterogeneous scenes, International Conference on Space Optics, ICSO 2014, 7-10 October 2014, Tenerife, Canary Islands, Spain, 2014.

/Chimot et al., 2014/ Chimot, Julien, Andrzej KLONECKI, Pascal PRUNET, Jean-François VINUESA, Claude CAMY-PEYRET, Gregoire BROQUET, Frédéric CHEVALLIER, Philippe CIAIS, François-Marie BREON, Emmanuel RENAULT, Sander HOUWELING, Heinrich BOVENSMANN, Dhanyalekshmi PILLAI, Maximilian REUTER, Michael BUCHWITZ, Julia MARSHALL, Dominik BRUNNER, Peter BERGAMASCHI, LOGOFLUX - CarbonSat Earth Explorer 8 Candidate Mission - Inverse Modelling and Mission Performance Study, Final Report of ESA study contract n° 400010537/12/NL/CO, 2014.

/Cogan et al., 2012/ Cogan, A. J., et al., Atmospheric carbon dioxide retrieved from the Greenhouse gases Observing SATellite (GOSAT): Comparison with ground-based TCCON observations and GEOS-Chem model calculations, J. Geophys. Res., 117, D21301, doi:10.1029/2012JD018087, 2012.

/Connor et al., 2008/ Connor, B. J., H. Boesch, G. Toon, B. Sen, C. Miller, and D. Crisp, Orbiting Carbon Observatory: Inverse method and prospective error analysis, J. Geophys. Res., 113, D05305, doi:10.1029/2006JD008336, 2008.

/Crisp et al., 2004/ Crisp, D., Atlas, R. M., Breon, F.-M., Brown, L. R., Burrows, J. P., Ciais, P., Connor, B. J., Doney, S. C., Fung, I. Y., Jacob, D. J., Miller, C. E., O'Brien, D., Pawson, S., Randerson, J. T., Rayner, P., Salawitch, R. S., Sander, S. P., Sen, B., Stephens, G. L., Tans, P. P., Toon, G. C., Wennberg, P. O., Wofsy, S. C., Yung, Y. L., Kuang, Z., Chudasama, B., Sprague, G., Weiss, P., Pollock, R., Kenyon, D., and Schroll, S.: The Orbiting Carbon Observatory (OCO) mission, Adv. Space Res., 34, 700-709, 2004.

/Crisp et al., 2012/ D. Crisp, B. M. Fisher, C. O'Dell, C. Frankenberg, R. Basilio, H. Bösch, L. R. Brown, R. Castano, B. Connor, N. M. Deutscher, A. Eldering, D. Griffith, M. Gunson, A. Kuze, L. Mandrake, J. McDuffie, J. Messerschmidt, C. E. Miller, I. Morino, V. Natraj, J. Notholt, D. M. O'Brien, F. Oyafuso, I. Polonsky, J. Robinson, R. Salawitch, V. Sherlock, M. Smyth, H. Suto, T. E. Taylor, D. R. Thompson, P. O. Wennberg, D. Wunch, and Y. L. Yung
Atmos. Meas. Tech., 5, 687-707, 2012

/CS L1L2-I-Study FR/ Bovensmann, H., Buchwitz, M., Reuter, M., Krings, T., Heymann, H., Boesch, H., Landgraf, J., CarbonSat Earth Explorer 8 Candidate Mission “Level-2 and Level-1B Requirements Consolidation Study“, Final Report, ESA Contract No 4000105676/12/NL/AF, Version: 2.2, 18. July 2014, doc. ID: IUP-CS-L1L2-FR-01, 2014.

/CS MRD v1.2, 2013/ ESA, CarbonSat – Candidate Earth Explorer Opportunity Mission – Mission Requirements Document, Issue 1, Revision 2, Reference EOP-SMA/2232/PI-pi, 23. May 2013, ESA Mission Science Division, 2013.

/CS RefSpec v5, 2013/ Buchwitz, M., CarbonSat Reference Spectra, Technical Report, Doc ID: IUP-CS-L12-TN-3e, version 5.0, 19. April 2013, IUP/IFE, Univ. Bremen, 2013.

/DeRooij and van der Stap, 1984/ W.A. DeRooij, C.C.A.H. VanderStap, Expansion of Mie scattering matrices in generalized spherical functions, Astron. Astrophys., 131, pp. 237–248, 1984.

/ESA S5 CO_2 Study, 2012/ Chimot, J., et al., Requirements for CO_2 monitoring by Sentinel-5, Final Report of ESA study contract n^o 4000103801 led by Noveltis, France, 30 Mar. 2012, 2012.

/Frankenberg et al., 2014/ Frankenberg, C. et al., Algorithm Theoretical Basis Document (ATBDv3) -The SRON IMAP-DOAS algorithm for the retrieval of XCH_4, v7.0 for the Essential Climate Variable (ECV), Greenhouse Gases (GHG), Version 3, 2014.

/Frankenberg et al., 2012/ Frankenberg, O’Dell, C, Guanter, L., and McDuffie,J., Chlorophyll fluorescence remote sensing from space in scattering atmospheres: Implications for its retrieval and interferences with atmospheric CO_2 retrievals, submitted to Atmos. Meas. Tech., 2012.

/Frankenberg et al., 2011a/ Frankenberg, C., Butz, A., and Toon, G. C.: Disentangling chlorophyll fluorescence from atmospheric scattering effects in O_2 A-

band spectra of reflected sun-light, Geophys. Res. Lett., 755 38, L03 801, doi:10.1029/2010GL045896, http://www.agu.org/pubs/crossref/2011/2010GL045896.shtml , 2011.

/Frankenberg et al., 2011b/ Frankenberg, C., Fisher, J., Worden, J., Badgley, G., Saatchi, S., Lee, J.-E., Toon, G., Butz, A., Jung, M., Kuze, A., and Yokota, T.: New global observations of the terrestrial carbon cycle from GOSAT: Patterns of plant fluorescence with gross primary productivity, Geophys. Res. Lett., 38, L17 706, http://dx.doi.org/10.1029/2011GL048738 , 2011.

/Frankenberg et al., 2011c/ Frankenberg, C., I. Aben, P. Bergamaschi, E. J. Dlugokencky, R. van Hees, S. Houweling, P. van der Meer, R. Snel, and P. Tol, Global column-averaged methane mixing ratios from 2003 to 2009 as derived from SCIAMACHY: Trends and variability, J. Geophys. Res., doi:10.1029/2010JD014849, 2011.

/Giannakaki et al., 2007/ Giannakaki, E., Balis, E. D., Amiridis, V., and Kazadzis, S: Optical and geometrical characteristics of cirrus clouds over a Southern European lidar station, Atmos. Chem. Phys., 7, 5519–5530, 2007.

/Guerlet et al., 2013/ Guerlet, S., A. Butz, D. Schepers, S. Basu, O. P. Hasekamp, A. Kuze, T. Yokota, J.-F. Blavier, N. M. Deutscher, D. W. T. Griffith, F. Hase, E. Kyro, I. Morino, V. Sherlock, R. Sussmann, A. Galli and I. Aben, Impact of aerosol and thin cirrus on retrieving and validating XCO_2 from GOSAT shortwave infrared measurements, J. Geophys. Res., doi: 10.1002/jgrd.50332, 2013.

/Guerlet et al., 2012/ Guerlet, S., Butz, A., Schepers, D., Basu, S., Hasekamp, O. P., Kuze, A., Yokota, T., Blavier, J.-F., Deutscher, N. M., Griffith, D. W. T., Hase, F., Kyro, E., Morino, I., Sherlock, V., Sussmann, R., Galli A., and Aben, I., Impact of aerosol and thin cirrus on retrieving and validating XCO_2 from GOSAT shortwave infrared measurements, submitted to J. Geophys. Res., 2012.

/Hamazaki et al., 2005/ Hamazaki, T., Y. Kaneko, A. Kuze, and K. Kondo, Fourier transform spectrometer for greenhouse gases observing satellite (GOSAT), in Proceedings of SPIE, vol. 5659, p. 73, 534, 2005.

/Hansen, 1998/ Hansen, P. C., Rank-deficient and discrete Ill-posed problems: Numerical aspects of linear inversion. SIAM - Monographs on Mathematical Modeling and Computation, 1998

/Hasekamp and Landgraf, 2002/ O. P. Hasekamp and J. Landgraf, “A linearized vector radiative transfer model for atmospheric trace gas retrieval,” J. Quant. Spectrosc. Radiat. Transfer 75, 221–238 (2002).

/Hasekamp and Landgraf, 2002/ O. P. Hasekamp and J. Landgraf, “Linearization of vector radiative transfer with respect to aerosol properties and its use in satellite remote sensing,” J. Geophys. Res. 110, D04203 (2005).

/**Hasekamp and Butz, 2008/** O. P. Hasekamp and A. Butz, “Efficient calculation of intensity and polarization spectra in vertically inhomogeneous scattering and absorbing atmospheres,” J. Geophys. Res. 113, D20309 (2008).

/Hess et al., 1998/ Hess, M., P. Koepke, and I. Schult, Optical Properties of Aerosols and Clouds: The software package OPAC, Bull. Am. Met. Soc., 79, 831-844, 1998.

/Hess and Wiegner, 1994/ Hess, M., and M. Wiegner, Cop: a data library of optical properties of hexagonal ice crystals, Applied Optics, 33 , 7740–7746, 1994.

/Joiner et al., 2011/ Joiner, J., Yoshida, Y., Vasilkov, A. P., Yoshida, Y., Corp, L. A., and Middleton, E. M.: First observations of global and seasonal terrestrial chlorophyll fluorescence from space, Biogeosciences, 8, 637–651, doi:10.5194/bg-8-637-2011, http://www.785 biogeosciences.net/8/637/2011, 2011.

/Kahn et al., 2001/ Kahn, R.; Banerjee, P.; McDonald, D. Sensitivity of multiangle imaging to natural mixtures of aerosols over ocean. J. Geophys. Res., 106, D16., 2001.

/Kauss 1998/ Kauss, Jean, Aerosol-Parametrisierung für Strahlungstransport-Simulationen im ultravioletten bis nahinfraroten Spektralbereich, Diplomarbeit im Studiengang Physik, Universität Bremen, Institut für Umweltphysik (IUP), 17.November 1998.

/Kawabata and Ueno, 1988/ Kawabata, K., and S. Ueno, The first three orders of scattering in vertically inhomogeneous scattering–absorbing media, *Astrophys. Space Sci.*, 150(2), 327–344, 1988.

/King et al., 1992/ M. D. King, Y. J. Kaufman, W. P. Menzel, D. Tanre: Remote-Sensing of Cloud, Aerosol, and Water-Vapor Properties from the Moderate Resolution Imaging Spectrometer (Modis). Ieee Transactions on Geoscience and Remote Sensing, vol. 30 (1), p. 2-27, 1992.

/King et al., 1997/ M. D. King, S.-C. Tsay, S. E. Platnick, M. Wang, K.-N. Liou: Cloud Retrieval Algorithms: Optical Thickness, Effective Particle Radius, and Thermodynamic Phase (Algorithm Theoretical Basis Documents). NASA Goddard Space Flight Center, ATBD-MOD-05, Version 5 (23.12.1997) http://modis.gsfc.nasa.gov/data/atbd/atbd_mod05.pdf, 1997.

/Kuze et al., 2009/ Kuze, A., Suto, H., Nakajima, M., and Hamazaki, T.: Thermal and near infrared sensor for carbon observation Fourier-transform spectrometer on the Greenhouse Gases Observing Satellite for greenhouse gases monitoring, Appl. Opt., 48, 6716–6733, 2009.

/Kriebel et al., 2003/ K. T. Kriebel, G. Gesell, M. Kastner, H. Mannstein: The cloud analysis tool APOLLO: improvements and validations. International Journal of Remote Sensing, vol. 24 (12), p. 2389-2408, 2003.

/Krings et al., 2011/ Krings, T., Gerilowski, K., Buchwitz, M., Reuter, M., Tretner, A., Erzinger, J., Heinze, D., Pflüger, U., Burrows, J. P., and Bovensmann, H., MAMAP - a new spectrometer system for column-averaged methane and carbon dioxide observations from aircraft: retrieval algorithm and first inversions for point source emission rates, Atmos. Meas. Tech., 4, 1735-1758, 2011.

/Krings et al., 2013/ Krings, T., K. Gerilowski, M. Buchwitz, J. Hartmann, T. Sachs, J. Erzinger, J. P. Burrows, and H. Bovensmann, Quantification of methane emission

rates from coal mine ventilation shafts using airborne remote sensing data, Atmos. Meas. Tech., 6, 151-166, 2013.

/**Landgraf et al., 2001/** Landgraf, J., Hasekamp, O.P., Box, M.A., Trautmann, T., "A linearized radiative transfer model for ozone profile retrieval using the analytical forward-adjoint perturbation theory", J. Geophys. Res., 106, p. 27291, 2001.

/Lindstrot et al., 2009/ Lindstrot, Rasmus and Preusker, Rene and Fischer, Jürgen: The retrieval of land surface pressure from MERIS measurements in the oxygen A band. Journal of Atmospheric and Oceanic Technology, 2009, 26, 1367-1377, 2009.

/Lindstrot et al., 2010/ Lindstrot, Rasmus and Preusker, Rene and Fischer, Jürgen: Remote Sensing of Multilayer Cloud-Top Pressure Using Combined Measurements of MERIS and AATSR on board Envisat. Journal of Applied Meteorology and Climatology, 2010, 49, 1191-1204, 2010.

/Litvinov et al., 1999/ Pavel Litvinov, Otto Hasekamp, Brian Cairns, Models for surface reflection of radiance and polarized radiance: Comparison with airborne multi-angle photopolarimetric measurements and implications for modeling top-of-atmosphere measurements, Remote Sensing of Environment 115, 781–792, doi:10.1016/j.rse.2010.11.005, 2011.

/Mioche et al., 2010/ Mioche, G., Josset, D., Gayet, J.-F., Pelon, J., Garnier, A., Minikin, A., and Schwarzenboeck, A.: Validation of the CALIPSO- CALIOP extinction coefficients from in situ observations in midlatitude cirrus clouds during the CIRCLE2 experiment , J. Geophys. Res., 115, D00H25, doi:10.1029/2009JD012376, 2010.

/Mishchenko and Travis, 1998/ Mishchenko, M.I., and L.D. Travis, 1998: Capabilities and limitations of a current FORTRAN implementation of the T-matrix method for randomly oriented, rotationally symmetric scatterers. *J. Quant. Spectrosc. Radiat. Transfer*, **60**, 309-324, doi:10.1016/S0022-4073(98)00008-9.

/Mishchenko et al., 1999/ M. I. Mishchenko, I. V. Geogdzhayev, B. Cairns, W. B. Rossow, and A. A. Lacis, “Aerosol retrievals over the ocean by use of channels 1 and 2 AVHRR data: sensitivity analysis and preliminary results,” Appl. Opt. 38, 7325–7341 (1999).

/Nadal and Breon, 1999/ Florence Nadal and Francois-Marie Breon, Parameterization of Surface Polarized Reflectance Derived from POLDER Spaceborne Measurements, IEEE TRANSACTIONS ON GEOSCIENCE AND REMOTE SENSING, VOL. 37, NO. 3, MAY 1999, 1999.

/Nakajima and King, 1990/ T. Nakajima, M. D. King: Determination of the Optical-Thickness and Effective Particle Radius of Clouds from Reflected Solar-Radiation Measurements.1. Theory. Journal of the Atmospheric Sciences, vol. 47 (15), p. 1878-1893, 1990.

/Natraj and Spurr, 2007/ Natraj, V. and Spurr, R. J. D.: A fast linearized pseudo-spherical two orders of scattering model to account for polarization in vertically inhomogeneous scattering absorbing media, J. Quant. Spectrosc. Radiat. Transfer, 107, 263–293, doi:10.1016/j.jqsrt.2007.02.011, 2007

/Natraj et al., 2008/ Natraj, V., Boesch, H., Spurr, R. J. D., and Yung, Y. L.: Retrieval of *XCO*2 from simulated Orbiting Carbon Observatory measurements using the fast linearized R-2OS radiative transfer model, J. Geophys. Res., 113, D11 212, doi:10.1029/2007JD009017, 2008.

/Nakajima and Tanaka, 1988/ Nakajima, T. and Tanaka, M.: Algorithms for radiative intensity calculations in moderately thick atmospheres using a truncation approximation. J. Quant. Spectrosc. Radiat. Transfer, 40, 51–69, doi:10.1016/0022-4073(88)90031-3, 1988.

/O'Dell, 2010/, O'Dell, C.W.: Acceleration of multiple-scattering, hyperspectral radiative transfer calculations via low-streams interpolation, J. Geophys. Res., 115, D10 206, doi:10.1029/2009JD012803, 2010.

/O'Dell et al., 2012/ O'Dell, C. W., B. Connor, H. Boesch, D. O'Brien, C. Frankenberg, R. Castano, M. Christi, D. Crisp, A. Eldering, B. Fisher, M. Gunson, J. McDuffie, C. E. Miller, V. Natraj, F. Oyafuso, I. Polonsky, M. Smyth, T. Taylor, G. C. Toon, P. O. Wennberg, and D.Wunch, The ACOS CO_2 retrieval algorithm – Part 1: Description and validation against synthetic observations, Atmos. Meas. Tech., 5, 99–121, 2012.

/Oshchepkov et al., 2008/ Oshchepkov S., Bril A., Yokota T., PPDF-based method to account for atmospheric light scattering in observations of carbon dioxide from space. J. Geophys. Res., 113, D23210, 2008.

/Parker et al., 2014/ Parker et al., Product User Guide Version 2 (PUG v2) for the University of Leicester Full -Physics XCO2 GOSAT Data Product (CO2_GOS_OCFP) for the Essential Climate Variable (ECV), Greenhouse Gases (GHG), version 2.1, 2014.

/Parker et al., 2011/ Parker,R., Boesch,H, Cogan,A., Fraser, A., Feng, L, Palmer, P., Messerschmidt, J., Deutscher, N., Griffth, D, Notholt, J., Wennberg, P. and Wunch, D., Methane Observations from the Greenhouse gases Observing SATellite: Comparison to ground-based TCCON data and Model Calculations, Geophys. Res. Lett., doi:10.1029/2011GL047871, 2011.

/Peters et al., 2007/ Peters, W., et al., An atmospheric perspective on North American carbon dioxide exchange: CarbonTracker, Proc. Natl. Acad. Sci. U. S. A., 104(48), 18,925–18,930, doi:10.1073/pnas.0708986104, 2007

/Phillips, 1963/ Phillips, D., A technique for the numerical solution of certain integral equations of the first kind, Journal of the ACM (JACM), 9 , 84–97, 1962

/Pollock et al., 2010/ Pollock, R., Haring, R. E., Holden, J. R., et al., The Orbiting Carbon Observatory Instrument: Performance of the OCO Instrument and Plans for the OCO-2 Instrument, in Proc. of SPIE, Vol. 7826, Sensors, Systems and Next-Generation Satellites XIV, edited by Roland Meynart, Steven P. Neeck and Haruhisa Shimoda, doi: 10.1117/12.865243, (corrected version provided by D. Crisp, JPL), 2010.

/Preusker, 1999/ R. Preusker: Fernerkundung des Luftdrucks am Oberrand von Wolken mit Messungen in der O2A-Bande. Dissertation, publisher J.Fischer, 2001, ISBN 3-931545-19-9, 1999.

/Preusker and Lindstrot, 2009/ Preusker, Rene and Lindstrot, Rasmus: Remote Sensing of Cloud-Top Pressure Using Moderately Resolved Measurements within the Oxygen A Band - A Sensitivity Study. Journal of Applied Meteorology and Climatology, 2009, 48, 1562-1574, 2009.

/Rascher et al., 2009/ Rascher, U., Agati, G., Alonso, L., Cecchi, G., Champagne, S., Colombo, R., Damm, A., Daumard, F., de Miguel, E., Fernandez, G., Franch, B., Franke, J., Gerbig, C., Gioli, B., Gomez, J. A., Goulas, Y., Guanter, L., Gutierrez-de-la-Camara, O´ ., Hamdi, K., Hostert, P., Jimenez, M., Kosvancova, M., Lognoli, D., Meroni, M., Miglietta, F., Moersch, A., Moreno, J., Moya, I., Neininger, B., Okujeni, A., Ounis, A., Palombi, L., Raimondi, V., Schickling, A., Sobrino, J. A., Stellmes, M., Toci, G., Toscano, P., Udelhoven, T., van der Linden, S., and Zaldei, A.: CEFLES2: the remote sensing component to quantify photosynthetic efficiency from the leaf to the region by measuring sun-induced fluorescence in the oxygen absorption bands, Biogeosciences, 6, 1181–1198, doi:10.5194/bg-6-1181-2009, 2009.

/Reuter et al., 2014/ Reuter et al., Algorithm Theoretical Basis Document (ATBD)-The Bremen Optimal Estimation DOAS (BESD) algorithm for the retrieval of XCO_2 for the Essential Climate Variable (ECV), Greenhouse Gases (GHG), Version 3, 2014.

/Reuter et al., 2011/ Reuter, M., H. Bovensmann, M. Buchwitz, J. P. Burrows, B. J. Connor, N. M. Deutscher, D. W. T. Griffith, J. Heymann, G. Keppel-Aleks, J. Messerschmidt, J. Notholt, C. Petri, J. Robinson, O. Schneising, V. Sherlock, V. Velazco, T. Warneke, P. O. Wennberg, and D. Wunch, Retrieval of atmospheric CO_2 with enhanced accuracy and precision from SCIAMACHY: Validation with FTS measurements and comparison with model results, J. Geophys. Res., 116, D04301, doi:10.1029/2010JD015047, 2011.

/Reuter et al., 2010/ Reuter, M., Buchwitz, M., Schneising, O., Heymann, J., Bovensmann,H., and Burrows, J. P., A method for improved SCIAMACHY CO_2 retrieval in the presence of optically thin clouds, Atmos. Meas. Tech., 3, 209-232, 2010.

/Rodgers 2000/ Rodgers, C. D.: “Inverse Methods for Atmospheric Sounding: Theory and Practice”, World Scientific, Singapore, 2000.

/Rooij and van der Stap, 1984/ W. A. de Rooij and C. C. A. H. van der Stap, “Expansion of Mie scattering matrices in generalized spherical functions,” Astron. Astrophys. 131, 237–248, 1984.

/Rossow, 1989/ W. B. Rossow: Measuring Cloud Properties from Space: A Review. Journal of Climate, vol. 2 (3), p. 201-213, 1989.

/Rossow et al., 1993/ W. B. Rossow, A. W. Walker, L. C. Garder: Comparison of ISCCP and Other Cloud Amounts. Journal of Climate, vol. 6 (12), p. 2394-2418, 1993.

/Rossow and Garder, 1993a/ W. B. Rossow, L. C. Garder: Cloud Detection Using Satellite Measurements of Infrared and Visible Radiances for Isccp. Journal of Climate, vol. 6 (12), p. 2341-2369, 1993.

/Rossow and Garder, 1993b/ W. B. Rossow, L. C. Garder: Validation of Isccp Cloud Detections Journal of Climate, vol. 6 (12), p. 2370-2393, 1993.

/Rothman et al., 2005/ L. S. Rothman, D. Jacquemart, A. Barbe, D. Chris Benner, M. Birk, L. R. Brown, M. R. Carleer, C. Chackerian, K. Chance, L. H. Coudert, V. Dana, V. M. Devi, J.-M. Flaud, R. R. Gamache, A. Goldman, J.-M. Hartmann, K. W. Jucks, A.G. Maki, J.-Y. Mandin, S. T. Massie, J. Orphal, A. Perrin, C. P. Rinsland, M. A. H. Smith, J. Tennyson, R. N. Tolchenov, R. A. Toth, J. Vander Auwera, P. Varanasi, and G. Wagner, “The HITRAN 2004 molecular spectroscopic database,” J. Quant. Spectrosc. Radiat. Transfer 96, 139–204 (2005).

/Rozanov et al. 2014/ Rozanov, V.V., A.V. Rozanov, A.A. Kokhanovsky, J.P. Burrows: Radiative transfer through terrestrial atmosphere and ocean: Software package SCIATRAN. Journal of Quantitative Spectroscopy and Radiative Transfer, http://dx.doi.org/10.1016/j.jqsrt.2013.07.004, Vol. 133, p. 13–71, 2014.

/Rozanov et al., 2006/ Rozanov, V., and A. Kokhanovsky, The solution of the vector radiative transfer equation using the discrete ordinates technique: Selected applications, Atmospheric Research 79, 241-265, 2006.

/**Rozanov et al., 2005/** Rozanov A., V. Rozanov, M. Buchwitz, A. Kokhanovsky and J.P. Burrows, SCIATRAN 2.0 - A new radiative transfer model for geophysical applications in the 175-2400 nm spectral region, Adv. Space Res., Vol. 36(5), 1015-1019, doi:10.1016/j.asr.2005.03.012, 2005.

/Schneising et al., 2011/ Schneising, O., Buchwitz, M., Reuter, M., Heymann, J., Bovensmann, H., Burrows, J. P., Long-term analysis of carbon dioxide and methane column-averaged mole fractions retrieved from SCIAMACHY, Atmos. Chem. Phys., 11, 2881-2892, 2011.

/**Schneising et al., 2012/** Schneising, O., P. Bergamaschi, H. Bovensmann, M. Buchwitz, J. P. Burrows, N. M. Deutscher, D. W. T. Griffith, J. Heymann, R. Macatangay, J. Messerschmidt, J. Notholt, M. Rettinger, M. Reuter, R. Sussmann, V. A. Velazco, T. Warneke, P. O. Wennberg, and D. Wunch, Atmospheric greenhouse gases retrieved from SCIAMACHY: comparison to ground-based FTS measurements and model results, Atmos. Chem. Phys., 12, 1527-1540, 2012.

/**Schneising et al., 2014a/** Schneising et al., Algorithm Theoretical Basis Document (ATBD)-SCIAMACHY WFM-DOAS (WFMD) XCO_2 and XCH_4 for the Essential Climate Variable (ECV), Greenhouse Gases (GHG), Version 3, 2014.

/**Schneising et al., 2014b/** Schneising, O., J. P. Burrows, R. R. Dickerson, M. Buchwitz, M. Reuter, and H. Bovensmann, Remote sensing of fugitive methane emissions from oil and gas production in North American tight geologic formations, Earth’s Future, 2, 548–558, doi:10.1002/2014EF000265, 2014.

/Schüller et al., 2005/ Schüller, Lothar and Bennartz, Ralf and Fischer, Jürgen and Brenguier, Jean-Louis: An algorithm for the retrieval of droplet number concentration and geometrical thickness of stratiform marine boundary layer clouds applied to MODIS radiometric observations. Journal of applied meteorology, 2005, 44, 28-38

/Spurr et al., 2001/ Spurr, R. J. D., Kurosu, T. P., and Chance, K. V.: A linearized discrete ordinate radiative transfer model 940 for atmospheric remote-sensing retrieval, J. Quant. Spectrosc. Radiat. Transfer, 68, 689–735, doi:10.1016/S0022-4073(00)00055-8, 2001.

/Spurr, 2002/ Spurr, R. J. D., Simultaneous derivation of intensities and weighting functions in a general pseudo-spherical discrete ordinate radiative transfer treatment, *J. Quant. Spectrosc. Rad. Tran.*, 75(2), 129–175, 2002.

/Stam e al., 1999/ Stam, D. M., De Haan, J. F., Hovenier, J. W., Degree of linear polarization of light emerging from the cloudless atmosphere in the oxygen A band, J. Geophys. Res., 104, D14, 16843-16858, 1999.

/Tol et al., 2011/ Paul Tol, Jochen Landgraf, and Ilse Aben: Instrument noise model for the Sentinel 5 SWIR bands, Technote SRON-TROPSC-TN-2011-002, Netherlands Institute for Space Research (SRON), Utrecht, The Netherlands, 2011.

/Toth et al., 2008/ R. A. Toth, L. R. Brown, C. E. Miller, V. Malathy Devi, and D. C. Benner, “Spectroscopic database of CO2 line parameters: 4300 7000cm−1,” J. Quant. Spectrosc. Radiat. Transfer 109, 906–921, 2008.

/Tikhonov, 1963/ Tikhonov, A., On the solution of incorrectly stated problems and a method of regularization, in Dokl. Acad. Nauk SSSR, vol. 151, p. 1, 1963.

/Twomey, 1963/ Twomey, S., On the numerical solution of Fredholm integral equations of the first kind by inversion of the linear system produced by quadrature. Journal of the Association Computer Machine, 10, 97–101, 1963.

/Wunch et al., 2011/ Wunch, D., et al., A method for evaluating bias in global measurements of CO_2 total columns from space, Atmospheric Chemistry and Physics, 11, 12317–12 337, doi:10.5194/acp-11-12317-2011, URL http://dx.doi.org/10.5194/acp-11-12317-2011.

/Yoshida et al., 2011/ Yoshida, Y., Ota, Y., Eguchi, N., Kikuchi, N., Nobuta, K., Tran, H., Morino, I., and Yokota, T.: Retrieval algorithm for CO_2 and CH_4 column abundances from short-wavelength infrared spectral observations by the Greenhouse gases observing satellite, Atmospheric Measurement Techniques, 4, 717–734, doi:10.5194/amt-4-717-2011, http://www.atmos-meas-tech.net/4/717/2011/, 2011.

***** End of Document *****